



UNIL | Université de Lausanne

Unicentre

CH-1015 Lausanne

<http://serval.unil.ch>

Year : 2022

GENERATION AND DESCRIPTION OF AN EXTENSIVE DATASET IN THE PERSPECTIVE OF GENERATING A 4D ATLAS OF THE DEVELOPING CEREBELLUM

Solanelles Farré Laura

Solanelles Farré Laura, 2022, GENERATION AND DESCRIPTION OF AN EXTENSIVE DATASET IN THE PERSPECTIVE OF GENERATING A 4D ATLAS OF THE DEVELOPING CEREBELLUM

Originally published at : Thesis, University of Lausanne

Posted at the University of Lausanne Open Archive <http://serval.unil.ch>

Document URN : urn:nbn:ch:serval-BIB_99F3949BD4C55

Droits d'auteur

L'Université de Lausanne attire expressément l'attention des utilisateurs sur le fait que tous les documents publiés dans l'Archive SERVAL sont protégés par le droit d'auteur, conformément à la loi fédérale sur le droit d'auteur et les droits voisins (LDA). A ce titre, il est indispensable d'obtenir le consentement préalable de l'auteur et/ou de l'éditeur avant toute utilisation d'une oeuvre ou d'une partie d'une oeuvre ne relevant pas d'une utilisation à des fins personnelles au sens de la LDA (art. 19, al. 1 lettre a). A défaut, tout contrevenant s'expose aux sanctions prévues par cette loi. Nous déclinons toute responsabilité en la matière.

Copyright

The University of Lausanne expressly draws the attention of users to the fact that all documents published in the SERVAL Archive are protected by copyright in accordance with federal law on copyright and similar rights (LDA). Accordingly it is indispensable to obtain prior consent from the author and/or publisher before any use of a work or part of a work for purposes other than personal use within the meaning of LDA (art. 19, para. 1 letter a). Failure to do so will expose offenders to the sanctions laid down by this law. We accept no liability in this respect.

Département de Neurosciences Fondamentales, UNIL

**GENERATION AND DESCRIPTION OF AN EXTENSIVE DATASET IN
THE PERSPECTIVE OF GENERATING A 4D ATLAS OF THE
DEVELOPING CEREBELLUM**

Thèse de doctorat en Neurosciences

présentée à la

Faculté de biologie et de médecine
de l'Université de Lausanne

par

Laura Solanelles Farré

Biologiste diplômé de l'Université de Barcelone

Jury

Prof. Olivier Braissant, Président
Prof. Ludovic Telley, Directeur de thèse
Prof. Nicolas Toni, Co-directeur de thèse
Prof. Fabrice Ango, Expert
Prof. Gioele La Manno, Expert

Thèse n° 340

Lausanne 2022

*Programme doctoral interuniversitaire en Neurosciences
des Universités de Lausanne et Genève*

Imprimatur

Vu le rapport présenté par le jury d'examen, composé de

Président·e	Monsieur	Prof.	Olivier	Braissant
Directeur·trice de thèse	Monsieur	Prof.	Ludovic	Telley
Co-Directeur·trice de thèse	Monsieur	Prof.	Nicolas	Toni
Expert·e·s	Monsieur	Prof.	Fabrice	Ango
	Monsieur	Prof.	Gioele	La Manno

le Conseil de Faculté autorise l'impression de la thèse de

Madame Laura Solanelles Farré

Titulaire d'un Master en Recherche Biomédicale de l'Université de Barcelone (ES)


intitulée

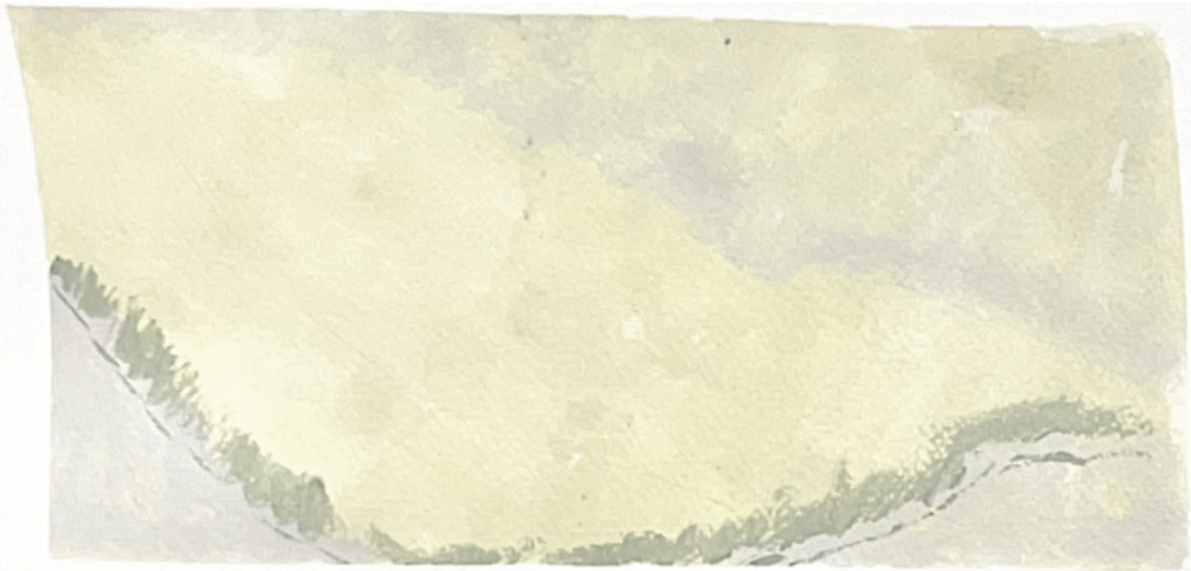
**GENERATION AND DESCRIPTION OF AN EXTENSIVE DATASET IN THE
PERSPECTIVE OF GENERATING A 4D ATLAS OF THE DEVELOPING CEREBELLUM**

Date de l'examen: 4 juillet 2022

Date d'émission de l'Imprimatur: Lausanne, le 2 août 2022

pour Le Doyen
de la Faculté de Biologie et de Médecine


Prof. Niko GELDNER
Directeur de l'Ecole Doctorale



ACKNOWLEDGMENTS |

I would like to start by thanking my supervisor, Prof. Ludovic Telley, for the opportunity he gave me in his new lab and his support. Thank you for having allowed me to evolve both academically and personally. The way was not always easy, but I come out of this experience stronger. Then I would like to thank the members of my committee Prof. Fabrice Ango and Prof. Gioele La Manno for their inputs and enthusiasm in evaluating my work. I have thoughts and a lot of gratitude for Prof. Alexandre Dayer, previous member of my committee who left us too soon, but who had the time to motivate me greatly during my midterm examination. My thanks as well to Prof. Nicolas Toni, my co-supervisor who was always available and ready to help. Thank you as well to president, Prof. Olivier Braissant, for his key role in moderating the whole process. I would also like to acknowledge the doctoral school, and specially Dr. Ulrike Toepel for her incredible support.

Next, I also wish to thank all the current and former members of the Telley lab. I would like to express my deepest gratitude to Andrea, with whom I started this adventurous path. Thank you for your patience, your help, your unconditional support and for having been there to witness many important milestones of my academic and personal life. Sister cells in this cluster. I very much appreciate the helpful contribution of Anurag Ranjak for his valuable input to the project.

Thanks should also go to Prof. Lukas Neuwkomm and Prof. Romano Regazzi and all the members of their labs, with whom we have shared the office and the lab space. I very much appreciate all the help you have provided. I would like to extend my gratitude to Arnau. Thank you for bringing a bit of home breeze when I needed the most. Gràcies amic.

Many thanks to the DNF and all the Professors and colleagues, with whom I had great pleasure working with. I would like to acknowledge the assistance of all the members of the CIF for their valuable contribution and experience, and for their kindness despite me saturating many times the free space of the server. I would also extend my gratitude to Prof. Jean-Yves Chatton as director of the CIF and the DNF.

I would like to thank all my friends and family without whom the completion of this PhD would not have been possible.

Merci beaucoup à ma famille et mes amis Suisses pour votre soutien, votre amour et votre merveilleux accueil pendant ces années de thèse.

Gràcies als amics de sempre, que malgrat la distància heu estat al meu costat al llarg d'aquests anys. Especialment gràcies a vosaltres, Ainara i Grego. Pel vostre suport, trucades en franges horàries incompatibles i per retrobades que sempre m'han omplert el cor.

Gràcies a la meva família. Especialment a vosaltres, Pare, Mare i Marta. Sense vosaltres no hauria arribat mai on soc ara. Gràcies per creure sempre en mi, per fer-me costat en tot moment, per la vostra preocupació i sobretot pel vostre amor.

Finally, thanks to you, Romain, for being the best colleague, friend and now husband. Thanks for your enormous contribution to this work. But mostly, thank you for having held tight to me all the way. T'estimo.

GENERATION AND DESCRIPTION OF AN EXTENSIVE DATASET IN THE PERSPECTIVE OF GENERATING A 4D ATLAS OF THE DEVELOPING CEREBELLUM

Laura Solanelles Farré

Department of fundamental Neuroscience, University of Lausanne, Switzerland

Cerebellum development is the result of a complex interaction between genetic programs and environmental factors from embryonic to postnatal stages. Despite recent efforts, there are still significant gaps in our understanding of how the precise cerebellar architecture is achieved. In particular, we lack insights regarding the molecular mechanisms that control the generation and differentiation of specific subtypes of cerebellar neuronal and non-neuronal populations. Although many studies have provided large amounts of data on how parts of this tangled developmental system function, one of the biggest challenges is still to understand how these data combine to precisely describe cerebellar development.

The work of this thesis presents the pioneering development of a novel integrative view of cerebellar structure and development. We aim to provide the first steps for the generation of a dynamic cerebellar framework over time, in the form of a 4D reference atlas, the 4D-CbF. This tool aims to achieve a sophisticated spatio-temporal multimodal data integration into its comprehensive framework, to ultimately model the cerebellar development.

By using the cell birth tracker FlashTag in combination with our 4D-CbF, we could reveal detailed spatio-temporal cell birth dynamics. Moreover, by combining FlashTag progenitor tracking together with cell type specific markers immunohistochemistry, we were able to show area specific developmental pathways of individual populations.

In addition, we produced a high throughput transcriptomics dataset of the developing CB with an unprecedented spatial resolution achieved by micro dissection. Altogether, these results gave precious information on the role of time, space, and expression dependent drive during the development of cerebellar structures and their cellular heterogeneity.

Overall, the work presented here greatly contribute to the improvement of available datasets for the developing CB, on top of demonstrating the development and usefulness of a novel and innovative way to integrate them together.

GÉNÉRATION ET DESCRIPTION D'UN VASTE JEU DE DONNÉES AVEC LA PERSPECTIVE DE CRÉER UN ATLAS EN 4D DU DÉVELOPPEMENT DU CERVELET

Laura Solanelles Farré

Département des Neurosciences Fondamentales, Université de Lausanne, Suisse

Le développement du cervelet, de l'état embryonnaire jusqu'après la naissance, est le résultat d'une interaction complexe entre programmes génétiques et environnement. Malgré de récents efforts, il existe encore de grandes lacunes dans notre compréhension de comment une si précise architecture peut être achevée. En particulier, les mécanismes moléculaires qui contrôlent la génération et la différenciation de sous-types cellulaires, tant neuronal que non neuronal, nous échappent encore. Bien que plusieurs études aient produit de grandes quantités de données donnant individuellement de précieux indices quant au déroulement de certains des aspects du développement du cervelet, le plus grand défi reste de comprendre comment ces résultats se combinent pour en décrire précisément le déroulement.

Le travail présenté dans cette thèse constitue les premiers pas vers la réalisation d'une nouvelle vue intégrative des structures du cervelet et de leur développement. Notre but est de générer un cadre modèle du cervelet, dynamique dans le temps, sous la forme d'un atlas de référence, le 4D-CbF. Cet outil a pour but de poser les bases pour l'intégration de plusieurs jeux de données venant de techniques différentes, et à terme, représenter un modèle complet du développement du cervelet.

Grace au traqueur cellulaire FlashTag injecté au stade embryonnaire, intégré et visualisé dans notre 4D-CbF, nous avons pu révéler les dynamiques spatio-temporelles précises des cellules du cervelet depuis leur jour de naissance. De plus, en ajoutant une étape d'immunohistochimie avec des marqueurs de populations spécifiques, nous avons mis à jour plusieurs trajectoires développementales de certains types cellulaires dans des zones individuelles.

En plus de cela, nous avons produit un jeu de données de transcriptomique à haut débit d'une résolution spatiale jamais atteinte grâce à la microdissection de zones correspondantes à notre atlas. Ensemble, nos résultats donnent de précieuses informations quant au rôle du temps, de l'espace et de l'expression génétique orchestrant le développement des structures du cervelet et de leur hétérogénéité.

En somme, le travail présenté dans cette thèse contribue grandement à améliorer les jeux de données existant sur le développement du cervelet, tout en démontrant la réalisation et l'utilité d'une nouvelle façon innovante de les intégrer les uns aux autres.

ABBREVIATION	MEANING
SERT	5-HT reuptake transporter
5-HT	serotonergic
ABA	Allen Brain Atlas
AD	Alzheimer's disease
AdevBA	Allen Developing Brain Atlas
Atoh1	Atonal homologue 1
ATXN1	ataxin 1
BCs	basket cells
BG	Bergmann glia
BMPs	bone morphogenic proteins
Calret	Calretinin
CB	cerebellum
CC	cerebellar cortex
CCF	Allen mouse brain common coordinate framework
CCF	common coordinate framework
CdCs	candelabrum cells
CFs	climbing fibers
CNS	central Nervous system
CP	copula of the pyramis
Crus I	crus I of the ansiform lobule
Crus II	crus II of the ansiform lobule
CSF	cerebrospinal fluid
D -V	dorsal - ventral
DA	dopamine
DCN	deep cerebellar nuclei
Dent	dentate nucleus
Emb	emboliform
En1	engrailed homeobox 1
Ephys	electrophysiology
ExM	expansion Microscopy
Fast	fastigial nucleus
Fl	flocculus
fMRI	functional magnetic resonance imaging
GCPs	Granule cells progenitors
GCs	granule cells
GIs	GABAergic
GL	granule cell layer
Glob	globose
GM	grey matter
GoCs	Golgi cells

H	hemisphere
hgRNA	self-homing guide RNA
I	lingula
ICA	independent-component analysis
iEGL	Inner EGL
IHC	immunohistochemistry
II	ventral lobule of the lobulus centralis
III	dorsal lobule of the lobulus centralis
IntA	anterior interposed nucleus
IntP	posterior interposed nucleus
iO	inferior olive
iPSCs	induced pluripotent stem cells
ISH	<i>in situ</i> hybridization
IsO	isthmus organizer
IV	ventral lobule of culmen
IX	uvula
k-NNGs	k-nearest neighbor graphs
LCs	Lugaro cells
Lmx1b	LIM homeobox transcription factor 1 beta
LSM	light-sheet microscopy
M-L	medio-lateral
MFs	mossy fibers
MHB	midbrain-hindbrain boundary
ML	molecular cell layer
MLIs	molecular layer interneurons
NA	noradrenergic
NET	NA transporter
Ngn	neurogenin
Ngrn	Neurogranin
oEGL	Outer EGL
Olig3	oligodendrocyte factor 3
Ophys	optical physiology
Par	Parvalbumin
PC	Purkinje cell
PCA	principal-component analysis
PCL	Purkinje cell layer
PCPs	PCs progenitors
Pfl	paraflocculus
PLIs	Purkinje layer interneurons
PM	paramedian lobule
Pv	paravermis
PWM	prospective white matter

R-C	rostral - caudal
RELN	Reelin
RG	radial glial
ROR α	retinoic acid-related orphan nuclear receptor α
SCA1	spinocerebellar ataxia type 1
scATAC-seq	single-cell assay for transposase-accessible chromatin
scRNA-seq	single-cell RNA sequencing
SCs	stellate cells
Shh	Sonic Hedgehog
SIM	simple lobule
SM	super-resolution microscopy
smFISH	single-molecule fluorescent <i>in situ</i> hybridization
snRNA-seq	single-nucleus RNA-seq
t-SNE	t-stochastic neighbor embedding
TEM	transmission electron microscope
TF	transcription factor
TGFB	transforming growth factor β
TH	tyrosine hydroxylase
TS	Theiler Stages
UBCs	unipolar brush cells
V	dorsal lobule of culmen
V	vermis V
VI	declive
VII	tuber
VIII	pyramis
VL	ventral Lateral Nucleus
WM	white matter WM
X	nodulus

LIST OF FIGURES	- 25 -
INTRODUCTION	- 29 -
CHAPTER 1	
THE CEREBELLUM	- 31 -
1. Cerebellar structure	- 32 -
1.1. Cerebellar gross anatomy	- 33 -
2. Cerebellar cytoarchitecture	- 34 -
2.1. Cerebellar Cortex	- 34 -
2.2. Deep Cerebellar Nuclei	- 36 -
3. Cerebellar connectivity	- 36 -
3.1. Cerebellar output	- 37 -
3.2. Cerebellar inputs and microcircuitry	- 39 -
3.2.1.1. Mossy Fibers	- 39 -
3.2.1.2. Climbing Fibers	- 40 -
3.2.1.3. Other afferences	- 41 -
4. Cerebellar function	- 42 -
4.1. Motor functions	- 43 -
4.1.1. Cerebro-cerebellar circuit	- 43 -
4.1.2. Vestibulo-cerebellar circuit	- 44 -
4.1.3. Spino-cerebellar circuit	- 45 -
4.2. Non-motor functions	- 45 -
5. Cerebellum in disease	- 47 -
5.1. Motor disorders	- 48 -
5.1.1. Ataxias	- 48 -
5.1.2. Parkinson Disease	- 49 -
5.2. Cognitive disorders	- 49 -
5.2.1. Autism	- 50 -
5.2.2. Alzheimer Disease	- 50 -

5.3.	Cancer	- 50 -
5.3.1.	Medulloblastoma	- 51 -
6.	Cerebellar evolution	- 52 -
7.	Cerebellar foliation and patterning	- 55 -
8.	Cerebellar development	- 56 -
8.1.	Midbrain-hindbrain boundary development	- 58 -
8.2.	Establishment of the cerebellar territory	- 61 -
8.3.	Specification of Cerebellar progenitors	- 63 -
8.3.1.	The rhombic lip	- 66 -
8.3.2.	The ventricular zone	- 67 -
8.4.	Neuronal development	- 68 -
8.4.1.	GABAergic lineage: description and development	- 69 -
8.4.1.1.	Purkinje cells	- 70 -
8.4.1.2.	Molecular layer interneurons: Stellate and Basket cells	- 73 -
8.4.1.3.	Golgi cells	- 75 -
8.4.1.4.	Lugaro cells	- 77 -
8.4.1.5.	Globular cells	- 78 -
8.4.1.6.	Inhibitory DCN neurons	- 78 -
8.4.2.	Glutamatergic lineage: description and development	- 79 -
8.4.2.1.	Granule cells	- 79 -
8.4.2.2.	Unipolar Brush cells	- 81 -
8.4.2.3.	Candelabrum cells	- 83 -
8.4.2.4.	Excitatory DCN neurons	- 83 -
8.5.	Non-neuronal development	- 84 -
8.5.1.	Astrocytes	- 85 -
8.5.2.	Oligodendrocytes	- 88 -
8.5.3.	Microglia	- 89 -
8.5.4.	Ependymal cells	- 89 -

CHAPTER 2

TOWARDS THE CONSTRUCTION OF A 4D CEREBELLAR MODEL: KNOWLEDGE AND TECHNOLOGY

- 90 -

1.	From observations to high-throughput profiling	- 90 -
1.1.	The histological era	- 93 -
1.2.	The physiological era	- 97 -
1.3.	The multiomic era	- 99 -
1.3.1.	scRNA-seq	- 100 -
11.3.1.1.	Differentiation Trajectory Reconstruction	- 101 -
1.3.2.	Lineage tracing	- 102 -
1.3.3.	Spatial transcriptomics	- 103 -
2.	Histological and multiomics available data sets	- 104 -
2.1.	ISH-based datasets (Allen Brain)	- 106 -
2.2.	ScRNA-seq based datasets	- 107 -
2.3.	Type-specific mRNA purification-based datasets (Buchholz)	- 109 -
2.4.	Neurogenic birthdate tagging-based datasets (Hirata)	- 109 -
3.	4D integration tools	- 110 -
	AIM OF THE PROJECT	- 113 -
	MATERIALS AND METHODS	- 117 -
	RESULTS	- 133 -
1.	The 4D reference atlas of the developing CB	- 135 -
1.1.	The 3D average CP template	- 137 -
1.2.	Annotation workflow for building 3D structures	- 137 -
1.3.	Automatic cell counting and 3D registration pipeline	- 137 -
2.	Spatio-temporal description of proliferation patterns in the CP	- 139 -
2.1.	Temporal patterns of proliferation in the CP	- 140 -
2.2.	Spatial patterns of proliferation in the CP	- 140 -
3.	Cell cycle dynamics of cerebellar progenitors is not equal across ages and areas within the CP	- 143 -
3.1.	EdU/BrdU dual labelling of the CP	- 143 -
3.2.	Spatio-temporal cell cycle dynamics in the CP	- 145 -
		- 23 -

4. FT allows for the labelling and tracking of cerebellar progenitors from embryonic to perinatal stages	- 147 -
4.1. Flash Tag labelling of newborn cells in the developing CB	- 147 -
4.2. Flash Tag validation in the CB	- 148 -
5. Cerebellar progenitors birth date seems to influence their migration rate and pathway within the CP	- 151 -
6. Cell birth Flash Tag analysis reveal identity- and spatio- temporal correlations in the P7 cerebellum	- 152 -
6.1. Cerebellar cells birth date influences their anatomical position in the P7 cerebellum	- 153 -
6.2. Cerebellar cortical neuronal cells populations temporal birth	- 157 -
7. Transcriptomics analysis of perinatal cerebellum reveals highly distinct cell populations	- 163 -
DISCUSSION	- 167 -
REFERENCES	- 193 -

INTRODUCTION

Figure 1	Schematic representation of cerebellar structure	-33-
Figure 2	Schematic representation of cerebellar cortex cytoarchitecture	-35-
Figure 3	DCN anatomy and cortico-nuclear connections	-37-
Figure 4	Cerebellar local circuitry	-39-
Figure 5	NA and 5HT afferences in the cerebellar cortex	-41-
Figure 6	Teleost cerebellar afferent and efferent circuitry	-53-
Figure 7	Cerebellar development schematic representation	-57-
Figure 8	Establishment of the MHB	-60-
Figure 9	Molecular pathways operating in the MHB and the establishment of the IsO	-62-
Figure 10	The cerebellar primordium	-65-
Figure 11	Schematic representation of cerebellar GABAergic lineage generation	-70-
Figure 12	Schematic representation of GCs neurogenesis and migration	-81-
Figure 13	From observation to high-throughput profiling	-91-
Figure 14	Allen Brain 3D Coordinate Framework	-92-
Figure 15	Summary of cerebellar histogenesis from Cajal's original drawings	-95-

AIM OF THE PROJECT

Figure 1	4D atlas of cerebellar development	-116-
-----------------	------------------------------------	-------

RESULTS

Figure 1	4D atlas of the developing cerebellum	-136-
Figure 2	Automatic cell counting and 3D registration pipeline	-139-
Figure 3	Proliferation patterns within the embryonic cerebellar primordium	-142-

Figure 4	Spatio-temporal cell cycle dynamics in CP	-144-
Figure 5	Spatio-temporal cell cycle dynamics of GABA- and glutamat- ergic progenitor cells	-146-
Figure 6	FlashTag (FT) labelling of new bon cells in the developing cerebellum	-150-
Figure 7	Cell birth in the CP	-152-
Figure 8	Cell cohort tracking in P7 cerebellum along the medio-lateral axis	-154-
Figure 9	Cortical neuronal populations generation in the P7 cerebellum	-159-
Figure 10	Transcriptomic profiling of the perinatal cerebellum	-164-
Figure 11	Transcriptomic profiling of the perinatal cerebellum linked to spatial information	-166-

DISCUSSION AND PERSPECTIVES

Figure 1	Perspectives: Embryonic cerebellar development profiling	-181-
-----------------	--	-------

CHAPTER 1

THE CEREBELLUM

The cerebellum (CB), also known as *the little brain*, is a region of the central nervous system (CNS) established exclusively in vertebrates (Lacalli et al., 1994)[1] (Hudson, 2016)[2]. The dominant view of cerebellar function over the past century assigned it a central role for the regulation of motor activities, such as the maintenance of balance and posture, as well as coordination of voluntary movements and motor learning (Cerminara et al., 2015)[3] (Leto et al., 2016)[4]. Interestingly, there is increasing evidence for the involvement of the cerebellar circuits in cognitive and emotional processes. Indeed, recent anatomical studies demonstrated that the projections from the cerebellum targets multiple non-motor areas in the prefrontal and posterior parietal cortex, on top of the well-known motor areas. (Strick et al., 2009)[5] The range of non-motor tasks associated with cerebellar activation is remarkable and includes tasks designed to assess attention, executive control, language, working memory, learning, pain, emotion, and addiction (Carta et al., 2019)[6] (D'Angelo et Casali, 2012)[7] (Watabe-Uchida et al., 2012)[8] (Beier et al., 2015)[9] (Wang et al., 2014)[10].

The multiple functions of the CB rely on neural circuits that involve a relatively small number of neuronal types, which have attracted the interests of scientists during the last century. However, there is still a lack of knowledge on how cerebellar precise architecture is achieved and the molecular mechanisms that underly this process, in particular, the generation and differentiation of specific subtypes of cerebellar cells populations (Haldipur et al., 2019)[11].

The modern age in the study of the CB started 130 years ago when Santiago Ramón y Cajal, pioneer of modern neuroscience, published his first important paper on the CNS with Golgi-impregnated material (Cajal, 1888)[12]. Indeed, a groundbreaking study of the CB brought the first evidence in favor of his well-known *neuron doctrine*, which proposes that between the nerve cell processes there is no continuity, only contiguity, including the laws that govern the morphology and the connections of nerve cells. In 4 years of intense investigation, Cajal was able to untangle the whole cerebellar circuit, providing the roots of our present knowledge on cerebellar organization. This knowledge has greatly expanded since then, mainly thanks to the emergence of new techniques (Sotelo, 2008)[13]. The technological evolution has led to the generation of an unprecedented amount of data, the development of mathematical methods and tools suited for its analysis. Despite some areas of the CNS enjoy thus far of optimized tools for such integration, such as the Allen mouse brain common coordinate framework (CCF) (Wang et al., 2020)[14], a similar approach is missing for a detailed study of the CB.

My thesis aims to provide the first steps to a novel integrative view of cerebellar structure and development. Concretely, this work contributes to the generation of a common spatial atlas for the murine CB in which we can harmonize multimodal datasets and allow their integration and comparison through time and space. Moreover, my work contributes to increase and ameliorate the available datasets, providing detailed information about cell birth dynamics, cerebellar progenitor behavior and cellular dynamics during embryonic development, as well as high throughput transcriptomics analysis of the developing postnatal CB cell types.

1. Cerebellar structure

The CB is a lobular structure located at the midbrain-hindbrain junction. Although it contributes to only 10% of total brain volume in humans, it hosts more than half of the total number of its neurons (Wang et al., 2001)[15] (Herculano-Houzel, 2009)[16]. Interestingly, cerebellar cells can be classified in a defined number of cellular types which are arranged in a highly conserved circuitry (Cerminara et al., 2015)[3] (Leto et al., 2016)[17] (Schilling et al., 2008)[18] (**Figure 1**).

In this section, I will first talk about cerebellar lobular structure and how cerebellar cells are organized on a large scale. I will then review cerebellar microarchitecture, treating cerebellar cortex (CC) and deep cerebellar nuclei (DCN) cellular diversity and organization. Finally, I will consider cerebellar connectivity, including its inputs and outputs, as well as the local circuitry.

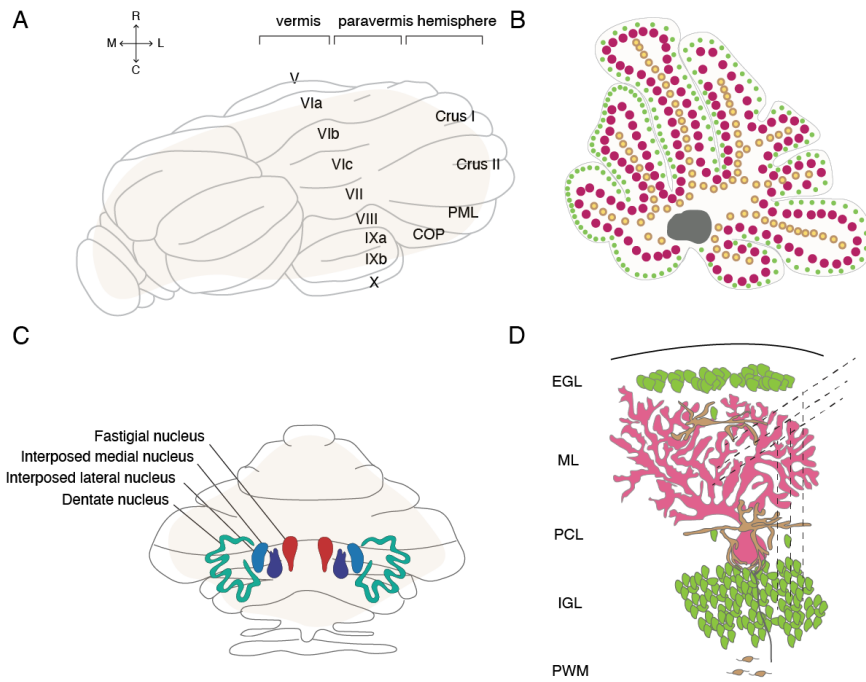


Figure 1. Schematic representation of the cerebellar structure. A) Medio-lateral division of the cerebellum. B) Sagittal view of the P0 vermis: DCN (grey) and CC (green, purple, yellow). C) DCN embed in the WM. Fastigial nucleus (red), Interposed medial nucleus (dark blue), Interposed lateral nucleus (light blue) and dentate nucleus (turquoise). D) CC local connectivity: PCs (pink), GCs (green) and GIs (brown). EGL (External granular layer), ML (molecular Layer), PCL (Purkinje cell layer), IGL (internal granule cell layer), PWM (prospective white matter).

1.1. Cerebellar gross anatomy

On a macroscale, the CB is divided along the medio-lateral (M-L) axis into two symmetric hemispheres (H) connected by a narrow midline known as the vermis (V). In between the H and the V, we can distinguish an intermediate region, the paravermis (Pv) (Sillitoe et al., 2012)[19] (Sudarov and Joyner, 2007)[20]. Like other structures of the CNS, the CB can be divided in grey matter (GM) and white matter (WM). The GM is distributed at the tightly folded cerebellar surface and contains most of the cerebellar cell bodies and dendrites forming the CC. The CC, in turn, is divided into different numbers of lobules across species (Larsell, 1952)[21] (Larsell, 1970). Lobules lie parallel to each other, extending from the V to the H. In mammals, including humans, and birds, the cerebellar V comprises ten major lobules that vary in size: lingula (I), ventral lobule of the lobulus centralis (II), dorsal lobule of the lobulus centralis (III), ventral lobule of culmen (IV), dorsal lobule of culmen (V), declive (VI), tuber (VII), pyramis (VIII), uvula (IX) and nodulus (X). In turn, the two H comprise the simple lobule (SIM), the crus I of the ansiform lobule (Crus I), the crus II of the ansiform lobule (Crus II), the

paramedian lobule (PM) and the copula of the pyramis (CP). Further laterally, there are the paraflocculus (Pfl) and flocculus (Fl) (Sillitoe et al, 2012)[19] (Sudarov et Joyner, 2007)[22]. Lobules are separated from each other by superficial fissures, and two deep fissures group lobules into 3 lobes: anterior and posterior lobes are separated by the primary fissure while the secondary (posterolateral) fissure divides the flocculonodular lobe from the posterior lobe. Anterior lobe includes lobules I – V, posterior lobe includes lobules VI – IX, and flocculonodular lobe includes the last lobule X (**Figure 1A-B**).

Underneath the CC, the WM provides the communication between different cerebellar cortical areas and connects to the rest of the body through the DCN projections to the thalamus and the brainstem. (**Figure 1C**) (Sillitoe et al., 2007)[23] (Rahimi-Balaei et al., 2015)[24]. The CB is connected to the brainstem with three pairs of cerebellar peduncles: inferior, medial, and superior cerebellar peduncles. The inferior cerebellar peduncle carries cerebellar afferents arriving from the spinal cord and medulla oblongata. The medial cerebellar peduncle, which lies rostro-lateral to the inferior one, carries afferents arriving from the pontine nuclei. The last cerebellar peduncle, the superior one, lies medial to the inferior peduncle and carries cerebellar efferents from the DCN rostrally. Uncinate tract and bulbar connections transfer cerebellar efferents to the brainstem (Carleton and Carpenter, 1983)[25]. Cerebellar afferents and efferents are further discussed in section 1.2.2 and 1.3, respectively.

2. Cerebellar cytoarchitecture

One of the most striking features of the CB is its three-layer crystal-like structure. Indeed, its sophisticated macrostructural organization opposes the regularity and apparent simplicity of its finest three-layer cellular structure. In this section, I will go over the cellular architecture of both CC and DCN, as well as their intercommunication circuits.

2.1. Cerebellar Cortex

Despite the complexity of the CB at the level of morphology and molecular coding, CC neuronal populations are homogeneously arranged in a highly conserved circuitry (**Figure 1D**, **Figure 2**). Glutamatergic and GABAergic neurons organize around Purkinje cells (PC), the main cell type of the cerebellar cortex, which provide the only output from the CB. As briefly mentioned above, neuronal populations in the CC are distributed in a three-layer structure tone (from ventral to dorsal):

- Granule cell layer (GL) (Mugnaini et al., 1997)[26] contains mainly the glutamatergic cells, Granule cells (GCs) (Wagner et al., 2017)[27], Unipolar brush cells (UBCs) and Candelabrum cells (CdCs), as well as GABAergic interneurons such as the Golgi cells (GoCs) and Lugaro cells (LCs).
- Purkinje cell layer (PCL) is the sole output of the CC, formed by an unilayer of PCs.
- Molecular cell layer (ML) contains the remaining GABAergic/ML interneurons (Gis/MLIs), such as Basket cells (BCs) and Stellate cells (SCs) (Glickstein and Voogd, 1998)[28], but also GCs axons and PCs dendrites.

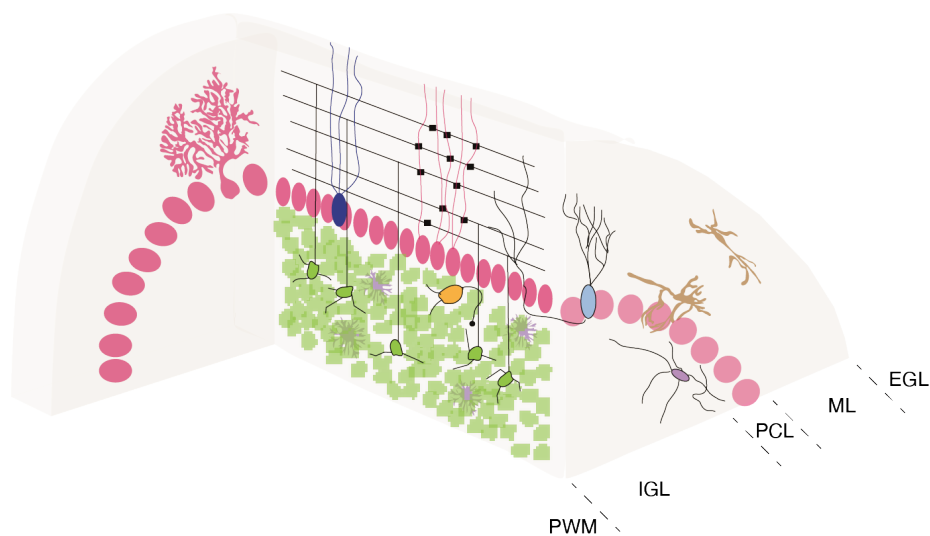


Figure 2. Schematic representation of cerebellar cortex cytoarchitecture. Cerebellar layers are represented from outside inwards: external granule cell layer (EGL), molecular layer (ML), purkinje cell layer (PCL), internal granule cell layer (IGL) and prospective white matter (PWM). Distinct cerebellar cell types are as well represented; Purkinje cells (pink), Granule cells (green), Unipolar Brush cells (yellow), Golgi cells (navy blue), Lugaro cells (light blue), Stellate cells (brown in ML), Basket cells (brown in PCL), non-neuronal cells (violet).

Of note, the CC is also constituted of non-neuronal population such as astrocytes, (Glickstein and Voogd 1998) [28] (Laine and Axelrad, 1994)[29] oligodendrocytes, and microglia, (Schilling et al., 2018)[30] (Sillitoe et al., 2007)[23] (Rahim-Balaei et al., 2015)[24] (Buffo et al., 2013)[31] (Leto et al., 2016)[4] which are not only essential for the proper cerebellar function, but also crucial for cerebellar developmental processes.

A detailed description of the cortical layers, as well of the distinct cell types that constitute them is given in section 5.

2.2. Deep Cerebellar Nuclei

The output gate of the CB is the DCN. The rodent DCN are arranged in 4 nuclei (from lateral to medial): dentate (Dent), interposed posterior (IntP) and anterior (IntA) and fastigial (Fast) (**Figure 3**). Magnetic Resonance Imaging (MRI)-based studies pointed out structural and anatomical characteristic organization of human DNC (Tellmann et al, 2015)[32]. They are the dent, the emboliform (Emb), the globose (Glob) and the fast. The human dent nucleus is greatly enlarged, and it has been portioned into a dorsal micro- and a ventral macrogyric part (Stilling, 1864). The Emb nucleus is located close to the medial side of the Dent while the Glob lies between the Fast nucleus medially and the Emb nucleus laterally. Both correspond to the above mentioned rodent IntP and IntA (Haroun, 2016)[33]. Each of these nuclei are composed of glutamatergic, GABAergic and glycinergic neurons but much less is known about their neuronal heterogeneity compared to the CC (Sugihara, 2011)[34]. The understanding of DCN cellular diversity and development is crucial to further differentiate their participation in the cerebellar circuitry and function. Interestingly, gene expression patterns in DCN neurons have revealed molecular heterogeneity that may mirror the molecular complexity of the CC (Chung et al., 2009)[35], (Person and Raman, 2011)[36] which, in turn, supports the tight functional correlation between the two main components of the CB. DCN cellular structure is composed of principal projection cells, inhibitory nucleo-cortical cells, non-inhibitory interneurons, nucleo-olivary projection cells and glycinergic premotor projection cells. Until now, DCN cell type distribution in the different nuclei has not been systematically investigated. However, some studies addressed cell distribution across a specific cerebellar nucleus or specific cell type distribution across the nuclei (Bagnall et al., 2009)[37], (Ruigrok et al., 2015)[38], (Hamodeh et al., 2014)[39].

3. Cerebellar connectivity

The CB contains the most elaborately patterned circuit of all the CNS structures, which may be essential for organizing the large number of functional and topographic zonal circuits (Reeber et al., 2013)[40] (White and Sillitoe, 2013)[41]. Thus, proper cerebellar function depends on the well-organized neuronal connections and the integration of afferent and efferent fibers throughout cerebellar circuitry.

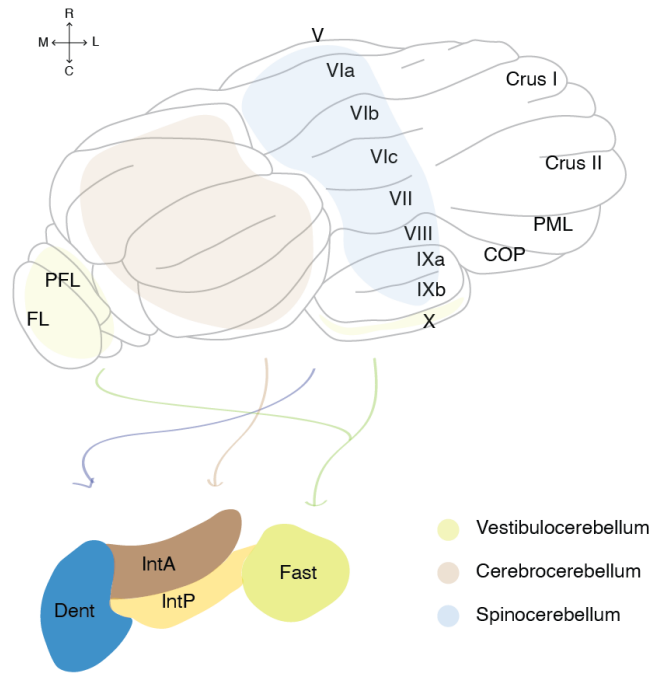


Figure 3. DCN anatomy and cortico-nuclear connections. Left hemisphere DCN are represented, from lateral to medial: dentate (Dent), Interposed Anterior (IntA), Interposed posterior (IntP) and Fastigial (Fast). Connections between the distinct cerebellar functional subdivisions and their corresponding DCN are as well illustrated: Vestibulocerebellum (green, caudal) - Fast; Cerebrocerebellum (brown, hemisphere and paravermis) - IntA and IntP; Spinocerebellum (blue, vermal) - Dent. (adapted from Sugihara and Shinoda, 2004)

3.1. Cerebellar output

Except for one direct projection to the vestibular nuclei, the DCN are an obligatory relay station for cerebellar output and are thought to act to coordinate and integrate PCs signals. The DCN project mainly to the neocortex (with a relay in the thalamus) and the brainstem. Intriguingly, cortico-nuclear connections are arranged in a topographical manner (Hawkes and Leclerc, 1986)[42] (Tabuchi et al, 1989)[43]. It has been shown that each nuclei receives projections from different regions of the CC: Dent from the cerebrocerebellum, IntA/IntP from the spinocerebellum and Fast from the vestibulocerebellum (**Figure 3**) (for CB functional divisions, see section 2). In turn, thalamic nuclei receiving projections from the DCN are divided into two different Ventral Lateral Nucleus (VL) subdivisions: anterior posterolateral area and X area, both directly projecting to the primary motor and premotor cortex. Therefore, the CB has access to the higher motor neurons which organize the muscle contraction sequence underlying the complex voluntary movements. The DCN project likewise the red nuclei, the superior colliculus, the vestibular nuclei, and the reticular formation.

In addition, viral studies have shown the existence of cerebellar projections to non-motor cortical areas which project back to this same cerebellar area, hence generating close loops, which are fundamental bricks for cerebellar function supporting and enhancing cerebellar learning (Gao et al., 2016)[44].

Another brain area receiving direct inputs from the DCN is the ventral tegmental area (VTA). DCN neurons projections were recently reported to be functionally sufficient as their optogenetic stimulation robustly increased the activity of VTA neurons (Carta et al., 2019)[6]. Being the origin of dopaminergic neurons projecting to the reward circuitry, the VTA is considered a central component of the reward circuitry. Indeed, in the same study DCN projection to the VTA was shown to be associated with reward (for non-motor functions of the CB, see section 2.2). The VTA is also known to be involved in the regulation of stress susceptibility and depression (Fox et Lobo, 2019)[45]. Cerebellar contribution to stress symptoms through DCN – VTA circuitry has been recently demonstrated in mice using chemogenetic manipulation during chronic stress application (Baek et al., 2022)[46]. Concretely, optogenetic activation of PCs in Crus I prevented stress-induced behavioral changes. The neuronal circuit from Crus I to the VTA through the Dent nucleus was identified using a combination of adeno-associated virus-based tracing and electrophysiological recording.

Strikingly, the recent demonstration of the cerebellar role in satiation and body weight homeostasis suggests a circuit connecting food-induced gut signals to the DCN (Low et al., 2021)[47]. Whether this connection is direct or instead, goes through the vagal signaling gut – hindbrain – CB remains to be proved. Using whole-brain functional magnetic resonance imaging (fMRI) blood oxygen level dependent analysis, the authors identified the CB as the only brain region showing significant differences in neural activity while fasting or after eating in individuals with Prader-Willi syndrome, characterized by a lack of satiation and obesity. RNA *in situ* hybridization analysis in mice, demonstrated that glutamatergic lateral DCN neurons are precisely activated by food intake. In addition, they used single-nucleus RNA sequencing (snRNA-seq) to uncover their molecular signature. Electrophysiological analysis demonstrated that cerebellar output markedly increases striatal dopamine levels, paradoxically leading to a reduction in the dopaminergic response to food and therefore a reduction in food intake.

Notwithstanding the outstanding functional diversity of the DCN and, broadly, the CB, there is still a significant gap in our understanding of the underlying molecular diversity and circuits. The results of my work might contribute to improve this downside by providing new insights into the cerebellar cell type diversity and generation.

3.2. Cerebellar inputs and microcircuitry

The CB receives information from two major afferent types: mossy fibers (MFs) and climbing fibers (CFs) (Sillitoe et al., 2007)[23]. In addition, a third set of afferents project to the CB as neuromodulatory fibers (Rahimi-Balaei et al., 2015)[24]. Directly or indirectly, PCs are the final destination of cerebellar afferents in the CC, which will eventually process the cerebellar output (**Figure 4**).

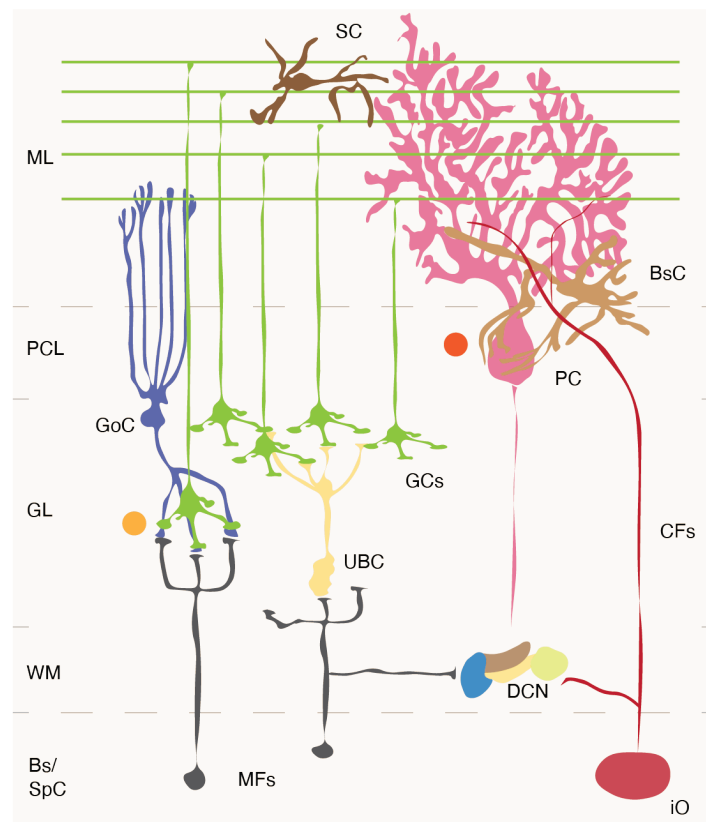


Figure 4. Cerebellar local circuitry. ML (molecular layer), PCL (purkinje cell layer), GL (granule cell layer), WM (white matter) Bs (brainstem), SpC (spinal cord), SC (stellate cell), BsC (basket cells), PC (purkinje cell), GoC (golgi cell), GCs (granule cells), UBC (unipolar brush cell), CFs (climbing fibers), DCN (deep cerebellar nuclei), MFs (mossy fibers), iO (inferior olive). Yellow circle (glomeruli), Red circle (Pinceau synapse) (Adapted from Consalez et al, 2021).

3.2.1.1. Mossy Fibers

MFs are composed by the axons coming mainly from pontine nuclei but also spinal cord, and transmit sensory and cortical information to GCs via excitatory synaptic contact in rosette-like structures, named glomerulus (Jakab and Hamori, 1988)[48], [49] (Ito, 2006)[49]. Here, MFs terminals, GCs dendrites and GoCs axon terminals make a 10um spherical junction shielded by a glial sheet. Thus,

GCs can be excited by MFs and inhibited by GoCs. From the GCs, the most abundant cell type of the whole brain, originate the parallel fibers (PFs). Ascending to the ML of the CC, these specialized axons bifurcate to generate T-shaped branches which will establish excitatory synapses with PCs dendritic spines. PCs dendritic branches represent the most notorious histologic characteristic of the CC. They extend from the PCL, where PCs bodies are located, to the ML above, and they extensively branch out in a single plane perpendicular with PFs trajectory, increasing therefore the synaptic contacts between these two cell types (~150000 PF synapse/PC) (Napper and Harvey, 1988)[50] (Zang and De Schutter, 2019) [51]. In addition, MLI contact each PC, and they provide feedforward inhibition on them (Eccles et al., 1967). Curiously, BCs-PCs specialized synaptic contacts are known as *Pinceau synapses* (Ango et al., 2004)[52] (Sillitoe et al., 2012)[19] (See more in section 4.4.1.4).

3.2.1.2. Climbing Fibers

PCs dendrites also receive excitatory modulatory afferences directly from the CFs, which originate from the inferior olivary nuclei in the brainstem. The function of the inferior olive (iO) is not clearly known, but current theories suggest that it takes part in movement error detection and movement timing control (De Zeeuw et al., 1998)[53] (Llinás et al., 2011)[54] (Mathy and Clark, 2014)[55]. A single CF innervates the proximal shafts of only one PC (Eccles et Llinás, 1966) [56]. Several models suggested that climbing fibers modulate the movement when modulating PFs – MFs connection with PCs (Marr, 1969)[57] (Albus, 1971)[58] (Ito and Kano, 1982)[59]. This theory has dominated cerebellar learning research for many years. However, recently it has been challenged by emerging experimental data at molecular, cellular, and behavioral levels (Gao et al, 2012)[60]. CFs input also affects interneurons through glutamate spillover in the M-L (Szapiro and Barbour, 2007)[61]. Altogether, the two excitatory inputs from MFs and CFs, and inhibitory inputs from MLI converge on the PCs and strongly modify ongoing PC activity according to their timings with respect to each other, by either depressing (long term depression, LTD (Ito and Kano, 1982) [59]) or potentiating (long term potentiation, LTP (Lev-Ram et al, 2002)[62] (Coesmans et al, 2004)[63]) the synapses.

Finally, PCs integrate excitation and inhibition they receive, and project to the DCN. As already mentioned, PCs are the sole output of the CC. PCs constitute a major part of the input that the DCN receives leading to a strong control of their principal cell activity (Palkovits et al., 1977)[64] (De Zeeuw and Berrebi, 1995)[65] (Uusisaari and Knöpfel, 2008)[66]. Remarkably, since PCs are GABAergic, direct projections from the CC are exclusively inhibitory. However, DCN also receive excitatory afferences from MFs and CFs collaterals. It has been observed that PCs inhibitory projection

in the DCN serves as modulator of these excitatory afferences, ultimately determining the final activity of DCN (Lang and Blenkinsop, 2011)[67] (Raman et al, 2000)[68].

3.2.1.3. Other afferences

Monoaminergic neuromodulatory afference to the CB, such as serotonergic (5-HT), noradrenergic (NA) and Dopamine (DA) have been also identified (Schweighofer et al., 2004)[69] (Longley et al., 2021)[70] (Flace et al., 2021)[71]. However, monoaminergic afferents have received less attention and their contribution to cerebellar functions is not yet well-understood.

5-HT or NA receptor expression has been detected in the main cerebellar cortical neuronal types (Papay et al., 2004) [72] (Papay et al., 2006)[73] (Hirono et al., 2008)[74]. Recently, full trajectories of 5-HT and NA afferent fibers and the geometry of their distribution relative to the vermal cerebellar architecture was revealed using 5-HT reuptake transporter (SERT) and NA transporter (NET) immunoreactivity (Longley et al., 2021)[70] (**Figure 5**).

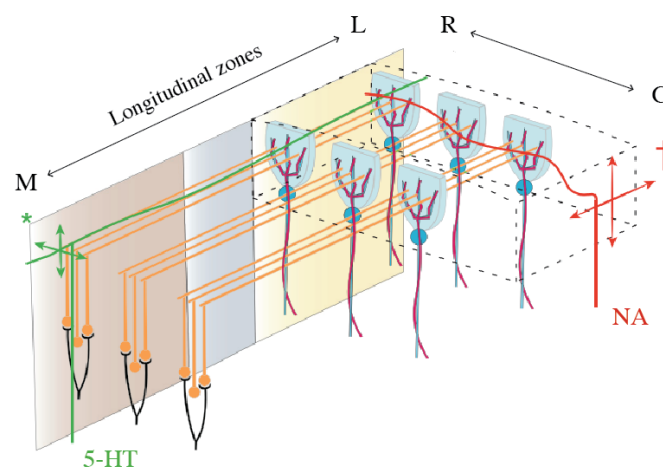


Figure 5. NA and 5HT afferences in the cerebellar cortex. Schematic representation of Serotonergic fibers (5-HT, green) and Noradrenergic fibers (NA, red) cortical projections. While 5-HT influence several longitudinal zones, NA are restricted to a single zone. Medial (M), Lateral (L), Rostral (R), Caudal (C). (Adapted from Longley et al, 2021)

5-HT fibers ascend to the ML before bifurcation and projecting for relatively long distances in the M-L plane, in a manner reminiscent of the PF. 5-HT fibers can cross three longitudinal zones and may cross even more. NA fibers project longer distances in the R-C plane than the M-L plane, though the

orientation preference is less complete than 5-HT fibers. The M-L and the D-V deviations of NA fibers are much smaller than their R-C extends, which could restrict their influence to a single zone. Interestingly, a previous study using electrophysiological slice recordings showed that serotonin GCs activity regulation does not occur directly, but instead via specific action on Golgi cells (Fleming and Hull, 2019)[75].

Available morphological, chemical, and functional data highlight the existence of a cerebellar DA system (Flace et al., 2021)[71], which consist of extrinsic fibers mainly originated from the midbrain cerebellar dopaminergic nuclei (Nelson et al., 1997)[76] and intrinsic dopaminergic neuronal subpopulations mainly composed of PCs and DCN neurons. Notwithstanding cerebellar involvement in DA-related neurological and psychiatric disorders (See section 3), the role of such dopaminergic system is still controversial. Through different methods, a wide distribution of the DA receptor subtypes has been observed in the CB of mammals. In the three layers of the CC, these receptors present a different cell-type-specific distribution pattern which suggested a detailed dopaminergic neurotransmitter mechanism in the CB (Flace et al., 2021)[71]. Interestingly, during the development of the mouse CC, a transient expression of tyrosine hydroxylase (TH), a DA biosynthesis marker, was detected in PCs from postnatal day (P) 3 to 11 months (Fuji et al., 1994)[77].

A better understanding of the cerebellar cellular diversity structure and development may contribute to improve the characterization of the specific local circuits underlying the DA cerebellar system and further elucidation of its precise role in cerebellar functioning.

4. Cerebellar function

In term of function, the CB is widely recognized to be a critical regulator of the maintenance of balance and posture (vestibulo-cerebellar circuit), coordination of voluntary movements (spino-cerebellar circuit) and motor learning (cerebro-cerebellar circuit). In addition, as previously mentioned, there are increasing signs for the involvement of cerebellar circuits in higher cognitive and emotional processes. The uniform microarchitecture of cerebellar circuitry suggests the possibility that both domains, movement and cognitive, are governed by a common computational model (Wang et al, 2014)[10].

For decades, it has been of great interest to decipher cerebellar learning algorithms (De Schutter, 1995)[78]. The cerebellar learning theory was first systematically proposed by Marr (Marr, 1969)[57]

and then Albus (Albus, 1971)[58], building upon previous knowledge of wiring connections and electrophysiological properties of the CC (Eccles et al, 1967). Interestingly, the prevalent view for pattern discrimination and associative learning based on random connectivity from the input layer to the output layer of the cerebellar cortex has been reviewed in a recent preprint, suggesting instead a structured and redundant connectivity underlying this fundamental cerebellar function (Nguyen et al., 2021)[79]. D'Angelo and Casali, proposed that the CB operates as a general-purpose co-processor, whose effects depend on the specific brain centers to which individual modules are connected. Abnormal functioning in these loops could eventually contribute to the pathogenesis of major brain pathologies including not just ataxia but also dyslexia, autism, schizophrenia, and depression (See section 3). Interestingly, the basic rules for cerebellar functioning seem to differ from those of other CNS areas. The CB is likely to adopt a *trial-and-error* learning rule, unlike the cerebral cortex and basal ganglia, which seem to learn, respectively, through frequency-based and reward-based rules (Doya, 2000)[80].

4.1. Motor functions

The primary motor function of the CB is the detection of difference or *motor error* between the intended movement and the real movement, and to ultimately reduce this error through its projections to higher neurons. These corrections can take place during the movement, but also in a motor-learning manner when the correction is stored. The motor CB can be subdivided in three main parts based on the differences in the afferences origin: cerebrocerebellum (Cerebro-cerebellar circuit), vestibulocerebellum (Vestibulo-cerebellar circuit) and spinocerebellum (Spino-cerebellar circuit) (Purves, 2010).

4.1.1. Cerebro-cerebellar circuit

The cerebrocerebellum constitutes the biggest cerebellar subdivision in humans, which occupies most of the lateral H and receives afferences from several neocortical areas. This region is linked to the regulation of fine-tuned movements, mostly the planification and execution of complex spatio-temporal movement sequences, including the speech. Cerebrocerebellum loops, including motor and somatosensory, oculomotor, but also prefrontal and parietal loops, are highly segregated and form complex interconnections also with the basal ganglia and subcortical areas (Habas et al., 2009)[81]. Of note, most cerebrocerebellum afferents pass through the basal (anterior or ventral) pontine nuclei

and intermediate cerebellar peduncle. In the case of motor and somatosensory loops, the CB projects both to motor and somatosensory areas. The output to the primary motor areas is conveyed through the ventrolateral nuclei projecting to intragranular and superficial layers (Molinari et al., 2002)[82]. Through these projections to the motor area, the CB modulates the motor cortex in relation to the incoming sensory input (Luft et al., 2005)[83]. Interestingly, the CB establishes connections with the premotor and supplementary motor areas which are involved in movement planning (Dum and Strick, 2003)[84] (Rouiller et al., 1994)[85]. On the other hand, the lateral and the posterior CB, mainly the V, are also involved in oculomotor regulation, such as the control of saccadic and smooth pursuit eye movements (Panouillères et al., 2011)[86]. In the oculomotor system, the retina project to the superior colliculus (Lefèvre et al., 1998)[87], which, in turn, sends afferents to the cerebellum and the lateral intraparietal area, connected with the frontal eye field and the basal ganglia and colliculus (Straube and Buttner, 2007).

4.1.2. Vestibulo-cerebellar circuit

The vestibulocerebellum is the phylogenetically most ancient portion of the CB. It is composed of the most caudal cerebellar lobules, involving the Fl, Pfl and nodulus (lobule X). The vestibulocerebellum receives afferences from the vestibular nuclei of the brainstem and it is mainly involved in the movements underlying the balance and posture. The primary and secondary afferents from the vestibular system to the CB have been recently reviewed (Ango et dos Reis, 2019)[88]. In particular, one of the best understood circuitries is the one responsible for sensing rotational and balancing movements of the head (Fernandez et al, 1988)[89] (Balmer and Trussell, 2019)[90]. Besides the GCs and the PCs, the pivotal role of UBCs in the vestibular-cerebellar circuit has been elucidated. Indeed, UBCs which are highly concentrated in the vestibular zone of the CB, are essential intermediates where signals between MFs and GCs are modulated. Interestingly, the different types of UBCs are differently involved in this modulation, amplifying, or dampening the signal (Borges-Merjane and Trussell, 2015)[91].

4.1.3. Spino-cerebellar circuit

The spinocerebellum occupies the vermal and paravermal areas of the CB and it is the only receiving afferences directly from the spinal cord. The lateral portion of the spinocerebellum is associated with the movement of the distal muscles, like the walking gross movements. The vermal part, it is fundamentally related with the movement of the proximal muscles, and it also regulates the ocular movements in response to the vestibular afferences. The spino-cerebellar circuit can be further subdivided into four different tracts: dorsal, ventral, cuneocerebellar and rostral. The dorsal and ventral spinocerebellar tracts are the two main lumbar components of the spinocerebellar pathways and they run in parallel. It has been described that both spinocerebellar pathways terminate ipsilaterally in the CC with respect to the location of their cell bodies in the spinal cord. Both pathways have shown anatomical and functional differences (Stecina et al., 2013)[92]. The dorsal tract transmits proprioception information from Golgi tendon organs and muscle spindles of the trunk and lower limb to the pseudo unipolar neurons in the dorsal root ganglion, and then ascends to the ipsilateral side to enter the cerebellum via the inferior peduncle, to eventually reach the MFs. This proprioceptive information is transmitted to the vermis and paravermis in the anterior lobe of the CB, and it is used to build and coordinate voluntary movements by knowing the position sense of the lower limbs and the trunk. In parallel, the ventral tract, which relays motor information, enters the CB through the contralateral superior cerebellar peduncle to transmit internally generated motor information about the movement (Koh et Markovich, 2021).

4.2. Non-motor functions

Whereas the CB has traditionally been considered to be important uniquely for motor coordination and learning, it became apparent that the CB is also involved in higher cognitive functions. Higher roles for the CB have been discussed since the mid-19th century (Steinlin and Wingeier, 2013)[93], with a renewal of interest in recent years. Anatomical analysis of cerebellar output has brought new insights into cerebellar functions. Indeed, cerebellar output to non-motor areas of the brain has been identified, suggesting that the CB participates not only to the generation and control of movement, but also to non-motor aspects of behavior, such as cognition and emotion (Strick et al., 2009)[94] (D'Angelo et Casali, 2012)[7] (Watabe-Uchida et al., 2012)[8] (Koziol et al., 2014)[95] (Mariën et al., 2014)[96] (Carta et al., 2019)[6] (Medina, 2019)[97] (Sendhilnathan et al., 2020)[98] (Wagner et al., 2017)[27] (Heffley et al., 2018)[99] (Kostadinov et al., 2019)[100] (Low et al., 2021)[47].

In addition, the CB participation in reward processing and control of social behavior through a DCN-VTA pathway has been shown (Carta et al., 2019)[6] using a combination of anatomical tracing and optogenetic stimulation, the authors of this study demonstrated that axonal projections from the DCN form synapses with both DA and non-DA neurons in the VTA. In addition, behavioral tests showed that CB-VTA projections were sufficient to cause short-term and long-term place preference, thereby demonstrating that the pathway was rewarding. Although calcium activity correlation suggested a role for the CB in social behavior, optogenetic activation as well as social behavioral tests indicated that the pathway is not sufficient for social behavior. Recently, it has been also demonstrated the cerebellar role in satiation and body weight homeostasis mediated by a modulation of the reward system triggered by food intake cues (Low et al., 2021)[47].

At a cellular level, GCs have been characterized to convey information about the expectation of reward, representing a major departure from the current understanding of these neurons (Wagner et al., 2017)[27]. Using two-photon calcium imaging of cerebellar GCs in behaving mice for the first time, the authors showed the preferential response of some GCs to reward or reward omission, whereas others selectively encoded reward anticipation. Tracking the same GCs over several days of learning revealed that reward-related responses are highly dynamic during learning, with reward responses becoming progressively more anticipatory, while omitted-reward response preferences growing in magnitude over days. In an attempt to further investigate the mechanisms by which PCs transform these reward-related signals to participated in reward-based learning, cerebellum role on visuomotor association learning was shown (Sendhilnathan et al, 2020)[98]. Using behavioral tests together with electrophysiological recordings, PCs in the monkey mid-lateral CB were demonstrated to be able to associate one arbitrary symbol with the movement of the left hand and another with the movement of the right hand.

Altogether, these evidences raise the question of how reward context contributes to cerebellar function. Strikingly, recent findings have shown that classical functions of the CB such as sensorimotor learning may depend as well on the reward system (Heffley et al., 2018)[99] (Kostadinov et al., 2019)[100]. Two studies have revealed that the role of CFs, which transmit information from the “teacher” neurons in the iO during sensorimotor learning, is likely to extend far beyond their well-known contribution to improving motor performance. Mice were trained to obtain a fluid reward by performing a specific forelimb action, either a properly timed bar release (Heffley et al., 2018)[99] or a precise steering-wheel movement (Kostadinov et al., 2019)[100]. CFs located in forelimb-controlling areas of the CC

were found to modulate their activity in response to the reward, and this modulation was stronger when the reward was surprising or unexpected. In addition, CFs fired in anticipation of the reward, when forelimb movements were being correctly executed. The discovery of reward-related signals in CFs is a game-changer and poses a serious challenge for classical theories of sensorimotor learning that have neatly divided neural systems into those used to improve action selection and those used to improve action execution. (Medina, 2019)[97] However, an exhaustive profiling of the specific cell populations which participate in these processes is still missing. The high throughput profiling analysis provided in this thesis, together with the first insights to a new integrative tool to study cerebellar structure and development, might contribute to a better understanding of this aspect.

Altogether, the incorporation of reward, reward-omission and reward-anticipation signals should allow the CC to integrate sensorimotor information with signals reflecting internal brain state and affective status, and in doing so substantially expanding its function as a learning machine and therefore generate the disparate higher functions in which the CB has been linked.

Moreover, the CB has been reported to assist brain operation by providing accurate timing of multiple series of signals coming from the cerebral cortex and the sensory systems. This could underlie the implementation of processes like sensory prediction, novelty detection, error detection, time matching and sequence ordering (D'Angelo et Casali, 2012)[7]. Interestingly, CB implication in shaping other brain regions during early life has been suggested. Namely, the CB role would process external sensory and internally generated information to influence neocortical circuit refinement during developmental sensitive periods (Wang et al., 2014)[10]. Therefore, cerebellar dysfunction may disrupt the maturation of distinct neocortical circuits leading to important cognitive and behavioral impairments (Vacher et al., 2021)[101] (See section 3).

5. Cerebellum in disease

Cerebellar perturbations have been related to a wide range of pathological conditions not only affecting the normal motor function but also higher cognitive and social behaviors. The research presented in this thesis, which aims to elucidate the main molecular mechanisms underlying the normal cerebellar development, enhances the improvement of cerebellar disorders management. On the same note, it is extremely important to highlight the relevance of fundamental research. Certainly, much of the spectacular progress in biomedical science over the last half-century is the direct consequence of the work of thousands of basic scientists whose primary goal was to understand the fundamental working of living things.

5.1. Motor disorders

Many of the clinical manifestations of cerebellar damage result in lack of coordination and disturbances of accuracy of movements, causing a constellation of symptoms and motor signs. In this section I will review one of the most prevalent cerebellar motor disorders: the cerebellar ataxia. I will also talk about Parkinson's disease, traditionally linked exclusively to the DA system.

5.1.1. Ataxias

Cerebellar ataxias comprise a heterogeneous group of neurological disorders characterized by gait disturbances, motor incoordination and imbalance, dysarthria, and oculomotor deficits (Sillitoe et al., 2012)[19] (Serra et al., 2006)[102] (Leto et al., 201)[17]. Considering the neurophysiology of the cerebellar system, some authors have classified ataxias in four groups depending on which system is affected: PCs, corticocerebellar, spinocerebellar and DCN systems. To regulate voluntary movements, the CB forms Internal models within its neural circuits that mimic the behavior of the sensorimotor system and objects in the external environment. It is speculated that loss of PCs leads to malformation of the internal cerebellar models, whereas disturbance of the afferent system, corticocerebellar system or spinocerebellar system results into mis-selection of the proper internal model (Tada et al., 2015)[103] (Keiser et al., 2015)[104].

For a long time, ataxias were considered a pure neurodegenerative disorder. This means that the cause of the cerebellar atrophy and thus the symptoms, were attributed exclusively to the progressive pathological changes in PCs and a substantial loss of these neurons. However, accumulative evidence suggested that developmental alteration and related early changes in PCs physiology might contribute as well to the disease. The first functional genetic evidence that compromising PCs development contributing to a severe neurodegeneration, comes from the study of Spinocerebellar ataxia type 1 (SCA1), one of the most dominant ataxias, caused by a repeat expansion in the Ataxin 1 (ATXN1) gene. The reduced severity of the phenotype when ATXN1 mutation was induced after CB maturation in a SCA1 mouse model, and the proven interaction between ATXN1 and retinoic acid-related orphan nuclear receptor α (ROR α), showed that ATXN1 plays an important role during normal PCs development (Serra et al., 2006)[102]. The observed PCs developmental defects commonly include impaired dendritic arborization, resulting in synaptic deficits affecting climbing fibers and parallel fibers connections. The volume of the DCN is reduced in some types of ataxias, being most pronounced in spinocerebellar ataxia type 6 (Stefanescu et al, 2015)[105]. Experimentally, intraperitoneal injection

of neurotoxin 3-acetylpyridine in rats induced cerebellar ataxia, and with it, a neuronal loss in all DCN. In addition, the CB proves to be an important target organ in ethanol consumption, and the cerebellar ataxia is the most consistent physical manifestation of acute ethanol intoxication (Dar, 2015)[106].

Overall, a better understanding of the underlying molecular mechanisms that cause abnormal cerebellar development and functions, is crucial for an efficient identification of possible therapeutic targets.

5.1.2. Parkinson Disease

Parkinson disease, the most common neurodegenerative movement disorder, has been traditionally considered a basal ganglia dysfunction, as the most obvious pathology is seen in the dopaminergic cells in the *substantia nigra pars compacta* (Lewis et al., 2016)[107]. However, many clinical features of Parkinson disease cannot be attributed exclusively to basal ganglia dysfunction. Interestingly, anatomical connections linking the basal ganglia and the cerebellum have led to a re-examination of the role of the CB in Parkinson disease (Mirdamadi, 2016)[108]. Indeed, several studies support a cerebellar role in the symptomology and compensatory mechanisms in Parkinson disease. Whether the CB plays a pathological role driven by striatal dysfunction or a compensatory role to overcome this dysfunction remains unclear. Interestingly, lateral and medial cerebellar-related origin has been associated with the generation of the well-known resting tremor in patients (Lewis et al., 2016)[107] (Lefaivre et al., 2016)[109]. Furthermore, neuroimaging studies in humans have found that Parkinson disease patients have altered cerebellar activation during motor execution, motor learning and rest (Wu and Hallet, 2013)[110].

5.2. Cognitive disorders

Correlating with the abovementioned non-motor functions of the CB, impairment of the normal cerebellar development and structure do not only result in movement deficits, but also in cognitive and affective function dysregulation which might severely impact patients' lives (Room et al., 2015)[111]. It is therefore essential the understanding of the molecular mechanisms that underlie normal cerebellar development prior to the design of effective therapies for such diseases.

5.2.1. Autism

Many brain regions have been linked to autism, but structural and functional cerebellar abnormalities are among the most consistent findings. Both neuronal dysfunctions, especially of cerebellar PCs, and WM changes have been linked to autistic phenotypes (Becker and Stoodley, 2013)[112] (Fatemi et al., 2012)[113] (Rogers et al., 2013)[114].

Namely, stereological analysis of PCs in the cerebellum of 14 autistic individuals aged 4 to 60 years showed a 25% reduction in number and a 25% reduction in density compared to controls (Weigel et al., 2014)[115]. In addition, MRI studies in autistic children have also shown a reduction in the cerebellar V volume (Webb et al., 2009)[116] Interestingly, the mouse model of Angelman syndrome, a syndrome comprised in the spectrum of autism disorders, has revealed regional-dependent degeneration of PCs in the Zebrin II-bands, the most extensively studied stripped marker of the CC (Strømme et al., 2011)[117] (See section 5.4.1.1).

Lately, placenta ALLO insufficiency has been shown to lead to cerebellar myelination abnormalities that correlate with autistic-like behaviors in a sex-linked manner (Vacher et al., 2021)[101]. At the molecular level, several genes with known roles in cerebellar development, such as engrailed 2, mesenchymal-epithelial transition receptor tyrosine kinase, are associated with autism (Marzban et al., 2015)[118].

5.2.2. Alzheimer Disease

In Alzheimer's disease (AD), despite the widespread of senile plaques and neurofibrillary tangles and the cerebral cortical atrophy, patients might also exhibit significant atrophy of the vermis, PCs degeneration and severe gliosis within the molecular layer. Decrease of PCs can reach up to 32% in late-stage AD patients. The genetic contribution appears to be important such that familial forms of AD display a stronger reduction in PCs density in comparison to the sporadic cases of AD (Fukutani et al., 1997)[119] (Sarna and Hawkes, 2003)[120] (Sjöbeck and Englund, 2001)[121] (Wegiel et al., 1999)[122].

5.3. Cancer

The CB is the most common site of CNS tumors in children, but exceedingly rare in adults (Stucklin et al., 2018)[123]. The differential diagnosis is broad and includes a variety of benign and malignant

entities. Cerebellar low-grade gliomas are the most common and benign, slow-growing tumors, while embryonal tumors, most commonly as medulloblastomas, are highly aggressive. Regardless of age and histology, cerebellar tumors are critical lesions that are often present with severe symptoms related to the compression of the CB and adjacent brainstem or obstruction of cerebrospinal fluid (CSF) flow, hence requiring urgent treatment.

5.3.1. Medulloblastoma

Medulloblastoma is the most common malignant brain tumor in children, accounting for nearly 10% of all childhood brain tumors. Medulloblastomas occur in the posterior fossa and have the potential for leptomeningeal spread (Khatua et al., 2018)[124]. Consequently, the presenting symptoms are often vague, and the diagnosis may be delayed compromising the recovery and survival of the patients. The treatment, which includes a combination of surgery and radiation, has been for long based on histopathology and clinic-radiological risk stratification leading to unpredictable relapses and therapeutic failures. However, the recent molecular classification of medulloblastomas seems to be crucial for potential prognostic and therapeutic implications. Indeed, over the last decade several transcriptional profiling studies have identified four molecular subgroups of medulloblastoma: WNT, Sonic Hedgehog (Shh), Group 3 and Group 4, three of them with cerebellar origin (Pomeroy et al., 2002)[125] (Cho et al., 2019)[126] (Fattet et al., 2009)[127] (Kool et al., 2008)[128] (Northcott et al., 2011)[129] (Thompson et al., 2006)[130] (Taylor et al., 2012)[131]. Interestingly, the study of the origin and development of medulloblastoma revealed transcriptional dynamics similarity to normal cerebellar cells development (Vladoiu et al., 2019)[132]. Concretely, Shh and group 3 medulloblastomas mirror the transcription program of cells from distinct, temporally restricted cerebellar lineages. While Shh medulloblastoma subgroup transcriptionally mirrors the GCs, as expected (Vanner et al., 2014)[133], group 3 resembles Nestin⁺ stem cells, and group 4, the UBCs. These findings did not only contribute to provide a better understanding of cerebellar tumors in early childhood, but also they increased our knowledge about the fundamental mechanisms underlying cerebellar development.

Overall, the elucidation of new signaling pathways and molecular mechanisms during cerebellar development, might provide exceptional insights for the development of newer more personalized therapies for these tumors. Hence, the results presented in this thesis certainly contribute to move forward in that direction.

6. Cerebellar evolution

The basic structure of the CB is conserved among vertebrates (Larsell,1947)[134] (Bone,1963) (Nieuwenhuys, 1967)[135] (Altman and Bayer, 1997) (Butler and Hodos, 2005). Certainly, the cardinal organization of afferent and efferent cerebellar connections appears to be conserved throughout evolution (Grishkat et Eisenman, 1995)[136]. However, during evolution, the vertebrate CB acquired diversity as animals changed in response to the environment and other factors leading to diversity in cerebellar gross morphology and neural circuits. CB projection neurons are one of many examples of this divergence: while in most vertebrates' cerebella projection neurons constitute the DCNs, in teleost they compose the eurydendroid cells. That is the case of Zebrafish (Bae et al., 2009)[137] (Heap et al, 2013)[138]. Eurydendroid cells are postsynaptic to PCs, receive input from PFs and CFs, and extend axons beyond the CB, indicating that they occupy the same circuit position as do the DCN in mammals (**Figure 6**). Spatial patterns of cerebellar output in zebrafish were described using a Gal4 tracing approach (Bae et al., 2009)[137]. Interestingly, the authors found that CB targets the thalamus and optic tectum and have confirmed the presence of presynaptic terminals from eurydendroid cells in these structures. In addition, topographic organization in the connectivity between the CB and the optic tectum was revealed, indicating that there is a spatial logic underpinning cerebellar output in zebrafish as it occurs in mammals.

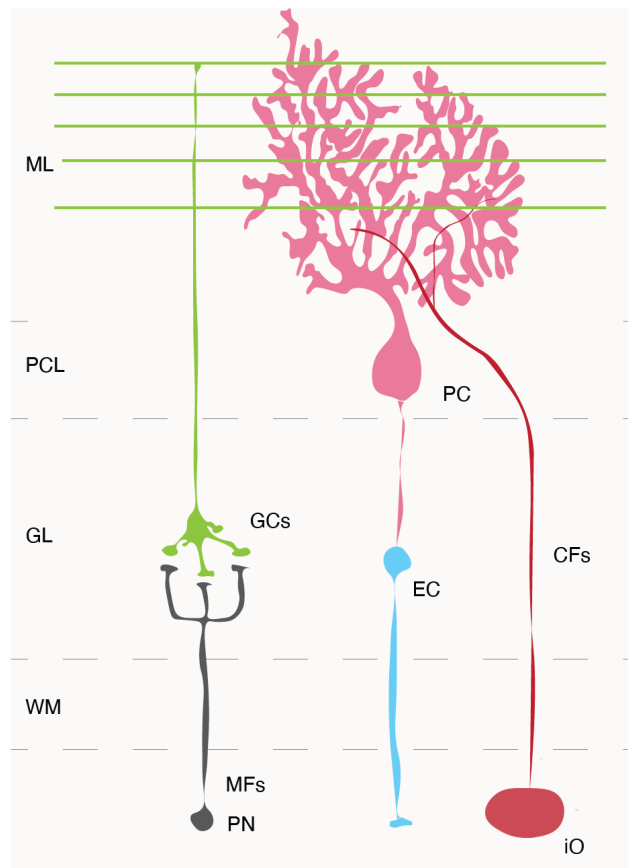


Figure 6. Teleost cerebellar afferent and efferent circuitry. Schematic representation of eurydendroid cell (EC)-based cerebellar circuitry. ML (molecular layer), PCL (Purkinje cell layer), GL (granule cell layer), WM (white matter), PC (Purkinje cell), GCs (granule cells), CFs (climbing fibers), MFs (mossy fibers), iO (inferior olive), PN (paracerebellar nuclei other than iO). (Adapted from Bae et al, 2009)

The factors that generate cell diversity in the CB and how these behaved during evolution is still largely unknown. However, the literature hints at important evolutionary changes in the diversity of neuronal subtypes and points to a change in the functional role for the CB as new networks of connections emerged in amniotes. Anatomic study of the zebrafish cerebellum using molecular markers and transgenic lines has served to reveal great similarities in structure and circuitry, but also the divergences and particularities of its cell type composition (Bae et al, 2009)[137]. Besides the above mentioned distinction in projection neurons, inhibitory neuron types diverge from those identified in mammals. Indeed, while PCs and interneurons such as GoCs and SCs, have been identified, zebrafish cerebellum does not contain BCs. Early morphological and electrophysiological studies have demonstrated that the frog cerebellar circuitry is much simpler than its mammalian counterpart, having a great dearth of MLIs, BCs and SCs, as well as GoCs (Llinás and Hillman, 1969)[139]. Interestingly,

the form of synapses between MFs and frog GCs differs very much from the glomerulus structure found in reptiles, birds, and mammals, since no rosette formation can be found, and the Golgi cell terminal boutons are absent. It is important to mention that while mammals and, more specifically, primates, modified their cerebellar neural circuits to elicit higher brain functions during evolution, they also became susceptible to certain brain diseases. Recently, it has been observed a 2-fold higher relative abundance of PCs during development in human compared to mouse and opossum (Sepp et al., 2021)[140]. This change in PC dynamics in the human lineage could potentially be related to differences in developmental durations between humans and the other mammals and/or the unique presence of basal progenitors in the human CB (Haldipur et al., 2019)[11] that may serve as an additional pool of PCs progenitors (PCPs). Since the transit amplification of GCs progenitors (GCPs) is known to be regulated in part by PCs derived Shh signaling, the increase in PCs numbers could necessarily match the expansion of the neocortex in the human lineage. On the other hand, the Shh-dependent expansion of GC progenitors not only contributes to the increased size and foliation of mammalian cerebella (Corrales et al., 2004, 2006)[141], [142], but also to the secondary generation of astrocytes and GABAergic interneurons from neural-stem-like cells in the prospective WM (Fleming et al., 2013)[143]. Interestingly, intermediate cells between astroglia progenitors and oligodendrocyte progenitor cells abundant in opossum, rare in human and not detected in mouse (Sepp et al, 2021)[140]. Noteworthy, cerebellar neuronal density decreases homogeneously with the addition of neurons across afrotherians, rodents and lagomorphs, and artiodactyls. In contrast, both primates and eulipothyplans stand out by having much larger neuronal densities than other mammalian species with similar number of cerebellar neurons, resulting in a higher neuronal density than other mammalian cerebella of similar mass. (Herculano-Houzel et al., 2014)[144] (Haldipur et al., 2019)[11] (Hibi et al., 2017)[145] (Marzban et al., 2015)[118]. Interestingly, during phylogenesis, the cerebellar hemispheres evolved in parallel with the associative rather than the motor or sensory areas, which supports the progressive involvement of the CB in cognitive processing (D'Angelo and Casali, 2013)[146].

Collectively, it becomes clear that establishing causal relationships between the molecular and phenotypic evolution of the CB in our species and other mammals is necessary to deeply understand cerebellar architecture, circuitry, functions, and development and vice versa.

7. Cerebellar foliation and patterning

The cerebellum has a peculiar morphology consisting of folia separated by fissures, on which the A-P organization of the distinct sensory-motor circuits is built. There are two main stages in the morphogenic process of folding of the cerebellum: formation of the cardinal lobes, which occurs embryonically (\approx E17 in mouse) by the inward thickening corresponding to the prospective fissures (preculminate, primary, secondary and posterolateral), acting as a driving force to form the so-called *anchoring centers* (Sudarov and Joyner, 2007)[22], and formation of the lobules and sub-lobules (folia), which occurs postnatally (P0-P14) (Sillitoe and Joyner, 2007)[147]. As already mentioned in section 5.4.2.1, the origins of this complex morphology were ascribed to the tight regulation of GPCs proliferation. Several mitogenic pathways were acknowledged as possible regulators of GPC proliferation in the oEGL. *Atoh1* and *N-myc*, required for GCs specification from the RL, were described to be also essential for the expansion of the pool of progenitor cells in the EGL at early postnatal stages (Ben-Arie et al., 1997)[148] (Knoepfler et al., 2002)[149]. Besides, Shh secreted by PCs is a major driver of GPCs expansion. Evidence of PCs involvement in the maintenance of GPCs pool came from several experimental observations, in which their loss was in turn accompanied by degeneration and death of nearby GPCs (Sotelo, 2004)[150]. Distinct functional tests performed *in vitro* and *in vivo* eventually demonstrated that PCs exert their pro-proliferative role through the secretion of Shh (Dahmane and Ruiz-i-Altaba, 1999)[151] (Wallace, 1999)[152] (Wechsler-Reya and Scott, 1999)[153]. Also, Shh signaling correlates spatially and temporally with fissure formation and its levels were shown to regulate the complexity of cerebellar foliation, as demonstrated in mutant models in which the Shh pathway had been perturbed (Corrales et al., 2006)[142]. In the iEGL, cells stop responding to Shh and, therefore, stop proliferating and begin the final steps of maturation, as confirmed by the decreased expression of the Shh target gene *Gli1* (Corrales et al., 2004)[141]. Another pathway involved in the expansion phase of GPCs is that of Notch2, activated through homotypic cell-to-cell contacts. Indeed, the Notch2 ligand jagged 1 (*JAG1*), expressed by GPCs themselves, binds to Notch2 on the surrounding cells therefore stimulating their proliferation and inhibiting their differentiation (Solecki et al., 2001)[154]. PCs and BGs, play also a crucial role in the phase of cerebellar foliation, starting after the inward thickening of the EGL. Indeed, a folding of the PCL, still in the form of a multilayer, was shown to occur where the GPCs accumulate, predicting the future position of the fissures: both PCs dendrites and BG fibers near the anchoring centers converge towards the base of each fissure, thereby allowing the correct unfolding of the foliation pattern. The maturation of a given fissure then proceeds in synchrony with the development of PCs and PCL progenitors

throughout that same fissure and with their gradual transition from a multilayer into a monolayer (Sudarov and Joyner, 2007)[22] (Hoser et al., 2007)[155] (Ma et al., 2012)[156] (Li et al., 2014)[157].

As mentioned in previous sections, the adult mouse cerebellum houses a complex topographical map which seems to involve most, if not all cell types in the CC. PCs patterned disposition (zones and stripes) serves as scaffold to organize afferent topography and restrict the distribution of excitatory and inhibitory interneurons. Namely, interneurons are restricted at stripe boundaries, and they establish their own topology using PCs cues. Interestingly, expression markers and lineage tracing reveal an intriguing GCs heterogeneity that aligns reliably with the stripe and zone architecture of the PCs (Consalez et al., 2021)[158]. In addition, functional boundaries seem to align with stripe boundaries. (Chockkan and Hawkes, 1994)[159] (Chen et al., 1996)[160] (Hallem et al., 1999)[161] (Apps and Garwicz, 2005)[162] (Wadiche and Jahr, 2005)[163]. Remarkably, specific target zones in the cerebellar and vestibular nuclei receive topographically ordered projections from CC stripes (Chung et al., 2009)[35] (Sugihara, 2011)[34] (Sugihara, 2018)[164]. The patterns of zones and stripes are highly conserved across species. However, how this complex patterning is achieved is not yet fully understood. Cerebellar pattern formation is conventionally divided into four broad stages, corresponding to PCs developmental stages: VZ formation, PCs birth, PCs migration and clustering, PCs cluster dispersal and refinement (see section 5.4.11). Therefore, PCs embryonic clusters are the prime organizers and restrict the distribution of different GCPs subpopulations in the EGL to align with the underlying transverse PC zones, and only then they further differentiate to generate what is known as GCs hyper-heterogeneity. It is thought to be unlikely that GCs heterogeneity is already defined at the RL level, but rather a PC inductive interaction together with MFs inputs (Consalez et al., 2021)[158].

8. Cerebellar development

The developing program of the CB is unique in the brain. It is one of the first brain structures to be formed in the embryo, yet its maturation is a long process that extends into several weeks after birth in mice, and up to 2 years after birth in humans (Leto et al., 2016)[4]. Although the global cerebellar development is well conserved between species (Sepp et al., 2021)[140], species-specific mechanisms have been shown to be in place (Haldipur et al., 2019)[11]. This is not surprising if we consider that the complexity increases in the CB and cerebral cortex during evolution. For example, compared to the mouse CB, the human CB has a 750-fold larger surface area, increased neuronal numbers, altered

neuronal subtype ratios, and increased foliar complexity (Van Essen, 2002)[165]. Differences in developmental patterns between these species, including spatiotemporal expansion of primary proliferative zones (Haldipur et al., 2019)[11], may explain this variability.

Spatio-temporal patterns of gene expressions are necessary for the normal development of the cerebellum, which control a variety of processes, such as cell survival, cell identity, neural precursor proliferation, neuronal differentiation, and axon guidance (Martinez et al., 2013)[166] (Marzban et al., 2015)[118]. This temporal pattern is superimposed onto dynamically maintained progenitor zones (Butts et al., 2014)[167](**Figure 7**).

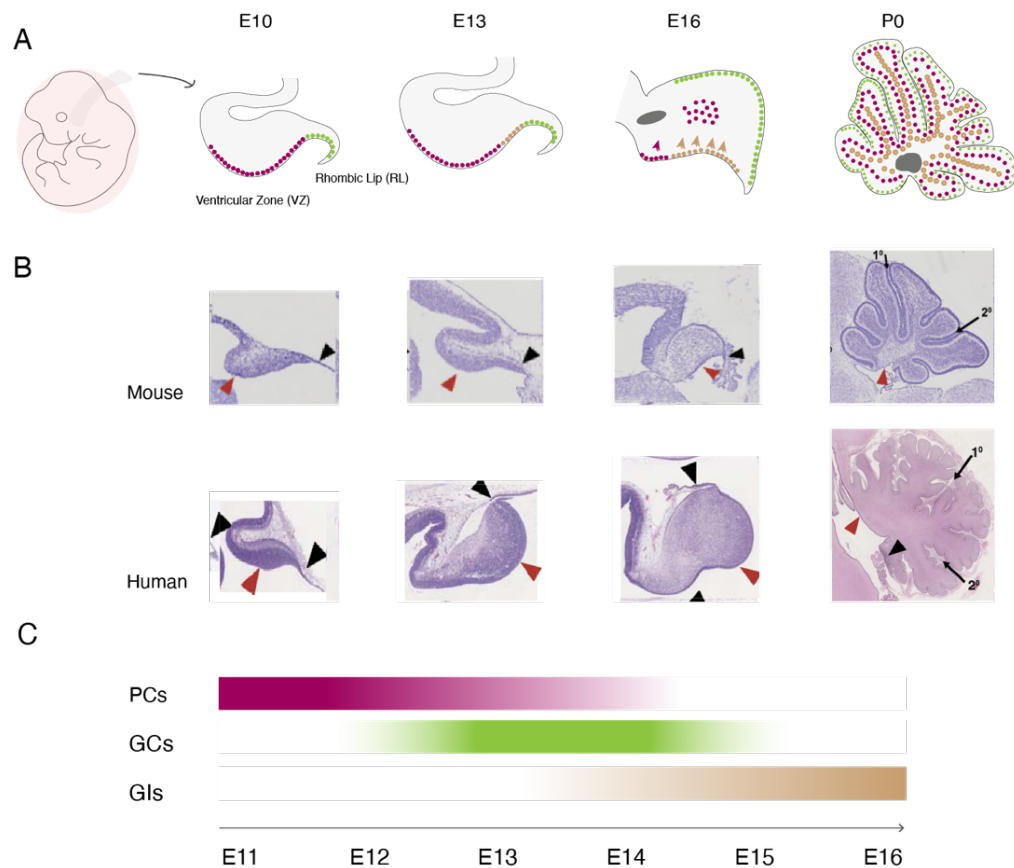


Figure 5. Cerebellar development schematic representation. A) Cerebellar primordium located in the alar plate of the Rhombomer 1 in the early embryo. Distinction of two proliferative zones: VZ (Ventricular Zone) for GABAergic lineage (purple) and RL (Rhombic Lip) for glutamatergic lineage (green). During the embryonic development precursors will proliferate, differentiate and migrate until occupy their final position in the post-natal cerebellum. B) Comparative cerebellar development between mouse and human (adapted from Vladoiu et al, 2019) C) Time-sequential generation of different cell types during cerebellar development: PCs (Purkinje cells) generated mainly in the early development, followed by the GCs (Granule cells) and ultimately GIs (GABAergic interneurons).

Over the last decades, many studies have brought new insights on the molecular machinery that regulates distinct aspects of cerebellar development, from the establishment of a cerebellar anlage in the posterior brain, to the identification of cerebellar neuron diversity at the single-cell level (Lowenstein et al., 2022)[168]. The advent of single-cell RNA sequencing (scRNA-seq) in cerebellar development is further expanding our knowledge on the elementary basis regulating progenitor cell progression and neuron specification. I will talk about this and other technological advances, and how they contribute to understand cerebellar development in Chapter 2.

In this section, I talk about the different events and molecular mechanisms that are known to take place during cerebellar development, from early neural tube patterning events to specific cerebellar cell types generation. Understanding morphogenic and molecular mechanisms of cerebellar development is essential to learn about the processes regulating cerebellar cytoarchitecture, its highly topographically ordered circuitry and its functions. Although cerebellar development has been investigated through multiple models and technologies over the years, there is still an important gap in our knowledge, due in part to a lack of an integrative approach to fully understand the process. The efforts of this thesis in setting the basis for such integration and data harmonization are therefore essential.

8.1. Midbrain-hindbrain boundary development

As already mentioned, the CB is located on the alar plate of the rhombomere 1 (r1), in the junction between the midbrain and the hindbrain. Therefore, to have a full understanding of cerebellar development one should go back to the early CNS development and the definition of the well-known midbrain-hindbrain boundary (MHB) (Barkovich et al., 2009)[169].

The CNS derives from the dorsal epiblast of the vertebrate embryo and is induced by a combination of signals originating in the region of Hensen's node at the posterior margin of the early embryo (Wurst and Bally-cuif, 2001)[170]. After many steps, a neural tube is formed and subsequently develops a series of vesicles at its anterior end. The differentiation of these vesicles along the AP axis, also called patterning (Lumsden and Krumlauf, 1996)[171], gives rise to the prosencephalon or forebrain (which soon divides into diencephalon and telencephalon), the mesencephalon (midbrain), and the rhombencephalon (hindbrain), which divides into the rostral metencephalon (pons and cerebellum) and caudal myelencephalon (medulla oblongata). In vertebrate, the rhombencephalon is transiently segmented into seven to eight small morphological subunits called rhombomeres. Despite recent

advances in understanding of the mechanisms that result in early anteroposterior patterning, they remain partially understood (Chambers et al., 2009)[172] (Solanelles-Farré and Telley, 2020)[173]. Pioneering studies showed that subdivision along the R-C axis of the developing CNS assigns regional identity to neuronal precursor pools, influencing the fate of their progeny and generating structural diversity (Lumsden and Krumlauf, 1996)[171]. Strategies for conferring detailed positional information vary along the length of the axis. For example, the hindbrain is a transiently rhombomeric structure organized by segmentally expressed *Hox* genes (Moreno-Bravo et al., 2014)[174]. By contrast, the development of the midbrain and forebrain is regulated by signaling centers generating graded patterning cues (Lupo et al., 2014)[175]. Interestingly, the r1, the most anterior hindbrain segment, displays aspects of both patterning systems. The transition point, where the hindbrain system of segmentation gives away to regional patterning by local gradients in the midbrain is known as the MHB.

The early establishment of the MHB is one of the first key events in cerebellar development. In murine and chick models, the location of the MHB is determined around mouse embryonic day I 7.5 by the expression of the homeobox gene *Otx2* in the caudal midbrain and *Gbx2* in the rostral hindbrain (**Figure 8**). Indeed, increase or posterior shift in the expression of *Otx2* or decrease in *Gbx2* shift the MHB caudally, while decrease in *Otx2*, or increase or anterior shift in *Gbx2* shift the MHB rostrally (Nakamura et al., 2005)[176]. In mice, the ablation of *Otx2*, and its close family member *Otx1*, results in the loss of midbrain structures, which in turn transforms them into cerebellar-like regions (Acampora et al., 1997)[177] (Suda et al., 1997)[178]. *Otx2*, together with *Otx1*, are involved in the pathology of medulloblastoma, correlating with the pathological classification of this tumors (de Haas et al., 2006)[179]. In this study, they demonstrated for the first-time the expression of *Otx1* in human fetal forebrain. *Otx1* mRNA was detected in the proliferative zone and the developing cortical plate of the human brain at 9 fetal weeks, mainly in the lateral regions of the dorsal cortex, which are the first to mature. *Otx1* expression starts when the anterior neuroectoderm develops into prosencephalon and mesencephalon. At this stage, the expression of *Otx1* is in the same areas as *Otx2*. However, at later embryonic stages their expression patterns diverge. Both *Otx1* and *Otx2* take part in the development of the CB. However, neither gene is expressed in cells of the cerebellar ventricular zone, but both are expressed within the external germinal layer, a secondary proliferative close to the pia, which is responsible for the production of granule cells (Larsen et al., 2010)[180].

The interaction of *Otx2* and *Gbx2* also specifies the location of the isthmic organizer (IsO), located at the MHB, adjacent to the hindbrain r1. Indeed, the misexpression of *Gbx2* at early somite stages, not

only alters the correct development of the CB, but also the positioning of the IsO (Millet et al., 1999)[181]. In this study, transgenic embryos showed an expanded hindbrain and a reduced midbrain at E 9.5-10, proving once more a role for *Gbx2* in sharpen the MHB border. The IsO is essential for normal brainstem and cerebellar development (Sotelo, 2004)[150]. The combination of spatial and temporally organized transcription factors and secreted molecules from the IsO has been shown to be both necessary and sufficient for setting up the cerebellar primordium, located at the alar plate of the r1, which in turn serves as a platform from which various cerebellar cell types are generated. Indeed, classic transplantation studies showed that transplantation of isthmic neuroepithelium into the hindbrain forced neighboring alar plate to differentiate into cerebellum (Martinez et al., 1995)[182]. Hence, confirming the function of the IsO as the organizer for the CB.

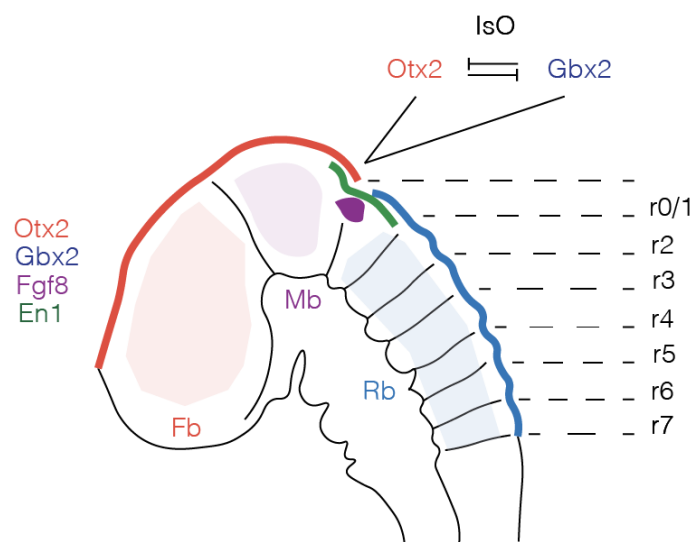


Figure 8. Establishment of the MHB. A) Schematic display of the molecular and anatomical establishment of the anterior and posterior brain borders by the expression of *Otx2* and *Gbx2*, respectively, in a developing mouse embryo. Forebrain (Fb), Midbrain (Mb), Rhombencephalon (Rb), Isthmic Organizer (IsO), Rhombomer (r). The expression of the essential factors FGF8 and En1 for cerebellar development are illustrated. (Adapted from Lowenstein et al, 2022)

Transforming growth factor β (TGF β) signaling has been implicated in the timing of developmental temporal switches in the nervous system (Dias et al., 2014)[183] (Meyers and Kessler, 2017)[184] (Rossi et al, 2020)[185]. TGF β is also important for controlling the timing of fate switches in the *Drosophila* nervous system, raising the possibility that it may serve as a general timer for the sequential generation of cellular subtypes (Rossi et al, 2020)[185].

8.2. Establishment of the cerebellar territory

Starting from the end of the 19th century, several efforts were made to define the physical margins of the neural territory from which the CB is specified. Originally, the cerebellar anlage was thought to entirely derive from the metencephalon (Hiss, 1890). Later, it became clear that this region was not the sole origin of the whole CB. Rather, elegant studies that aimed at defining the boundaries of the brain neuromeres using quail-chick grafting highlighted that it arises from the caudal portion of the mesencephalic vesicle and the rostral portion of the metencephalic vesicle (Martinez and Alvarado-Mallart, 1989)[186] (Hallonet et al., 1990)[187] (Sotelo, 2004)[150] (Alvarado-Mallart, 2005)[188].

As already mentioned, early cerebellar development is strongly dependent on signaling from the IsO, strategically located in the isthmus of the neural tube, which orchestrates the complex cellular diversity of the CB (Martinez et al., 2013)[166]. Indeed, loss of function studies disrupting the expression domains centered in the IsO resulted in the deletion of most of the mesencephalic and/or metencephalic regions (Thomas and Capecchi, 1990)[189] (McMahon and Bradley, 1990)[190] (Wurst et al., 1994)[191] (Favor et al., 1996)[192] (Meyers et al., 1998)[193]. The IsO functions via secreted *Wnt* and *Fibroblast growth factor (Fgf)* signaling molecules to organize expression of genes and specify cell types (**Figure 9**) (Broccoli et al., 1999)[194] (Wurst and Bally-Cuif, 2001)[170].

In the early 1990s, two independent groups discovered the essential function of *Wnt1* (by then called *int-1*) gene in the correct development of the midbrain and the CB, as its mutation results in the total loss of these two brain structures (McMahon et Bradley, 1990)[190] (Thomas et Capecchi, 1990)[189]. The function of *Wnt-1* in mice was explored disrupting one of the two alleles in mouse embryo-derived stem cells using positive-negative *neo^r* selection method. This cell line was used to generate chimeric mice that transmitted the mutant allele to its progeny. While heterozygous mice for *Wnt-1* mutation were normal, homozygous mice exhibited a range of phenotypes from birth before death to survival with severe ataxia. Further examination at several stages of embryogenesis revealed severe abnormalities in the development of the mesencephalon and metencephalon, indicating a prominent role for *Wnt-1* in the induction of mesencephalon and CB.

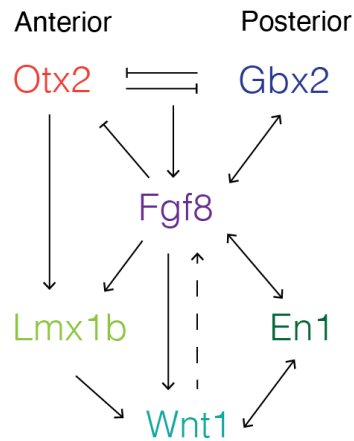


Figure 9. Molecular pathways operating in the MHB and the establishment of the IsO.

Few years later, the function of the diffusible factor *Fgf8* in the development of midbrain and cerebellar structures was evidenced by experiments in chick embryos and quail-chick chimeras (Crossley et al., 1996)[195]. There are 8 isoforms of *Fgf8* (Nakamura et al., 2005)[176] (Crossley et al., 1996)[195]. Despite *Fgf8a* and *Fgf8b* isoforms are specifically expressed in the isthmus (Sato et al., 2001)[196], the presence of all isoforms has been demonstrated to be indispensable for the correct development of the midbrain and CB (Guo and Li, 2007)[197]. *Fgf8a* and *Fgf8b* seem to act differentially in the specification of the midbrain and the CB, respectively.

Since its identification as an instructive signal, *Fgf8* has received enormous attention as a pivotal factor in patterning the midbrain and the CB. *Fgf8* ectopic transplantation induced midbrain and cerebellar tissues in gain of function studies (Marin and Puelles, 1994)[198] (Hidalgo-Sanchez et al., 1999)[199] (Martinez et al., 1999)[200]. In addition, ablation of *Fgf8* expression was translated to midbrain and prospective cerebellum deletion (Chi et al., 2003)[201]. In this study, the authors have studied the function of *Fgf8* in mouse mesencephalon / metencephalon development using a conditional gene inactivation approach to eliminate its expression at early stages (somite stage 10, E8.75). This resulted in a failure to maintain expression of *Wnt-1*, but also *Fgf17*, *Fgf18* and *Gbx2*. Moreover, the absence of the midbrain and cerebellum was attributed mainly to ectopic cell death by staining with Nil Blue Sulfate in mutants MHB. Altogether, these results supported the idea that *Fgf8* is a part of a complex gene regulatory network that is essential for cell survival in the MHB.

Indeed, the regulation of *Fgf8* expression appears to result from the hierarchical and sequential expression of the diffusible *Fgf4* ligand from the notochord, which induces the expression of the

engrailed homeobox 1 (En1) in the midbrain. The expression of *En-1* and its close relative *En2* is critical for cerebellar development, as inactivation of *En-1* causes cerebellar aplasia, while the loss of *En-2* causes cerebellar hypoplasia with abnormal foliation in mice. *En-1* in turn activates the expression of *Fgf8* in the IsO, via a retroviral vector approach to ectopically express *En-1* (Shamim et al., 1999)[202]. Of note, sustained *Fgf8* expression is critical to restrict the expression patterns of *Otx2* and *Gbx2*. In addition, it regulates the expression of *LIM homeobox transcription factor 1 beta (Lmx1b)*, which directly contributes to the maintenance and stabilization of *Wnt-1* expression in the IsO. The simultaneous ablation of *Lmx1b*, and its closely related family member *Lmx1a*, severely alters the general specification of the hindbrain, which adopts a much more posterior fate, and lack a recognizable cerebellum (Lowenstein et al., 2022)[168]. Nevertheless, *Fgf8* expression is transient. Indeed, a decreasing gradient of its concentration is fundamental for both cell survival and the development of the distinct cerebellar regions (Xu et al., 2000)[203] (Suzuki-Hirano et al., 2010)[204].

Altogether, this coordinated molecular network creates a zone in which the CB can form. This is the cerebellar primordium (CP). The CP, also known as cerebellar anlage, is located at the alar plate of the r1. In mice, it can be detected at E8.5-E9. It emerges from a region in which rostral and caudal borders are limited by the expression of *Otx2* (above described) and the transcription factor *Hoxa2*, respectively. Ablation of *Hoxa2* causes caudal expansion of cerebellar tissues, whereas the ectopic expression of this factor in r1 suppresses the specification of cerebellar neurons (Eddison et al., 2004)[205]. Indeed, microsurgery, coupled with electroporation to target *Hoxa2* overexpression, revealed loss of GCs markers and depletion of the cell bodies from the EGL, overall supporting its role in the correct specification of the CB.

The A-P patterning of the CP depends as well on this molecular network. The D-V patterning and the proliferation of cerebellar progenitor cells are primarily mediated by *Shh*, which is expressed by cells located in the ventral midline and the floor plate of the neural tube (De Luca et al., 2016)[206] (Lowenstein et al., 2022)[168].

8.3. Specification of Cerebellar progenitors

In the ventral part of the CP, in a continuum along the fourth ventricle, we can distinguish two specialized proliferative zones: the ventricular zone (VZ), from which all the GABAergic cells will be generated, and the rhombic lip (RL), for all glutamatergic cell generation (**Figure 5A**) (**Figure 10A**). These two germinal zones can be defined by the mutually exclusive expression of *Ptfla* and *Atho1*, respectively. Their deletion was shown to result in the complete loss of the neuronal phenotypes

specified from the corresponding proliferative niche (Ben-Arie et al., 1997)[148] (Wang et al., 2005)[207] (Hoshino et al., 2005)[208] (Pascual et al., 2007)[209]. In addition, ectopic expression of *Atoh1* in the VZ and of *Ptf1a* in the RL highlighted the strong and mutually exclusive specification potential of these two bHLH transcription factors (TFs) (Yamada et al., 20014)[210]. The strict regionalization by bHLH transcription TFs is very reminiscent of the one in the telencephalon (Wilson and Rubenstein, 2000)[211]. However, the dual niche conformation of the CP diverges from other areas of the CNS, where a sole primitive ventricular neuroepithelium gives rise to all neuronal and astroglia phenotypes. Interestingly, parabrachial neurons and a small group of noradrenergic neurons, which will migrate to the brainstem during development, are as well generated in a time dependent manner from the cerebellar VZ (Millen et al, 2014)[212]. Likewise, extra-cerebellar isthmus nuclei neurons are generated from the RL, and they are located in the anterior nuclear transitory zone (NTZ) during development.

Nonetheless, while genetic and viral lineage tracing studies provided crucial information about the origin and birthdate of distinct subtypes of cerebellar neurons (Leto et al, 2016)[4], the molecular mechanisms controlling their generation, as well as their post-mitotic differentiation remain largely unknown.

Two models for explaining the specification mechanism of progenitor cells in the CNS have been proposed with respective evidence: progressive specification model and early allocation model (Haldipur et al., 2019)[11] (Tong et al., 2015)[213] (**Figure 10B**). On one hand, the progressive specification model, derived from the embryonic development of the neocortex, describes the generation of different types of neurons via continuous specification from the neural stem cells. On the other hand, the early allocation model proposes that neural stem cells are specified at an early stage to give rise to different populations of specific neuronal cell types.

Despite what appears to be independent from spatial and temporal origins, increasing evidence suggest the developmental specification of the regional heterogeneity among the cerebellar cell types (Lowenstein et al., 2022)[168]. Pseudo-time trajectory analysis of scRNA-seq embryonic mouse CB data suggests that a common pool of progenitors branches out into either glutamatergic fate or GABAergic fate (Vladoiu et al., 2019)[132]. In addition, the classic neural stem cell marker *Sox2*, which is known as an early VZ marker (Pibiri et al., 2016)[214], was shown to be co-expressed with the glutamatergic RL marker *Atoh1* in human cerebellar organoids (Muguruma et al., 2015)[215], suggesting that both germinal lines share common *Sox2* progenitors. Moreover, very recent fate mapping and single-cell analysis of *Sox2* progenitors in the RL have shown that they can give rise to

excitatory neurons (Selvadurai et al., 2020)[216]. In support of this, recent work has revealed that Notch signaling between *Sox2* cerebellar progenitors at the VZ/RL boundary determines whether they give rise to glutamatergic (low Notch) or GABAergic (high Notch) (Zhang et al., 2021)[217]. Overall, it seems plausible that common progenitors in the CP can create cell-type diversity across different time scales. Noteworthy, the diversity of neuronal populations, both inhibitory and excitatory, in the developing CB is paralleled by the heterogeneity among the progenitor population (Sepp et al., 2021)[140]. Early embryonic cerebellar neurogenic progenitors display a R-C gradient of molecular variation along the neuroepithelium, while in later stages they are gradually outnumbered by bipotent progenitors which have decreased expression of cell cycle-related genes in comparison to early progenitors.

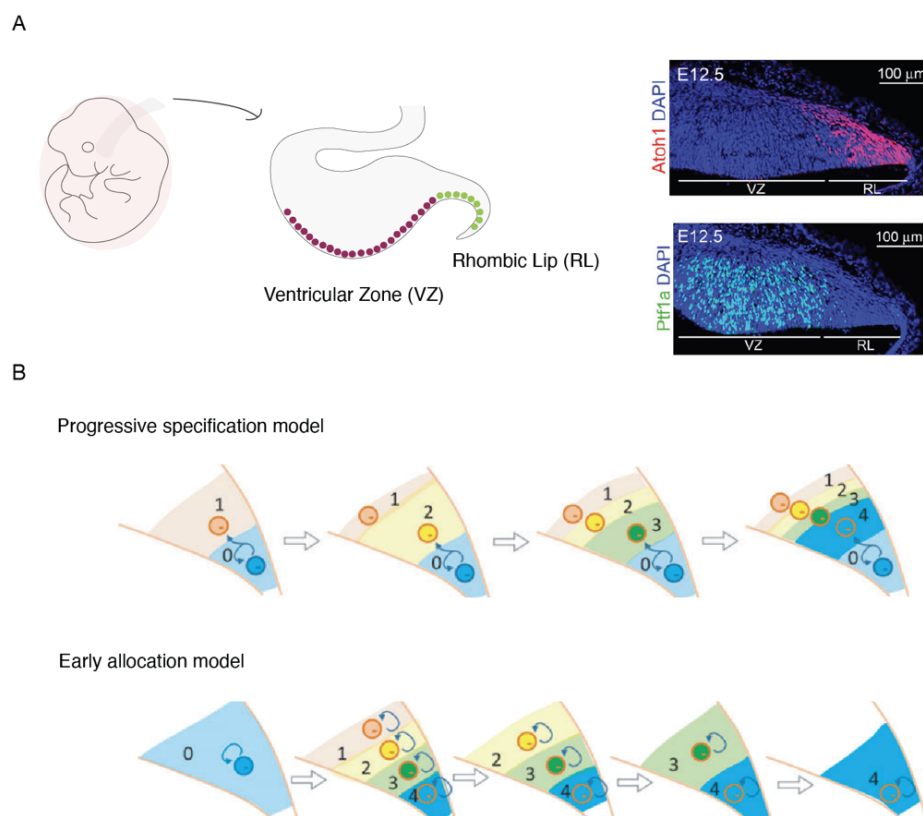


Figure 10. The cerebellar primordium A) Schematic representation of the cerebellar primordium in the E12 embryo (left). Two proliferative zones can be distinguished: Ventricular Zone (VZ) and Rhombic Lip (RL). Mutual exclusive expression of *Atoh1* (red) and *Ptf1a* (green) in the E12 cerebellar primordium. (Adapted from Lowenstein et al, 2022) B) Schematic diagrams illustrating the differences between the progressive specification model and the early allocation model in the cerebellar RL (Adapted from Tong et al, 2015).

8.3.1. The rhombic lip

The RL was first described by Hiss in 1891. It is located at the dorsal most part of the developing rhombencephalon. It is subdivided into a rostral RL (in r0/r1) and caudal RL (that expands from r2 to r7/r8). Initial birth-dating studies revealed the rostral RL to be the neurogenic source of cerebellar glutamatergic neurons, whereas the caudal RL was the source of excitatory afferent MFs (Hirsch et al., 2021)[218]. Excitatory neurons neurogenesis in the CB is driven by the expression of *Atonal homologue 1* (*Atoh1*, formerly known as *Math1*) as early as E9.5 (Ben-Aire et al., 1997)[148] (Wingate, 2001)[219]. *Atoh1* expression persists selectively in the RL and many of its derivatives. Indeed, *Atoh1* ablation results in the complete loss of GCs population without affecting PCs, therefore highlighting the precise compartmentalization of these two lineages (Ben-Aire et al., 1997)[148]. The roof plate (RP) located immediately next to the RL, acts as a signaling center that imposes a dorsal fate to its neighboring neuronal tube progenitor cells (in the rhombencephalon and spinal cord) by secreting signaling cues such as *Wnt* ligands and bone morphogenic proteins (BMPs) (Chizhikov and Millen, 2004) [220]. The RP is known to express *Lmx1a*, the expression of which is particularly critical for the correct specification of the cerebellar excitatory neurons destined to populate the cerebellar V. Available evidences illustrate that the double mutation of *Lmx1a/Lmx1b* in mice results in the absence of the RP and affect the expression of *Atoh1* in the RL (Mishima et al., 2009)[221]. More in detail, the authors of this study showed that *Lmx1a* and *Lmx1b* are individually dispensable for RP induction. Complete loss of both genes, however, abolishes hindbrain RP demonstrating that both genes have overlapping roles in inducing this critical embryonic signaling center. Double conditional mutant mice showed severe fourth ventricle RP size reduction. The viability of these conditional mutant mice with small RF allowed them to further demonstrate that r1 RP directs multiple aspects of cerebellar morphogenic, including RL proliferation.

The rostral RL, from now on RL, is the source of three distinct excitatory neuronal derivatives that emerge in a stereotyped temporal order: DCN (predominantly between E10.5 and E12.5), EGL (between E12.5 and birth) and UBCs (between E14.5 and the first days of postnatal life) (Wang et al., 2005)[207] (Kita et al., 2013)[222] (Green and Wingate, 2014)[223] (Hagan and Zervas, 2012)[224] (Lowenstein et al., 2022)[168]. This contrasts with a long-standing model proposing the GCs as the unique cell type derived from the RL. Interestingly, a recent study shows that the bHLH transcription factor *Oligodendrocyte factor 3* (*Olig3*) is an early determinant for cerebellar excitatory neurons specification, particularly for the development of DCN neurons and early born EGL neurons

(Lowenstein et al., 2021)[225]. Lineage tracing experiments using CRE-based approaches and immunofluorescence, showed that *Olig3* expression can be detected in the presumptive RL already from E9.5, preceding the expression of *Atoh1*. A partial overlap in the expression of *Olig3* and *Atoh1* was shown between E10.5 and E13.5, after which *Olig3* expression becomes downregulated. In turn, ablation of *Olig3* compromised the generation of DCN neurons and resulted in the elimination of about a half of EGL cells. Of note, although BrdU-based proliferative and Tunel-based apoptosis assays demonstrated that impairment in *Olig3* did not affect VZ proliferation, GFP genetic labeling in mutant mice elucidated its role in controlling the specification of PCs. Indeed, misspecification of PCs was identified, evidenced by the adoption of an inhibitory interneuron identity.

The detailed development of RL-derived cell types is described in section 5.4.2.

8.3.2. The ventricular zone

The VZ, whose name derives from its location facing the fourth ventricle, was described more recently than the RL (Hallonet et al., 1990)[187] (Hatten and Heintz, 1995)[226] (Mathis et al., 1997)[227]. This proliferative niche is the source of most types of cerebellar GABAergic neurons (PCs and interneurons) as well as of astrocytes (Sudarov et al., 2011)[20]. It is characterized mainly by the expression of *Ptf1a* which is the earliest VZ known marker. Like *Atoh1* in the RL, the ablation of *Ptf1a* was shown to result in the inhibition of GABAergic neurons and, eventually, in the peculiar loss of the entire CC (*cerebellless mice* (Hoshino et al., 2005)[208]). In addition, unusual GCs production in the VZ was observed in *Ptf1a*-null mice, raising the fascinating hypothesis that cerebellar progenitors in the VZ possess an intrinsic glutamatergic developmental program (Pascual et al., 2007)[209]. In contrast, ectopic expression of *Ptf1a* in dorsal telencephalon precursors, which are physiologically the source of solely glutamatergic neurons, resulted in the ectopic production of GABAergic neurons with their typical morphological and migratory features (Hoshino et al., 2005)[208].

In contrast to the RL, that uniformly produces all types of cerebellar neurons, the VZ has been divided into distinct domains recognized as responsible for the generation of different classes of GABAergic neurons (Dastjerdi et al., 2012)[228] (Hori and Hoshino, 2012)[229]. At the early neurogenic stage (around E12 in mice), this primary niche can be divided dorsally and ventrally into two domains, which express E-cadherin strongly or weakly, respectively (Minaki et al., 2008)[230] (Mizuhara et al., 2010)[231]. The expression of two non-overlapping TFs, *Gsx1* (rostrally) and *Olig2* (caudally) further distinguished these two domains. Lineage tracing experiments revealed that, while *Gsx1* territory hosts

Pax2⁺ GI progenitors, the Olig2⁺ domain give rise exclusively to PCs (Seto et al., 2014)[232]. This is consistent with the observation that, in the tissue overlying the Gsx1 and Olig2 domains, two non-overlapping populations of postmitotic immature neurons can be distinguished and differentially express Pax2 and Corl2, corresponding to Gis and PCs, respectively (Minaki et al., 2008)[230] (Seto et al., 2014)[232]. Interestingly, the gradual ventral expansion of the Gsx1 domain as development proceeds inhibits Olig2 activity and consequently leads to the production of Gis at the expense of PCs, that are no longer produced after E14. In addition, the expression of other proneural genes such as *Neurogenin (Ngn) 1*, *Ngn2* and *Ascl1* was reported in the VZ (Zordan et al., 2008)[233]. *Ngn1* and 2 appear to differently regulate the generation of GABAergic neurons. Namely, Ngn1⁺ progenitors produce all Gis but those in the DCN, together with a subset of PCs (Vue et al., 2007)[234] (Lundell et al., 2009)[235] (Kim et al., 2011)[236], whereas *Ngn2* is responsible for PCPS cell cycle exit and maturation (Florio et al., 2012)[237]. On the other hand, *Ascl1* broadly overlaps the Ptf1a⁺ domain from early embryonic stages and it was shown to participate in the specification of all GABAergic neurons (Grimaldi et al., 2009)[238] (Sudarov et al., 2011)[20]. Hence, the VZ appears to be a mosaic of distinct progenitor subtypes, defined by the expression of spatially regulated combinations of TFs.

The detailed development of RL-derived cell types is described in section 5.4.1

8.4. Neuronal development

The source of cellular heterogeneity remains poorly understood, but it is commonly thought to be modulated by the balance between intrinsic regulatory networks and extrinsic cellular microenvironment. Cellular diversity is the result of a dynamic combination of several genes that define the genetic signature of a neuron during development and determine its properties (Telley et al., 2016)[239] (Galloway et al., 2016)[240] (Wilsch-Brauniger et al., 2016)[241].

As demonstrated in previous studies, different cell types are sequentially generated during cerebellar development (Leto et al., 2016)[4]. Regarding CC cell populations, PCs are born from VZ progenitors early in development (between E10 and E13), after which GCs are generated between E13 and P10 from RL progenitors. Ultimately, Gis are generated at mid-to late stages of development. Remarkably, PCs are directly generated from terminal divisions of VZ progenitors in contrast to GCs and Gis, born through transient precursors that start to proliferate during the first post-natal week to generate these post-mitotic neurons. Thus, while PCs rapidly form PCL, other cerebellar cortical layers are only formed postnatally as newly generated GCs and Gis migrate and assemble whit PCs (Leto et al,

2016)[4]. DCN spatio-temporal development starts around E10 with the specification of the excitatory DCN neurons from the RL, followed by inhibitory DCN neurons from the VZ around E12-E13. However, what is missing so far is a dynamic understanding of the molecular processes underlying cerebellar development as well as a more precise characterization of the cerebellar cell heterogeneity. The results presented in this thesis contribute to better understand the spatio-temporal sequence of events that occurs during cerebellar development. In addition, we present the first insights towards an integrative view and understanding of cerebellar development.

In this section, I will review the development of cerebellar inhibitory (GABAergic) and excitatory (Glutamatergic) lineage, raising the main molecular mechanisms involved in the generation of each specific cell type. This includes PCs, MLIs, GoCs, LCs, Globular cells and inhibitory neurons of the DCN for the GABAergic lineage; and GCs, UBCs, Candelabrum cells and excitatory neurons of the DCN for the glutamatergic lineage.

8.4.1. GABAergic lineage: description and development

Like RL-derived glutamatergic neurons, GABAergic cells are generated from VZ progenitors according to a well-defined time schedule (**Figure 11**) (Miale and Sidman, 1961)[242] (Pierce, 1975)[243] (Altman and Bayer, 1997) (Morales and Hatten, 2006)[244] (Sepp et al., 2021)[140]. The first cells to be born are the GABAergic nucleo-olivary projection neurons of the DCN, followed by PCs (between E10.5 and E13.5 in mouse). Progenitor cells immediately migrate into the prospective white matter (PWM), which is then populated by post-mitotic precursors of the DCN neurons below the cerebellar surface and, underneath, by postmitotic PCs organized in cluster-like manner. Between E14 and E17, DCN neurons and PCs migrate to opposite directions, reaching their final positions in the deep cerebellar parenchyma and beneath the nascent EGL, respectively. On the other side, Gis are generated during late embryonic and postnatal development supposedly from common precursors. Namely, all Gis were shown to derive from a common pool of PAX2⁺ progenitors that appear in the VZ at around E13 and thereafter migrate in the PWM. Here, they keep on proliferating until late embryonic and postnatal development (Zhang and Goldman, 1996)[245], producing different GI types according to a peculiar inside-out sequence from DCN to GL, and eventually, ML (Altman and Bayer, 1997) (Schilling, 2000)[246] (Leto et al., 2006)[247] (Leto et al., 2008)[248]. Interestingly, 5 Gis subtypes have been recently defined already in the developing CB which directly match the

transcriptionally-defined subtypes in the adult mouse cerebellum (Sepp et al., 2021)[140] (Kozareva et al., 2021)[249], suggesting an early specification of GIs in cerebellar development.

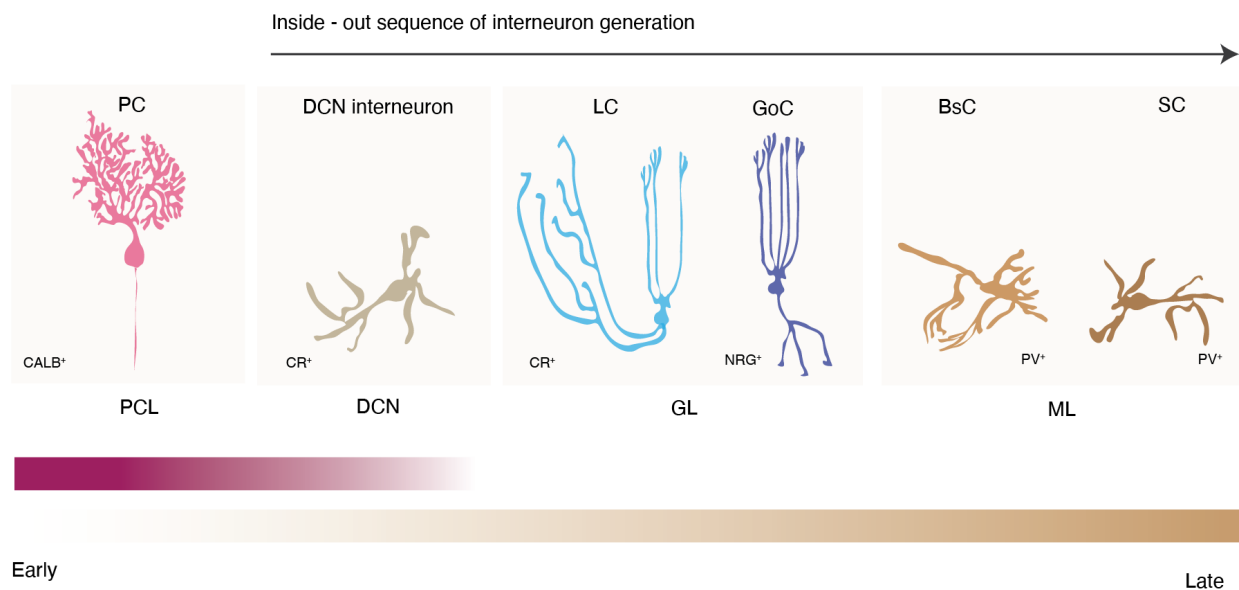


Figure 11. Schematic representation of cerebellar GABAergic lineage generation. The different cerebellar GABAergic cells are represented, as well as their location in the cerebellar cortex and their corresponding molecular markers: Purkinje cell (PC), Deep cerebellar nuclei interneuron (DNC interneuron), Lugaro cell (LC), GoC (Golgi cell), BsC (Basket cell), Stellate cell (SC), Purkinje cell layer (PCL), Deep cerebellar nuclei (DCN), Granule cell layer (GL), molecular layer (ML), Calbindin (CALB), Calretinin (CR), Neurogranin (NRG), Parvalbumin (PV). PCs generation precedes GABAergic interneuron generation during cerebellar development. Interneurons generation occurs in an inside-out sequence fashion along the cerebellar cortex. (Adapted from Leto et al., 2016)

8.4.1.1. Purkinje cells

PCs, first described by Johannes Purkinje in 1837, are the principal cells of the CC. PC dendrites shape a planar arborization which lays in the ML in a sagittal plane orthogonal to the plane of PFs. A single PC receives ≈ 175000 excitatory synapses from PFs. These contact PCs on dendritic spines located on branchlets (thinner ramifications from secondary and tertiary PCs dendrites), and each dendritic spine receives only one PF connection most of the time (Harvey et Napper, 1988)[250] (O'Brien and Unwin, 2006)[251]. In contrast, CFs establish a single connection to each PC, but with hundreds of release sites that cover PCs' dendritic trunk instead (Palay and Chan-Palay, 1974). PCs send their projection to the DCN and make GABAergic inhibition in a projection areas containing several different types. Projection areas of different PCs overlap (Pantó et al., 2001)[252] and thus, each nuclear cell receives inhibition from several PCs. PCs axonal collaterals also contact several other cell types of the CC (other PCs, LCs, MLIs, GoCs) (Palay and Chan-Palay, 1974) (Hirono et al., 2012)[74]

(Consalez et al, 2021)[158]. Because PCs are the sole output of the CC, they are the final determinant of any functional heterogeneity (Cerminara et al., 2015)[3]. The different subtypes of PCs are organized first into five *transverse zones*, each of them being further subdivided into dozens of reproducible *stripes*. This patterned disposition serves as scaffold to organize afferent topography and restrict the distribution of excitatory and inhibitory interneurons (see section 6) (Consalez at Hawkes, 2012)[253] (Hawkes, 2018)[254]. At intermediate stages of development and in mature CB, parasagittal cerebellar organization, first described by Feirabend in the embryonic chicken (Feirabend, 1983), is mirrored by various biochemical markers and the expression of large variety of genes by specific PCs clusters (Redies et al., 2011)[255]. Zebrin II is the most extensively studied striped marker and was shown to be expressed by parasagittally-distributed subsets of PCs giving rise to Zebrin II⁺ and Zebrin II⁻ stripes (Brochu et al., 1990)[256] (Ahn et al., 1994)[257]. Interestingly, the expression of a wide variety of molecular markers correlating, complementing or subdividing Zebrin II patterning have been characterized, revealing a whole new level of cerebellar complex partitioning (Eisenman and Hawkes, 1993)[258] (Murase et al., 1996)[259] (Mateos et al, 2001)[260] (Armstrong et al., 2001)[261] (Jeong et al., 2003)[262] (Marzban et al., 2008)[263] (Sarna et al., 2006)[264] (Croci et al., 2006)[265] (Chung et al., 2007)[266]

For many years, whether the molecular diversity of PCs was established early in the development remained unclear. During early specification of PCs, several bHLH factors have been reported to be co-expressed with *Ptf1a* in progenitor cells of the VZ, including *Ascl1*, *Neurog1*, *Neurog2*, *Olig3* and *Olig2*. Although *Ascl1* and *Neurog1* are highly expressed in the VZ during PCs specification, ablation of their expression did not significantly alter the development of PCs (Grimaldi et al., 2009)[238] (Sudarov et al, 2011)[20]. However, *Neurog2* has been shown to play a role in regulating PCPs proliferation in the VZ. Interestingly, ablation of *Neurog2* did not interfere with PCs specification but altered their postmitotic maturation and the correct elaboration of their dendritic arbors (Florio et al., 2012)[237].

Single-cell profiling of E13.5 mice embryos identified five transcriptionally unique subtypes of PCs, defined by their expression of *Etv1*, *Nrgn*, *En1*, *Cck* and *Foxp1*. Immunofluorescence analysis revealed that these subtypes occupied distinct regions in the CB, and they could also be identified at E18.5 (Wizeman et al., 2019)[267]. These results support the idea that PCs subtype is specified, at least, shortly after leaving the cell cycle, and this might determine their final spatial location. Moreover, snRNA-seq analysis of the adult CB, further expanded the number of PCs subtypes to nine (Kozareva et al., 2021)[268], raising the question of how the embryonic CP subtypes relate to the clusters found

in the adult CB. Recent characterization of molecular differentiation of cerebellar cells during development has elucidated four developmental PCs subtypes emerging from VZ neuroblasts: medial (*Rorb* and *Cdh9*), lateral (*Foxp1*, *Etv1*), late born (*Cdh9*, *Etv1*) and early born (*Rorb*, *Foxp1*) (Sepp et al., 2021)[140]. Despite a shared transcriptomic program, combinatorial expression of TFs *Ebf1* and *Ebf2* along the spatio-temporal axes, respectively, differentiate the subtypes. Noteworthy, the abovementioned subtypes were linked to known adult PCs populations, suggesting that PCs heterogeneity is generated not only by birthdate but also by birthplace.

PCs are generated between E10.5 and E13.5 and their relative abundances peak at the transition from embryonic to fetal development (E13.5-E15.5 in mouse) (Sepp et al., 2021)[140]. From the VZ, postmitotic PCs migrate dorsally along radial glia processes (Morales and Hatten, 2006)[244]. They stack till E14 to form a transient several cells thick mass named *PC plate*. At E18, the PC plate reorganizes giving rise to an array of PCs clusters of multiple molecular phenotypes (Sugihara et al., 2011)[34] (Tran-Anh et al., 2020)[269]. The number of PC clusters also increases during this period. Indeed, a recent study revealed that the 9 molecularly recognized PCs at E14.5 become 37 at E17.5 (Tran-Anh et al., 2020)[269]. Then, spatial rearrangement of PCs clusters occurs, which is essential for adult cerebellar compartmentation and necessary in organizing the dual somatotopic areas in the adult mouse (Tran-Anh et al., 2020)[269]. Namely, PCs clusters transform into stripes, triggered by Reelin (RELN) secreted from the EGL. RELN has proven to be critical, as its deletion in the *Reeler* mouse blocks cluster dispersal. Interestingly, cluster dispersal seems not to be a pre-requisite for phenotypic maturation (D’Arcangelo et al., 2014)[270] (Tran-Anh et al., 2020)[269]. Indeed, ectopic PCs *Reeler* and other mice model for cluster dispersal blocking (*disabled1*, *weaver*), express their normal subtype phenotypes although trapped at the cluster stage (Hawkes, 2018)[254]. It seems plausible that TF such as *FoxP2* and *Corl2* may control the expression of compartment-specific molecules since differences in their expression levels among PC are useful to detect trackable PC cluster in the developing CB (Tran-Anh et al., 2020)[269]. Of note, distinct cohorts of PCs born on distinct days have been shown to settle in distinct M-L and A-P positions in the CC. Indeed, if early birth-date analysis in rat had already given a hint if a gradient of production of PCs from lateral (H) to medial (V) (Altman and Bayer, 1997), fate mapping analyses exploiting the *Ascl1* promoter in mice have confirmed the predicted and distinct M-L organization of the PCs targeted on different days (Sudarov et al, 2011)[20]. Along the A-P axis of the V, instead, the earliest born PCs were shown to occupy the central lobes, followed by those settled in the posterior and, at last, anterior lobes (Altman and Bayer, 1997) (Sudarov et al., 2011)[20]. Recently, snRNA-seq analysis of the developing CB

supports the early spatiotemporal patterning of PCs (Sepp et al., 2021) [140]. Overall, these studies suggest that the specification of PCs might occur very early in development.

A question that remains to be answered is whether the VZ contains two distinct progenitor cells that exclusively generate PCs or GIs, or whether the same progenitor cells can transit from generating PCs to interneurons. In 2014, Seto et al. postulated a “temporal identity transition” model, based on detailed short-term lineage-tracing experiments, in which *Olig2*⁺ PCs progenitors transition into GI progenitors (Seto et al., 2014)[232]. From this model, one would expect that GIs would have a history of *Olig2* expression. However, long-term lineage tracing experiments using *Olig2*^{cre} and *Olig3*^{creERT2} mice showing that PAX2⁺ GIs rarely express none of these factors during their developmental progression, challenging this model (Ju et al., 2016)[271] (Lowenstein et al., 2021)[225]. In addition, *Olig3* is expressed in most VZ proliferative cells during development of PCs. Also, the ablation of *Olig2/ Olig3* does not result in the specification of GIs but rather the misspecification of PCs, which are later transformed into GIs by the action of PAX2. Altogether, these evidences raise the hypothesis that two progenitor cell types might exist in the VZ, one active for PCs and a second quiescent in early development, which later generates GIs.

8.4.1.2. Molecular layer interneurons: Stellate and Basket cells

Molecular layer interneurons (MLIs), located in the upper layer of the CC, the ML, are small inhibitory interneurons. They are contacted and excited by PFs and they provide a feedforward inhibition to PCs and other interneurons in the same layer. Like PC dendrites, MLI dendrites are projected in the parasagittal plane. However, it is known that they can also inhibit neighboring PCs laterally that do not receive the same beam of PFs (Eccles, 1967)[272] (Llinás and Sugimori, 1980)[273] (Cohen and Yarom, 2000)[274]. Interestingly, several physiological studies both *in vitro* and *in vivo* suggested that the inhibitory fields of MLIs are confined to a single stripe, with ML inhibition restricted parasagittally. To what extent MLIs are indeed restricted to particular stripes and how they acquire their parasagittal orientations remains unclear (Consalez and Hawkes, 2012)[253].

MLIs have been historically divided into stellate (SCs) and basket (BCs) cells. Even so, for many years the distinction between the two types was not totally clear and a smooth transition between cell types was suggested in several studies (Sultan and Bower, 1998)[275] (Mittman and Häusser, 2007)[276] (Schilling et al., 2008)[18]. Nevertheless, differences in the short-term dynamics of PF connections to SCs and BCs have been shown (Bao et al., 2010)[277]. The two cell types were shown to differ in

their respective locations as well: SCs located mostly on the superior part of the ML, while BSc mostly in the lower part. BCs, first described by Ramon y Cajal (Ramon y Cajal, 1911), have a special axonal extension which is found to cover the soma and the axonal initial segment (AIS) of PCs. These paint brush shaped synapse formation it is also known as *Pinceau* synapse (Ango et al., 2004)[52] (Telley et al., 2016)[278] (Sillitoe et al., 2012)[19]. In a mature rodent cerebellar cortex, a single BCs innervates up to ten PCs that are hundreds of microns apart, and a single AIS receives inputs from five to seven BCs (Palay and Chan-Palay, 1974). There is little evidence of distinct subclasses of BCs and/or SCs. Still, *protein kinase C* δ^+ MLI were shown to strongly concentrate in the anterior zone in the rat CB (Chen and hillman, 1993)[279]. Besides their morphological, innervation and positional specificities, no genetic marker to differentiate them has been elucidated so far (Carter et al., 2018)[280]. Interestingly, recent scRNA-seq adult data revealed two classes of MLI which they termed as class I (MLI1, *Sorcs3*⁺) and class II (MLI2, *Nxph1*⁺) (Kozareva et al., 2021)[249]. Both classes of interneurons differ in their electrophysiological properties, and many class I, but not class II, were coupled to one another via gap junctions, suggesting that the transcriptomic differences between these two classes are also functionally relevant. However, whether these two classes correlate with the distinction of BCs and SCs, remains to be resolved.

The first studies of cerebellar neurogenesis postulated that MLIs derive from the EGL, a secondary germinal layer known to be active during postnatal development (See section 5.4.2.1). Later, analysis of chick-quail chimeras, transplantation experiments and retroviral injections demonstrated that EGL exclusively generates GCs and indicated that MLIs derive from the VZ (Leto et al, 2016)[4]. The production of MLI occurs from late embryonic life to the second postnatal week, according to a precises inside-out sequence (Leto et al., 2008)[248] (Carletti et Rossi, 2008)[281]. Namely, in rat, BCs are born between P2 and P17 with a peak at P6, while SCs are born between P4 and P10, with a peak at P10 (Altman and Anderson, 1972)[282]. In support of that, temporal fate mapping of cerebellar interneurons by using the *Ascl1*^{CreER} mice revealed that tamoxifen injection from P1 to P7 mainly labeled SCs, indicating that the majority of BCs are already specified before P1 (Sudarov et al., 2011)[20].

The dividing intermediate MLIs progenitors responsible for the extensive amplification of this cell type strongly express *Ptf1a*. Like all GABAergic interneurons, MLIs progenitors transiently express *Pax2* during cell cycle exit. Then, indistinguishable SCs and BCs progenitors reside for several days in the PWM, where they progress in their maturation, and acquire their final identities, before homing in on their final destination in the CC (BCs, inner ML; SCs, outer ML). The understanding of MLIs

migration and integration into cerebellar circuits has remains poorly understood. Earlier studies using retroviral tracing showed that BCs and SCs precursors migrate from the PWM through the PCL to reach the ML (Zhang and Goldman, 1996)[245]. Phenotypic differences between the two classes of MLIs recently shed a light on the cell-type-specific divergences during the process of their circuit integration (Cadilhac et al., 2021)[283]. Using a combination of genetic tracing and two-photon live-imaging experiments, the authors of this study demonstrated that despite their common origin, BCs and SCs use separate migratory paths to reach their cortical position and ultimately, differentiate. After reaching the ML, BCs directly start to differentiate, as identified by loss of *Pax2* expression and the subsequent expression of the mature neuronal marker *Parvalbumin (Parv)*. In parallel, a fraction of cells enters the EGL and performs an additional step of tangential migration and, therefore delaying the onset of its differentiation. These differences have been suggested to contribute to a change in environmental cues critical for cell diversity generation. In addition, conditional depletion of GCs using *Atoh1^{CreER}*; *Atoh1^{Flx/Flx}* mice affected only SCs differentiation, which likely occurs through cellular interactions with GC progenitors. Supporting the idea of distinct MLIs differentiation paths, the examination of *NeuroD2* – deficient mice showed that *NeuroD2* it is required for the terminal differentiation of BCs, but not SCs (Pieper et al., 2019)[284]. Indeed, BCs axons of mutant mice followed irregular trajectories, and their inhibitory terminals were absent from PCs. Interestingly, early ablation of *NeuroD2* proved to be essential for postnatal survival of both MLIs, as well as GCs. Finally, the terminal differentiation and morphogenesis of MLIs depends on PCs. Specifically, neurofascin was shown to play a critical role in defining the complexity of MLIs axonal arborization and their position on PCs (Ango et al., 2004)[52] (Buttermore et al., 2012)[285], together with Semaphorin (*Sema3a*)/neuropilin-1-mediated signaling between PCs and differentiation MLIs (Cioni et al., 2013) [286]. Conversely, BCs/SCs dendritic differentiation seems to be sensitive to GCs signaling, including BDNF and *Glud1* receptor (Mertz et al., 2000)[287], whose ablation resulted in reduced survival and impaired growth of early mature MLIs (Konno et al., 2014)[288]. Overall, these data suggest that local interaction between excitatory and inhibitory progenitors in the CB are critical for interneuron subtype differentiation and proper circuit assembly.

8.4.1.3. Golgi cells

The Golgi cells (GoCs), located in the GCL, play a central role in regulating spatio-temporal topologically organized GCL activity (D'Angelo et al., 2013)[146]. They receive excitation from MF and GCs, and then inhibit the GCs in the glomerulus (as described in section 1.3). Its name comes

from Camillo Golgi (Golgi, 1874) , who first described the morphology of these cells. This description was further extended by Ramon y Cajal, predicting its function as a local interneuron (Ramon y Cajal, 1911). Marr (Marr, 1969)[57] suggested that GoCs were driven by PFs and MFs. Later descriptions postulated that these cells receive inputs not only from GCs and MFs but also from CFs, PCs and MLIs (Palay and Chan-Palay, 1974) (Galliano et al., 2010)[289]. GoCs have an irregular soma with a series of basal dendrites, two or three apical dendrites and a widely ramified axon (Barmack and Yakhnista, 2008)[290]. The axonal part of GoCs makes a big plexus which sends projections to several glomeruli. In turn, basal dendrites ascend into the ML traversing the PF bundle. Gap junction connections between GoCs have been noticed as well, suggesting an activity synchronization to generate a network inhibition on the excitatory inputs of the CC (D'Angelo and De Zeeuw, 2009)[291] (Vervaeke et al., 2012)[292] (Szoboszlay et al., 2016)[293]. The functional relevance of GoCs was demonstrated by selective depletion of this cell type using immunotoxin-mediated cell targeting ablation technology (IMCT), to conditionally disrupt both mitotic and postmitotic neuronal cells in adult transgenic mice. Metabotropic glutamate receptor 2 (mGluR), preferentially expressed in GoCs, was used to specifically target IMCT, which resulted in the reduction of GABA-mediated inhibition translated into major motor impairments (Watanabe et al., 1998)[294].

Attempts to identify GoCs subtypes by their biochemical fingerprints have revealed differential expression of certain biochemical markers such as *calretinin* (*Calret*) and *neurogranin* (*Ngrn*), and of their co-expression with glycine, which can be co-released with GABA in certain GoCs subpopulations. Based on that and their morphology, five distinct classes of GoCs have been identified. (Geurts et al., 2003)[295] (Simat et al., 2007)[296]. A detailed neurochemical and morphological characterization of GoCs of glycinergic and GABAergic *Gfp* expressing mice in combination with dual immunofluorescence against mGluR2 and *Ngrn*. *Ngrn* was found to label GABAergic GoCs selectively, whereas mGluR2 was detected almost exclusively in GoCs with dual neurotransmitter phenotype. Thus, the majority (about 65%) of GoCs seemed to be glycinergic and GABAergic and expresses both markers. The second and third groups also expressed mGluR2, but not *Ngrn*. They form two morphologically distinct subsets of cells (each representing about 5-15% of GoCs). Among the small cells, some are glycinergic only. The fourth group is made uniquely of GABAergic cells expressing *Ngrn* (15%). Finally, a fifth small population of glycinergic GoCs lacking mGluR2 and *Ngrn*, with a large polygonal cell body was also observed. Yet, the physiological differences among these subtypes are not fully understood (D'Angelo et al., 2013)[146].

The origin of Golgi cells has been under debate for several decades. Both prevalent views, the EGL origin and the VZ neuroepithelium origin, seem likely correct, and it has been suggested that this may explain some of the subpopulation variability of this cell type. Indeed, cerebellar transplantation experiments have provided evidence that Golgi cells originate from the EGL between E13 and E16 (Hausmann and Sievers, 1985)[297] (Chung et al., 2011)[298], which was previously suggested by Popoff (Popoff, 1896) and Athias (Athias, 1896). In parallel, retroviral lineage tracing data suggest that Golgi cells derive from the VZ. By this view, pioneered by Ramon y Cajal (Ramon y Cajal, 1911) and Altman and Bayer (Altman and Bayer, 1977), Golgi cells, like the other types of GIs, originate from *Ascl1*⁺ progenitors that delaminate from the VZ into the PWM, exit the cell cycle and express Pax2, as all other GABA interneurons of the CB.

8.4.1.4. Lugaro cells

Another kind of GABAergic interneuron of the CC is the Lugaro cell (LCs). LCs were first described in 1894 (Lugaro, 1894) as large cells lying in the upper GCL of the cat and generating a peculiar axonal arborization that runs longitudinally, with the PFs in the lower ML. LCs are not located in defined parts of the CC, like Unipolar Brush cells (see section 5.4.2.2), but are present throughout the CC. Two types of LCs have been identified in the CC: fusiform and triangular, being located at different levels of the GCL. Due the dense innervation by PCs axons, LCs have often been regarded as the same as GoCs. Still, they should be identified as a separate group of interneurons. In turn, LCs form parasagittal plexuses and establish mixed inhibitory contacts (GABA and glycine) with GoCs via long axons running with the PFs, but never on PCs (Melik and Fanardzhyan, 2004)[299] (Simat et al., 2007)[296]. Recent elucidation of LCs circuit configuration thanks to a novel Yellow Camaleon mouse line supports the idea that LCs integrate various excitatory, inhibitory and modulatory inputs, and effectively disinhibit cerebellar cortical activities in a compartment-dependent manner through inhibition of GABAergic interneurons selectively targeting PCs and GCs (Miyazaki et al., 2021)[300]).

LCs, described later than GoCs, are still most enigmatic among cerebellar neurons. They are glycinergic/GABAergic and lack the expression of mGluR2 and *Ngrn*. Instead, they are positive for GlyT2, GAD67 (Simat et al., 2007)[296] and *Calret* (Laine and Axelrad, 2002)[301]. Despite the increasing interest for the understanding of this cell type, little is known about the development of LCs. As the rest of GABAergic interneurons, they are produced from late embryonic life to the second postnatal week from the VZ.

8.4.1.5. Globular cells

Globular cells are the least characterized interneurons in the CC. Initially, they were considered a subset of LCs (Laine and Axelrad, 2002)[301] (Simat et al., 2007)[296]. Their globular cell body is in the GCL and extend dendrites and axons to the ML. From their similar location, *Calret* expression and axonal projection, they are often considered to be the same than Lugaro cells (Laine and Axelrad, 2002)[301]. Globular cells are often neglected from the cerebellar cell composition, partially due to insufficient understanding of their input-output relationships in the cerebellar circuits. Likewise, their developmental processes remain unknown.

8.4.1.6. Inhibitory DCN neurons

DCN neurons integrate sensorimotor information and form the final output of the CB, projecting to a variety of brain targets. This implies that, in contrast to specialized cortical cell, neurons within the DCN encode and integrate complex information that is most likely reflected in a heterogeneous cell population. Yet, DCN cell heterogeneity generation and how this correlates with their role in information transmission are still poorly understood.

DCN neurons develop in parallel to the CC, using much the same molecular machinery. The neurons of the DCN, which can be grouped into inhibitory and excitatory types, develop according to different timetables (Fink et al., 2006)[302]. Pioneering birthdate studies assigned the VZ as the sole source of DCN neurons. However, this assumption was overturned by genetic lineage maps using *Atoh1* reporter (Fink et al., 2006)[302] (See section 5.4.2.4). In addition, more recent mapping using *Ptf1a* reporter revealed that VZ give rise only to inhibitory neurons of the DCN (Yamada et al., 2014)[210]. Hence, just as for the CC, the generation of DCN neurons is defined by the coordinated expression of *Ptf1a* and *Atoh1*.

Inhibitory DCN neurons comprise medium-sized GABAergic nucleo-olivary projection neurons (*Gad6⁺*) and small local GABAergic interneurons (*Calret⁺*). BrdU birthdate studies in combination of retrograde axonal tracing, revealed that projection neurons are born between E13 and E15, whereas local interneurons are generated over a longer time window extended to early postnatal days (Leto et al., 2006)[247]. Interestingly, the GABAergic interneuron precursors pool, seems to be shared with the one of cortical GABAergic interneurons. It expresses *Pax2* and continues to divide during the first postnatal week, as they migrate through developing WM to the DCN and the CC, respectively.

8.4.2. Glutamatergic lineage: description and development

Glutamatergic neurons are produced from RL progenitors in a time dependent manner. In mice, DCN neurons are the first to be generated (E10-E12.5), followed by UBCs (E12.5 – E18.5) and, shortly after, by GC precursors (GCPs) (E13-perinatal). Strikingly, the same temporal schedule is followed even when glutamatergic neurons are produced from the VZ, after ectopic expression of *Atoh1* (Yamada et al., 2014)[210], thus suggesting that glutamatergic progenitors in the RL may be multipotent and change their temporal identity as the development progresses. In addition, the role of external factors in defining cellular identity during development is also outlined by this evidence.

Comprehensively, the first wave of RL progenitors follows an EGL – PWM migratory pathway and eventually these become excitatory neurons of the DCN (Wang et al., 2005)[207] (Fink et al., 2006)[302]. Interestingly, we know now that glutamatergic DCN progenitors diversify into two spatiotemporal-dependent populations (Sepp et al., 2021)[140]. A second pool of *Eomes*⁺ (*Tbr2*) cells, corresponding to developing UBCs, leaves the RL towards the PWM before homing in the GL (Englund et al., 2006)[303]. Shortly later, GCPs tangentially migrate from the RL along the cerebellar surface forming the EGL, which plays a crucial role during cerebellar postnatal development. It is in the EGL where GCPs will intensely self-amplify until they become postmitotic, upon *Atoh1* expression cessation, and finally migrate inwards to form the mature GL. Noteworthy, work on adult mouse and developing CB demonstrates that developing UBCs and GCs display continuous variation (Kozareva et al., 2021)[249] (Sepp et al., 2021)[140].

8.4.2.1. Granule cells

The cerebellar granule cells are the smallest (4.82 μm somatic size on average (Harvey and Napper, 1988)[250]), and most abundant neurons in the vertebrate brain, representing about 80% of all neurons in the human brain, which roughly corresponds to 100 billion cells (Andersen et al., 1992)[304] (Azevedo et al., 2009)[304]. Their soma densely fills up the volume between PCL and the WM in the CC, also known as GCL. GCs relay and process neural inputs into the CB from the MFs to PC. Each GC dendrite receive contacts from a single MF bouton, which has the capacity to promote combinatorial encoding and enhanced processing of sensory input to the CB (Nguyen et al., 2021)[79]. Despite the long-standing view of the GCs as a homogeneous population, recent publications have shown the existence of GCs heterogeneity in the CB (Consalez et al., 2021)[158] Indeed, recent advances in high-throughput transcriptional profiling proved once more their outstanding power. Single-nucleus RNA-seq (snRNA-seq) was used to molecularly define cell types across individual

lobules of the adult CB. This data revealed five subtypes of GCs in the adult CB (Kozareva et al., 2021)[248].

Interestingly, the analogy between adult GCs subtypes and the three lately identified GCs precursors subtypes supports the notion that the topographic heterogeneity of GCs is at least partially driven by the temporal ordering of GCs differentiation (Sepp et al., 2021)[140].

GCs dominate at late developmental stages, outnumbering all other cell types already in postnatal day P4 in mouse (Sepp et al., 2021)[140]. In mice, between E12.5 and E16, GCPs migrate tangentially from the RL over the dorsal surface of the CP to form the EGL. In this germinative layer, which covers the surface of the CB until P16 and then gradually disappears, GPCs undergo a prolonged clonal expansion through many symmetric divisions. Namely, the EGL can be further divided into an outer and inner half (oEGL and iEGL, correspondingly), where GCPs actively proliferate or stop dividing, respectively. Of note, the regulation of GCPs proliferation in the EGL is crucial for the proper cerebellar foliation (See section 6). Interestingly, GCs A-P position in the EGL appeared to be temporally linked to the delamination time from the RL. Thus, GPCs that migrate first are located more anteriorly than those at later time points (Machold and Fishell, 2005)[305]. Clonal analyses performed with the MADM method allowed to follow the development of single GCs clones, showing that GPCs within each family stop dividing and differentiate *en masse* within a narrow time window of about two days (Espinosa and Luo, 2008)[306]. The TF *neurod1* has been shown to be necessary for GCs differentiation. Indeed, its absence results in GC death (Miyata et al., 1999)[307], particularly of the late-born GCs subset. Experiments on chick embryo have shown that *neurod1* plays a key role in terminating the proliferation of GCPs by downregulating the expression of *Atoh1* (Butts et al., 2014)[167]. Other factors, such *Zic1*, *Cxcl12*, *FOXCl*, neurotrophin and contactin-1 have been characterized to control and balance GPCs proliferation and differentiation (Consalez et al., 2021)[158]. When GCPs begin to exit the cell cycle and differentiate, they extend horizontal parallel axon fibers and undergo tangential migration within the pre-migratory layer of the EGL. They then switch from tangential to radial (vertical to the pial surface) migration along the Bergmann glial (BG) fibers (Sillitoe and Joyner, 2007)[147] (Chédotal and Richards, 2010)[308], thanks to the expression of surface adhesion molecules, in particular of astrotactin (Edmondson et al., 1998)[309]. This switch from tangential to radial migration was described to be regulated by Semaphorin 6a (*Sema6a*) (Kerjan et al., 2005)[310]. Then, mature GCs send their PFs to contact PC dendrites in the ML, while their cell bodies are positioned in the IGL (Espinosa and Luo, 2008)[306] (Zong et al., 2005)[311]. Upon their arrival in the IGL, GCs receive inputs from MFs presynaptic terminals, and trans-synaptically induce

their maturation by secreting *Wnt* family ligands (Hall et al., 2000)[312]. Thus, developmental regulation of GCs dendrite/synapse formation, which is central to cerebellar circuitry, is voltage sensitive. GCs development and stage-specific genes have been recently reviewed (Consalez et al., 2021)[158](Sepp et al., 2021) [140] (**Figure 12**).

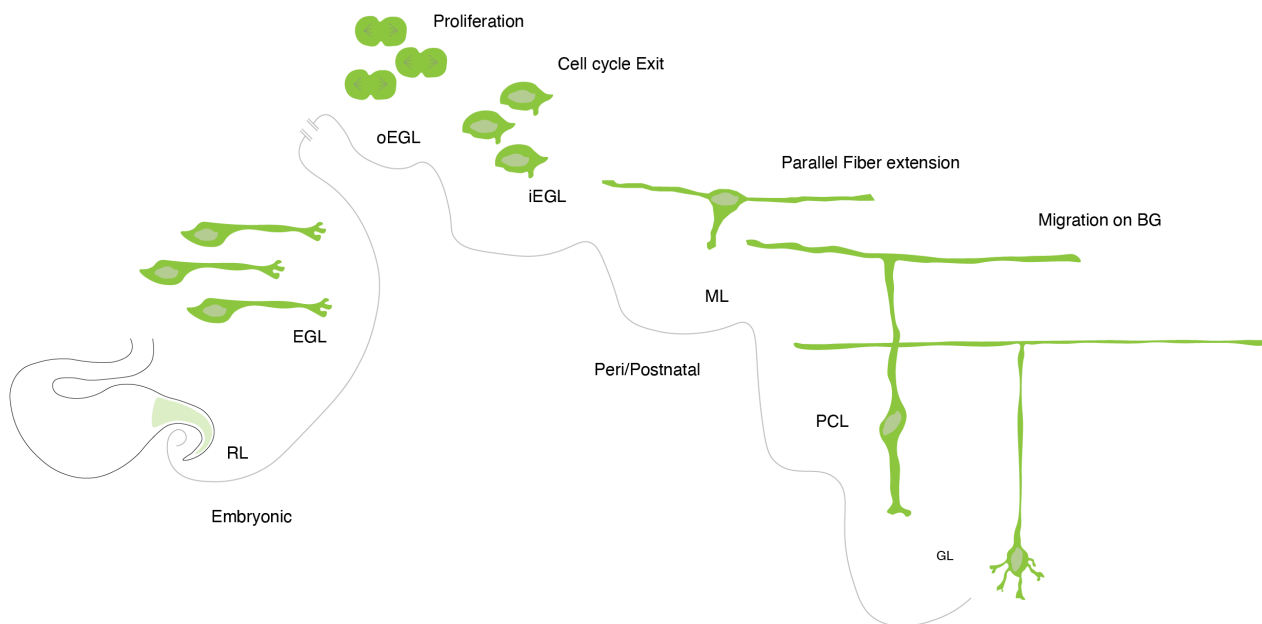


Figure 12. Schematic representation of GCs neurogenesis and migration. GC progenitors (GCPs) of the Rhombic Lip (RL) migrate to give rise to the EGL and expand in number. Once in the outer External granule cell layer (oEGL), GCPs start dividing symmetrically (clonal expansion, promoted by PCs secreted signals). Once they exit the cell cycle, GCPs extend the parallel fibers (PFs). Migrating neurons extend a leading process that enwraps the glial fiber (not shown) until their somas reach the GL. (Adapted from Leto et al., 2016 and Consalez et al, 2021)

8.4.2.2. Unipolar Brush cells

Unipolar Brush cells (UBCs) are glutamatergic interneurons in the cerebellar cortex and dorsal cochlear nucleus (Kalinichenko and Okhotin, 2005)[313]. First recognized by Altman and Bayer in 1977, UBC unique morphology was not described until several decades later (Harris et al., 1993)[314] (Mugnaini and Floris, 1994)[315]. UBCs are characterized by a single thick dendrite ending in a “brush” of fine dendrioles. Interestingly, the fact that cerebellar and cochlear UBCs exhibit the same characteristic morphology, suggests cell autonomous mechanisms for their morphological differentiation. (Englund et al., 2006)[302] (Kita et al., 2013)[221] Located in the GCL, cerebellar UBCs receive MF innervation, mostly from primary vestibular afferents, and project in turn to GCs

dendrites to finally tune PCs activity. In turn, PCs inhibit UBCs activity, thus constituting a recurrent functional loop. UBCs amplify inputs from vestibular ganglia and nuclei, by spreading and prolonging excitation within the IGL (Nunzi et al, 2001)[316]. Thus, cerebellar UBCs are abundant in regions linked to vestibular functions, especially lobule X (nodulus) and the ventral portion of the lobule IX (uvula) in the vermis (Diño et al., 1999)[317]. Interestingly, dopaminergic regulation of UBCs – GCS – PCs functional loop has been recently demonstrated. Namely, dopaminergic activation of *Drd1*⁺ UBCs induces a decrease in PCs firing PCs (Canton-Josh et al., 2021)[318]. Two subtypes of UBCs have been identified in the adult CB by marker expression and neurochemical phenotypes: Type I UBCs expressing *Calret* (Arai et al., 1991)[319] (Floris et al., 1994)[320] (Morin et al., 2001)[321] (Nunzi et al., 2002)[316] (Kalinichenko and Okhotin, 2005)[313] (Englund et al., 2006)[302] and type II UBCs, expressing *mGluR1 α* (Takacs et al., 1999)[322] (Spatz, 2001)[323] (Kalinichenko and Okhotin, 2005)[313]. Despite this distinct classification, *Tbr2* serves as a pan marker for UBCs, being expressed in UBCs continuously from development to adulthood (Englund et al, 2006)[302] (Pimeisl et al., 2013)[324]. Besides, the pivotal role of TBR2 for timely migration of UBC precursors from the RL into the GL and their differentiation has been characterized in *Tbr2* conditional knock-out mice (McDonough et al., 2021)[325], supporting its involvement in the proper development of UBCs. Interestingly, differential *Tbr2* expression levels has allowed the recent classification of developing UBCs in two subtypes, one of which largely uncharacterized so far (Sepp et al., 2021)[140]. However, the origin of this dopaminergic control remains unknown.

In rodents, UBCs are shown to be born between E15 and P2 (Abbot and Jacobwitz, 1995)[326] (Sekerková et al., 2004)[327] (Chung et al, 2009)[35]. Yet, their origins remained unclear. The majority arises ventrally, possibly from the VZ (Ilijic et al., 2005)[327], [328] but more likely from the RL since RL ablation in slice cultures significantly reduced the number of UBCs (Englund et al., 2006)[302]. In addition, it has been demonstrated that the null mice for *Math1*, required for the development of RL derivatives (Machold and Fishell, 2005)[329] (Wang et al., 2005)[206], displayed a decrease in UBCs production. In any case, UBCs guided by PCs cues, will migrate and reach the white matter tracks. Interestingly, a second small population of UBCs arises dorsally from the EGL (and therefore, from the RL) and then follows the same dorsoventral migratory route, as the GCs to reach the GCL. Remarkably, UBCs precursors migrate along the same pathways in humans as well as in rodent CB, producing a fountain-like migration in sagittal histological sections (Englund et al., 2006)[302].

8.4.2.3. Candelabrum cells

The candelabrum cells (CdCs) are one of the most mysterious neuron-type of the CC. CdCs were first identified based on their distinctive morphology (Laine and Axelrad, 1994)[29]: small cell body near the PCL, dendrites that extend to the surface of the ML and rolled axons that make numerous local synapses within the molecular layer. Their electrophysiological properties, synaptic connections and function remained largely unknown. Noteworthy, in a recent study the authors found that CdCs are the most abundant interneuron in the PCL, and they are present in all cerebellar lobules. CdCs receive excitatory synaptic inputs from MFs and GCs, and inhibitory inputs from PCs, and in turn, Candelabrum cells inhibit MLIs, which leads to PCs disinhibition (Osorno et al., 2021)[330]. Because of their unique position within the cerebellar circuit, candelabrum cells are predicted to be a critical element for cerebellar processing. In addition, using single-molecule fluorescent *in situ* hybridization (smFISH), the distinctive molecular characteristics of this cell type were elucidated, which appears to be *Nxph1*⁺, *Aldh1a*⁺, *Slc6a5*⁻ (Osorno et al., 2021)[330]. This molecular characterization of CdCs might help towards a better understanding of the developmental trajectory of CdCs, which remains elusive so far.

8.4.2.4. Excitatory DCN neurons

The DCN are the main output centers of the CB, but relatively little is known about their development. Glutamatergic projection neurons are produced first, from E10 to E12.5 in mice. They initially blend in the nuclear transitory zone (NTZ), which is located just below the pial surface at the rostral end of the CP, as shown by means of radioactive thymidine labeling (Altman and Bayer, 1985)[331]. The embryonic origins of DCN glutamatergic neurons have been for long time undefined. Morphological studies suggested that these cells could originate from the VZ. Recently, *Atoh1* β -galactosidase genetic lineage tracing suggested that the RL may produce the majority of DCN projection neurons (Wang et al., 2005)[206]. In this study, β -Gal embryos were collected at different timepoints of the embryonic development from E10.5 to E18.5. The positive signal in the rostral CB at early stages correlated with the previously identified NTZ. Later, from E14.5, β -Gal signal descended into the CB, as theorized for the NTZ, therefore confirming their identity as DCN neurons. They next used morphology and known molecular markers to assess whether *Atoh1* ablation correlated with the loss of DCN neurons. Nissl staining showed gross disruption of the cytoarchitecture of the DCN. The expected region of the Fast nucleus lacked β -gal, *Lhx9* (known to be expressed in *Atoh-1* cells (Bermingham et al., 2001)[15], and

Tbr1 (known to label DCN neurons of the developing Dent nucleus). Overall, this study indicated that at least a subset of DCN neurons is derived from the RL in a *Atoh-1* dependent manner.

In 2006, Fink and colleagues further characterized the spatio-temporal development of DCN neurons from the RL using a combination of antibodies against transcription factors characteristically expressed in excitatory neurons, such as *Pax6*, *Tbr1* and *Tbr2* (Fink et al., 2006)[301]. In doing so, the authors found that most DCN neurons become specified around E10.5 in the RL and initiate a tangential migration forming a stream of cells under the pial surface before reaching the NTZ. Interestingly, during their migration to the NTZ, DCN neurons undergo a series of transcriptional changes that might account for their maturation. First, they express *Pax6* as they become post-mitotic and initiate their migration away from the RL; second, they initiate expression of *Tbr2* as they reach the NTZ; and finally, they downregulate their expression of *Pax6* and *Tbr2* while upregulating *Tbr1* expression. Interestingly, this sequential expression appears to be shared, and possibly conserved, with the inhibition of excitatory pyramidal neurons of the neocortex (Englund et al., 2005)[332]. As cerebellar development progresses, DCN neurons become organized medial to lateral in the different nuclei.

8.5. Non-neuronal development

As mentioned in section 1.2.1, cerebellar anatomical and functional complexity is reflected not only by the variety of its neuronal types, but also by a remarkable heterogeneity of non-neuronal cells, such as astroglial and oligodendroglia cells. Many of these glial types are also characterized by highly distinctive morphological features and functional properties, which are unique among the glial cells of the entire CNS. Cerebellar astrocytes and oligodendrocytes participate to crucial developmental processes and contribute to regulate physiological functions in the mature cerebellum.

The three-layered neuronal structure of the cerebellar cortex is mirrored in the architectonics of the neuroglia. Thus, each layer has a different population of neuroglial cell types. All these cells engage in intricate relations with the nerve cells and fibers of the CC. As in the interneuronal connections, the focal cell in this neuroglial relation is the PCs.

In contrast to other CNS areas in which gliogenesis follows neurogenesis, in the cerebellum the generation of glia occurs in parallel to the generation of GCs and interneurons (Altman and Bayer, 1997). What triggers the activation of gliogenesis and regulates its course in this territory is still poorly understood. The VZ origin of cerebellar astroglia, first proposed by Ramon y Cajal, has been proven on several occasions by means of fate mapping analysis (Yuasa et al., 1996)[333] (Anthony and Heintz,

2008)[334] (Mori et al., 2006)[335] (Hoshino et al., 2005)[207]. However, a small contribution of the RL to cerebellar astrogliogenesis has also been proposed (Jensen et al., 2004)[336] but so far remains controversial (Buffo and Rossi, 2013)[31].

8.5.1. Astrocytes

Astrocytes are abundant cells of the brain essential to support and shape neuronal activity. Increasing evidence supports the morphological, molecular and functional heterogeneity of astrocytes across and within distinct regions of the developing and adult CNS (Bayraktar et al., 2015)[337] (Ben Haim and Rowitch, 2017)[338]. Indeed, the remarkable anatomical and functional complexity of the CB is mirrored not only by the variety of its neuronal phenotypes but also by a notable heterogeneity of astroglial cells. Based on their morphological and functional properties, cerebellar astrocytes have been classified in three main subclasses (Ramon y Cajal, 1911) (Palay and Chan-Palay, 1974), (Altman and Bayer, 1997) (Leto, 2016)[4]: the Golgi neuroepithelial cells (Palay and Chan-Palay, 1974), commonly known as Bregman glia (BG), the fibrous astrocytes of the WM, characterized by processes oriented along the direction of axonal tracks, and the astrocytes of the GL, further divided into velate astrocytes with star-shaped bushy processes and more rare protoplasmic astrocytes. So far, these subtypes can be distinguished only by means of morphological/functional criteria, since known neurochemical markers are shared by all the different types with minor variations.

The most extensively studied astrocytic type in the CB is the BG, (Buffo and Rossi, 2013)[31], which is peculiar to the CC and characteristic of the PCL and the ML. More precisely, BG cell bodies are aligned to PCs soma and several ascending processes span radially the ML, up to contact the subpial basement membrane. BG functions in development, synaptogenesis and circuit activity have been partially described. Distinctly, during cerebellar development, BG provide physical trails to guide the migration of various cell types and regulate the directional elongation of axons and dendrites. Developing PCs and BG, for example, form complex interaction through which they reciprocally orchestrate their maturation (Farmer et al., 2016)[339]. Besides, BG have been proposed to be involved as well in the guidance of MLI from the PWM outwards (Simat et al., 2007)[295]. BG also actively participates to the maturation of PCS synapses. Following a proximo-distal direction from the deepest to the outermost regions of the ML, BG fibers extend numerous processes that gradually enwrap PCs dendrites and their growing synapses, and have been suggested to provide both physical and trophic support for the elongation of the PC tree (Yamada et al., 2000)[340], [341] (Ango et al, 2008)[341]. Finally, within the adult cerebellar circuit, BG actively participate in shaping the electrical activity,

enwrapping the synapses between PCs, PFs, CFs and MLI constituting the so called *microdomains* (Hoogland and Kuhn, 2010)[342] and tightly controlling the local extracellular increases of neurotransmitters. On the other side, specific function of astrocytes in the GL and WM remains largely unknown (Kimelberg, 2010)[342], [343] (Hoogland and Kuhn, 2010)[342].

In the last decades the interest on the development, lineage, heterogeneity and functions of cerebellar astrocytes has lagged behind studies on cerebellar neurons and circuits. As a result, how astrocyte heterogeneity is ontogenetically achieved remained largely unknown. Like neurons, glial cells in the developing CNS derive from neuroepithelial cells that line the ventricle. Indeed, at the beginning of neurogenesis, neuroepithelial progenitors differentiate into radial glial (RG), which in turn, act as primary progenitor cells. Once neurogenesis is completed, RG will produce astrocyte precursors and eventually, transform into astrocytes themselves (Mallamaci, 2013)[344]. The traditional view posits that radial RG, through asymmetric divisions, produce intermediate progenitor cells (Miyata et al., 2004)[307], which in turn, expand in number before producing astrocytes (Noctor et al., 2004)[345] (Noctor et al., 2008)[346]. The tightly regulated developmental interval during which RG along the VZ transit from neurogenesis to gliogenesis is commonly known as *gliogenic switch*. RG were also shown, after their asymmetric division, to translocate and directly transform into astrocytes. Eventually, astrocytes can be produced during postnatal development, as described for the postnatal cortex (Ge et al., 2012)[347]. The VZ appears as the main source of astrocytes which, according to our current knowledge, before final specification, delaminate from the VZ, first to the PCL and, later, to the PWM where they go through an intermediate phase of amplification (Buffo and Rossi, 2013)[31]. A small contribution of the RL to cerebellar astrogliogenesis has also been proposed (Sievers et al., 1994)[348], but so far remains controversial (Hoshino, 2012)[349].

Recently, *in vivo* clonal analyses demonstrated that cerebellar astrocyte types emerge according to a developmental program tightly regulated in space and time. (Cerrato et al., 2018)[350]. In the mature CB, E12 and E14 derived clones are distributed along the different axes according to a well-defined pattern established at birth and link to the organization of the cerebellar territory. In the same study, it has been suggested that cerebellar astrocyte heterogeneity does not emerge from a unique multipotent progenitor pool, but may also require committed components. Interestingly, the expression of the growth and differentiation factor 10 (*Gdf10*), glial marker specific for both developing and mature BG, was previously described in the posterior part of the lateral VZ and through the whole VZ of the vermis (Mecklenburg et al., 2014)[351]. Therefore, although it is still not known whether the

glycogenic progenitors lining the cerebellar VZ are compartmentalized in distinct domains, this evidence suggests that, at least in the lateral CB, BG may selectively derive from precursors located in the posterior VZ.

A fundamental question that awaits to be answered is whether the distinct astrocyte types belong to separate lineages and originate from equivalent or fate-restricted progenitors. The well characterized and distinguishable astroglia phenotypes offer a clear experimental advantage to tackle this question, compared to more complex and phenotypically undefined systems such as the cerebral cortex.

Cerebellar neurons and astrocytes are generated by the same germinal niches according to a precise temporal sequence, raising the hypothesis that they might be clonally related. Indeed, several fate-mapping analyses, in which embryonic progenitors were targeted and followed based on the expression of specific markers, suggested a common origin between the two lineages. In detail, classical RG markers, such as *Blbp*, *Glast* and *TnC*, labeled progenies comprising cerebellar GABAergic neurons as well as BG and parenchymal astrocytes (Mori et al., 2006)[335]. Moreover, *in vivo* targeting of ventricular RG through injections of LCMV-pseudotyped lentiviral vectors displaying a particular tropism towards astroglial cells demonstrated that RG could generate astrocytes and interneurons during late (E15) embryonic development (Parmigiani et al., 2015)[352]. In addition, when fate mapping was performed exploiting the regulatory regions of transcription factors known to be necessary for the specification toward the neuronal lineage, some astrocytes could be detected among the offspring cells as well. Indeed, both *Ptf1a* and *Neurog2* expressing progenitors, located in distinct domains of the embryonic VZ, were shown to be able to generate a small number of astrocytes (Hoshino et al., 2005)[207] (Florio et al., 2012)[236]. Moreover, both BG and parenchymal astrocytes appeared to be produced by *Ascl1*⁺ progenitors, which are present in the VZ between E10.5 and E13.5, overlapping with *Ptf1* and *Neurogenins* (Sudarov et al., 2011)[20]. Nevertheless, the low frequency of astroglial cells observed in these studies questioned the actual origin of most cerebellar astrocytes from these cell populations.

Common ancestors for cerebellar neurons and glia are also suggested by distinct functional studies performed at embryonic stages. Indeed, manipulation of Notch/BMP signaling resulted in an altered balance between the numbers of neurons and astrocytes, with macroscopic cerebellar defects. Selective Notch ablation in the cerebellar territory resulted in a reduction of both neurons and astrocytes and to hypomorphic cerebella, due to a too rapid exhaustion of the progenitor pool (Grandbarbe et al., 2003)[353]. On the contrary, a constitutive activation of the same signaling promoted the generation of astrocytes at the expense of neurons (Machold et al., 2011)[305]. On the other side, in the absence

of the BMP-repressor *Bmi1*, the number of astrocytes increased concomitantly to the decrease in the amount of interneurons (Zhang et al., 2011)[354]. Moreover, both *Ascl1* null (Grimaldi et al., 2009)[237] and conditional knockout mice lacking this transcription factor specifically in the cerebellar VZ (Sudarov et al., 2011)[20] showed lower numbers of *Pax2*⁺ interneurons and increased *Sox9*⁺ astrocytes in the cerebellum, compared to wild type animals. Conversely, when *Ascl1* expression was increased in the cerebellar VZ, interneurons increased at the expense of GLAST and S100-expressing astrocytes (Grimaldi et al., 2009)[237]. Several evidences based on both *in vitro* and *in vivo* studies have also pointed to the existence of bipotent neuroglial precursors in the postnatal cerebellum and PWM (Silbereis et al., 2009)[355] (Klein et al., 2005)[356] (Fleming et al., 2013)[143]. However, the most conclusive evidence was recently provided by Parmigiani and colleagues (Parmigiani et al., 2015)[352]. In this study, by *in vitro*, *ex vivo* and *in vivo* clonal analyses at the single progenitor level, the authors showed that GABAergic interneurons and astrocytes share a common ancestor in the PWM. Whether such progenitors also exist at earlier developmental stages and, if so, what neuron and astroglia subpopulations they might generate remains to be elucidated.

8.5.2. Oligodendrocytes

Cerebellar oligodendrocytes are also detected throughout the CC, but since they are intimately correlated with myelination, they have the same distribution as the myelinated fibers, that reside mostly in the GCL and deep ML.

While oligodendrocytes development has been well studied in the telencephalon and the spinal cord, the development of this cell type in the cerebellum has been relatively poorly investigated so far, which results in a low understanding of neither their exact origin nor the underlying molecular mechanisms. In mice, transplantation studies showed that dissociated cells from the cerebellar primordium did not contain oligodendrocyte progenitor cells (OPCs), suggesting an extracerebellar origin of cerebellar oligodendrocytes (Grimaldi et al., 2009)[237]. A further study had demonstrated that most of the cerebellar oligodendrocytes (94%) derived from a discrete neuroepithelial region in the ventral r1, while the rest (6%) is produced from the VZ. In the same study, the authors revealed that the transcription factor *Sox9* plays a pivotal role in cerebellar oligodendrocytes development by regulating multiple processes including generation timing, proliferation, maturation and survival. Intriguingly, *Sox9* has been as well reported to be involved in the cerebellar GABAergic lineage generation (PCs and interneurons) (Vong et al., 2015)[357]. In addition, SHH secreted by PCs has been shown to stimulate OPCs proliferation at early postnatal stages, whereas by the end of the first postnatal week,

PCs start producing vitronectin, which drives oligodendrocytes maturation and myelin formation (Bouslama-Oueghlani et al., 2012)[358]. After leaving the neuroepithelium, OPCs proliferate becoming committed oligodendrocyte precursors and finally postmitotic oligodendrocytes (MAG) migrate towards their destination (Sepp et al., 2021)[140] (Hashimoto et al., 2016)[359]

8.5.3. Microglia

Microglia are the innate immune cells of the CNS and are also important participants in normal development and synaptic plasticity. Early development studies showed the involvement of microglia in regulating the survival of PCs and GCs during developmental time period of neuronal apoptosis. (Ashwell, 1990)[360] (Cardoso et al., 2015)[361].

In the mature cerebellum, microglia interact dynamically with both the dendritic arbors and somas of PCs. It has been demonstrated that cerebellar microglia represent a unique population compared to cortical microglia, being more sparsely distributed and having a markedly less ramified morphology. (Stowell et al., 2018)[362] Interestingly, recent studies have shown that isolated murine microglia from the cerebellum have a higher expression of immunological genes compared to other brain regions. This differential expression increases with age, suggesting that these cells may have a distinct transcriptome and distinct roles (Grabert et al., 2016)[363] (Tay et al., 2017)[364].

8.5.4. Ependymal cells

Ependymal cells are ciliated glial cells that form the ependyma, an epithelial barrier lining the ventricular system. They develop from radial glia along the surface of the ventricles, and they play a critical role in CFS homeostasis, brain metabolism and waste clearance (MacDonald et al., 2021)[365]. Ependymal cells have been identified in small numbers in the developing cerebellum in mouse and opossum, in the latter, showing high transcriptional similarities with glioblasts (Sepp et al., 2021)[140].

CHAPTER 2

TOWARDS THE CONSTRUCTION OF A 4D CEREBELLAR MODEL:

KNOWLEDGE AND TECHNOLOGY

1. From observations to high-throughput profiling

Sensory, cognitive, and motor operations of the brain are translated to specific behaviors (observations). The understanding of these behaviors can be broken down into distinct blocks which together contribute to elucidate the underlying molecular mechanisms. Establishing the relation between those molecular mechanisms which explain a specific behavior, represents a major aim in neurobiology. The technological evolution came along with the emergence of valuable tools to reach this goal (**Figure 13**).

We can distinguish three main categories when it comes to profile/elucidate the mechanisms priming a specific behavior: identity, connectivity, and activity. Neuronal identity studies, aiming to characterize the cell type composition and generation of the different regions of the brain, evolved from simple histological studies to more advanced high-throughput next-generation -omics technologies (Ginhoux et al., 2022)[366]. Omics technologies (genomics, transcriptomics, epigenomics, proteomics and metabolomics/lipidomic), have significantly improved the resolution of our knowledge, and their application has brought already valuable insights into the understanding of the brain cellular identity and structure (Solanelles-Farré et Telley, 2020)[172] (Lopes et al, 2020)[367]. Secondly, the formation of accurate neuronal connectivity during nervous system development is essential for higher-order cognitive and motor behaviors. Technological progress, and more specifically advances in histological and genomic tracking, have impacted the many ways of analyzing the neural networks as well as the mechanisms involved in the establishment of precise neuronal connectivity (Zeng 2018)[368]. Finally, neuronal activity is an important player during the maturation phase of neuronal development, modulating the establishment and refinement of neuronal connections through multiple mechanisms (Sahores and Salinas, 2011)[369]. It is essential to understand the variability in neuronal activity and how this ultimately affects the structure and function of the brain. Advances in electrophysiological recording techniques together with the advent of optical physiology allowed the researchers to tackle this aspect with unprecedented precision (Glasgow et al, 2019)[370] (Roth et Ding, 2020)[371].

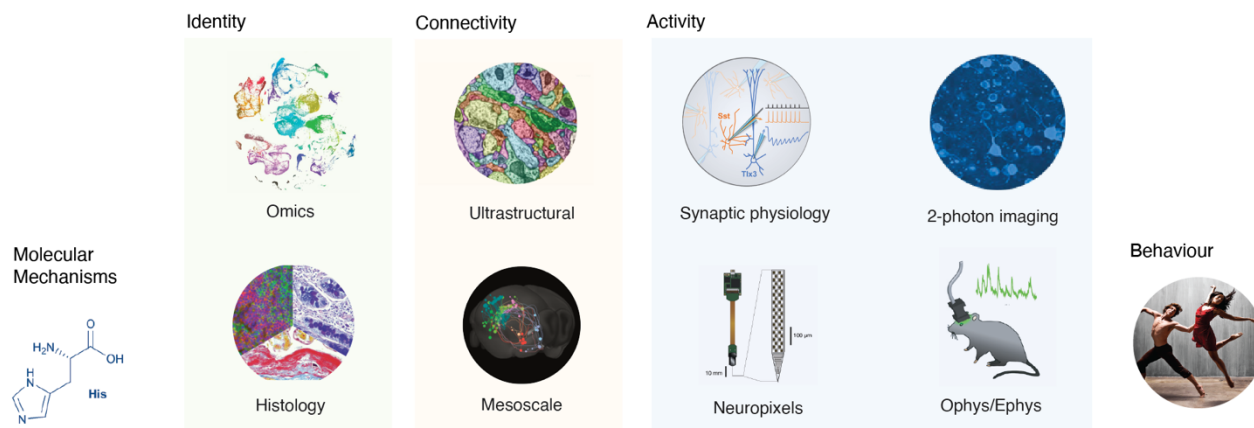


Figure 13. From observations to high-throughput profiling.

Despite the significant advances in our understanding of the brain, a more exhaustive examination of certain areas, such as the cerebellum, and an integrative understanding of multimodal data remains to be achieved. Indeed, a unifying view of data coming from all different categories of study is required to fully understand the system (high-throughput profiling). Hence, this integration is the *raison d'être* of 4D modeling. Developing and optimizing computational tools able to integrate multiple datasets within different experimental contexts and measurement modalities remains a key challenge. I will talk about some of the available methods for integration and their limitations later in this chapter (See section 3).

A good case in point is the outstanding work of the Allen Institute to generate the most advanced mouse 3D reference atlas: the Allen mouse brain common coordinate framework (CCF) (Wang et al., 2020)[14]. Several years of a hard-working process led to the creation of a 3D average template brain from 1675 mice at a 10um resolution. It is now used for large-scale data mapping, quantification, presentation, and analysis as well as support for the generation of similar resources, such as the one I contributed to produce during my thesis. The generation of the CCF can be explained in three phases: (1) Acquisition. The initial data used for the generation of the CCF comes from using two-photon serial imaging systems, allowing for intact high resolution brain imaging. (2) Averaging. Average from 1675 mice, using as initial template the Allen Brain Atlas (See section 1.2). An unbiased shape of the average brain was achieved thanks to the iterative process of deformation and registration, providing detailed anatomical information. (3) Annotation. For every structure, they underwent exhaustive research of available information / tools / atlases (for example, histological information from Nissl, ISH, IHC and transgenic mouse data). This information was then unified and used to accurately define the anatomical locations in the average template brain. However, they rapidly realized how the curved

shape of the brain came with constraints for accurate 3D annotation, for instance in the neocortex. A curved cortical coordinate system was therefore developed to enable the integration of information from different cortical depths. To recast a curvature-related 3D problem to a 2D problem, they solved Laplace's equation (Jones et al., 2000)[372] between pia and white matter surfaces to generate intermediate equipotential surfaces as analog to the cortical depth: the *approximate columns*. The curved cortical coordinate system has the advantage in that it allows the translation of any point from 3D surface views into 2D space or vice versa, and therefore increase the accuracy of their annotations and layer distribution (**Figure 14**). Other complex brain structures, such as the highly lobulated cerebellar cortex, would benefit from a similar approach.

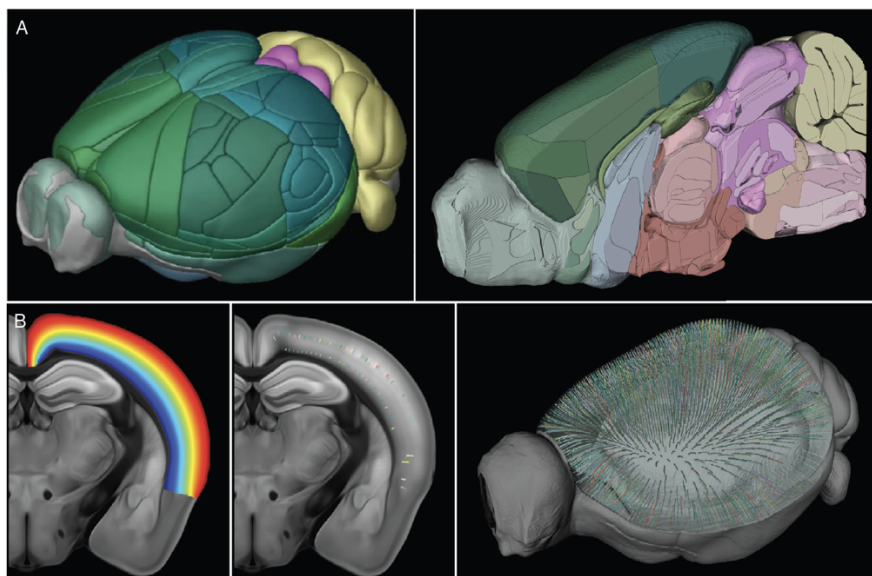


Figure 14. Allen Brain 3D Coordinate Framework. A) Whole (left) and parasagittal (right) view of the parcellated 3D Coordinate Framework. B) Isocortex curvature solved using Laplace's equation. (left) Equidistant fields are shown in jet color map. (center) Subsampled and randomly colored streamlines descend from the cortical surface to layer 6 in a single coronal section. (right) 3D projection showing the curved cortical streamlines (*approximate columns*) in a dorsoventral view (Adapted from Wang et al, 2020)

The generation of the CCF came together with the development of different applications and resources. They developed a website tool for screening and browsing of the different datasets that had been used, projections, quantifications, and 3D visualization. Notably, available resources for image registration into the CCF enable direct comparison and integration across multiple data sets in the same space. For example, Itk-SNAP (Yushkevich et al., 2006)[373], originally a software application for 3D

segmentation of medical images, allows the loading of CCF files together with other compatible files. Therefore, Itk-SNAP not only allows the visualization and easy navigation through the 3D space, but also a possibility for the image registration and comparison with the CCF. Besides these visual tools, AllenSDK and Phyton, mainly focused on connectivity, allow numerical analysis and querying of published datasets. Other resources such as Elastix, ANTS (registration packages) or Cell locator (single-cell data integration), are available to integrate different kinds of data to the CCF.

Despite the unprecedented anatomic and spatial resolution of the CCF, the effort has mainly been focused in neocortical areas (somatosensory cortex, auditory system, cortical projections). In addition, temporal resolution for the 3D CCF (4D CCF) is not yet achieved. Numerous multifaceted data sets have been already generated for other brain areas and, in particular, for the cerebellum. However, no similar integrative approach has been yet developed. In this chapter, while we dive into the details of technological evolution, we will go through the different available datasets for the understanding of cerebellar cellular composition and generation. We will also introduce some accessible integration tools and how these could be used for the modeling of the cerebellum.

1.1. The histological era

Understanding the CB and its development requires knowledge of its basic elements and how they are organized. Therefore, a cell type catalogue is a much-needed touchstone not only for understanding the generation of the CB, but also to understand its circuits and the complex functions those circuits drive. Santiago Ramón y Cajal was the first to show just how many different cell types there was not only in the cerebellum but in the whole mammalian brain. One century ago, he stained neurons so that they could be seen under a microscope, and then made extremely precise and beautiful drawings of their shapes (Garcia-Lopez et al., 2010)[374]. He was able to identify dozens of cell types, each of them with different appearance, axonal extensions, and trajectories. He shared the 1906 Nobel Prize in Physiology or Medicine for his discoveries with Camilo Golgi, who had devised the main staining technique used by Cajal: the Golgi staining. Cajal was made aware of the existence of this technique in 1887 and he rapidly realized how useful this method was to explore the structure of the nervous system. However, he noticed that this method needed to be further elaborated and modified to increase reproducibility and therefore be truly useful. He introduced some modifications such as a double impregnation and variable immersion time according to the structure to study. At last, to avoid the problems encountered in staining myelinated neurons, part of Cajal studies were carried out on

embryos and very young animals: the ontogenetic or embryonic method. His first intuition was to analyze embryonic animals to retrieve the basic schemes of the more complex organization of the adult nervous system (Tello, 1935). In this way, Cajal began to describe aspects of the development of the nervous system, at first calling special attention to cerebellar histogenesis (Ramon y Cajal, 1888)[12] (Ramon y Cajal, 1909-1911). He identified different stages in the development of a neuron, completing the earlier descriptions of His: germinal cell, bipolar stage, neuroblast, postmitotic and mature neuron; and the first description of a game-changing piece, the growth cone and the chemotactic or neurotropic hypothesis (Ramon y Cajal, 1890) (Ramon y Cajal, 1892). Also, he meticulously described the entire development of specific cerebellar cell types (**Figure 15**). This can be seen for the formation of the axon and the dendritic tree of PCs, or the complete formation of GCs and their axons, the PFs. Indeed, he observed that from a spherical morphology without processes, prospective GCs generate polar processes, transiently displaying a bipolar morphology and adopting a horizontal disposition. Likewise, he reported GCs migration, elucidating tangential and radial cell migration mechanisms. Cajal also point out and characterized cerebellar afferences, MFs and CFs. He obtained impressive impregnations of contacts established by the incoming axonal buttons on the PCs bodies throughout the development. He called this type of contacts pericellular or basket, hence he named the BCs.

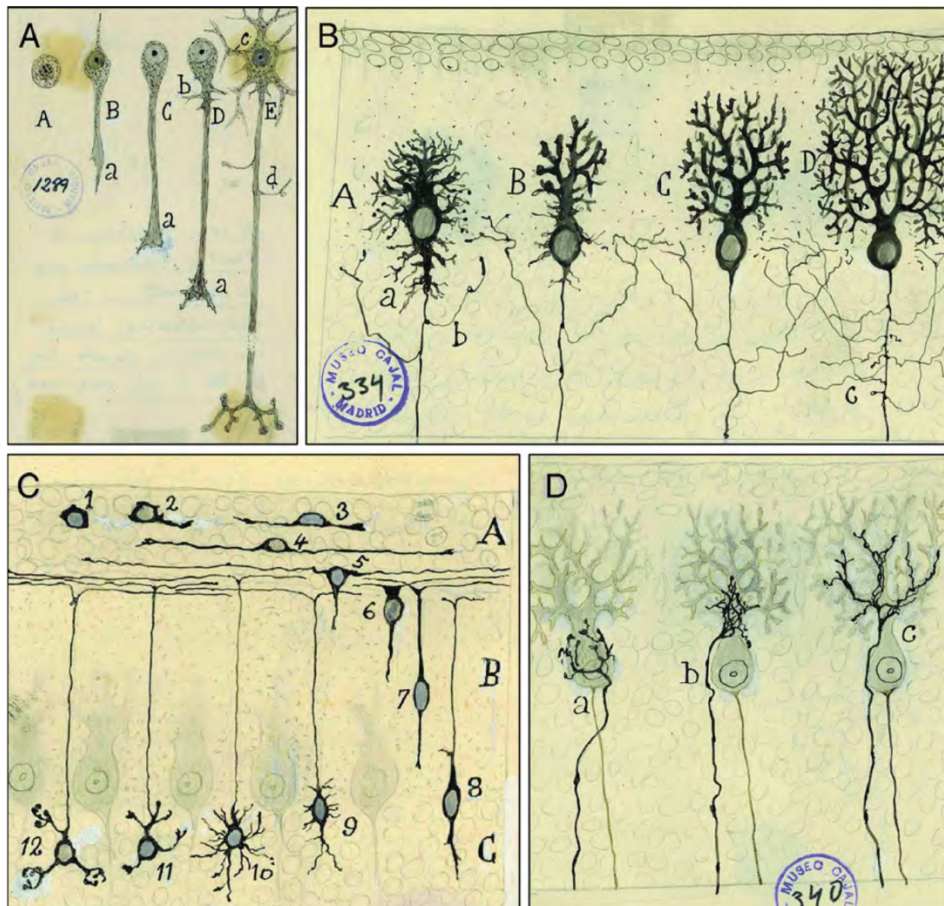


Figure 15. Summary of cerebellar histogenesis from Cajal's original drawings
 (A) Cell and nerv fiber development phases. Primary embryonic nerve cell (A); bipolar phase (B), showing the beginning of the growth cone; neuroblast (C); development of dendrites (D); formation of the collateral and terminal axon branches (E). (B) Successive branching of Purkinje cell branching development: temporal dendrites (a); axon collaterals (b,c). (C) Migration and transformation of the granule cells: primary embryonic cell (1); beginning of polar outgrowths (2,3); formation of a horizontal bipolar cell (4); start of descending outgrowth (5,6); phase of vertical bipolarity (7,8); production of provisional dendrites (9,10), pruning and refinement of the definitive processes (11,12). (D) Development of the climbing fibers: phase of the pericellular nets over the Purkinje cell body (a); climbing fiber along the dendrites of a Purkinje cell (b,c) (Adapted from Castro et al, 2007)

Over the decades, researchers have used every suitable new technology that came their way to fine-tune Cajal's histology-based discoveries and more concretely, the definition of what constitutes a distinct cell type. Until the 1950s, a major limitation in histology was that recognition of cells was mainly based on their mere morphology. During the 1970s, the increased knowledge on immune response and antibody production, offered a formidable precision tool to recognize the molecules uniquely expressed by a given cell type, giving rise to immunohistochemistry (IHC). IHC studies focused on the CB allowed better characterization of cerebellar cells and structure. This, together with

the rapidly growing theoretical and technical knowledge on lenses, represented an authentic turning point in histology and cell type identification. For example, early stages of PCs maturation were demonstrated by Thy-1 IHC on postnatal rat and mouse cerebellum (Morris et al., 1985)[375] (Bolin and Rouse, 1986)[376]. Thy-1 is a cell membrane differentiation antigen widely expressed in the CNS. However, the expression patterns in the neonatal CB were shown to be much lower than the rest, most likely linked to the protracted development of this structure. Thy-1 was shown to be expressed in PCs, some kind of interneurons such as GoCs and neurons of the DCN. The dynamic changes of Thy-1 expression in the CB, and concretely in PCs, allowed the authors not only to further characterize the structure, but also to demonstrate the final stage of migration and the transition to dendritic growth of these cells.

The first half of the 20th century saw the emergence of electronic microscopes with the development of the first transmission electron microscope (TEM) (Knoll and Ruska, 1932)[377]. Attaining a 100- to 1000- fold higher magnification and resolving power than optical microscopes used up to that moment, electron microscopy (EM) allowed us to observe subcellular structures. Moreover, the emergence of EM shed a light on the connections between individual neurons at the synapse level and the reconstruction of axons and dendrites contained in a specific volume / local circuit, being pivotal for microscale connectivity studies (Kubota et al., 2018)[378]. Three-dimensional reconstruction of the CNS and its cellular components was still laborious and challenging by then. Advances in scanning electron microscope (SEM) provided a tool with considerable potential in these regards, being able to offer high magnification 3D images of cell bodies and dendrites, details of presynaptic and postsynaptic morphology, axonal structure, neuroglia, and microvasculature. The fine structure of the cerebellar cortex was studied by means of SEM, providing remarkable 3D views of PCs, GCs, BCs, MLIs as well as MFs (Scheibel et al., 1981)[379].

The second half of the 20th century saw the discovery of lasers (Light Amplification by Stimulated Emission Radiation) as well, and the development of confocal laser scanning microscopes. This allowed for the detection of specific fluorescence markers of cells and tissues and therefore the emergence of immunofluorescence (IF). The beginning of the 2000s was accompanied by significant advances in super-resolution microscopy (SM), and its rapid application in neuroscience (Igarashi et al., 2018)[380], allowing to overcome optical limitations to zoom in at the nanometer range. Two main approaches, (1) non-linear optical based and (2) photon molecular state transition based, gave rise to a plethora of methods including: (1) STED (Stimulated Emission Depletion) (Dyba and Hell, 2003)[381], SSI/SIM (Saturated Structured Illumination microscopy) (Gustafsson, 2005)[382], (2)

STORM (Stochastic Optical Reconstruction Microscopy) (Rust et al., 2006)[383] and PALM² (PhotoActivated Localization Microscopy) (Manley et al, 2008)[384] (Reinhard et al., 2018)[385]. Since then, available microscopy methods kept on upgrading. The discovery that it was possible to isotopically swell a preserved biological specimen through hydrogel embedding, mechanical homogenization, and water swelling marked the birth of Expansion Microscopy (ExM) (Chen et al., 2015)[386]. The physical magnification of ExM enables super resolution imaging with several fundamental new properties, such as the usage of standard fluorophores and diffraction-limited microscopes. Therefore, ExM may empower fast methods, such as light-sheet microscopy (LSM) to become super resolution methods. LSM, first proposed over 100 years ago (Siedentopf and Zsigmondy, 1902)[387], takes a different approach than the most conventional methods to optical sectioning. Instead of using laser point scanning, where a small point of focused light is moved sequentially to different 3D positions, in LSM the plane of interest is illuminated with a thin sheet of light while a camera is carefully focused onto this plane. Thereby, a 3D image can be formed by moving this coaligned excitation and detection plane relative to the sample. LSM delivers significant benefits over point scanning in terms of simplicity, light efficiency, low phototoxicity, and the potential for high volumetric imaging speeds. (Hillman et al., 2019)[388]. LSM came together with the development of tissue clearing techniques. With their origins back to 1914 with the Spalteholz's clearing (Spalteholz, 1914), early tissue clearing techniques dehydrated samples, replacing water with lipophilic compounds that matched the refractive index of lipid membranes to reduce scattering (Dodt et al., 2007)[389]. Recent advances in tissue clearing have enabled the *in situ* preservation of rich biochemical information as well as fluorescent proteins, improved labeling during post processing, improved clearing performance, and decreased tissue processing time and complexity (Ertürk et al., 2012)[390] (Chung et al., 2013)[391] (Renier et al., 2014)[392] (Murakami et al., 2018)[393].

1.2. The physiological era

Specific activity patterns of individual neurons and the coordinated activity of populations of neurons can represent sensory information, internal states, behavioral planning, or action execution. Neuronal activity occurs mostly in electric form through changes in membrane potential during action potential (Bean, 2007)[394]. The advent of electrophysiological science in the 18th century set the first brick for the development of measurement techniques aiming to record the electrical activity of excitable cells, and therefore, to the emergence of electrophysiology (Ephys) (Rubaiy, 2017)[395]. In general, one can distinguish two main kinds of Ephys recordings depending on the spatial component of the

measurement: intracellular and extracellular. Intracellular recording methods, i.e., patch clamp (Neher and Sakmann, 1978)[396], involve measuring voltage and/or current across the membrane of a cell. The gold standard and powerful Ephys technique of patch clamp was invented by Erwin Neher and Bert Sakmann, for which they received the novel prize in 1991. Using the same electrical principles as voltage-clamp (Hodgkin and Huxley, 1945)[397], patch-clamp technique allows for clamping the membrane voltage through the attachment of a glass micropipette with a micron size diameter to the membrane. It can be applied *in vivo* or *in vitro*, and includes a few different configurations enabling high-resolution recordings. Which configuration is used will be determined by a few factors, such as ion channel type, regulation, and modulation, as well as research interest. The different configurations are the following: cell attached, (cell remains intact) inside-out (pulling of the membrane patch to enable the study of the effects of cytosolic factors on ion channels), whole-cell (most common, the membrane patch is disrupted by applying higher suction to achieve direct contact with the cytoplasm. Measure the ion channels' currents across the entire plasma of a single cell), perforated (instead of disruption, to preserve integrity of cytoplasmic components) and outside-out (pipette pulled slowly away so the membrane reseals) (Rubaiy, 2017) [395]. On the other hand, in extracellular Ephys recordings, an electrode is not inserted into a single cell, but instead placed in the extracellular fluid, near the cell of interest. The type of recording will depend on the type and size of the electrode, and the proximity to the signal of origin. One example of such technology is the microelectrode array (MEA) (Spira et al., 2018)[398]. Using an array of microscopic electrodes distributed over a small surface area, this approach allows for the recording of high-throughput field potential recording of different samples-kinds (brain slices, dissociated tissues, organoids, spheroids, 2D neuronal cultures). MEA is a non-invasive recording technique widely used in studies on the cell network, mainly because of the recordings' standardization possibilities (multiple recordings and standard distances between stimulation and recordings) however its resolution is lower than the one of patch-clamp. Using this same Ephys approach, modern electrodes such as *Neuropixels*, are capable of recording from hundreds of neurons simultaneously with high temporal resolution (Jun et al., 2017)[399]. Notwithstanding, Ephys approaches have traditionally been limited in their ability to deliver spatial information about the neurons sampled. In recent times, optical imaging has emerged as a powerful approach to record neuronal activity in a spatially resolved manner, bringing out optical physiology (Ophys) (Lin et Schnitzer, 2016)[400] (**Figure 17**).

1.3. The multiomic era

The advent of gene cloning (Cohen et al., 1973)[401] (Morrow et al., 1974)[402] (Cohen et al., 2013)[403] created a new period of understanding, in which anatomy coupled to molecular genetics to discover the origins of anatomical structure in terms of the activity of specific genes. Thereby, *The House Mouse*, first published in 1972 offering an anatomical description of the mouse development and the well-known Theiler Stages (TS), was refined by the emerging techniques: transgenics, *in situ* hybridization (ISH), and IHC (Theiler, 1989) From the 1990s, genes activity in different cell types and how their expression reflected their properties began to be studied. In 2005, the Allen Institute created an ISH – based gene-expression atlas showing the spatial distribution of roughly 20 000 genes in the mouse brain, including the cerebellum (Lein et al., 2005)[404] (Lein et al., 2007)[405] (Dong et al., 2008). It took 3 years, around 50 scientists and a combination of great technical challenges to build the unquestionably useful Allen Brain Atlas (ABA) one gene at a time (Jones et al., 2009)[406]. The atlas is constantly updated (Version 1, 2008; Version 2, 2011; Version 3; 2015) and still now remains widely used as a fundamental reference tool for neuroscientists. Using the same production processes with few adaptations, in 2008 the Allen Institute launched the Allen Developing Brain Atlas (AdevBA), which provides a characterization of the expression of approximately 2 000 genes in the brain across seven developmental stages from mid-gestation through to juvenile/young mouse. Events that shape the development of the brain, including the cerebellum, from an undifferentiated set of precursors to a mature, functioning organ occur at different times in different regions, and thus the ability to localize gene expression at specific stages of development is highly desirable. The developing atlas provides a framework to explore temporal and spatial regulation of gene expression, effectively a 4D atlas, with a highly powerful and accessible database (See section 2). Noteworthy, technologies for high-throughput data production, management and informatics were maturing in parallel, making genome-wide studies and the integration of genomic and neuroanatomical data feasible (**Figure 18**)

Recently, we have experienced a revolution in the study of CNS development thanks to the advances in single-cell multiomic technologies and, mostly, the use of single-cell transcriptomics (Zeng et al., 2018)[407] (Solanelles-Farré and Telley, 2020)[172] (Lopes et al., 2020)[367]. The emergence of novel sequencing methods (Ginhoux et al., 2022)[366] such that allow the profiling of single-cell transcriptomes (single-cell RNA sequencing: scRNA-seq (Tang et al., 2009)[408] and chromatin states (single cell assay for transposase-accessible chromatin) scATAC-seq (Buenrostro et al., 2015)[409]

(Cusanovich et al., 2015)[410]) from thousands of individual cells has been critical to provide an unbiased definition of cell identity and for determining the sequence of developmental events.

1.3.1. scRNA-seq

RNA-seq was developed more than a decade ago and since then has become a ubiquitous tool in molecular biology. The essential workflow begins with RNA extraction, followed by mRNA enrichment or ribosomal RNA depletion, reverse transcription, cDNA synthesis and preparation of an adaptor-ligated sequencing library. The library is then sequenced on a high-throughput platform. The final steps, which are computational, include: aligning and/or assembling the sequencing reads to a transcriptome, quantifying reads that overlap transcripts, filtering and normalizing between samples, and statistical modeling of significant changes in the expression levels of individual genes and/or transcripts between sample groups (Stark et al., 2019)[411]. As our understanding of cellular complexity and variability advanced, conventional bulk sequencing, which allows the measurement of only the average transcript expression in a cell population, evolved towards sequencing at a single-cell level. Noteworthy, for the measurement of transcripts in individual cells, reverse transcription and cDNA amplification must be performed from very small amounts of RNA. Several methods have been reported, including Smart-seq (Ramsköld et al., 2012)[412], CEL-seq (Hashimshony et al., 2012)[413], Drop-seq (Macosko et al., 2015)[414], Quartz-seq (Sasagawa et al., 2013)[415], Microwell-seq (Han et al., 2018)[416], RamDa-seq (Hayashi et al., 2018)[417], C1-CAGE (Kouno et al., 2019)[418].

Interestingly, single-cell sequencing technologies had rapidly evolved not only to observe the transcriptomic level of single cells, but also to elucidate genomic, epigenomic and proteomics heterogeneity and the changes at these levels (Kashima et al., 2020)[419].

Withal, integration of single cell multimodal data, such as scRNA-seq and scATA-seq, has served to overcome the limitations of each individual technique and thus improving cell identity annotation (Baek and Lee, 2020)[420]. Cerebellar progenitors' developmental trajectories have been recently addressed by means of such integration (Khoury-Farah et al., 2022)[421]. Therefore, single-cell multiomics represents a significant advance on standard single-cell technologies, drawing a broader and more detailed picture by integrating different kind of data. Recent studies using multiomics approaches proved already their impact into CNS development understanding (Solanelles-Farré et Telley, 2020)[172]. This unbiased cell type classification has enabled the generation of high-resolution

cell population atlases in adults (Tasic et al., 2018)[422] (Munoz-Machado et al., 2018)[423] and developing embryos (Cusanovich et al., 2018)[410] (Cao et al., 2019)[424] (Pijuan-Sala et al., 2019)[425], as well as time-course data-based reconstruction of gene expression dynamics underlying cell state transitions along differentiation trajectories (Carter et al., 2018)[279] (Mayer et al., 2018)[426] (Telley et al., 2016)[238]. Undoubtedly, this new era has allowed researchers to provide systematically precise spatial and temporal mapping of brain cellular transcriptomic dynamics. Likewise, the understanding of cerebellar development has substantially expanded due to technological revolution in molecular biology (Leto et al, 2016)[4] (Leto et al, 2006)[246] (Leto et al., 2009)[427], (Sotelo, 2015)[428] (Gupta et al., 2018)[429] (Vladoiu et al., 2019)[132] (Peng et al., 2019)[430] (Buchholz et al., 2020) [431](Sagner, 2021)[432]. Indeed, although previous studies have already demonstrated that different cell types are sequentially generated during cerebellar development (Leto et al, 2006)[246] (Leto et al, 2009)[427] (Sotelo, 2015)[428], recent multi-omics-based studies further improved our understanding of these mechanisms.

1.3.1.1. Differentiation Trajectory Reconstruction

One major dimension when it comes to developmental studies is certainly the time. Temporal information is mostly addressed by consecutive sampling, enabling projection of temporal-related changes. Several approaches have also tried to infer cellular trajectory by *in silico* ordering cells based on transcriptional similarity (*pseudo time ordering*) (Trapnell et al., 2014)[433]. Many of the differentiation trajectory reconstruction methods rely on some forms of dimensionality reduction, such as independent-component analysis (ICA), principal-component analysis (PCA) or t-stochastic neighbor embedding (t-SNE). One of the first and commonly applied algorithms is Monocle. The *pseudo time* ordering of the cells using this method is not directional, meaning that high *pseudo time* could mean either most or least differentiated cells. Being restricted to linear analysis in his first version, Monocle allows now to build the lineage tree in a higher dimensional space, retaining more data for highly complex differentiation trajectories (Qiu et al., 2017)[434]. Several other algorithms employing a similar strategy as Monocle have been developed since then. These include SLICE (Guo et al., 2017)[435], TSCAN (Ji and Ji, 2016)[436], Waterfall (Shin et al., 2015)[437], SCUBA (Marco et al., 2014)[438] and Slingshot (Street et al., 2017)[439]. Another class of differentiation trajectory reconstruction algorithms is based on k-nearest neighbor graphs (k-NNGs), in which similar cells are linked to each other. Algorithms in this class include Wanderlust (Bendall et al., 2014)[440], Wishbone (Setty et al., 2016)[441], Markov Affinity-based Graph Imputation of Cells (MAGIC) (van Dijk et

al., 2017)[442], partition-based graph abstraction (PAGA) (Wolf et al., 2019)[443] and population balance analysis (PBA) (Weinreb et al., 2018)[444]. In 2018, an analytical breakthrough occurred with RNA velocity (La Manno et al., 2018)[445]. It uses information on the ratio of un-spliced and spliced mRNAs in scRNA-seq data to project cellular dynamics and developmental trajectories.

Noteworthy, reconstructing differentiation trajectories from single-cell transcriptomics data heavily relies on sufficient sampling of cells that transition between the different states in the lineage trajectory. In the scenario of little or no cell differentiation, predictors on lineage relation become incredibly challenging. In addition, differentiation trajectories based on single-cell data reconstruction are purely phenotypic, hence they do not necessarily reflect the genetic relations between the true cell lineages.

1.3.2. Lineage tracing

Reconstruction of the lineage connection between cells throughout development is a long-standing aim in biology. A comprehensive record of changes in cell states as tissues and organs develop can give insights into the molecular mechanisms and order of events by which cells choose their terminal identity. A variety of *in vivo* and *in silico* technologies for mapping the progeny of specific cells have been recently developed (Kester et al., 2018)[446] (McKenna and Gagnon, 2019)[447] (Wagner et al., 2020)[448] (Bandler et al., 2022)[449] to ultimately determine the molecular mechanisms that govern how cells differentiate into their final state. Traditionally reliant on microscopy, lineage-tracing approaches have recently evolved to allow the tracking of cell clones via sequencing of inherited DNA sequences, or *barcodes*. Particularly, *in vivo* barcoding and lineage tracing in mammalian mouse model system it is possible thanks to the CRISPR-Cas9 based mouse model MARC1 (Kalhor et al., 2018)[450]. The tracing mechanism in this mouse relies on the incorporation in its genome of a set of loci that are translated into self-homing guide RNA (hgRNA) molecules constitutively expressed. In the presence of the Cas9 protein, the hgRNA will drive Cas9 to target their own loci, inducing random mutation that will be inherited by all generated daughter cells. Random mutation will likely disrupt the hgRNA properties, preventing further mutations of each locus. Due to the multitude of randomly mutation loci and the diversity and the diversity in their mutation efficiency, each cell lineage will yield a unique mutation profile able to recapitulate its lineage history. However, these approaches still face some limitations and challenges in defining cell identity and accurate lineage reconstruction. For example, DNA-damage-induced toxicity derived from double-strand break repair by non-homologous end joining (NHEJ) related to CRISPR-Cas9 activity has been shown in human induced pluripotent

stem cells (iPSCs) (Ihry et al., 2018)[451], cell lines (Haapaniemi et al., 2018)[452] and mouse embryos (Chan et al., 2019)[453]. One alternative that may not face the same concern is TracerSeq (Wagner et al., 2018)[448]. This clonal barcoding method makes use of ongoing transposase activity to successively integrate a pool of predefined barcodes, delivered as an injected plasmid into embryos. The progressive integration of plasmids into the genome provides a heritable label of clones and sub-clone without inducing unrepaired double-strand breaks, yet it does require injection or electroporation. Noteworthy, most available methods for reporting lineage information lack precise and detailed information on cell state and identity. The combination of single-cell profiling data and lineage information may provide a solution to overcome this downside (Bowling et al., 2020)[454] (Spanjaard et al., 2018)[455], offering an opportunity for synthesized views of differentiation dynamics. In 2016, two studies using imaging to perform lineage tracing and obtain phenotypic information from either scRNAseq or smFISH served as an example of the power achieved by the convergence of these two modalities (Hormoz et al., 2016)[456] (Kimmerling et al., 2016)[457].

1.3.3. Spatial transcriptomics

Another fundamental layer of information to accurately understand development, is the cellular spatial distribution. Temporal patterning often results from its interaction with spatially regulated factors across the developing tissue. To give an example, the combination of spatially and temporally organized TFs and secreted molecules from the IsO has been shown to be both necessary and sufficient to distinguish cerebellar cell types. However, a major drawback in standard single-cell profiling technologies is the loss of such spatial information. A further step toward the integration of localization and transcriptomic data is represented by advances in the emerging field of spatial transcriptomics (Noel et al., 2022)[458] (Rao et al., 2021)[459]. Spatial transcriptomics techniques localize RNA within tissue, offering promising tools to dissect the events driving cerebellar development (Zeisel et al., 2018[460]) (Chen et al., 2021)[461] (Gyllborg et al., 2020)[462]. For example, in Slide-seq (Rodriques et al., 2019)[463], RNA molecules are transferred from tissue on a 10 um microbeads barcoded slide. cDNA amplification and sequencing it is then possible by the addition of DNA oligonucleotides which can bind to 3' RNA poly-A ends. This technique provides a clear resolution enough to distinguish mononuclear layers, such as ependymal cells from the hippocampus. Additional methods based on the multiplexed variation of single-molecule FISH, such as MERFISH and seq-FISH (Lubeck et al., 2014)[464] (Chen et al., 2015)[386] (Eng et al., 2019)[465] (Xia et al., 2019)[466], a set of probes covering the full transcriptome is used in multiple sequential rounds of

hybridization. Both methods provide high sequencing depth and subcellular resolution. Yet, no method currently provides a resolution profiling as fine as scRNA-seq does, highlighting the need for single-cell and spatial data integrative approaches (Longo et al., 2021)[467].

The opportunities arising from the single cell/ multiomics field are enormous and keep unquestionably providing ground-breaking insights into cerebellar development research. Yet, the advance is accompanied with unique data science problems (Lähnemann et al., 2020)[468]. Among which, a pressing problem in the single cell / multiomics field is post-hoc data annotation due to two main reasons: the exponential growth of data and the absence of universal references. Integration tools are paving the way to the generation of comprehensive atlases where data from different datasets/modalities can reliably be mapped into the same space (See section 3) (Lähnemann et al., 2020)[468].

2. Histological and multiomics available data sets

The generation of a massive amount of data, in addition to sophisticated deep machine learning algorithms, allowed researchers to study important aspects of CNS development from a completely new integrative point of view. This way, as a non-traditional open research model, the Allen Institute broke new ground providing its dataset as a free, open resource. This sets the stage for the creation of a suite of similar resources and powerful analytical options for the scientific community to examine the publicly available datasets for further discovery (**Table 1**).

Authors	Year of publication	Method	Specie	Age	Region	Available data location
Allen Brain Institute	2005, 2007, 2008, 2011, 2015	ISH	Mouse	Embryo, Postnatal, Adult	Brain	https://brain-map.org
Carter <i>et al.</i>	2018	scRNA-seq (10x chromium)	Mouse	Embryo (E10-E17), Postnatal (P0, P4, P7 and P10)	Cerebellum	Raw data: European Nucleotide Archive (PRJEB23051) Code: - data processing https://github.com/CerebellumDev/CerebellumDev.Rmd . - Cell Seek https://cellseek.stjude.org/cerebellum/ -
Vladoiu <i>et al.</i>	2019	scRNA-seq (10x chromium)	Human, Mouse	H:Tumor; M: Embryo (E10, E12, E14, E15, E18), Postnatal (P0, P5, P7, P14)	Cerebellum	Raw data: - BAMS and filtered gene matrices of mouse developmental time points scRNA-seq (GSE118068)- FASTQs of PFB bulk RNA-seq and microarray expression (EGAS00001002696, GSE64415) - BAMS of human tumour scRNA-seq and either BAMS or FASTQs of bulk PFA/C-PA RNA-seq (EGAS00001003170) - FASTQs of MB bulk RNA-seq (EGAD00001004435)
Peng <i>et al.</i>	2019	scRNA-seq (10x chromium)	Mouse	Postnatal (P0 and P8)	Cerebellum	Raw data: GEO (GSE122357) or (SRP165255)
Gupta <i>et al.</i>	2018	scIsoform RNA-seq (10x chromium)	Mouse	Postnatal (P1)	Cerebellum	Raw data: Sequence Read Archive Bioproject (PRJNA428979) Processed data: query at isoformAtlas.com
Sepp <i>et al.</i>	2021	snRNA-seq (10x chromium)	Human, Mouse, Opossum	H: Embryo (7wpc, 8wpc, 9wpc, 11wpc, 17wpc, 20wpc), newborn, infant, toddler, adult; M: Embryo (E10.5, E11.5, E12.5, E13.5, E14.5, E15.5, E17.5), Postnatal (P0, P4, P7, P14), Adult (P63); O: Embryo (E14.5), Postnatal (P1, P4, P5, P14, P21), P42, P60, Adult	Cerebellum	Raw data: https://doi.org/10.11588/data/QDOC4E . Processed data: https://apps.kaessmannlab.org/sc-cerebellum-transcriptome . Code: https://gitlab.com/kleiss/mammalian-cerebellum .
La Manno <i>et al.</i>	2021	scRNA-seq (10x chromium), ISS (HybISS)	Mouse	Embryo (E9-E18)	Brain	Raw data: - RNaseq (Sequence Read Archiven PRJNA637987) - HybISS (http://mousebrain.org/downloads - Code: https://github.com/linnarsson-lab
Pijuan-Sala <i>et al.</i>	2019	scRNA-seq (10x chromium)	Mouse	Embryo (6.5-8.5)	Brain	Raw data: Arrayexpress: Atlas – E-MTAB-6967; Smart-seq2 endothelial cells – E-MTAB-6970; Tal1 chimeras – E-MTAB-7325; WT chimeras – E-MTAB-7324 Processed data: https://github.com/MarioniLab/EmbryoTimecourse2018 Code: https://github.com/MarioniLab/EmbryoTimecourse2018
Zeisel <i>et al.</i>	2018	scRNA-seq (10x chromium), FISH (osmFISH)	Mouse	Postnatal (P12-P30), Adult (6 and 8 weeks)	Brain, spinal cord, peripheral nervous system and enteric nervous system	Raw data: archive under accession SRP135960 Code: https://github.com/linnarsson-lab
Saunders <i>et al.</i>	2018	scRNA-seq (Drop-seq)	Mouse	Adult	Brain	Raw data: GEO: GSE116470 Processed data: http://dropviz.org/
Korzareva <i>et al.</i>	2021	snRNA-seq (10x chromium), FISH (smFISH)	Mouse	Perinatal (E18, P0, P4, P8, P12, P16), Adult	Cerebellum	Raw data: GEO (GSE15371) Processed data: https://singlecell.broadinstitute.org/single_cell/study/ SCP795/ Code: https://github.com/MacoskoLab/cerebellum-atlas-analysis .
Buchholz <i>et al.</i>	2020	RNA-seq (SMART - seqv4, Microarray, TRAP)	Human, Mouse	H: hPS-PCs; M: Postnatal (P0, P7, P15, P21, P56)	Cerebellum	Raw data: GEO - Microarray (GSE140307) - RNAseq (GSE140306) -
Hirata <i>et al.</i>	2021	NeuroGT	Mouse	Postnatal (P7)	Brain	Raw data: SSBD:repository (https://doi.org/10.24631/ssbd.repos.2021.03.001) Processed data: https://ssbd.riken.jp/neurogt/ .

Table 1 Available datasets for cerebellar development research

2.1. ISH-based datasets (Allen Brain)

As described above, the AdevBA dataset contains ISH data over embryonic and postnatal timepoints. The computational data processing pipeline developed by the Allen Institute enables the navigation and analysis of this large and complex dataset, and identifies gene expression with precise spatial and temporal regulation. The pipeline consists of the following components: a set of 3D reference models, an alignment module, an expression gridding module and a Structure Unionizer module. The alignment module registers each ISH image to the common coordinates of a 3D reference model. The expression gridding module produces an expression summary in 3D for downstream analysis. The structure unionizer module generates structure-based statistics by combining grid voxels with the same 3D structural label from the correlations to support developmental Anatomic Gene Expression Atlas (developmental AGEA) functions, an interactive 3D atlas that reveals brain organization based on the spatio-temporal organization of the transcriptome (Ng et al., 2009)[469].

The output of the pipeline is a quantified expression value at a grid *voxel* and a structure level according to the accompanying developmental reference atlas ontology, which uses a single unified 13 *levels*-based ontology for all ages (Level 0 representing neural plate, and Levels 11-13 representing individual nuclei). Therefore, such that brain structures in different developmental timepoints can be roughly related based on ontology, despite the existence of transient or migratory structures. The gene expression was annotated (four patterns: undetected, full, regional, and gradient; four densities: undetected, low, medium, and high; four intensities: undetected, low, medium, high, and mixed) at each developmental stage for anatomical structures belonging to the most detailed level of ontology. The downstream grid level data are used to provide anatomical search (genes enriched in a particular region), a temporal search (genes with higher expression in a particular age), and a correlative search (genes with similar 3D spatial gene expression profiles) service and to support visualization of tempo-spatial relationships (Developmental AGEA).

The data is publicly displayed via Web-based data viewers and downloadable through various freely available data mining tools, such as the Brain Explorer 3D viewer (Lau et al., 2008)[470] and Neuroblast (Ng et al., 2007)[471] Derived from the concept behind the Basic Local Alignment Search Tool (BLAST) (Altschul et al., 1990)[472], that is used to identify genes with sequences similar to a gene of interest, NeuroBlast identifies genes with similar patterns of expression in 20 different anatomical regions of the brain, covering the CB. Starting with a gene of interest, users can generate a ranked list of genes with similar 3D expression patterns. For example, seeding NeuroBlast with

calbindin 1 returns other genes with similarly enriched expression in PCs. On the other hand, Brain Explorer is an interactive tool for visualizing mouse brain anatomy together with both ABA and AdevBA gene expression, in the framework of the corresponding reference atlas. Users view an interactive, 3D rendering of the mouse brain and can rotate views, virtually slice in three planes, turn individual brain structures on and off, and view expression patterns of one or more genes. Noteworthy, NeuroBlast searches and direct access to the raw gene expression data on which the 3D renderings are based, are also available.

2.2. ScRNA-seq based datasets

Furthermore, recent multi-omics-based studies improved the understanding of the complex mechanisms underlying cerebellar development and lead to the generation of valuable worldwide available datasets (Carter et al., 2018)[279] (Vladoiu et al., 2019)[132] (Peng et al., 2019)[430] (Gupta et al., 2018)[429] (La Manno et al., 2021)[473] (Sepp et al., 2021)[140] (Rosenberg et al., 2018)[474]. In 2018, in a first attempt to generate a single-cell transcriptional atlas of the developing murine cerebellum, an initial scRNA-seq dataset of the murine CB development was published by Carter and colleagues (Carter et al., 2018)[279]. scRNA-seq profiles were generated throughout cerebellar development, including 12 different time-points (E10-E17, P0, P4, P7 and P10) and the raw sequence data and processing tools were shared with the community. In the study, the authors presented an example of how their transcriptional atlas could be used to gain a deeper understanding of glutamatergic and GABAergic fate specification and the TFs coordinating these processes. With the ultimate aim to facilitate individualized exploration of the dataset, they developed an interactive web-based interface called Cell Seek, where different types of analysis can be performed on any selected subsets of data, such as identifying TF expression correlation networks, as well as linear and bifurcating trends in the pseudo time. The same year, postnatal (P2 and P11) developmental trajectories of cerebellar cells were as well tackled using a single-cell profiling platform based on barcoding split-pool rounds (SPLiT-seq) (Rosenberg et al., 2018)[474]. Another valuable mouse cerebellum development dataset was published and shared later in 2019 by the Taylor laboratory (Vladoiu et al., 2019)[132]. In this study, scRNA-seq was used to profile more than 60 000 cells from 9 time-point throughout the developing mouse cerebellum (E10, E12, E14, E16, E18, P0, P5, P7, P14), and showed that different molecular subgroups of childhood cerebellar tumors mirrored the transcription of cells from distinct, temporally restricted cerebellar lineages. Moreover, Luo laboratory made available a post/perinatal development (P0 and P8) transcriptional profiling dataset of the murine cerebellum (Peng et al., 2019)[430], effectively drawing a systematic landscape of cerebellar gene expression in

defined cell types and the general gene expression framework for this developmental window. Temporally dynamic gene expression patterns were shown to correlate with states of various neuronal types. The dataset allowed the authors to identify novel markers of various cerebellar cell types and suggested factors that might be involved in neuronal differentiation, morphogenesis, neuro-glia interactions or cerebellum-associated diseases mechanisms, such ataxia.

Alternative splicing and isoform switching play a central role in cell function and thus, cell identity. Yet, short read-based methods must ignore these differences. Full length isoform quantification is therefore a plus in molecular profiling and is reflected in how active the community has been in developing suitable methods. Striving for the development of such approaches, Gupta et al came out with ScISOr-Seq and a postnatal mouse cerebellum (P1) single-cell isoform profiling available dataset (Gupta et al., 2018)[429]. Lately, in an effort to understand shared and lineage-specific programs governing cellular development of the mammal cerebellum, Sepp and colleagues submitted an extensive snRNA-seq based atlas of cerebellar development across ages and mammalian species (mouse, human and opossum) (Sepp et al., 2021)[140]. With that, developmental dynamics of cerebellar cell types in mammals appeared to have been largely conserved in evolution, except for human PCs. (Previously discussed in Chapter 1 Section 4). The datasets generated (raw sequencing data) and analyzed (fully annotated containing UMAP and LIGER embeddings) during the study are accessible, as well as their data processing/analysis codes. In parallel, they launched an interactive interface to explore the snRNA-seq atlases both in single species and comparative analysis across them. The source code for this application is also available. Another compelling dataset comes from the systematic characterization of cell states over the entire spatiotemporal range of brain development (La Manno et al., 2021)[473]. Aiming to elucidate the complex interactions underlying brain cell heterogeneity generation, the accurate spatial organization of neuronal progenitors during nervous system patterning was revealed combining *in situ* sequencing (ISS)-based mapping (HybISS (Gyllborg et al., 2020)[462]) and scRNA-seq cell state profiling from gastrulation (Pijuan-Sala et al., 2019)[425] to birth (E9-E18). The mapping was achieved by means of a modified version of a previously designed deep learning pipeline: Tangram (See section 3) (Biancalini et al., 2020)[475]. The raw sequencing data (292 495 single cells), HybISS data (750 000 *in situ* sequencing voxels) and source code are available.

Single cell profiling datasets of the adult mouse nervous system, including the CB, are also available. An important piece is the work of Zeisel et al. provided a clear picture of cell diversity by region,

including the CB, and a reference atlas for studying the mammalian nervous system by means of scRNA-seq and spatial transcriptomics (omFISH – RNAscope) (Zeisel et al., 2018)[460]. The raw sequencing data for the systematic survey of transcriptomic cell type in the mouse nervous system and the analysis software developed for this study are freely accessible. Additionally, they provided a wiki with a report card for each cell type. The wiki can be browsed by taxon, cell type, tissue, and gene, with information on enriched genes, specific markers, anatomical location and more. In 2021, extending a preceding adult mouse brain dataset (Saunders et al., 2018)[476] specifically to the cerebellum, the Macosko laboratory has made available a transcriptional atlas of the adult mouse cerebellar cortex in the context of a study aiming to molecularly identify cell types across individual lobules (Kozareva et al., 2021)[248]. Combining snRNA-seq and smFISH, PCs revealed considerable regional specialization, with the greatest diversity occurring in the posterior lobules. On the other hand, for several types of interneurons, the authors noticed rather a continuous variation. Remarkably, UBCs molecular diversity correlates with physiological properties variation. Also, two types of MLI were identified based on physiological properties although a continuous molecular variation. The dataset also includes transcriptional profiling data from peri/postnatal mouse cerebellum (ranging from E18 to P16), which has been used for the examination of the developmental specification of these two populations. All raw and processed data supporting this study, together with the code and scripts to reproduce their analysis, have likewise been made available for the community.

2.3. Type-specific mRNA purification-based datasets (Buchholz)

A comparative transcriptional profile between pluripotent stem cell-derived PCs (hPSC-PCs) and developing mouse PCs (P0, P7, P15, P21, P56) is also available (Buchholz et al., 2020)[431]. The metagene projection analysis based on cell-type specific mRNA purification by translating ribosome affinity purification (TRAP) (Heiman et al., 2014)[477], served to identify both classical PCs markers as well as novel mitochondrial and autophagy gene pathways. Additionally, differences in timing and expression of key genes sets between mouse and hPSC-PCs were identified.

2.4. Neurogenic birthdate tagging-based datasets (Hirata)

Lately, and in a lower scale, a birthdate-based atlas of the murine brain, the NeuroGT, has become available (Hirata et al., 2021)[478]. Aiming to overcome classical birthdate techniques limitations and provide a tool to study neuronal birthdate in living animals, a neurogenic tagging CreER driver mouse relying in early transient expressed genes was developed. The database contains P7 coronal A-P serial

sections tagged from E9.5 to E18.5 using different lines. Interestingly, the Neurog2^{CreER} line (*Neurogenin 2*), which displays cerebellar tagging, is available in the resource.

3. 4D integration tools

The integration of multifaceted datasets and the generation of comprehensive models represents a critical step in understanding and predicting cellular trajectories in the developing CNS. Indeed, once the baseline model is achieved, it becomes a great tool to systematically analyze system perturbations and develop hypotheses to guide the design of new experimental tests. A good illustration is weather forecasting. Almost all currently adopted forecasting techniques involve the use of predictive models. As a rule, the models are running within computerized real-time forecasting systems which involve automated collection, checking, and numerical analysis of different sorts of features (meta-levels) necessary to provide information on the expected weather and forecast projection times ranging from hours to a few months. Therefore, the meta-levels hypothesis leads to testable predictions and opens the ways for new experimental designs.

As discussed in previous sections, multimodal data integration would surely help to overcome technique-specific downsides, to improve our understanding and deciphering of scientific conundrums, such as cerebellar development. Indeed, to understand complex biological processes such as neuronal development, it is not sufficient to identify and characterize individual events. It is also necessary to obtain a thorough understanding of the interaction between these discrete events and their components across time. To date, neuroanatomical atlases provide the most logical framework for integrating various data modalities, by organizing and presenting the data for the broad, multidisciplinary neuroscience community. As an example, the Allen Institute pioneered large, enterprise-wide projects, like the AdevBA, relying on integrated efforts and expertise across its multidisciplinary collaborators. Another example is found in the multimodal reference atlas that has been recently generated for the primary motor cortex by the NIH's Brain Research through Advancing Innovative Neurotechnologies (BRAIN) Initiative Cell Census Network (BICCN). Within this atlas, they integrated information coming from eleven coordinated multi-laboratory complementary datasets. This illustrates how cell type identification from large-scale multiomics datasets, together with comparative analysis across species and the generation of a wiring diagram for this brain area, have returned important biological insights in understanding the structure-function relationships in the mammalian brain. Therefore, developing methods to unify heterogeneous datasets without

compromising the integrity and interpretation of the data is now a must. For instance, it is crucial to correct for batch effects when comparing different studies, while still maintaining the feature diversity within the same dataset. The LIGER method tries to circumvent this issue by employing an integrative non-negative matrix factorization to identify shared and dataset-specific factors (k) (dimensionality reduction), such as genes defining a particular cell type (Welch et al., 2019)[479]. The dataset-specific effects are then adjusted by a tuning parameter, which reflects the differences in the analyzed datasets (similarity method).

Although essential, it is an enormous computational challenge to link different types of biological information together in the same space. The method of integration remains an open question and strongly depends on the nature of the data and the specific aim. Numerous dynamic mathematical models have been developed with the aim of integrating distinct types of generated data in space to investigate how complex regulatory processes are connected and how disruptions of these processes may contribute to the development of disease. The Cell2location method aims to achieve a comprehensive integration of single-cell and spatial transcriptomics data employing a hierarchical Bayesian model (Kleshchevnikov et al., 2022)[480]. First, a negative binomial regression model is used to estimate cell type reference signatures from single-cell / single-nucleus profiles. These signatures are then used, together with one or more spatial transcriptomics datasets, as input for assigning individual spatial locations to each reference cell type.

Despite the remarkable achievements, these methods still fail at generating entirely automated pipelines. Manual annotations from researchers are still required for registration (anatomical regions annotation and landmark identification in experimental and atlas images). Such supervision prevents complete automation. Computational researchers are therefore working to break this barrier mostly using machine/deep learning. An outstanding deep learning framework to address these challenges was recently developed and used to assess brain embryonic development (Biancalini et al., 2020)[475] (La Manno et al., 2021)[473]. Known under the name of Tangram, the method aims to align any type of single-cell profiling data to different kinds of spatial data collected from the same brain region, towards the generation of a high-resolution integrated atlas. Tangram's probabilistic mapping/registration pipeline is available for any further application. However, it requires a common coordinate framework, or in other words, an annotated reference atlas for the region of study. The validation of the computational alignments can be done by recovering cell type specific spatial maps and predicting their gene expression profiles.

A major future frontier for cell atlas generation is the 3D mapping of tissues at a cellular resolution. The abovementioned spatial mapping approaches can be used as the foundation for 3D atlases.

Precisely, multimodal techniques can be applied to consecutive tissue sections across the region of interest and then reconstructed in 3D using 3D reference atlas as scaffold. Else, regional cell type maps can be generated directly from intact tissue volume imaging approaches. Some methods have tried to reconstruct datasets volumetric conformation (xyz) without a 3D reference. That is the case for Novosparc (Moriel et al., 2021)[481], which tries to project single-cell data into a 3D framework by similarities. Although this method proved to be suited for simple structures/organisms, it might present considerable constraints as the system complexity increases.

Cerebellum development is the result of a complex interaction between genetic programs and environmental factors from embryonic to postnatal stages. Despite recent efforts, there are still significant gaps in our understanding of how the precise cerebellar architecture is achieved. In particular, we lack insights regarding the molecular mechanisms that control the generation and differentiation of specific subtypes of cerebellar neuronal and non-neuronal populations. Although many studies have provided large amounts of data on how parts of this tangled developmental system function, one of the biggest challenges is still to understand how these data combine to precisely describe cerebellar development.

The work of this thesis aims to provide the first steps to a novel integrative view of cerebellar structure and development. By generating a common space (3D) atlas for the developing (4D) murine CB, I wish to provide a reliable framework in which we can harmonize multimodal datasets and allow their integration and comparison through time and space (**Figure 16**). We can divide the process as follows: (1) generation of 3D annotated cerebellar reference atlas at distinct points of cerebellar development from embryonic to postnatal stage, combining organ clearing and 3D imaging experiments with an anatomical annotation workflow (2) production / refinement of multimodal datasets relevant for understanding cerebellar development underlying mechanisms, (3) multimodal datasets integration into the corresponding reference atlas. Noteworthy, this work contributes to increase and ameliorate the available datasets, providing detailed information about cell birth dynamics, cerebellar progenitors behavior and cellular dynamics during embryonic development, as well as high throughput transcriptomics analysis of the developing postnatal CB.

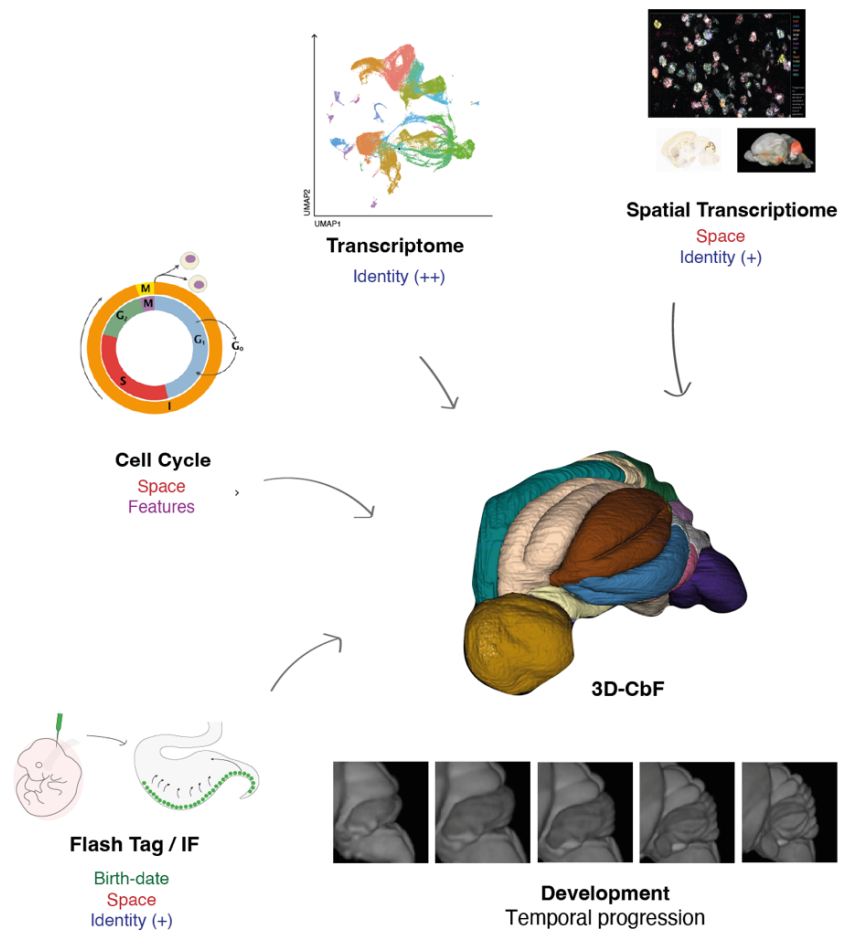


Figure 16. 4D atlas of cerebellar development. A 3D cerebellar framework (3D-CbF) is generated for different ages throughout development, from embryonic to postnatal stages (4D). Distinct types of information (time (birth-date, features), space, identity) obtained through diverse techniques are integrated into the corresponding 3D-CbF, using machine learning/data mining in the perspective of generating a dynamic description of cerebellar development.

Mice

Timed pregnancy CD1 female mice were used (Charles Rivers, #022CD1) in this study. Experiments were carried with permission of the Vaud Cantonal Authorities, Switzerland.

In utero microinjection

Experiments

Embryonic FT tracking, Postnatal FT tracking, Spatial transcriptomics, snRNA-seq and snATAC-seq

Reagents and equipment

CFSE (Cell Trace™ CFSE, Life Technologies, #C34554), DMSO, Fast Green 4%, Isoflurane, Tamgesic (Provet AG, #2222), NaCl 0,9%, Glass capillary (World precisions Instruments, #1B100F-3.), Picosplitzer, Heat pad, 6-0 Coated vicryl absorbable suture (Ethicon), Betadine, Hair removal cream, Capillaries loader tips (VWR, #612-7933)

Procedure

Timed-pregnant mice were anesthetized with isoflurane/oxygen (5% initially, followed by 2.5% during surgery) and a small abdominal incision was performed to access the uterine horns. Surgeries were performed on embryonic days I 11, 12, 13, 14, 15 and 16. [Flash Tagging] 0.5 μ l of 10 mM of a carboxyfluorescein succinimidyl ester (CFSE) was injected into the third ventricle of the embryos under visual guidance (Fast green 4%) (Telley et al., 2016)[238] Embryos were therefore replaced into the abdominal cavity. The peritoneum and the skin were sutured using 6-0 Coated vicryl absorbable suture. The embryos continued their normal development until the collection day.

[Principle of action of FT compounds] Carboxyfluorescein succinimidyl esters act by covalently binding intracellular proteins with the fluorescent dye carboxyfluorescein. CellTrace CFSE initially is diacetylated carboxyfluorescein diacetate succinimidyl ester (CFDA-SE). The acetyl group is responsible for the initial membrane permeability of the compound and is cleaved by intracellular esterases upon entry into the cell to give rise to CFSE, which is fluorescent and accumulates intracellularly. Covalent binding of CFSE to intracellular proteins through amino-reactive succinimidyl side chains is responsible for the stable labeling of the cells (Quah et Parish, 2010)[482].

Edu/BrdU dual labeling

Experiments

Cell cycle

Reagents and equipment

BrdU powder (VWR, # ALFAH27260.MD), EdU powder (WVR, #CAYM20518-50), PBS 1x

Procedure

[Labeling of dividing cells] Solutions of BrdU (10 mg/ml) and EdU (5 mg/ml) were dissolved in phosphate-buffered saline (PBS). The pregnant mouse was weighed, and injection volumes for a 50 mg/kg EdU injection and 50 mg/kg BrdU injection were calculated. We used mice at embryonic stages I 11, 12, 13, 14, 15 and 16. At time-point 0, we gave the pregnant mouse an intraperitoneal injection of the appropriate volume of the EdU solution. One hour and a half after this (time-point 1,5 h), we gave an intraperitoneal injection of the BrdU solution. 2 h after the first injection, the pregnant mouse was euthanized via cervical dislocation. The gravid uterus was gently removed from the abdomen and placed in ice-cold PBS. Samples were fixed, cryopreserved, sectioned, stained and acquired (see Fixation/Perfusion, Cryopreservation, Cryostat sectioning, Sections Immunofluorescence, Image acquisition)

[Calculation of Ts and Tc] The following calculation methods were adapted from Martynoga et al. (2005)[483] and Harris et al. (2018)[484]. The calculations of cell cycle length assumed that all cells in the population of interest (as defined by Ki67) were actively progressing through the cell cycle in an asynchronous manner (Nowakowski et al. 1989)[485]. Cell cycle pipeline The total number of cells labelled with Ki67 in the cerebellar anlage were quantified (detected and located), and we determined: (1)The number that were EdU⁺ and BrdU⁺ (these cells had remained in S-phase for the duration of the EdU to BrdU injection interval),(2)The number that were EdU⁺ and BrdU⁻ (these cells had exited S-phase during the EdU to BrdU injection interval), (3)The number that were BrdU⁺ (independent of EdU reactivity) (these cells were in S-phase at the completion of the experiment and (4) The number that were BrdU⁻ (independent of EdU reactivity) (these cells were not in S-phase at the completion of the experiment). We then used the following formula to determine Ts: $T_s = \text{injection interval} \times (\text{EdU}^+; \text{BrdU}^+ \text{cells} / \text{EdU}^+; \text{BrdU}^- \text{cells})$. The numerator reflects the number of cells that remained in S-phase

during the EdU to BrdU injection interval, whereas the denominator reflects the number of cells that left S-phase during the injection interval. With these cell counts, we then used the following formula to determine T_c : $T_c = T_s / (\text{BrdU}^+ / \text{Ki67}^+)$. Here the denominator reflects the fraction of the progenitor population that was in S-phase at any one moment in time.

Fixation/Perfusion

Experiments

Embryonic FT tracking, Cell Cycle, Postnatal FT tracking, Spatial transcriptomics, 3D reference atlas

Reagents and equipment

Ice-cold PBS 1x, Paraformaldehyde 4% (PFA, Sigma), Pentobarbital , Syringe

Procedure

Embryonic brains were collected in ice-cold PBS and fixed in 4% paraformaldehyde (PFA) overnight at 4°C. Postnatal mice were perfused with 4% PFA and brains were post-fixed in 4% PFA overnight at 4 °C.

Cryopreservation

Experiments

Embryonic FT tracking, Cell cycle, Postnatal FT tracking, Spatial transcriptomics

Reagents and equipment

Sucrose (Sigma, #84100-1KG) 30%, 20% and 10% in PBS1x, OCT (O.C.T compound tissue Tek, Systemex), Cryomold, 2-methylbutane (Sigma, #m3263-1L.), Dry ice

Procedure

Fixed brains were incubated with increasing sucrose solutions (10%, 20% and 30%) O/N for each concentration. Thereafter, brains were wiped out carefully using absorbent paper and placed in the cryomold in the desired disposition. Then, OCT compound was used to embed the brains and fill up

the cryomold. Finally, cryomolds were placed in pre-cooled 2-methylbutane (-60°C to -80°C) for snap freezing (approximately 1'30'' immersion). OCT embedded brains were kept at -80°C until use.

Cryostat sectioning

Experiments

Embryonic FT tracking, Cell cycle, Postnatal FT tracking, Spatial transcriptomics

Reagents and equipment

Leica Cryostat, Super Frost slides (VWR, #631-9483), OCT (O.C.T compound tissue Tek, Sysmex), Microtome blades (WVR, #LEIH14035843489), 24 well-plates, PBS 1x

Procedure

OCT embed brains were equilibrated at -20°C for 1h before starting the sectioning.

[Embryonic FT tracking] Brains were sectioned in the coronal plane *on slide* in a serial manner at 25 um thickness.

[Cell Cycle] Brains were sectioned on slide in a serial manner in the sagittal plane at 20 um thickness.

[Postnatal FT tracking] For 2D analysis, brains were sectioned on floating in a sagittal plane at 60 um thickness. After sectioning, PBS 1x was replaced for fresh one and kept at 4°C, for immediate usage, or conserved in a 1:1 mixture of ethyl glycol and glycerol dissolved in PBS 1x at -20°C, for long-term storage. For 3D analysis, brains were section on slide in a serial manner in the sagittal plane at 14 um thickness.

[Spatial transcriptomics] Brains were sectioned on slide in a serial manner in the sagittal plane at 14 um thickness.

For *on slide* sectioning, slides were warmed up at 37°C in a heat pad prior sectioning and all along the procedure to ensure proper sections – slide fixation. Slides were dry out at RT from 1h to O/N before

starting Immunofluorescence (See sections Immunofluorescence). Remaining slides were kept at -80°C until usage.

Sections Immunofluorescence

Experiments

Embryonic FT tracking, Cell cycle, Postnatal FT tracking, Spatial transcriptomics

Reagents and equipment

Sodium citrate buffer 0,5M buffer pH 6 (J61815.AK, WVR), Fluoromont-G (00-4958-02, ThermoFisher), Mounting (ProLong Antifade Mountan), Donkey Normal Serum (017-000-121, Jackson Immunoresearch), ImmEdge™ Pen (VC-H-4000-1, AdipoGen), Triton (X100-500ML, Sigma-Aldrich), HCl

[Antibodies] mouse anti-BrdU 5 μ g/ μ l (G3G4, DSHB), rabbit anti-Ki67 1:500 (ab15580, Abcam), mouse anti-PH3 1:500, goat anti-Fluorescein 1:1000 (AB19224, Abcam), rabbit anti-PAX2 (716000, Life Technologies), mouse anti-PAX6 5 μ g/ μ l (PAX6, concentrate, DSHB), rabbit anti-PAX6 1:500 (AB2237, Merk Millipore), rabbit anti-Neurogranin 1:500 (Ab5620, Merk Millipore), rat anti-TBR2 1:500 (14-4875-82, Invitrogen), rabbit anti-BLBP 1:500 (ABN14, Merk Millipore), mouse anti-Calretinin 1:500 (6B3, Swant), Click-it EdU 647, Alexa Fluor 568 Donkey anti-Goat 1:500 (10463972, ThermoFisher), Alexa Fluor 568 Donkey anti-Rabbit 1:500 (10617183, ThermoFisher), Alexa Fluor 568 Donkey anti-Mouse 1:500 (10236683, ThermoFisher), Alexa Fluor 647 Donkey anti-Rabbit 1:500 (10543623, ThermoFisher), Alexa Fluor 647 Chicken Anti-Rat 1:500 (10634773, ThermoFisher), Alexa Fluor 488 Donkey anti-Mouse 1:500 (A-21202, ThermoFisher), Alexa Fluor 488 Donkey anti-Goat 1:500 (A-11055, ThermoFisher), Hoechst 1:5000

Procedure

[Embryonic FT tracking, Postnatal FT tracking *on slide*] Slides were washed once with PBS 1x before antigen retrieval * (AR) with Sodium citrate Buffer 10mM (20' at 80°C). Then, slides were washed three times with PBS 1x and incubated with a blocking solution (5% Donkey Serum in PBS-Triton 1%) for 1h at room temperature (RT). Slides were then incubated with primary antibody solution (blocking solution + primary Antibody **) O/N at 4°C or 4h at RT. Slides were then rinsed three times

with PBS-Triton 1% before secondary antibody incubation (Blocking solution + secondary Antibody *) Slides were rinsed in PBS 1x and then incubated in Hoechst (5' at RT). Slides were rinsed again in PBS, then cover slipped using fluorescent mounting media (ProLong Antifade Mountan for Spatial transcriptomics) and stored at 4°C until imaging

[Cell Cycle] In order to open the DNA and make possible BrdU detection, before AR sections were incubated 30' at 37°C in pre-warmed 2N HCl.

[Postnatal FT tracking *floating*] Sections were incubated for 20' in Sodium Citrate Buffer at 80°C for AR*, 1h in blocking solution (5% Donkey Serum in PBS-Triton 1%) and then incubated overnight with primary antibodies diluted in blocking solution**. Sections were then washed in 3x in PBS for 15 minutes each and incubated for two hours at room temperature with secondary antibodies and washed. Sections were mounted in fluorescent mounting media and stored at 4°C until imaging.

* AR was necessary for nuclear markers: TBR2, PAX2, Ki67, PH3, PAX6, BLBP

** Antibody Concentration was determined experimentally or following specifications from provider (See – 2D Immunofluorescence – *Material*)

Whole brain Immunofluorescence

Experiments

Reference atlas generation

Reagents and equipment

Methanol (20847.360, VWR), Gelatin (24350.262, VWR), Saponin (S4521, Sigma-Aldrich), Triton X100 (X100-500ML, Sigma-Aldrich), Thimerosal (T878-5G, Sigma-Aldrich), Hydrogen peroxide 30% (216763, Sigma-Aldrich), Thimerosal (T878-5G, Sigma-Aldrich), 10xPBS (VWR) [Antibodies]

Procedure

Fixed samples were incubated in MeOH solutions of increasing concentrations (50%, 80% and 100%) for 1h 30' at RT with agitation (rotator wheel) at 12 RPM, using 15 mL falcon tubes. Then, samples were bleached O/N with MeOH + 6% H₂O₂ at 4°C protected from light. Samples were rehydrated with

MeOH solutions of decreasing concentrations (2x100%, 80% and 50%) for 1h 30' at RT with agitation at 12 RPM. Samples were then incubated with PBSG-T with rotation at RT for blocking. Incubation times varied depending on the sample size* (Small: 1 day; Large: 4 days) PBSG-T 1% was prepared by dissolving by gentle heating 2g of gelatin (0.2%) in 880mL of distilled water. Once chilled, 100mL of 10xPBS, 40mL of 25% Triton X-100 (125mL of Triton X-100 were gently added and dissolved in 375 mL of sterile distilled water with stirring) and 0.1g of Thimerosal were added to the solution (solution was stored at 4°C up to 2 months). Next, samples were incubated in primary antibody solution** at 37°C with agitation (Small: 7 days; Large: 14 days). Primary antibody solution was prepared in PBSG-T 1% + 10x Saponin (10mg/mL). Again, samples were rinsed in PBSG-T 1% 6 times for 1 day (each 1h 30') at RT with agitation. Secondary antibodies solutions were prepared in PBSG-T 1% + 10X Saponin (10mg/mL) ***, and samples incubated with rotations at 37°C (Small: O/N; Large: 4 days). Samples were then rinsed 6 times for 1 day (each 1h 30') at RT with rotation and stored at 4°C until clearing.

* Small: up to E15; Large: E15-postnatal, adult

** Antibody Concentration was determined experimentally (See – Whole brain Immunofluorescence – *Material*)

*** Antibody concentration (See- Sections Immunofluorescence). To-Pro nuclear staining was added in the solution (Small 1:1000; Large 1:500)

Whole brain clearing (iDisco+ adapted)

Experiments

Reference atlas generation

Reagents and equipment

Methanol (20847.360, VWR), Dichloromethane (270997, Sigma), Benzyl Ether (108014, Sigma), Ethyl cinnamate (112372-100G, Sigma), 10xPBS (VWR)

Procedure

Samples were processed following an adaptation of iDisco+ protocol (Renier et al., 2014)[392]. Samples* were incubated in 20%, 50%, 80% and 2 x 100% MeOH dilutions in PBS 1x, each for 1h in

rotation, followed by O/N incubation in 1/3 Dichloromethane (DCM) in MeOH. The day after the brains were incubated 30' in DCM before transferring them to Benzyl Ether (DBE) for clearing. Once cleared, samples were placed in Ethyl cinnamate until imaging.

* Small samples were embedded in agarose 4% (prepared in TAE 1x) before clearing

RNAscope® HiPlex

Experiments

Spatial transcriptomics

Reagents and equipment

ImmEdge™ Pen (VC-H-4000-1, AdipoGen), RNAscope® HiPlex Cleaving Stock Solution (324130, Bio-Techne/ACD), RNAscope® Wash Buffer Reagents (310091, Bio-Techne/ACD), RNAscope® Protease III & Protease IV Reagents (322340, Bio-Techne/ACD), RNAscope® Target Retrieval Reagents (322000, Bio-Techne/ACD), RNAscope® HiPlex Probe Diluent (324301, Bio-Techne/ACD), RNAscope® HiPlex Probes (T1- *Pvalb*, T2- *Gdf10*, T3- *Fgf3*, T4- *Scrg*, T5- *Neurod6*, T6- *Evol7*, T7- *Naaa* , T8- *Robo3*, T9- *Nxph1*, T10- *Clic*, T11- *Ppplr3c*, T12- *Bhlhe23*)

Procedure

P7 Flash-Tag injected at E11, E12, E13, E14, E15 and E15; P7 and P0 WT on slide cerebellar sections were used (see Cryostat sectioning – Spatial transcriptomics). Samples were processed following RNAscope® Assay protocol (Wang et al., 2012)[486]. For Flash-Tag samples, an additional round of immunofluorescence anti-Fluorescein was done prior to the RNAscope® Assay protocol (see Immunofluorescence).

Image acquisition

Experiments

Embryonic FT tracking, Cell cycle, Postnatal FT tracking, Spatial transcriptomics, Reference atlas generation

Reagents and equipment

Axioscan Z1 widefield scanner (Zeiss), LSM 710 Quasar Confocal Microscope (Zeiss), Light sheet microscope (LaVision Biotech Ultramicroscope II).

snRNA sequencing and analysis

Experiments

Transcriptomics analysis of embryonic and perinatal cerebellum

Procedure

[Nuclei preparation and FACS sorting] Embryos or mice were sacrificed, and brains were extracted in ice-cold oxygenated ACSF. Each brain was then directly processed or sectioned coronally at 600 μm using a vibrating microtome. For embryonic time point the brain were directly snap freeze in liquid nitrogen. The cerebellar primordium or the cerebellum was micro-dissected under a stereomicroscope and then incubated for 5 min in 500 μl chilled 0.1X NP40 Lysis Buffer (Tris-HCL pH 7.4 10mM, NaCl 10mM, MgCL2 3mM, Tween-20 0.1%, NP40 0.1%, BSA 1%, DTT 1mM and Rnase inhibitor), mechanically dissociated using a pellet pestle (15 goings and ongoings) and finally incubated on ice for 5 min. The suspension was then washed with 500 μL chilled wash buffer (Tris-HCL pH 7.4 10mM, NaCl 10mM, MgCL2 3mM, Tween-20 0.1%, BSA 1%, DTT 1mM, Rnase inhibitor). Nuclei were then filtered through a 30- μm cell strainer, centrifuged (1000g, 10 minutes at 4°C) and resuspended in 500 μL of FACS buffer (Tris-HCL pH 7.4 10mM, NaCl 10mM, MgCL2 3mM, BSA 1%, DTT 1mM, Rnase inhibitor). The embryonic and postnatal conditions were multiplex using hashtag antibody from (Biolegend), for postnatal ages to reduce granule cells proportion in our sample we use an anti-Neun antibody in order to enrich non granule cell to a theoretical ratio of 1:10. Positive nuclei were sorted using a BD FACS Aria II flow cytometer (BD Biosciences) and collected in ice-cold FACS buffer.

[Libraries preparation and Analysis] After sorting, cells were immediately processed according to the 10X multiome Chromium protocol. Briefly, an appropriate volume of each cell suspension containing cells from each condition were combined with 10X Chromium reagent mix and samples were loaded into separate lanes. Cell capture, lysis, mRNA reverse transcription, DNA transposition, cDNA amplification, and mRNA/ATAC libraries were performed following 10X Genomics Chromium dual indexing Single Cell 3' V3.1 reagent kit instructions. Hashtag library was performed following Total-seq (Biolegend) dual indexing protocol. Libraries were then multiplexed and sequenced according to

manufacture recommendations with paired-end reads using a HiSeq4000 platform (Illumina) with an expected depth of 100'000 reads per single cells. All the sequencing experiments were performed within the Genomics Core Facility of the University of Lausanne. Alignment of sequenced reads to the mouse genome (GRCm38) and filtered gene–barcode matrices were realized by running Cell Ranger Single-Cell Software (10X Genomics). The cell ranger function was used to generate filtered gene/cell expression UMI corrected matrices by selecting probable cells and removing empty lipid droplets. To filter only high-quality cells, we applied selection based on mitochondrial genes percentage (<10 %) and number of genes per cell (>500 genes). Demultiplexing of the Hashtag and potential doublets were identified using a consensus analysis from multiple demultiplexing algorithms. The cells were then integrated with reference cerebellar single cell dataset using Seurat. The raw count matrix was normalized and scaled using the SCTransform procedure from the Seurat package. For UMAP visualization, dimensionality reduction was performed using standard function from Seurat. We first adopted a graph-based clustering approach using “FindClusters”.

Cerebellar Reference Atlas

Experiments

Generation of annotated 3D atlas of the developing cerebellar primordium and postnatal cerebellum.

Procedure

[Definition of anatomical zones] 4 compartmentation trees (CT) were defined to match with the dynamic evolution of the primordium during development: (1) E11-E14 (**Table M1**), (2) E15-E17, (3) E18-P0 and (4) P7-P56 (**Table M2**). (CT 1-3) Our annotations cover the medio-lateral (M-L), rostro-caudal (R-C) and dorso-ventral (D-V) compartmentation of the cerebellar primordium. Cerebellar primordium boundaries were defined by the Isthmus (Isth) in the most rostral part, and the Roof Plate (RP), most caudal. We consider these two morphological boundaries the ones matching the best the molecular boundaries, which have been shown to be crucial to determine the cerebellar territory.

In the M-L axis we considered 3 levels: Lateral (Lat), Intermediate (Int) and Medial (Med). In each of these levels and in accordance with the literature, we divided the primordium in 2 main areas along the R-C: the ventricular zone (VZ) and the Upper Rhombic Lip (URL), which correspond to the GABAergic and Glutamatergic germinal zones respectively. Inspired by the work of Zordan *et al.* [232], where they presented a possible compartmentation of the cerebellar primordium based on different molecular expression, we further divided the VZ in 3 compartments (from caudal to rostral):

C1, C2 and C3. Each of these compartments have been divided in 3 zones in the D-V axis: Precursor domain (Pr), Post-mitotic domain (Pm) and mantle zone (M) (Schaper, 1894), from ventral to dorsal. From E15 to E17 M zone in the periventricular stratum (pM) and the Intermediate stratum (iM). The Subpial stream (SS), containing migrating cells from the URL, is established at the most external layer going from the URL to the Isth. From E15 the SS is substituted by the external granule cell (EGL) layer and the prospective Purkinje cell layer (pPCL) is defined. Deep cerebellar nuclei (DCN) can also be tracked at early stages of the cerebellar development. We defined the Nuclear Transitory Zone (NTZ), which contains migrating nuclear cells, in the Lat and Int levels from E11 to E14. From E15 to P0, the different nuclei can be already identified. Thus, we have defined the Dentate nucleus (Dent) at the Lat level, the Interposed nucleus (Inter) at Int level and the Fastigial nucleus (Fast) at the Med level. (CT4) Annotations on P7 reference atlas are based on Allen Brain postnatal compartmentation.

[Delineation] We used the 3D segmentation software ITK-snap for structure delineation.

Registration pipeline

Our pipeline uses a multi scale registration approach. For every step in the image pyramid, the moving image is first registered to the fixed image using a rigid registration step. At this step, we optimize for the translation and rotation parameters. Next, we optimize for the scale and shear parameters, prior to the non-linear registration step, which estimates the displacement field ϕ . For the linear registration steps, Mutual Information is used as the similarity metric. The non-linear registration step employs the Greedy-SyN algorithm which uses local cross-correlation as the similarity metric. Gradient descent is used to minimize the negative of the similarity metric. The registration pipeline is implemented using ANTsPy.

[Landmark guidance] The Greedy-SyN algorithm used in our registration pipeline has achieved state of the art results in various medical image registration benchmarks. Deformable registration can nonetheless be challenging when applied to samples with complex morphologies, or images with large local deformations, significant contrast and illumination differences. Deformable registration algorithms based on intensity similarity measures can therefore get stuck in local minima in the presence of such confounding factors. In such scenarios, incorporation of landmark guided registration can greatly improve registration results. Landmark-guided optimization is here divided in two steps:

1. Landmark detection in fixed and moving images. As a first step, points are manually annotated along the folds of the cerebellar sections in both the fixed and moving images. We use a Bspline to resample the curve into 250 equidistant points, according to the arc length parameterization. After this operation, each curve along the folds of the cerebellum is given by a list of a tuple of x and y coordinates ordered along the anteroposterior axis of the cerebellum. This ordering is essential for our landmark matching approach. We treat the problem of finding corresponding landmarks in the fixed and moving images as a curve alignment problem.
2. Landmark registration using LDDMM. The LDDMM (Large Deformation Diffeomorphic Metric Mapping) framework is a standard fluid based registration framework that is capable of capturing large, smooth and invertible deformations (Certigolu et al., 2010).

Template atlas creation

Assuming brains are indexed as b_1, b_2, b_3 . We implement the following iterative procedure to create the template for embryonic stages. We average the three brains to create an initial template.

1. Register b_1, b_2, b_3 to this average template. After registration let the transformed images be denoted as b_{1x}, b_{2x}, b_{3x} and the transform parameters be denoted as t_1, t_2, t_3
2. Average the transformed images to create the new template
3. Average all the transform parameters to create a single transform
4. Apply the average transform to the new template created in step 2. To warp the template towards the true mean shape.
5. Use an image sharpening filter on the new warped template

And repeat.

Cell detection

Cell detection was done using Stardist. We replaced the Unet backbone in Stardist with a Unet backbone with self and cross attention (Schmidt et al., 2018)[492]. AttentionN has been shown to improve performance in a variety of computer vision and NLP tasks.

Analysis and statistics

The analysis and statistics were done in Python 3.7. Specifically, data handling and processing was done mostly using the numpy 1.21.6 and pandas 1.3.5 libraries. Statistics were carried on with the pingouin 0.5.1 library. In this thesis, statistical analyses were done following the classical pipeline of ANOVA followed by t-tests corrected for multiple comparisons. Significance was set at $\alpha = 0.05$. Due to our aim of creating this large dataset for future integration, we prioritized extensive and multimodal description of single technical replicate over their number. Thus, the n number for each condition is relatively low, which renders normality and homoscedasticity not reliably inferable. However, since every staining picture composing one replicate was visually validated and developmental data are reliably reported as coming from normally distributed populations in literature, we applied the ANOVAs and t-tests assuming no violation of prior assumptions. Depending on the nature of the data, we used on-way, repeated, or mixed-model ANOVAs. The F values, degrees of freedom and p-values are reported for each factor and their interaction in the figure legends. The p-values are as well shown on the plots for convenience. Post-hoc t-tests were carried on only if a significant interaction effect was reported. Depending on the nature of the data, we used paired or unpaired t-tests, applying the Welch correction for unequal variances whenever the sample sizes were unequal. Every post-hoc tests are reported in the supplementary statistical table. Again, due to the overall low n number, the power is greatly affected, and the risk of type II error (false negative) is high. On the other hand, the nature of the t distribution with its heavy tails strongly reduces the risk of type I error (false positive). For this reason, we reported both the uncorrected and the Sidak corrected p-values (for multiple comparisons) in the supplementary post-hoc tables for the reader's own appreciation (**Table M3-M11**).

1. The 4D reference atlas of the developing CB

A dynamic coordinate cerebellar 3D framework over time to integrate and harmonize multimodal information is a masterpiece for the ultimate modeling of cerebellar development. The work of this thesis constitutes the first steps towards the generation of such framework: the 4D Cerebellar Framework (4D-CbF). The 4D-CbF is composed by annotated age-specific 3D references (3D-CbF) spanning from embryonic to adult stages (**Figure 1**). These include E11, E12, E13, E14, E15, E16, E17 and E18 for embryonic development (EDv), and P0, P7, P12, P21 and P56 for postnatal development (PDv) (**Figure 1A**). Thus far, we were able to complete the generation of 3D-CbF for E11, E12, E13 EDv stages and P7 PDv stage. EDv 3D-CbFs provide information for 3 M-L levels, 2 proliferative zones, 12 precursor/post-mitotic domains and 36 unique structures. The PDv P7 3D-CbF provides information for 3 M-L levels, 3 A-P regions, 1 cortical and 3 nuclear divisions, 15 subcortical divisions, 4 layer levels and 87 unique structures. The high resolution of the 4D-CbF largely surpasses the existing available resources, which lack anatomical and temporal detailed information for cerebellar developmental stages.

To do so, we designed a combination of whole organ clearing and 3D imaging experiments to obtain age-specific 3D templates together with an anatomical annotation workflow for building 3D structures and/or compartments (**Figure 1B, C**). Whole CPs for EDv stages and CB for P7 were dissected and immunolabeled with the nuclear staining To-PRO. Next, we cleared them using an adapted iDisco (Renier et al, 2014)[392] protocol. Light-sheet imaging was used to obtain a 3D reconstruction for each stage. These reconstructions were then used as 3D reference template to generate the age-specific 3D-CbFs. As shown in (**Figure 1B**), the 3D reconstruction of the E12 primordium and P7 CB allows accurate anatomical distinction of different compartments in the 2D planes, proving their utility as a template for structure annotation. Compartment annotation was done by 2D manual voxel labeling at the sagittal, coronal, and horizontal planes. Meticulous manual delineation of all structures at the left hemisphere of each reference, resulted in the generation of spatially located 3D labeled structures, all of which together composing a 3D-CbF. (**Figure 1C**).

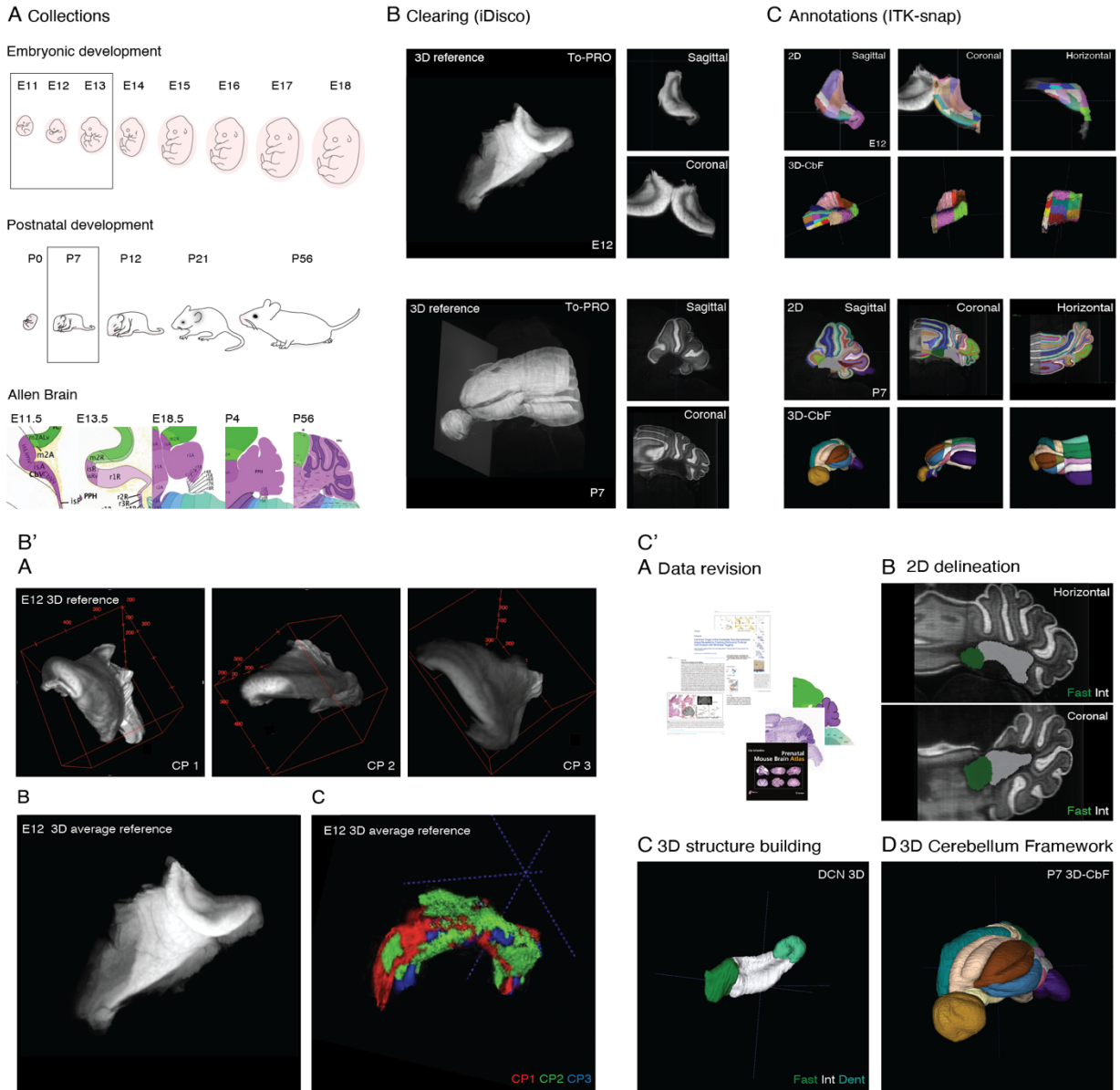


Figure 1. 4D atlas of the developing cerebellum. **A**) Schematic representation of collection time-points during embryonic (E11-E18) and postnatal development (P0, P4, P12, P21, P56). Representative images of available sources (Allen Brain). Notice the low annotation resolution. **B**) 3D Light-sheet image reconstruction of cleared E12 cerebellar primordium (upper panel, left) and P7 cerebellum (lower panel, left). Sagittal and coronal 2D views are shown (right). **C**) Generation of 3D age-specific cerebellar frameworks (3D-CbF). Compartments/structures of the developing cerebellum manually labeled at sagittal, coronal and horizontal 2D planes (upper boxes). 3D reconstruction of each compartment/structure (lower boxes). **B'**) The 3D average primordium template (A) 3D reference for 3 individual cerebellar primordiums (from left to right: CP1, CP2, CP3) at E12. (B) CP1, CP2, and CP3 3D average. (C) CP1 (red), CP2 (green) and CP3 (blue) overlap details. **C'**) Annotation workflow for building 3D structures. (A) Multisource data revision to define developmental time point specific structures/compartments. (B) 2D delineation of visible structures of the left hemisphere in each 3D reference template using ITK-snap. DCN delineation is shown. Fastigial (Green), Interposed (Gray). (C) 3D structure reconstruction obtained at the end of step B. 3D DCN reconstruction is shown. Fastigial (Green), Interposed (Gray), Dentate (Cyan). D) Voxel labelling is completed for all structures to obtain a 3D cerebellar framework (3D-CbF). 3d-CbF at P7 is shown.

1.1. The 3D average CP template

CPs anatomical simplicity makes it especially susceptible to individual variability. Aiming to increase the reliability of our EDv reference templates we generated a 3D average primordium of 3 individual reconstructions (CP1, CP2, CP3) at each stage (E11, E12, E13) (**Figure 1B'**). The 3D average template allows anatomical distinction CP compartment for an appropriated annotation and therefore, generation of 3D-CbF.

1.2. Annotation workflow for building 3D structures

For every developmental stage, we first reviewed relevant data from multiple sources, including available publications and atlases to define the appropriate reference compartmentalization (**Figure 1. C'A**). (Marzaban et al., 2015)[118] (Dastjerdi et al., 2012)[487] (Rahimi-Balaei et al.,2028)[488] (Tran-Anh et al., 2020)[268] (Martinez et al., 2013)[166] (Martinez et al., 2020)[489] (Wang et al., 2005)[206] (Lawton et al., 2019)[490] (Sillitoe et Joyner, 2007)[23] (McNeil et al., 2011)[491] (Sugihara, 2018)[164] (Ramon y Cajal, 1972) (Schambra, 2016) In order to match the dynamic evolution of the developing CB, we have defined 4 distinct compartmentalization trees (CT): (1) E11-E14, (2) E15-E17, (3) E18-P0 and (4) P7-P56 (see Material and Methods). CT1 (**Table M1**) and CT4 (**Table M2**) were used to generate the E12 and P7 3D-CbF respectively. We then delineated in 2D the visible structures on the left hemisphere of our templates using the medical annotating software ITK-snap (Yushkevich et al, 2006)[373]. In (**Figure 1C'B**) we can see a representative example of the P7 DCN 2D annotation in the horizontal and coronal plane. When the delineation along the whole z-stack was completed, the 3D reconstruction of the DCN was automatically generated. (**Figure 1C'C**). Delineation and 3D structure building for all the compartments was done to produce the P7 3D-CbF. (**Figure 1C'D**)

1.3. Automatic cell counting and 3D registration pipeline

As mentioned above, the 4D-CbF aims to serve as a framework for multimodal data integration. One of the main sources of data we consider for such integration is that coming from histology-based assays. In the context of this thesis, these assays include CP proliferation (section 2) and cell cycle dynamics analysis (section 3), fluorescence-based cell birth tracking (section 4) and cell marker

detection for specific population identification (section 6). All these modalities share the same sample processing workflow: collection, sectioning, labeling and imaging (See Material and Methods). This makes them particularly suited for optimal intermodality integration. So, during my thesis I participated in the generation of a 3D reconstruction pipeline from 2D serial sections which can be applied to all modalities aforementioned (**Figure 2**). In addition, the pipeline counts with an automatic cell segmentation step, thus significantly increasing the analytic throughput.

Our pipeline consists of four main steps: serial images acquisition, image segmentation, 3-CbF registration and 3D projection. By opting for 2D serial sectioning we achieve a $\approx 100\mu\text{m}$ resolution representation of the CP and/or CB through any of their axes (**Figure 2(1)**). The sections are then processed specifically depending on their experimental modality and imaged using different microscopy technologies including confocal, spinning disk and axioscan slide scanner. Automatic cell detection is based on StarDist image segmentation models (Schmidt et al., 2018)[492]. For a best fit with our images, we trained a new set of segmentation models for different signals and image resolutions. Namely, a nuclear segmentation model based on Hoescht signal for embryonic images and a high and a low image resolution model for fluorescent cell birth marker FITC segmentation at P7 (**Figure 2(2)**). Co-localization analysis with other markers is possible thanks to multichannel intensity detection. Next, individual images are registered to their corresponding age-specific 3D-CbF (**Figure 2(3)**). First, each section is manually mapped to the 3D-CbF to assign its specific location. Then, intensity-based (embryonic) and deformation/rotation landmark-based (postnatal) algorithms serve to accurately match experimental and reference sections anatomy. As a result, experimental images acquire the anatomic annotations information contained in the 3D-CbF. Moreover, this registration step assigns a specific 3D location to individual cells. At the end of the registration step, each detected cell has been assigned a (x,y,z) coordinate and can therefore be projected into the 3D-CbF (**Figure 2(4)**).

Overall, this progress represents a crucial milestone for an integrative understanding of cerebellar development. With the completion of the 4D-CbF, we hope to provide a master tool for increasing the temporal, spatial and modal resolution of cerebellar development.

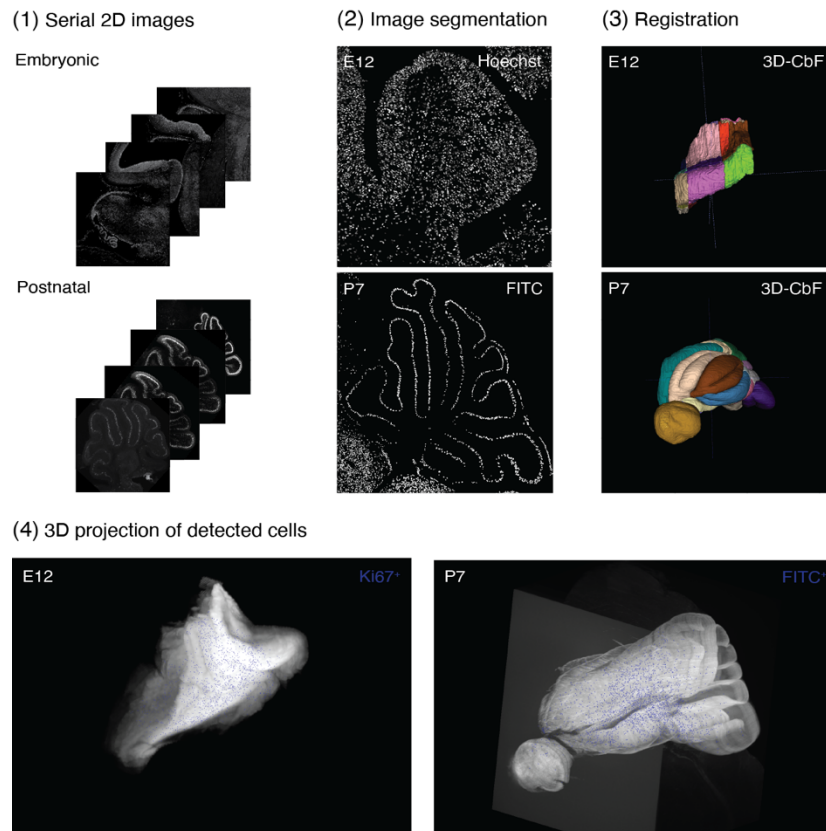


Figure 2. Automatic cell counting and 3D registration pipeline. Four major steps: (1) 2D serial sectioning for a M-L representation of the developing cerebellum. Sections from multimodal assays, including immunofluorescence and spatial transcriptomics, can be integrated. (2) Images are automatically segmented based on stardist trained models. Nuclear detection (Hoechst) for embryonic images, FITC detection for postnatal. Multichannel colocalization analysis are performed based on intensity. (3) 2D sections are registered to the age-corresponding 3D-CbF (3D reference brain + annotations). Each section is manually mapped to the corresponding 3D-CbF. (4) Detected cells are projected into the 3D-CbF (blue dots). Each cell has assigned (x,y,z) coordinates and anatomical location. Ki67⁺ cells projection at E12 (left). E13 FITC⁺ cells projection at P7 (right).

2. Spatio-temporal description of proliferation patterns in the CP

The CP sets the stage for cerebellar development. As a neurogenic tissue, it is highly dynamic and its structure evolves in parallel with development progression. As already discussed in the introduction, the CP is far from being an homogeneous structure. The well-established proliferative domains VZ and RL, are known to generate distinct cell types, to follow different temporal patterns and to have

their own molecular signature (Leto et al., 2016)[4]. Recently, increasing evidence points to the possibility of additional levels of heterogeneity within these structures, and also to the existence of other potentially defined proliferative domains. To further investigate this, here I used the proliferative marker Ki67 to specifically label proliferative cerebellar precursors (PCbP) through EDv.

2.1. Temporal patterns of proliferation in the CP

To identify and characterize temporal progression of cerebellar proliferative cells within the CP, developing WT embryos were collected from E11 to E15 and stained using the proliferative marker Ki67 (**Figure 3A**). As observed in (**Figure 3B**), Ki67 signal in sagittal sections of E11-E15 CPs revealed differences in proliferation dynamics within and across developing CPs.

Analysis on automatic cell segmentation data obtained using our pipeline demonstrate significant differences along the progression of proliferative cells within the CP in between ages (temporal progression) ($***p\text{-value}= 4.00 \times 10^{-18}$) (**Figure 3C**). As expected, a general decreasing tendency of proliferative cell proportion (Ki67⁺/Hoechst) along development (E11-E15) is observed. Interestingly, the decreasing tendency breaks at E15, where the proportion of proliferative cells rises up again. Therefore, suggesting that a switch on progenitors' dynamics might occur at that stage.

In addition, differences in proliferative cells proportion along the M-L axis were as well detected ($*p\text{-value} = 2.85 \times 10^{-2}$) within this developmental time window. Interestingly, the distinct M-L levels proliferative composition proved to be dependent on the EDv stage ($***p\text{-value}=1.52 \times 10^{-4}$).

2.2. Spatial patterns of proliferation in the CP

To further characterize the proliferative composition of the primary proliferative zones of the CP, VZ and RL, I took advantage of the E11, E12 and E13 3D-CbF we developed. Hence, automatic cell segmentation data from these EDv timepoints was registered into the corresponding 3D-Cbf, allowing detailed spatial identity to be taken into account.

2.2.1. Proliferation in the VZ

When looking at the temporal progression of proliferative cells proportion exclusively in the VZ, the analysis reveals significant differences over time (age effect $***p\text{-value}= 4.03 \times 10^{-5}$) (**Figure 3D, upper panel left**) (**Figure 3B, E11-E13**). While at E11 the proportion of proliferative cells in the VZ is $\approx 85\%$, at E13 it had decreased to $\approx 35\%$. Proliferative cells composition along the M-L axis proves

to be different between the distinct EDv stages (age effect *** p -value= 1.76×10^{-4}) (**Figure 3D, upper panel, right**). As observed in the graphic, E11 proliferative cells proportion is constant throughout the lateral, intermediate and medial level. However, at E12 a latero-medial gradient is noticed, with the medial part showing the highest proportion of proliferative cells. This gradient is then inverted at E13, where the proliferative cells proportion in the lateral level increases while it decreases in the medial.

2.2.2. Proliferation in the RL

Age-related differences in PCbP composition have been found as well in the RL (age effect *** p -value = 4.7×10^{-4}) (**Figure 3D, lower panel left**) (**Figure 3B, E11-E13**). The proportion of PCbP decreases from E11 to E12, and it rises again at E13. When looking at the spatial progression through the M-L axis, no significant differences have been detected between the distinct levels. However, the distribution of PCbP within the medial, intermediate, and lateral level over the distinct EDv stages seems to be significantly different (interaction age-space effect * p -value = 0.027).

Along with the previous observations, temporal, and spatial progression of PCbP in the VZ vs the RL were detected to be significantly different at E11 (VZ/RL effect * p -value= 0.0078), E12 (VZ/RL effect * p -value= 0.035) and E13 (VZ/RL effect * p -value= 0.008).

Altogether, this results support spatio-temporal differences of PCbP which might contribute to cerebellar diversity generation.

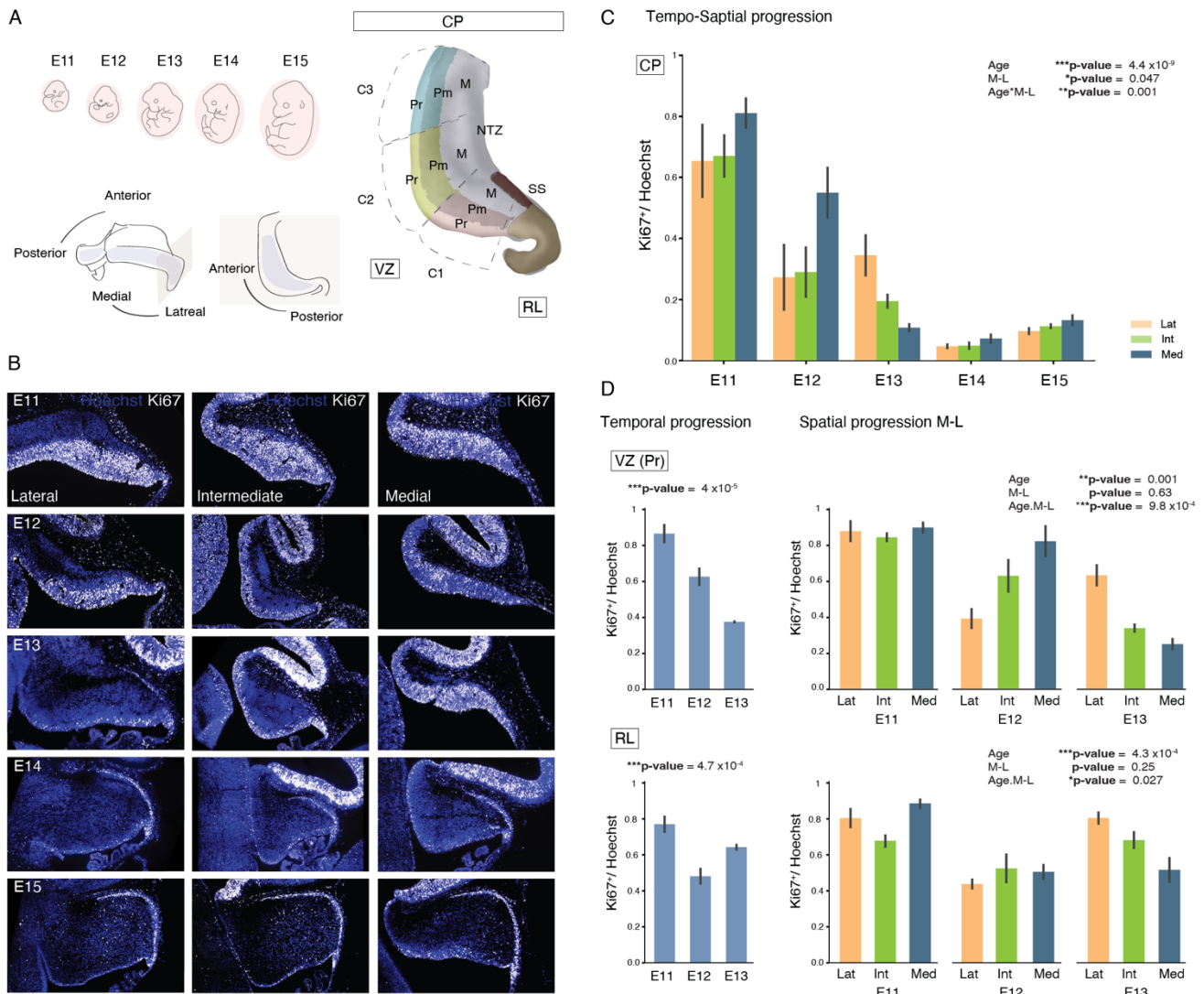


Figure 3. Proliferation patterns within the embryonic cerebellar primordium. **A**) Schematic representation of E11-E15 embryonic development (left, upper panel) and M-L/A-P axis of the CP (left, lower panel). Sagittal sectioning plan is shown in brown. (right) Representative atlas section of the cerebellar primordium (CP). Precursor (Pr, light), Post-mitotic (dark) and Mantle zone (M, grey) domains of C1, C2 and C3 compartments of the VZ are shown. Glutamatergic domains Rhombic lip (RL, brown), Subpial stream (SS) and Nuclear Transitory Zone (NTZ) are also indicated. **B**) CPs from E11 to E15 labeled with the proliferative marker Ki67 (white). Sagittal sections of Lateral, Intermediate and Medial levels are shown per each age. **C**) Proliferative cells (Ki67⁺) proportion over the total amount of cells in the CP at E11-E15. M-L (medial, blue; intermediate, green; lateral, orange) distribution of proliferative cells is shown per age (ANOVA, Age $F_{(4,10)} = 164.71$ *** p -value = 4.43×10^{-9} , M-L level $F_{(2,20)} = 3.56$ * p -value = 0.047, Age.M-L level $F_{(8,20)} = 5.2$ *** p -value = 0.001). **D**) (upper panel) Spatio-temporal analysis of proliferative cells within the VZ. (Left) Temporal progression of the proportion of progenitors (Ki67⁺/Hoechst) from E11 to E13 (ANOVA, Age $F_{(6,6)} = 84.53$ *** p -value = 4×10^{-5}). (Right) Spatial progression of the proportion of progenitors (Ki67⁺/Hoechst) through the M-L axis at E1, E2 and E3. Lateral (Lat), Intermediate (Int) and Medial (Med) levels are shown. (ANOVA, Age $F_{(2,5)} = 29.75$ *** p -value = 0.001, M-L level $F_{(2,10)} = 0.48$ p -value = 0.63, Age.M-L level $F_{(4,10)} = 11.33$ *** p -value = 9.8×10^{-4}) (Lower panel) Spatio-temporal analysis of proliferative cells within the RL. (Left) Temporal progression of proliferative cells proportion (Ki67⁺/Hoechst) in the RL from E11 to E13 (ANOVA, Age $F_{(6,6)} = 35.62$ *** p -value = 4.7×10^{-4}). (Right) Spatial progression of Ki67⁺/Hoechst cells through the M-L axis within the RL (ANOVA, Age $F_{(2,5)} = 52.8$ *** p -value = 4.3×10^{-4} , M-L level $F_{(2,10)} = 1.59$ p -value = 0.25, Age*M-L level $F_{(4,10)} = 4.33$ * p -value = 0.027). (**Suppl**) VZ vs RL temporal progression (ANOVA, Age $F_{(2,6)} = 44.4$ *** p -value = 2.5×10^{-4} , VZvsRL $F_{(1,6)} = 0.402$ p -value = 0.09, Age.VZvsRL $F_{(2,6)} = 560.1$ *** p -value = 1.5×10^{-7}). VZ vs RL spatial progression: E11 (ANOVA, M-L level $F_{(2,2)} = 9.08$ p -value = 0.1, VZvsRL $F_{(1,1)} = 6542.8$ * p -value = 0.0078, M-L level.VZvsRL $F_{(2,2)} = 5.9$ p -value = 0.14), E12 (ANOVA, M-L level $F_{(2,4)} = 4.58$ p -value = 0.092, VZvsRL $F_{(1,2)} = 26.75$ * p -value = 0.035, M-L level.VZvsRL $F_{(2,4)} = 6.2$ p -value = 0.059), E13 (ANOVA, M-L level $F_{(2,4)} = 10.67$ * p -value = 0.024, VZvsRL $F_{(1,2)} = 123.2$ * p -value = 0.008, M-L level.VZvsRL $F_{(2,4)} = 3.06$ p -value = 0.15).

3. Cell cycle dynamics of cerebellar progenitors is not equal across ages and areas within the CP

Having noticed that PCbP at different ages and locations undergo different spatio-temporal progressions, we then sought a distinctive molecular feature that could explain this variability. Thus, we decided to look at the cell cycle dynamics in different compartments of the CP at different EDv stages (**Figure 4**).

3.1. EdU/BrdU dual labeling of the CP

In order to assess cell cycle kinetics of cerebellar populations in developing embryos from E10 to E15, I applied an adapted protocol for dual thymidine analogue labeling using EdU and BrdU (Harris et al, 2018)[484]. Thymidine analogues are taken up by cells during S-phase acting as a proxy marker for cells currently at this phase of the cell cycle. Through the analysis of a population of cells progressing through S-phase, both S-phase duration and total cell cycle duration can be calculated. As represented in (**Figure 4A**), an intraperitoneal injection of EdU was given to the pregnant mouse at time-point (t_0). 1.5 h (injection time, T_i) subsequently, at time-point t_1 , a second intraperitoneal injection of BrdU was administered. The experiment was stopped 2h after the first injection. CPs were collected, sectioned at the sagittal plane from lateral to medial and immunolabeled for Ki67, BrdU and EdU. From this, it was determined: (a) cells that remained in S-phase for the duration of the T_i (S_{cells} , BrdU⁺EdU⁺) and (b) cells exiting S-phase during T_i (L_{cells} , EdU⁺BrdU⁻). S-phase duration (T_s) is calculated from the proportion of S_{cells} relative to L_{cells} adjusted per T_i . Cell Cycle duration (T_c) is obtained by the factorization of T_c with S_{cells} proportion relative to all proliferative cells in the cerebellar VZ (P_{cells} , Ki67⁺). Ki67⁺ cells, seen in red, correspond to all proliferative cells in the cerebellar primordium. EdU⁺ cells (grey) are detected by Click-it reaction while immunofluorescence is used to detect BrdU⁺ cells (green) (**Figure 4B-E**).

As perceived in **Figure 4F**, and correlating with the PCbP progression shown in the previous section, BrdU and EdU dynamics seem to differ not only across ages but also between the different compartments of the CP. Notice that at early EDv stages, BrdU⁺ and EdU⁺ cells are mainly located within the VZ and its derivatives. Yet, from E13, BrdU⁺ and EdU⁺ cells start to be more dominant in the RL and its derivatives, particularly in the Subpial Stream (SS). If we now pay closer attention to the VZ and its different compartments along the A-P axis (C1, C2 and C3), the representation of S_{cells} and L_{cells} seems to be constant within the same EDv stage.

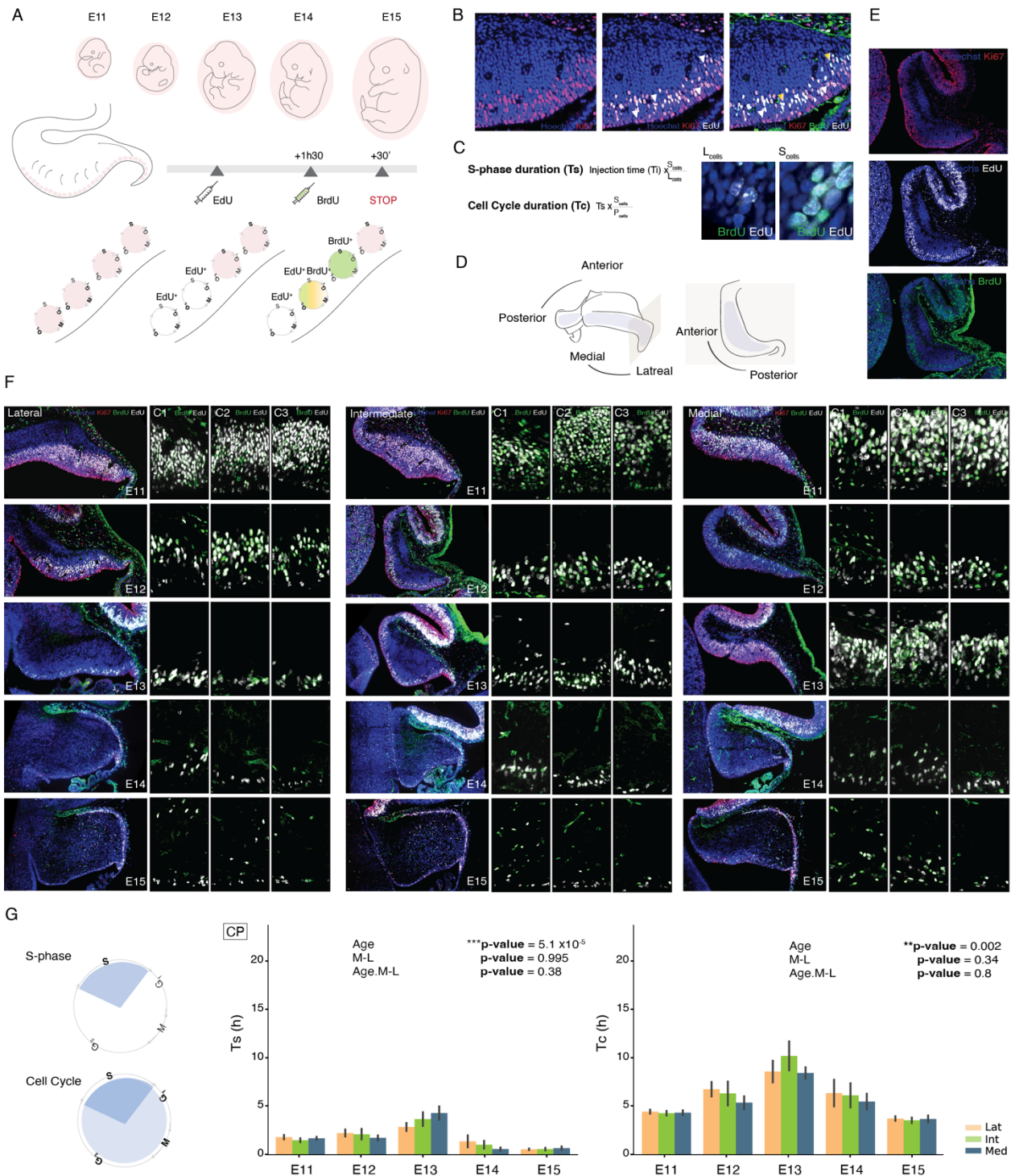


Figure 4. Spatio-temporal cell cycle dynamics in the CP. **A)** Schematic representation of EdU/BrdU dual labeling protocol. EdU is subadministered to developing embryos from E11 to E15. A BrdU pulse is given 1h30 after EdU injection. Embryos are collected 30 minutes after the last injection. **B)** Cells exiting (L_{cells} , EdU^+BrDU^-) and remaining (S_{cells} , EdU^+BrDU^+) in cell cycle during T_i are identified by immunofluorescence detection (BrdU, green) and Click-it reaction (EdU, grey). Proliferative cell population is also detected by immunofluorescence (Ki67, red). **C)** T_s and T_c calculation. **D)** Schematic representation of the A-P and M-L axis in the CP. Sagittal sectioning plan is shown in brown. **E)** E12 intermediate sagittal section labelling for Ki67 (red), EdU (gray) and BrdU (green). **F)** EdU/BrdU dual labelling (Ki67+ cels (red), BrdU (green), EdU (gray)) through the M-L axis (Lateral, Intermediate and Medial) of embryonic ages E11-E15 CP. High-magnifications of C1, C2 and C3 VZ compartments are shown. **G)** S-phase length (T_s) (ANOVA, Age $F_{(4,10)} = 22.8$ $**p\text{-value} = 5.1 \times 10^{-5}$, M-L level $F_{(2,20)} = 0.01$ $p\text{-value} = 0.995$, Age.M-L level $F_{(8,20)} = 1.14$ $p\text{-value} = 0.38$) and Cell cycle length (T_c) (ANOVA, Age $F_{(4,10)} = 9.4$ $**p\text{-value} = 0.002$, M-L level $F_{(2,20)} = 1.12$ $p\text{-value} = 0.34$, Age.M-L level $F_{(8,20)} = 0.55$ $p\text{-value} = 0.8$) bar plots for Lateral (Lat, orange), Intermediate (Int, green) and Medial (Med, blue) levels of the CP from E11-E15.

3.2. Spatio-temporal cell cycle dynamics in the CP

Using the automatic cell detection pipeline together with an additional manual verification and optimization step, I first investigated cell cycle dynamics in the whole CP from E11 to E15 (**Figure 4G**). Consistent with previous studies (Cremisi et al., 2003)[493] the analysis reveals a significant variation of Tc over time (age effect $***p\text{-value} = 3.23 \times 10^{-7}$), therefore suggesting a time-dependent progression of the cell cycle in the CP. As observed in the graph, Tc increases from E11 to E13, followed by a decreasing tendency at E14-E15. These differences might explain the emergence of cerebellar cellular heterogeneity. Besides this age-related variability, Tc does not appear to be different between different M-L levels in the distinct EDv stages, neither across them, as the absence of interaction effect seem to show.

To further evaluate the specific spatio-temporal cell cycle dynamics of GABA- and glutamat-ergic progenitor cells in the CB, E11-E13 data were registered to the corresponding 3D-CbF so the spatial identity could be assigned. We first checked for Tc temporal dynamics similarities and differences within the different areas of the CP over time. To do so, we used principal component analysis (PCA). Each area (point in the plot) was defined by its value of Tc at E11 (1D), E12 (2D) and E13(3D), therefore reducing 3 Tc values (mean of 3N) to 2 components. As observed in **Figure 5B**, PCA analysis for Tc dynamic similarity revealed higher similarity between VZ-derivate structures (C1, C2, C3 – Precursor (Pr), Post-mitotic (Pm), Mantel zone (M)), while RL-derivate structures (Subpial stream (SS) and Nuclear transitory zone (NTZ)) dynamics seem to diverge not only from VZ but also between them. I then focused my analysis into the precursor zone (Pr) of the C1, C2 and C3 compartments of the VZ, and the RL (**Figure 5G**). Tc temporal progression inspection at the VZ (Pr) and RL from E11 to E13, suggests common Tc increase, in concordance with the dynamic observed in the whole CP (**Figure 5C**). Yet, this variation over time was significant only for VZ (Pr) (age effect $*p\text{-value} = 0.017$), most likely due to high technical-derived variability (registration, cell segmentation). Spatial progression of Tc was likewise investigated in both VZ (Pr) and RL (**Figure 5C, D**). In concordance with our PCA results, no significant differences appear neither along the M-L nor the A-P.

Altogether, these results support the temporal variability of cell cycle during development, along with spatio-specific dynamics between the VZ and the RL. Both temporal and spatial components might contribute to cell heterogeneity generation during cerebellar development.

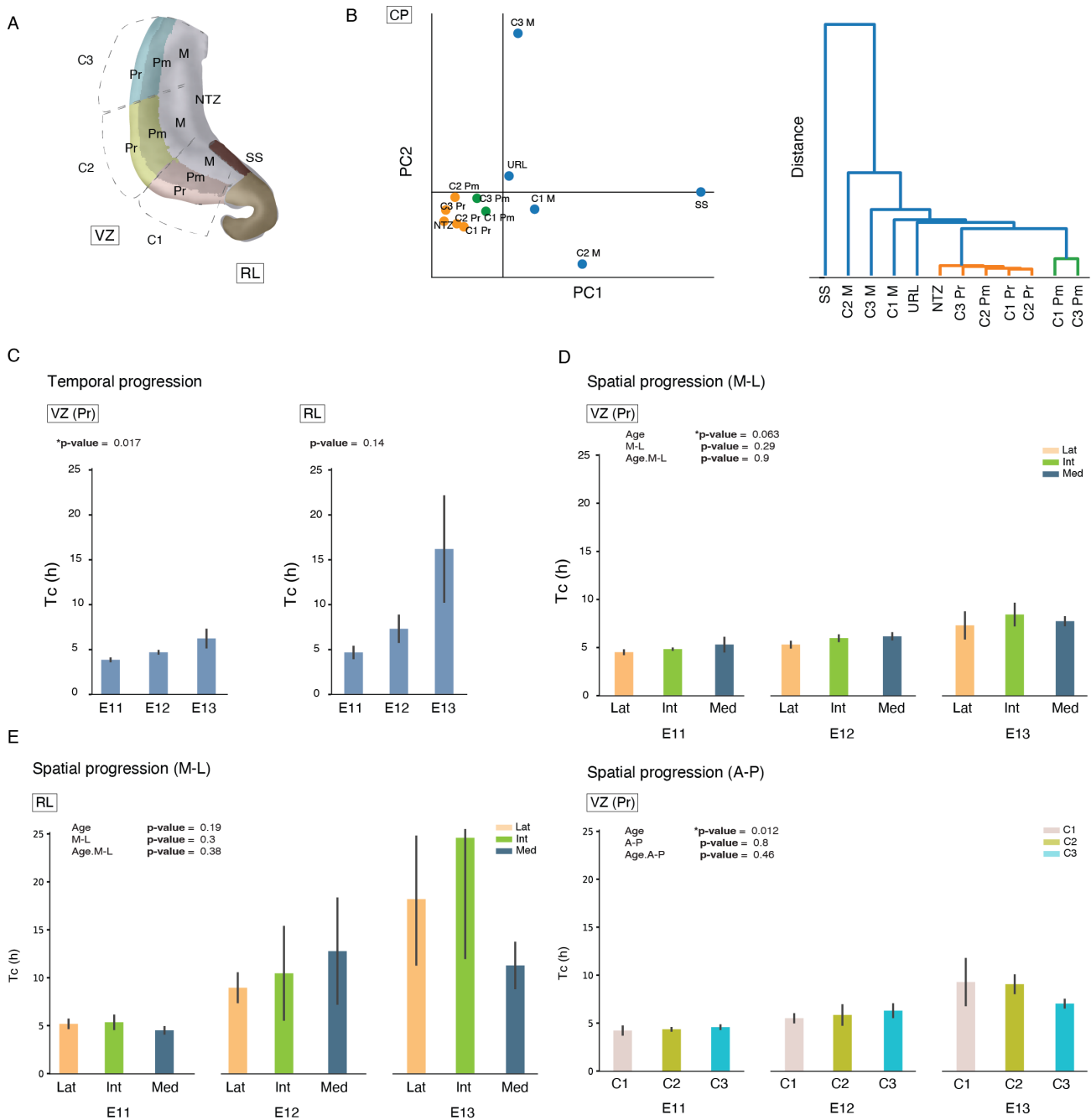


Figure 5. Spatio-temporal cell cycle dynamics of GABA- and glutamatergic progenitor cells. **A**) Representative atlas section of the cerebellar primordium (CP). Precursor (Pr, light), Post-mitotic (dark) and Mantle zone (M, grey) domains of C1, C2 and C3 compartments of the VZ are shown. Glutamatergic domains Rhombic lip (RL, brown), Subpial stream (SS) and Nuclear Transitory Zone (NTZ) are also indicated. **B**) Principal component analysis (PCA) for CP subcompartments spatio-temporal Tc dynamics similarity. **C**) Temporal progression of Tc (h) from E11 to E13 in the precursor zone of the VZ (VZ (Pr), left) (ANOVA, Age $F_{(6,6)}=8.5$ * p -value=0.017) and RL (ANOVA, Age $F_{(6,6)}=2.7$ p -value=0.144). **D**) Spatial progression of VZ Tc at E11, E12 and E13 along the medio-lateral (M-L) (ANOVA, Age $F_{(2,5)}=6.88$ * p -value=0.036, M-L level $F_{(2,10)}=1.4$ p -value=0.29, Age.M-L level $F_{(4,10)}=0.21$ p -value=0.9) and anterior-posterior (A-P) (ANOVA, Age $F_{(2,6)}=9.98$ * p -value=0.012, A-P level $F_{(2,12)}=0.22$ p -value=0.8, Age.A-P level $F_{(4,12)}=0.95$ p -value=0.46) axis. **E**) Spatial progression of RL Tc at E11, E12 and E13 along the medio-lateral (M-L) (ANOVA, Age $F_{(2,5)}=2.28$ p -value=0.19, M-L level $F_{(2,10)}=1.34$ p -value=0.3, Age.M-L level $F_{(4,10)}=1.15$ p -value=0.38) (Suppl) VZ vs RL temporal progression (ANOVA, Age $F_{(2,6)}=5.3$ * p -value=0.047, VZvsRL $F_{(1,6)}=2.43$ p -value=0.17, Age.VZvsRL $F_{(2,6)}=1.3$ p -value=0.34). VZ vs RL spatial progression (M-L): E11 (ANOVA, M-L level $F_{(2,2)}=1.76$ p -value=0.3, VZvsRL $F_{(1,1)}=0.31$ p -value=0.67, M-L level.VZvsRL $F_{(2,5)}=28.7$ * p -value=0.033), E12 (ANOVA, M-L level $F_{(2,4)}=0.21$ p -value=0.8, VZvsRL $F_{(1,2)}=4.51$ p -value=0.16, M-L level.VZvsRL $F_{(2,4)}=0.11$ p -value=0.9), E13 (ANOVA, M-L level $F_{(2,4)}=1.55$ p -value=0.3, VZvsRL $F_{(1,2)}=2.73$ p -value=0.24, M-L level.VZvsRL $F_{(2,4)}=1.5$ p -value=0.32).

4. FT allows for the labeling and tracking of cerebellar progenitors from embryonic to perinatal stages

So far, our observations point towards a time effect during cerebellar development. At different EDV stages, progenitors' populations seem to be present in different proportions and localizations, as well as follow different cellular dynamics as observed for the cell cycle. To better characterize the role of time in cerebellar mechanisms development we thought to track specifically time-locked cohort of cells.

The main limitation for the study of the distinct pathways underlying cerebellum development is the challenging ability to track specific neuronal subpopulations as they define their cellular fate. The classical birth dating techniques have specific limitations (Hashimoto et al., 2003)[494]: no spatial restriction within a defined structure (BrdU and other thymidine analogues), no temporal restriction (*in utero* electroporation, not only cells in a specific time-point will be labelled, but also some of the progeny will be labelled) and delay in reporter expression (viral labeling, *in utero* electroporation). To circumvent these limitations, we use a fluorescence-based birth dating technique: Flash Tag (FT). (Telley et al., 2016)[238].

4.1. Flash Tag labeling of newborn cells in the developing CB

FT allows to specifically label spatially defined isochronic cohorts of cell cycle phase-locked (M-phase) progenitors, by the *in-utero* injection of the short-life fluorescent dye carboxyfluorescein ester (CFSE) into the ventricular system. The short extracellular half-life of FT in the mouse ventricular space has been shown to ensure effective pulse-labeling of juxtaventricular dividing cells in the developing neocortex (Telley et al., 2016)[238]. Intracellularly, FT is linearly diluted at each mitosis, such that fluorescence intensity can be used as a proxy for cell division number since the time of injection. Mitotic progenitor cells closely located on the ventricular surface uptake FT, becoming fluorescently labeled (FT⁺) (**Figure 6A and B**). As observed in (**Figure 6B**), FT injected in the third ventricle at E12 is effective for cerebellar progenitor cohort labelling (FT⁺, arrowheads). FT⁺ cells are still laying close by the ventricular wall 1h after the injection and co-localization with the M-phase marker phospho-histone 3 (PH3) is detected. Cerebellar progenitors labeled at E12 are tracked 1h, 6h, 24 h and 96h after the injection in the CP (**Figure 6C**). Notice that FT⁺ cells in each collection time-point, display different locations within the cerebellar primordium. E12 FT +1h, +6h are located still close to the VZ, while +12h, +24h, +96h are placed in more apical regions. The gradual progression

of FT⁺ cells correlates to precursor cells migration behavior in cerebellar development, proving FT ability to track progenitor cells as they advance in the developing cerebellum. FT⁺ cells are detected in the P7 cerebellum using anti-FITC antibody, proving that cerebellar cells can be tracked until perinatal stages.

4.2. Flash Tag validation in the CB

To further validate the FT potential to specifically label and track cerebellar progenitors over development along the whole CP, FT was injected into the third ventricle of E11 developing embryos and collected at 1h, 12h and 24h after the injection. Serial coronal sections spanning the A-P axis of the CP were generated to obtain a representation of the whole primordium. Sections were stained for Ki67 and PH3 for specific targeting of proliferative and mitotic cells, respectively, in the CP (**Figure 6D**). As previously shown for E12, cells labeled at E11 (FT⁺) are detected 1h, 6h, 12h and 24h after the injection (**Figure 6E**).

Co-localization with PH3 and Ki67 seems to be different over time after injection. At +1h, PH3⁺ cells, in contact with the ventricular wall, co-localize with FT, indicating that mitotic cells are certainly uptaking FT. In addition, all FT⁺ cells do co-localize with KI67 at that moment, indicating that they are indeed in a proliferative state. Still at this first time point, we can notice at both A-P levels, FT cells are still in tight contact with the ventricular wall. 6h after injection, we can see that FT⁺ cells have migrated inwards the CP, not being anymore in contact with the ventricular wall. With it, the amount of PH3⁺ FT⁺ cells had greatly decreased. Yet, FT⁺ cells at that stage still co-localize with Ki67, indicating that they are still proliferating. At +12h, FT⁺ cells had notably advanced towards even more apical positions in the CP. Almost no PH3⁺ FT⁺ cells are detected. This shows that mitotic cells FT uptake ceased, supporting again the time restricted labeling power of FT. Moreover, some apical Ki67⁺FT⁺ cells are detectable at this time, indicating that they stopped proliferating. This last observation becomes even more evident at + 24h after injection. Interestingly, at +12h and +24h after injection few FT⁺PH3⁺ cells close to the ventricular wall can be spotted. This might correspond to the secondary round of division that some of the labeled progenitors undergo. Finally, our data suggest differences in FT⁺ progression along the M-L axis. Lateral portions of the CP seem to show higher migration rates than medial ones (Notice that sections are in the coronal plane. Lateral levels of the CP correspond to the right part of the image, while medial, to the left).

Altogether, these observations support the ability of FT for tracking specific time-locked cohorts of cells within the CP along the cerebellar development.

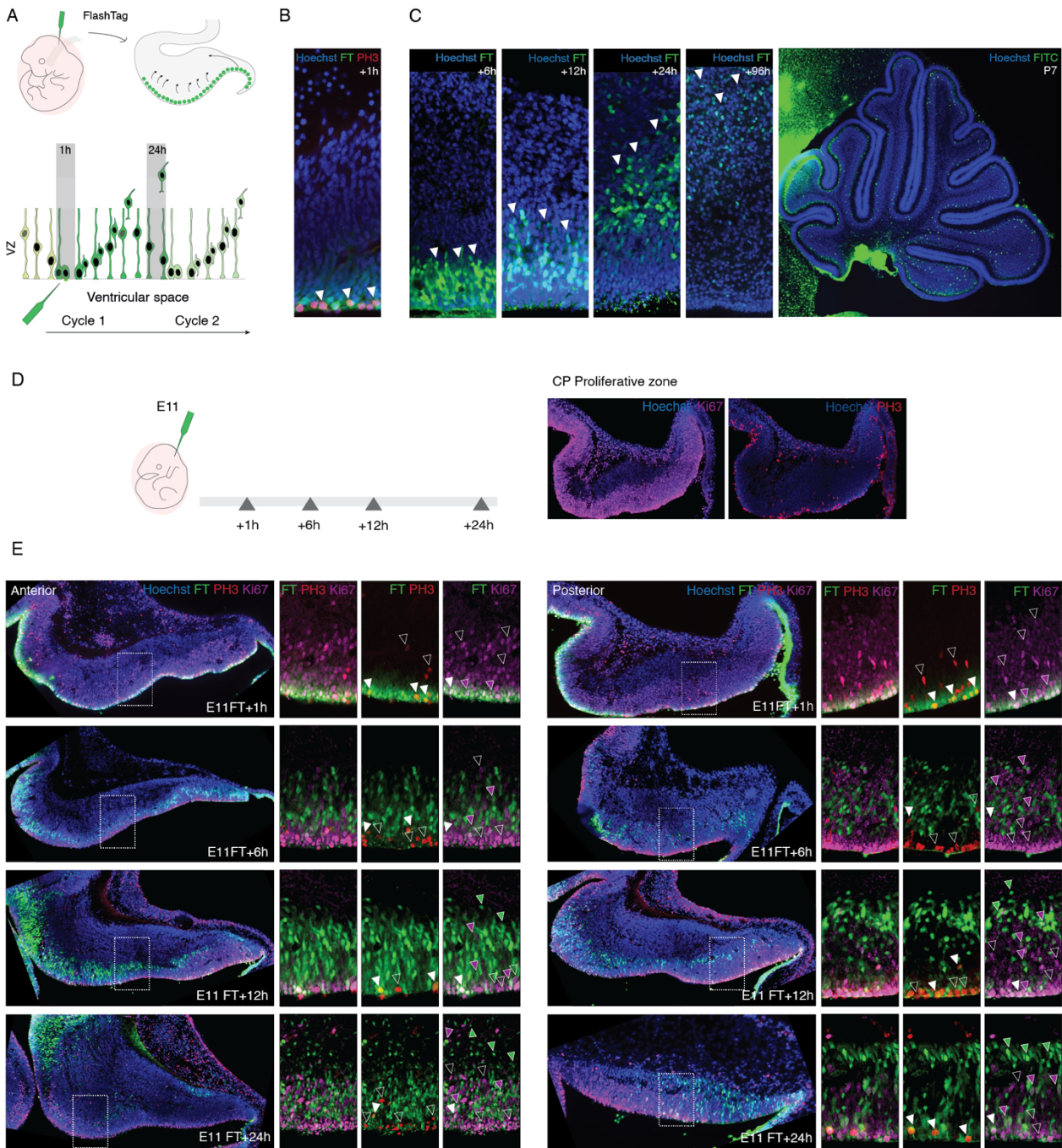


Figure 6. FlashTag (FT) labeling of new born cells in the developing cerebellum. **A)** FT injection in the third ventricle during embryonic stages results in the spatially-defined labelling of cerebellar cells. Progenitor cells located in the VZ are characterized by an interkinetic nuclear migration during cell division: mitosis is a focal event which occurs apically in the VZ whereas S-phase occurs at a basal position. Progenitor cells closely located to the ventricular surface uptake FT, becoming fluorescently labeled. (Adapted from Telley et al., 2016) **B)** E12 FT cell cohort (green) 1h after injection. Mitotic cells (PH3+, red) laying on the 4th ventricle wall were labeled with FT in the moment of the injection. **C)** E12 FT cell cohort (green) tracking 6h, 12h, 24h and 96h after injection and P7 cerebellar vermis. **D)** FT validation in the CP. Schematic representation of the experimental procedure. E11 embryos were injected with FT and collected +1h, +6h, +12h and +24h after injection. Proliferative and mitotic cells in the CP were identified using Ki67 (purple) and PH3 (red), respectively. **D)** Sagittal sections of Anterior and Posterior E11 FT (green) injected CP and collected at the different collection time points. Higher magnifications of discrete portions of the CP are shown. Arrowheads indicate cells expressing Ki67 or PH3 exclusively (empty arrowhead), Ki67 or PH3 together with FT (purple or white filled arrowhead, respectively) or Ki67, PH3 and FT (white filled arrowhead).

5. Cerebellar progenitors birth date seems to influence their migration rate and pathway within the CP

To further investigate the spatio-temporal differences of cerebellar progenitors, we injected FT to E11, E12, E13, E14 and E15 embryos and collected them after 24h (**Figure 7A**). Observe an A-P representation for the CP at each of the collections in **Figure 7C**. FT⁺ cells are detected in green.

The total amount of cells generated at each time does not seem to differ over time. Yet, a diminution seems to be spotted at E14. How this is due to sample variability or level representation, remains to be seen. As previously observed, FT injected cells migrate inwards the CP with time, heading to their final destination. Interestingly, our observations suggest that this migration occurs in a different manner over time. While E11 generated cells are located in more apical positions, E12 and E13 cells are still located closer to the ventricular wall. This suggests a decrease of migration rate from E11 to E13. Interestingly, the tendency seems to shift again at E14 and E15. These observations correlate with our cell cycle analysis, where T_c was increasing from E11 to E13 and then decreasing again at E14-E15.

Spatially, some differences can be observed along the M-L and the A-P axes. However, further analysis using our pipeline in combination with whole brain IF of cleared brains are required for a better understanding.

Overall, our primary results suggest spatio-temporal dependent cell generation in the CP. Cells born at different ED_v stages would display distinct migration behaviors which could ultimately be linked to fate determination variability.

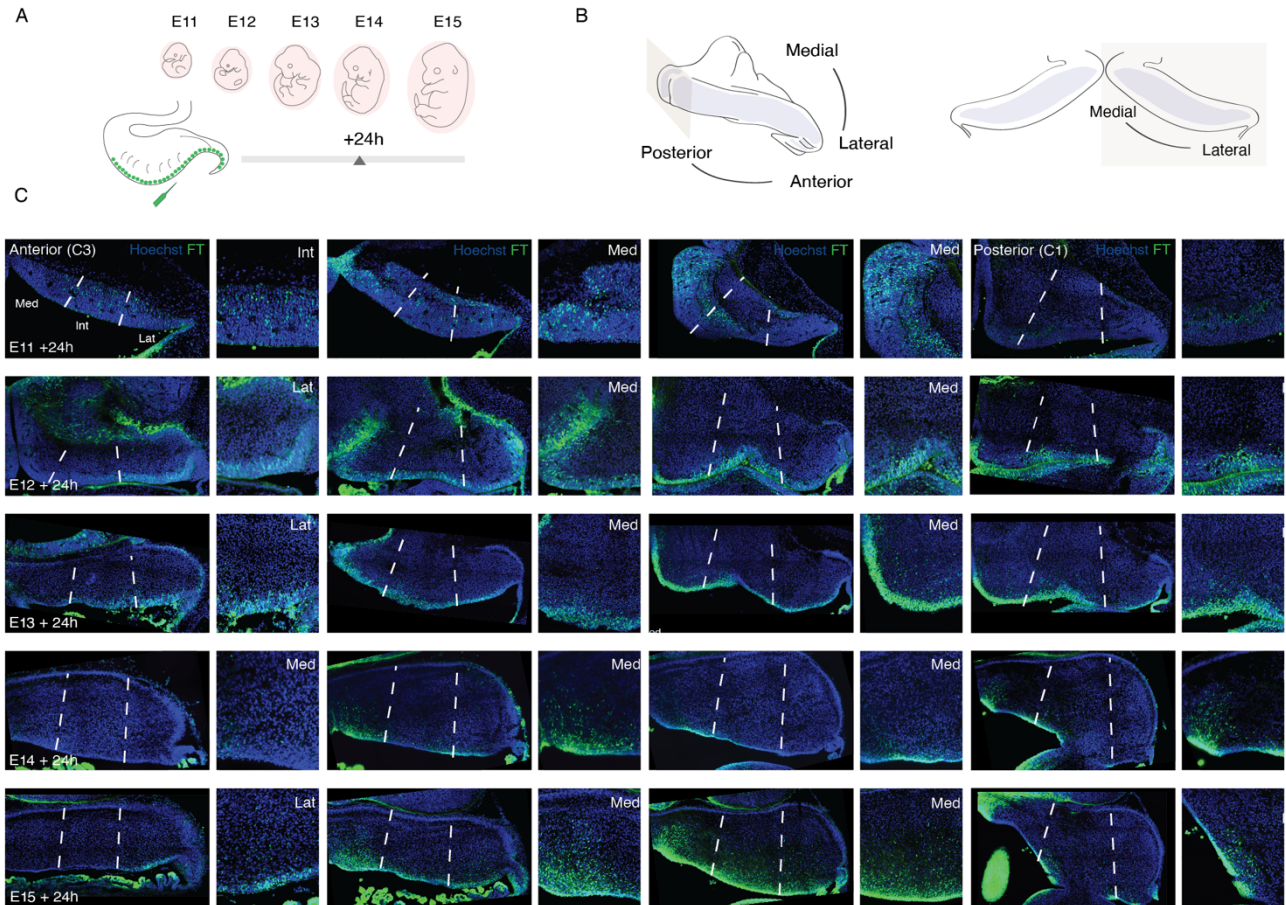


Figure 7. Cell birth in the CP A) Schematic representation of the experimental procedure. E11, E12, E13, E14 and E15 embryos were injected with FT and collected +24h after injection. FT⁺ cells in the CP were tracked along the A-P/M-L axis. B) Schematic representation of the A-P and M-L axis in the CP. Coronal sectioning plan is shown in brown. C) Anterior to posterior (C3>C2>C1) coronal sections of E11-E15 injected CP. FT⁺ cells were detected by endogenous FT signal (green). M-L levels are delineated (dashed line). Med (medial), Int (intermediate), Lat (lateral).

6. Cell birth Flash Tag analysis reveal identity- and spatio- temporal correlations in the P7 cerebellum

To specifically label isochronic cohorts of cells along cerebellar development and characterize the different cellular populations along the M-L axis, FT was injected in the third ventricle of developing embryos each day from E11 to E16, and collected at PDv day 7 (P7)(**Figure 8**). Due to the weak endogenous fluorescence of FT at P7, we performed immunofluorescent detection of FT⁺ cells using anti-FITC (green).

6.1. Cerebellar cells birth date influences their anatomical position in the P7 cerebellum

FT proved to be efficient in tracking directly born progenitors during embryonic cerebellar development and shed light on spatio-temporal differences in cerebellar progenitors' dynamics. Also, as observed in (**Figure 3**), proliferative activity in the CP is dependent on time and space. How all this variability is projected at later stages of the development, when cell types and cerebellar structures are already well-defined, is still an open question.

To investigate that, FT was injected at EDv stages E11, E12, E13, E14, E15 and E16; and collected at P7. For each collection, serial sections spanning from lateral to medial were generated in order to have a continuous representation of the M-L cerebellar axis. As previously seen in **Figure 6C** for E12, in **Figure 8A** we observe that FT⁺ cells are detectable at P7 for all injection timepoints. Immunofluorescence detection of FT⁺ was performed and our images were processed using our automatic cell segmentation and registration pipeline.

As observed in **Figure 8C**, FT⁺ cell distribution hints at a differential pattern along the M-L axis correlating with the cell generation time-point. Aiming to thoroughly explore this potential cell birth date dependent pattern, we took advantage of our registration pipeline and the previously described P7 3D-CbF. We first looked at the temporal progression of FT⁺ cells in the whole CB. As observed in **Figure 8D**, the contribution of each EDv stage cell generation to the total number of cells tracked (total FT⁺ cells) from E11 to E16 appears to be constant (E11 19.4%, E12 14%, E13 17.5%, E14 19.4%, E15 14.5%, E16 15.3%). These results match our previous observations during embryonic stages.

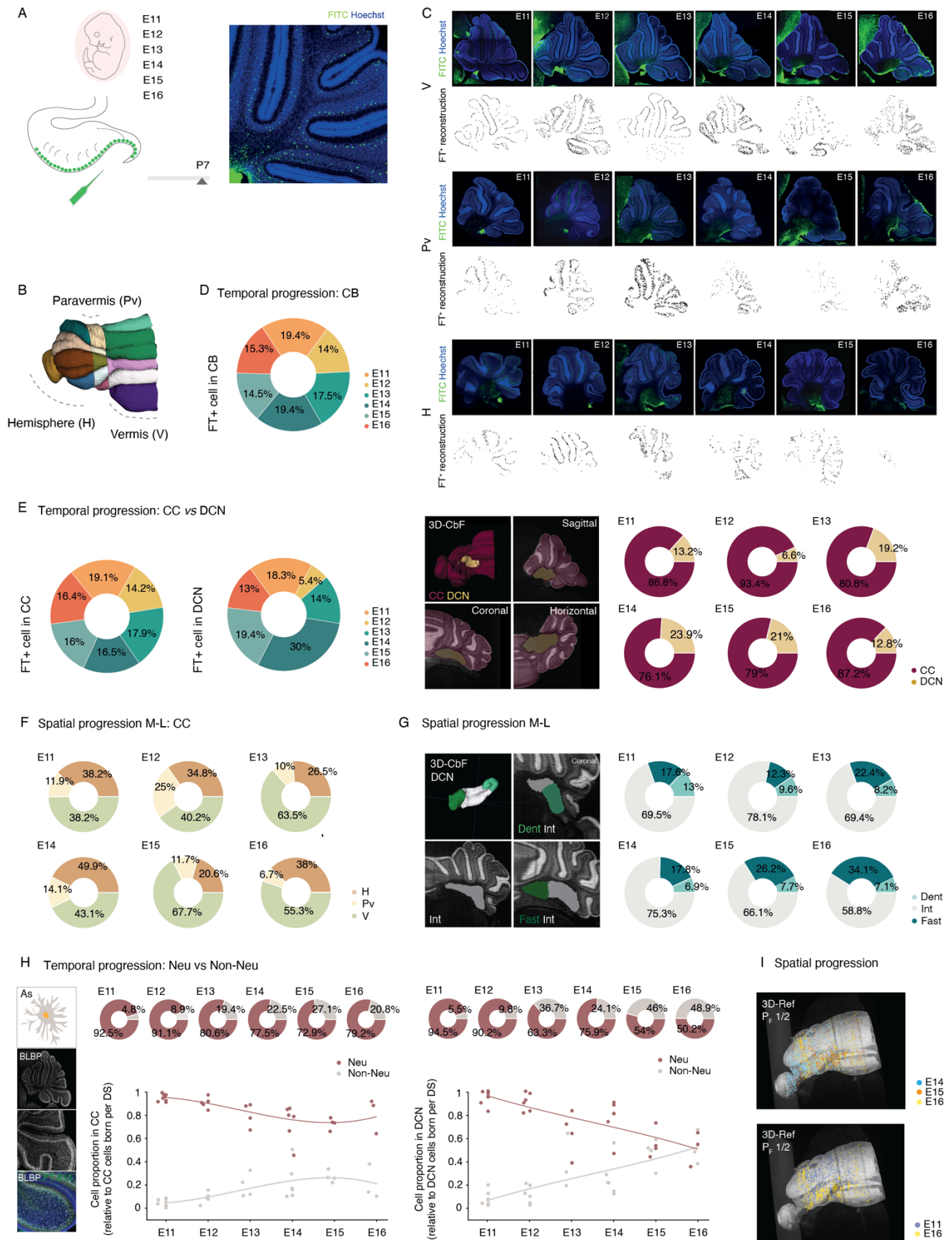


Figure 8. Cell cohort tracking in P7 cerebellum along the medio-lateral axis. (See legend on next page)

Figure 8. Cell cohort tracking in P7 cerebellum along the medio-lateral axis **A)** Schematic representation of the experimental procedure. **B)** Medio-lateral levels representation in the P7 3D-CbF (coronal view). **C)** P7 Vermis, Paravermis and Hemisphere sagittal sections of E11-E16 injections. FT⁺ cells are detected with anti-FITC (green). FT⁺ cells manual counting reconstructions shown below each corresponding image. **D)** Pie plot showing the temporal progression (from E11 to E16) of FT⁺ in the P7 CB. **E)** Pie plot showing the temporal progression (from E11 to E16) of FT⁺ in the P7 cerebellar cortex (CC, right) and deep cerebella nuclei (DCN, left). Representative P7 3D-CbF and 2D sagittal, coronal and horizontal view of CC (violet) and DCN (light brown). Cerebellum (CB = CC + DCN). Pie-plots displaying CC and DCN cell generation proportions at E11, E12, E13, E14, E15 (relative to the total FT⁺ cells at each age) **F)** Pie plots showing FT⁺ cells spatial progression through the CC medio-lateral (M-L) axis at E11, E12, E13, E14, E15 and E16. Hemisphere (H), Paravermis (Pv), Vermis (V) **G)** Representative P7 3D-CbF and 2D Coronal a view of DCN: Dentate (Dent, blue-green), Interposed (Int, gray), Fastigial (Fast, green). Pie-plot displaying Dent, Int, and Fast nuclei cell generation proportion at E11, E12, E13, E14, E15 (relative to the total DCN cells at each age). **H)** Neuronal (Neu, BLBP⁺) and non-neuronal (Non-Neu, BLBP⁻) temporal generation dynamics in the CC (upper panel) and DCN (lower panel). In each panel: Pie-plot showing Neu and Non-Neu (Astrocytes, As) cell generation proportion at E11, E12, E13, E14, E15 (relative to the total CC (upper) or DCN (lower) cells at each age). Progression plot showing Neu and Non-Neu cells generation tendency from E11 to E16. **I)** 3D-Ref cell projection. Projection Factor (P_p , 3D-ref projected cells = total detected cells * P_p).

6.1.1. Temporal cell birth progression of DCN vs CC

Thanks to our registration pipeline and the accurate generation of the P7 3D-CbF, we were then able to look at specific spatial components of the CB and its cell generation dynamics. This first level of a FT⁺ cells classification (LI), aimed to identify the contribution of each EDv stage cell generation to the total number of FT⁺ cells either in the CC or the DCN. To do so, all FT⁺ cells detected at each timepoint were classified according to their anatomical position (**Figure 8E, middle panel**). As noticed in **Figure 8E (left panel)**, FT⁺ cells in the CC are constantly generated from E11 to E16 (E11 19.1%, E12 14.2%, E13 17.9%, E14 16.5%, E15 16%, E16 16.4%), pointing that the different studied EDv stages have the same contribution in CC cells generation. In contrast, FT⁺ contribution to the DCN cells generation over time, varies in a time-dependent manner (E11 18.3%, E12 5.4%, E13 14%, E15 30%, 19.4%, E16 13%). Yet, DCN cell production is tracked without interruption from E11 to E16. Indeed, differential cell generation ratios CC vs DCN at given EDv stage were detected (**Figure 8E (left panel)**). Generally, CC cells generation proportion is greater than that of DCN at all EDv stages (CC 76.1-93.4%, DCN 23.9-6.6%), matching their anatomical differences in size. Still, DCN cells generation proportion increases from E13 to E15 (19.2%, 23.9% and 21%, respectively), going back down at E16 (12.8%). Altogether, these results indicate a constant tendency of CC and DCN generation, although an increase in DCN cells generation proportion is noticed in later ages.

Referring to my previous point, differences along the M-L axis seem to appear for FT⁺ cells distribution. To investigate that, we first looked at the M-L progression of cell generation in the CC (**Figure 8F**). Cortical FT⁺ cells detected at each developmental stage were classified depending on their anatomical position in the M-L axis into H, Pv and V. Then, the contribution of FT⁺ cells at each EDv stage to generate the H, Pv and V was calculated. As suspected, the contribution of FT⁺ to the

generation of the different structures differs in all EDv stages, most likely due to the difference in size between the structures. Interestingly, the proportions are not constant throughout the development. Next, we checked at the M-L progression of DCN generation (**Figure 8G**). As already described in the introduction, in rodents we can distinguish 3 nuclei from lateral to medial: Dent, Int (which is divided in its anterior and posterior parts) and Fast. To assess the spatial progression of DCN generation, we checked for the proportion of FT⁺ cells in the DCN at each time point that contribute to the generation of each of the nuclei. Notice that all DCN are always being generated from E11 to E16. Differences in nuclei generation proportions are detectable in all ages. Int generation contribution is greater in all ages (58.8% - 78.1%), correlating to the bigger size of this nucleus. Interestingly, the highest production of Dent cells is observed at early ages (E11 13%, E12 9.6%), while Fast cells, at later ages (E15 28.8%, E16 34.1%). Therefore, suggesting a latero-medial generation of the distinct DCN over time.

6.1.2. Neuronal vs non-neuronal cells generation in the CC and the DCN

CB sophisticated structure and functionality does not only rely on a great heterogeneity of neuronal cell population, but also on non-neuronal cells like astrocytes, oligodendrocytes, and microglia. Thus, in our next level of analysis (LII) we determined the proportion of neuronal and non-neuronal cells generated at the different EDv stages, in both CC and DCN (**Figure 8H**). To assess the temporal birth of neuronal and non-neuronal populations, all detected FT⁺ cells in each EDv stage were checked for co-localization with the astrocytic marker BLBP. The proportion of neuronal and non-neuronal cells generated at E11, E12, E13, E14, E15 and E16 (relative to the total amount of FT⁺ cells in each EDv stage) is shown in **Figure 8H (left, CC; right, DCN)**. Notice that neuronal generation proportion displays higher values than non-neuronal generation in all EDv stages, for both CC and DCN. Interestingly, an increasing tendency of non-neuronal cell generation can be observed overtime, especially in the DCN. In the case of the CC, while at E11 the generation proportion of neuronal cells is 4.8%, at E16 it represents 20.8%. In the DCN, the increase is higher: from a 5.5% at E11 to a 48.9% at E16. Hence, our results indicate that although the generation of non-neuronal cells is lower than that of neuronal cells throughout development, a time-dependent increase for non-neuronal development does occur. SOX10 oligodendrocyte marker co-staining with FT was as well performed. However, we did not observe any co-localization for both markers, supporting the extra ventricular origin of oligodendrocytes.

Spatial analysis of non-neuronal cells generation distribution along the M-L axis indicates a mild lateral to medial generation from E14 to E16, ages where the production of non-neuronal cells is higher. (**Figure 8I**) However, when comparing the distribution along the M-L axis during the whole developmental window, no special spatial distribution pattern is noticed in that axis (upper image). Interestingly, as seen in **Figure 8I** (lower image), non-neuronal cells generated at E11 are located in anterior positions of the CB, while E16 generated cells, in more posterior positions. This observation matches with the later EDv stages generation of non-neuronal DCN cells (located towards the posterior part of the CB).

Comprehensively, these results demonstrate the ability of FT to track directly born cells from embryonic development to postnatal stages. FT cells production appeared to be more or less constant over time. Interestingly, interaction between time of generation and space seem to be key for cerebellar development and spatial heterogeneity in both CC and DCN.

6.2. Cerebellar cortical neuronal cells populations temporal birth

In our next level of FT⁺ cells analysis (LIII), we focused exclusively on the CC and its neuronal populations generation (**Figure 9A**). To do so, FT⁺ neuronal CC cells at each age were classified using a battery of markers (*population marker*): CALB for PCs, PAX2 for immature Gis, TBR2 for UBCs, CALRET labeling LCs but also UBCs, NRG labeling GoCs and PCs and PAX6 for GCs (**Figure 9B**). The total neuronal fraction of detected FT⁺ cells at each age was calculated according to our previous results (number of FT⁺ cells corrected by the proportion of neuronal cells at each age). For group classification, we evaluated co-localization of FT with each of the markers mentioned above and obtained their proportion over the total neuronal fraction.

The proportion of the distinct *population marker*⁺ cells generation from E11 to E16 is shown in **Figure 9A and C**. Observe that CALB⁺ cells generation, classical marker for PCs, is the most represented at early stages (E11 47.1%, E12 46.8%), whereas it decreases as development advances (from 15.4% at E13 to 2.4% at E16). In contrast, PAX2⁺ cells (immature Gis) generation is barely represented at E11 (5.7%) and E12 (8.2%), with an increase at E13 (from 22.6% to 33.8%). TBR2⁺ cells generation, classical marker for UBCs, is visible without interruption from E11 to E16. Yet, it increases overtime (from 6.1% at E11 to 19.8% at E16). CALRET⁺ cells are known to label LCs but also a subset of UBCs and even some GoCs. Therefore, analysis of this marker does not give us a specific population generation dynamics information, but rather an approximation. CALRET⁺ cells are generated from

E11 to E16, with a general lower representation than other populations. Overall, the generation tendency is quite similar to that of UBCs, which might be due to the UBCs subset included in CALRET⁺ cells population. NRG⁺ cells, labeling GoCs and a subpopulation of PCs, are also being generated from E11 to E16. However, higher proportions appear at E11-E13. While at E11 and E12 this generation proportions might correspond to PCs, from E13 we hypothesized that the generated cells are GoCs. As suspected, no co-localization was found for FT⁺ and PAX6⁺ cells at any age. As previously described, during postnatal development, GCs precursors will go through exponential rounds of clonal expansion. Hence, the fine FT labeling of GCs cohorts might get diluted, preventing the tracking of this specific population throughout cerebellar development. The specific contribution of each EDv stage for each population genesis progression over time is shown in **Figure 9C** (lower panel).

Overall, these data indicate a differential time-tendency for the genesis of the different neuronal populations in the CC. Birth date of cerebellar cells seems therefore to carry an important predictive power for their final identity.

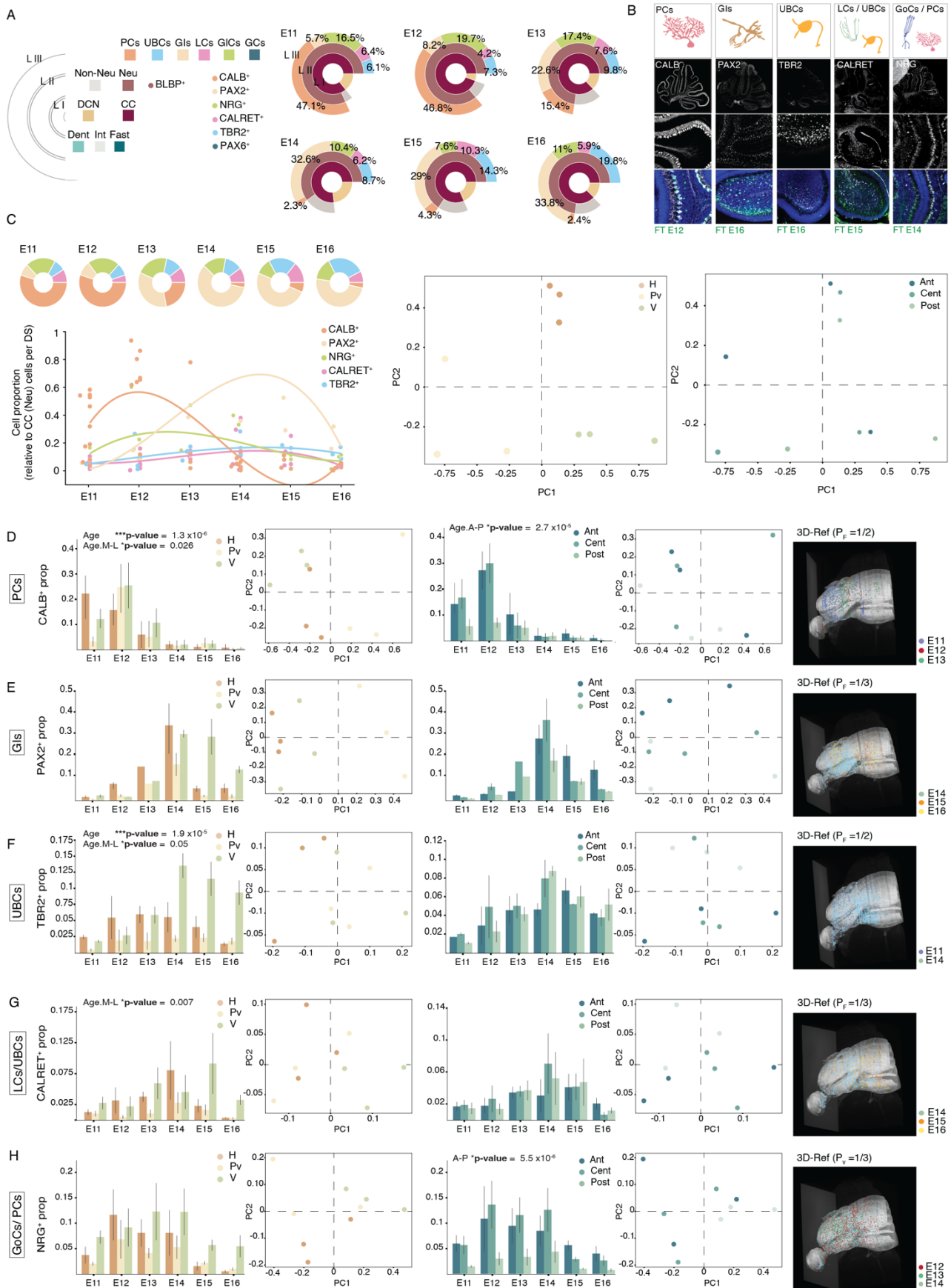


Figure 9. Cortical neuronal populations generation in the P7 cerebellum. (See legend on next page)

Figure 9. Cortical neuronal populations generation in the P7 cerebellum. **A)** Multi-layer pieplots showing FT⁺ cells classification at E11, E12, E13, E14, E15 and E16. From inside outwards: CC vs DCN, Neu vs Non-Neu (in CC), neuronal populations. **B)** Neuronal markers for population identification: Calbindin (CALB), Purkinje cells (PCs); Paired box gene 2 (PAX2), GABAergic interneurons (GIs); Eomes (TBR2), Unipolar brush cells (UBCs); Calretinin (CALRET), Lugaro cells (LCs) and UBCs; Neurogranin (NRG), Golgi cells (GoCs) and PCs. Co-localization with FITC is shown in the lower image for each marker. **C)** Neuronal population temporal generation dynamics in the CC. (upper panel) Pie-plot showing cortical neuronal populations cell generation proportion at E11, E12, E13, E14, E15 (relative to the total CC Neu cells at each age). (lower panel) Progression plot showing neuronal populations cells generation tendency from E11 to E16. **D)** PCA analysis for M-L (Hemisphere, H; Paravermis, Pv; Vermis, V) (left) and A-P (Anterior, Ant; Central, Cent; Posterior, Post) (rights) similarity in cell population generation dynamics. **E)** PCs. Spatial progression in the M-L axis. (ANOVA, Age $F_{(5,33)} = 11.82$ *** p -value = 1.3×10^{-6} , M-L level $F_{(2,66)} = 2.01$ p -value = 0.14 , Age.M-L level $F_{(10,66)} = 2.83$ * p -value = 0.005) Spatial progression in the A-P axis. (ANOVA, Age $F_{(5,35)} = 13.11$ *** p -value = 3.2×10^{-7} , A-P level $F_{(2,70)} = 18.64$ *** p -value = 3.2×10^{-7} , Age.A-P level $F_{(10,70)} = 4.8$ *** p -value = 2.7×10^{-3}). PCA. FT⁺CALB⁺ cell projection into the P7 3D-Ref. **F)** GIs. Spatial progression in the M-L axis. (ANOVA, Age $F_{(5,6)} = 3.52$ p -value = 0.078 , M-L level $F_{(2,12)} = 5.18$ p -value = 0.02 , Age.M-L level $F_{(10,12)} = 1.47$ p -value = 0.2) Spatial progression in the A-P axis. (ANOVA, Age $F_{(5,6)} = 3.5$ p -value = 0.08 , A-P level $F_{(2,12)} = 2.76$ p -value = 0.1 , Age.A-P level $F_{(10,12)} = 1.2$ p -value = 0.37). PCA. FT⁺PAX2⁺ cell projection into the P7 3D-Ref. **G)** UBCs. Spatial progression in the M-L axis. (ANOVA, Age $F_{(5,13)} = 1.93$ p -value = 0.15 , M-L level $F_{(2,26)} = 16.9$ *** p -value = 1.9×10^{-5} , Age.M-L level $F_{(10,26)} = 2.55$ * p -value = 0.026). Spatial progression in the A-P axis. (ANOVA, Age $F_{(5,13)} = 1.9$ p -value = 0.16 , A-P level $F_{(2,26)} = 0.88$ p -value = 0.42 , Age.A-P level $F_{(10,26)} = 1.07$ p -value = 0.41). PCA. FT⁺TBR2⁺ cell projection into the P7 3D-Ref. **H)** LCs/UBCs. Spatial progression in the M-L axis. (ANOVA, Age $F_{(5,24)} = 1.36$ p -value = 0.27 , M-L level $F_{(2,48)} = 7.3$ * p -value = 0.001 , Age.M-L level $F_{(10,48)} = 1.87$ * p -value = 0.07). Spatial progression in the A-P axis. (ANOVA, Age $F_{(5,25)} = 1.43$ p -value = 0.25 , A-P level $F_{(2,50)} = 2.087$ p -value = 0.13 , Age.A-P level $F_{(10,50)} = 1.53$ p -value = 0.1). PCA. FT⁺CALRET⁺ cell projection into the P7 3D-Ref. **I)** GoCs/PCs. Spatial progression in the M-L axis. (ANOVA, Age $F_{(5,13)} = 0.98$ p -value = 0.46 , M-L level $F_{(2,26)} = 7.6$ * p -value = 0.00125 , Age.M-L level $F_{(10,26)} = 0.65$ p -value = 0.7). Spatial progression in the A-P axis. (ANOVA, Age $F_{(5,13)} = 0.97$ p -value = 0.47 , A-P level $F_{(2,26)} = 20$ *** p -value = 5.5×10^{-6} , Age.A-P level $F_{(10,26)} = 1.22$ p -value = 0.32). PCA. FT⁺NRG⁺ cell projection into the P7 3D-Ref.

Next, we assessed whether birth date would also contribute to spatial variability (**Figure 9C, left**). PCAs analysis for the similarities of distinct regions in the M-L (H, Pv and V) and A-P (Ant, Cent, Post) divisions of the P7 CB are shown. Similarities are inferred based on the proximity of the different areas on the first two component projection plot. The features reduced in this first PCA are the proportion of all the investigated populations at all EDv stages, meaning the populations generation dynamics over time for each division. Interestingly, we can observe that in the M-L level, all regions from H, Pv and V cluster together, suggesting that they share similar dynamics of cell type generation, differing from the other regions. However, the different levels of the A-P axis components seem to display very different dynamics. Notice that Post levels seem to be the ones with the most different dynamics, especially in H and V.

We then sought spatio-temporal dynamics of the specific populations. To do so, we looked at the total number of cells of the population of interest at each EDv stage and how this distributes in the H, Pv and V (for M-L progression) and Ant, Cent and Post (for A-P progression). In both these axes, we also looked at the similarities between these different areas for the specific population generation dynamics, by restricting the PCA to the features of each population separately (**Figure 9D-H**).

6.2.1. PCs

Analysis in PCs spatio-temporal dynamics (**Figure 9D**), here identified by CALB⁺, indicates significant differences in their generation depending on the EDv stage (age effect *** p -value= 1.3×10^{-6}). We have seen that the production of cells from this population occurs mainly at the beginning of the development. No significant differences are detected between M-L levels. PCs are known to be uniformly distributed in the whole CC. Nonetheless, differences in EDv stage contribution to a specific M-L level generation have been detected (age-space interaction effect * p -value= 0.005). Notice that E11 contributes mainly to H cells production, while at E12 H contribution decreases and Pv and V increase. Finally, at E13, the higher proportion is seen in the V. Therefore, this suggests a lateromedial time-dependent generation gradient of PCs. A-P distribution of PCs generated over time proved to be significantly different (age-space interaction effect*** p -value= 2.7×10^{-5}). A big representation of anterior and central areas is observed at E11 and E12, followed by a decrease from E13, where the contribution to the different levels homogenizes. These observations support a potential A-P time-dependent generation pattern additionally to the M-L. Although these effects are clear, the PCA does not produce a clean clustering of the different areas composing each of the M-L or A-P levels. This indicates that the distinct cerebellar portions might have their own specific PCs dynamics. However, comparing between M-L and A-P divisions, we still observe a clearer clustering in the M-L axis. We can therefore conclude that the temporal progression of PCs occurs mainly in the M-L direction with less variability in the A-P.

6.2.2. GIs

Analysis in GIs spatio-temporal dynamics (**Figure 9E**), here identified by PAX2⁺, reveal no significant differences. This might be due to the low number of replicates for this condition and variability, which translates into a power decrease. Yet, data exploration seems to indicate time-dependent differences for their generation, with a peak at late EDv stages (from E14), just after PCs peak of generation ceases. In addition, a lateral to medial generation pattern for GIs is suggested in our data, with GIs in the H and the Pv being generated first, followed by the ones located at the V. A similar PCs-GIs A-P pattern seems to point out as well. Overall, these observations suggest generation dynamics in canon for PCs and GIs. The PCA does not result in a clear separation. However, PC1 seems to separate mostly for M-L variability and PC2 for A-P variability.

6.2.3. UBCs

Examination of UBCs (TBR2⁺) generation spatio-temporal dynamics (**Figure 9F**), demonstrates generation without interruption from E11 to E16. Differences within these ages are detected (age effect *** p -value= 1.9×10^{-5}), with an increase of UBCs generation at later stages (from E14 to E16). Lateral to medial time-dependent generation tendency is noticed (age-space interaction effect * p -value= 0.026), similar to our observations for PCs and Gis. Generation proportion for the Pv is detected in lower proportions at all EDv stages than that for H and V. This property actually matches the preferential anatomical distribution of this cell type (Fl, Pfl in the H, lobule X in the V). No significant differences were detected for UBCs generation along the A-P axis. Yet, matching with the anatomical position of UBCs, posterior generation proportion is higher from E14, where the generation peak for UBCs occurs. Similarity in generation dynamics between the posterior divisions of H, Pv and H are as well detected in PCA analysis.

These results suggest that UBCs generation occurs unceasing along the development in a lateral to medial fashion. The generation increases at late EDv stages, mainly localized in the posterior vermis indicating that the “classic” vestibular UBCs population would not be completely restricted but still dependent on that stage of cell generation.

6.2.4. LCs/UBCs

Up to now, no spatial restriction has been demonstrated for LCs in the CC. In addition, their developmental features are still largely unknown. Here we used CALRET as a proxy for LCs spatio-temporal generation dynamics (**Figure 9G**). As previously mentioned, CALRET is not exclusive expressed in LCs, but also a subset of CALRET⁺ UBCs has been identified. CALRET⁺ cells generation was detected constantly from E11 to E16, with a lower representation than other populations. An age-dependent generation gradient from lateral to medial is revealed (age-space interaction effect* p -value= 0.007). The higher similarity with PAX2⁺ M-L generation, rather than the one of TBR2⁺ suggests that LCs are still more represented than UBCs within the CARLET⁺ cells population. No significant differences are observed in the A-P axis, other than E14 which could match with UBCs peak of generation. The PCA does not reveal any preferred axis for cellular generation between M-L and A-P.

6.2.5. GoCs

GoCs are known for their role in regulation spatio-temporal topologically regulation of GCL activity. Like LCs, there is little information about their generation. Here we use NRG for GoCs generation dynamics scrutiny. However, it is known that not all subsets of GoCs are NRG⁺ (75-80%). In addition, a subset of NRG⁺ PCs is known to exist. Despite the lack of significant age effect, we observe a tendency for higher NRG⁺ cell generation proportions at early stages. This might be attributed to PCs, which we showed to be generated during this time window. NRG⁺ cells generated at later ages might correspond to GoCs (as all other GABAergic interneurons, later ages generation). A lateral to medial tendency over time is also observed, however the effect of the interaction does not appear significant in our analysis. Differential distribution of NRG⁺ cells in the M-L (space effect **p-value*=0.00125) and A-P (space effect **p-value*= 5.5 x 10⁻⁶) axes are detected, with a preferred tendency for Ant and Cent portions. This distribution appears constant over time.

Comprehensively, these results support the differential spatio-temporal generation dynamics of distinct neuronal populations in the CC. The earlier generation of PCs and their strong patterning suggest that this cell population would have a master role for the generation dynamics of the populations that follow. Whether this is genetically encoded or externally induced needs to be elucidated.

7. Transcriptomics analysis of perinatal cerebellum reveals highly distinct cell populations

Population identity characterization using FT/immunofluorescence combination is limited by technical issues such as the feasible number of marker combinations, as well as for the specific population markers that have been elucidated so far. To better characterize the cerebellar cell types of heterogeneity at P7, we decided to add high throughput transcriptomic profiling information. Hence, we combined available perinatal cerebellum scRNA-seq datasets (Carter et al., 2018)[280] (Sepp et al., 2021)[140],(Vladoiu et al., 2019)[132] with data sets generated in the lab, and then applied clustering analysis to elucidate different population identity and their corresponding transcriptomic signature (**Figure 10**).

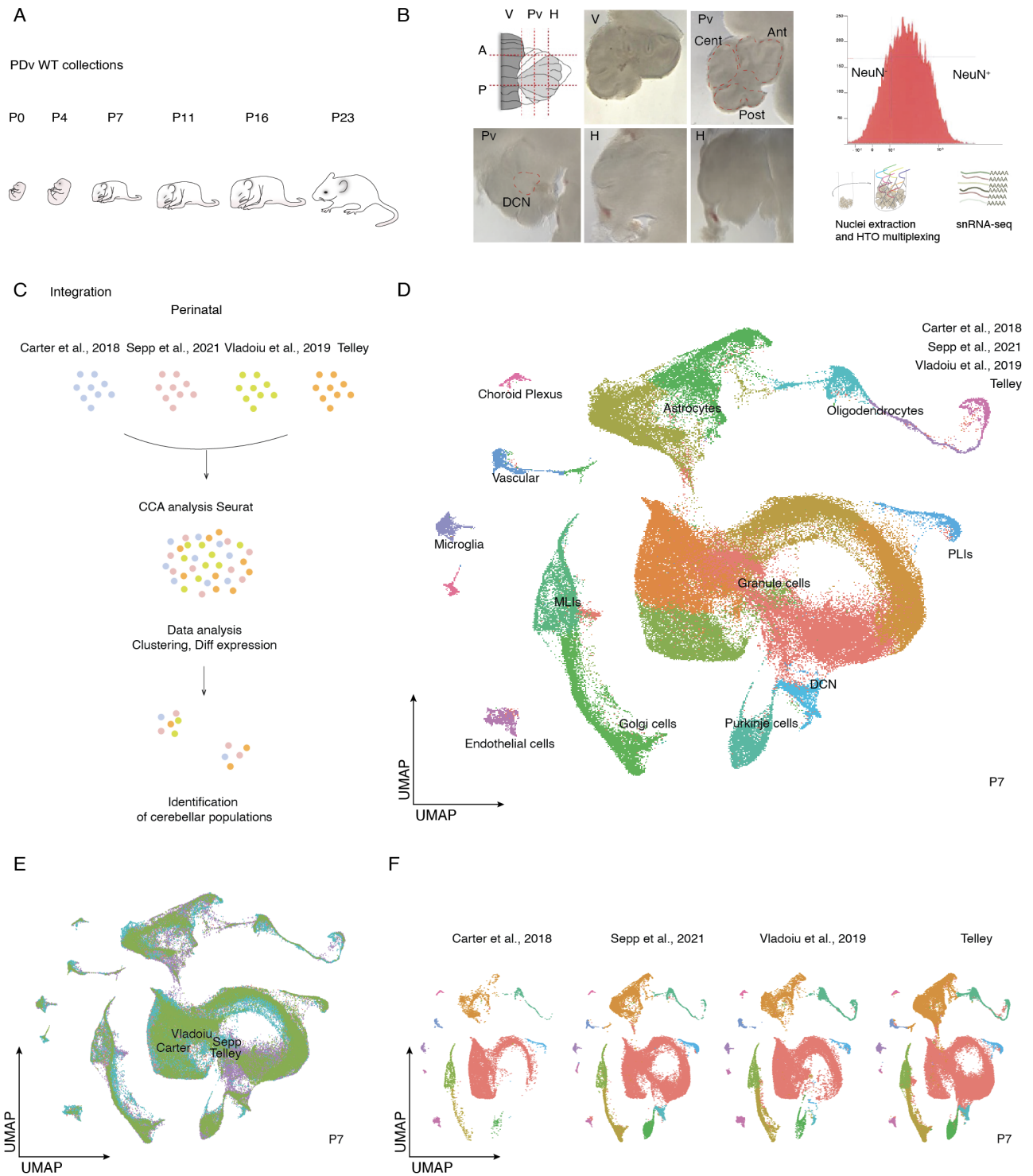


Figure 10. Transcriptomic profiling of the perinatal cerebellum. **A)** Schematic representation of collection time-point during PDV. **B)** Representative images for medio-lateral (M-L) and antero-posterior (A-P) spatial division of the CB used for generating the transcriptomic data-set. NeuN balancing histogram. Schematic illustration of nuclei straction, multiplexing and snRNA-seq. **C)** Schematic representation of available data sets integration. **D)** UMAP showing the integrated cell clustering at P7 cerebellum **E)** UMAP showing overlapping datasets integration. **F)** UMAPs for individual datasets.

A comprehensive understanding of the spatial distribution of the distinct populations throughout the cerebellar development stream remains to be resolved. In a first attempt to integrate available high throughput profiling information with such spatial information, we have generated a perinatal transcriptomic data set which contains specific information for cerebellar divisions along the M-L and A-P axis. To do so, WT CB at PDv stages P0, P4, P7, P11, P16 and P23 were collected. Prior nuclei extraction, CB were micro dissected into different zones along the M-L (H, Pv and V) and A-P axes (Ant, Cent, Post, DCN) (**Figure 10A-B**). Neu-N⁺/Neu-N⁻ cells were balanced using FACS sorting in order to prevent GCs overrepresentation in our cell capture. Samples from different zones were multiplexed using the HTO-based system. HTOs are monoclonal antibodies directed against ubiquitously and highly expressed immune surface markers (CD45, CD98, CD44, and CD11a) conjugated to a distinct Hashtag oligonucleotide, henceforth referred to as HTO. The HTOs contain a unique 12-bp barcode that can be sequenced alongside the cellular transcriptome, with only minor modifications to standard scRNA-seq protocols, therefore allowing in that case, post hoc cell spatial identity retrieval.

The generated time-linked transcriptomic dataset was then integrated to the aforementioned available datasets (**Figure 10C**). Cell clustering data analysis at P7 reveal 12 cell clusters: GCs, PCs, MLIs, Purkinje layer interneurons (PLIs), GoCs, DCN, Astrocytes, Oligodendrocytes, Microglia, Plexus Choroid, Vascular and Endothelial cells (**Figure 10D**). As observed in **Figure 10E-F**, the general cell classification shape overlaps between the distinct data sets. Yet, higher cell representation seems to appear in our data set. Notice in **Figure 10F**, an enrichment of DCN, MLIs, GoCs, PCs and astrocytes in Telley dataset compared to Carter, Vladoiu and Sepp.

Spatial distribution of specific populations was next studied during PDv in our dataset (**Figure 11**). scRNAseq data integration from P0-P23 reveals 12 cell clusters: GCs, PCs, MLIs, Purkinje layer interneurons (PLIs), GoCs, DCN, Astrocytes, Oligodendrocytes, Microglia, Plexus Choroid, Vascular and Endothelial cells (**Figure 11A**). Spatio-temporal analysis reveal a rather uniform distribution for most cell populations (**Figure 11B-E**). Remarkably, we can observe a M-L and A-P distribution of cells within the PCs cluster. Indeed, we can observe in **Figure 11C** that PC located in the H, Pv and V appear to have distinct molecular features, thus creating individual area-specific clusters. Interestingly, the same phenomenon is observed in **Figure 11D**. Cells located in the Ant, Cent and Post zones of the CB, cluster independently, indicating a shared molecular profile dependent to the area of distribution.

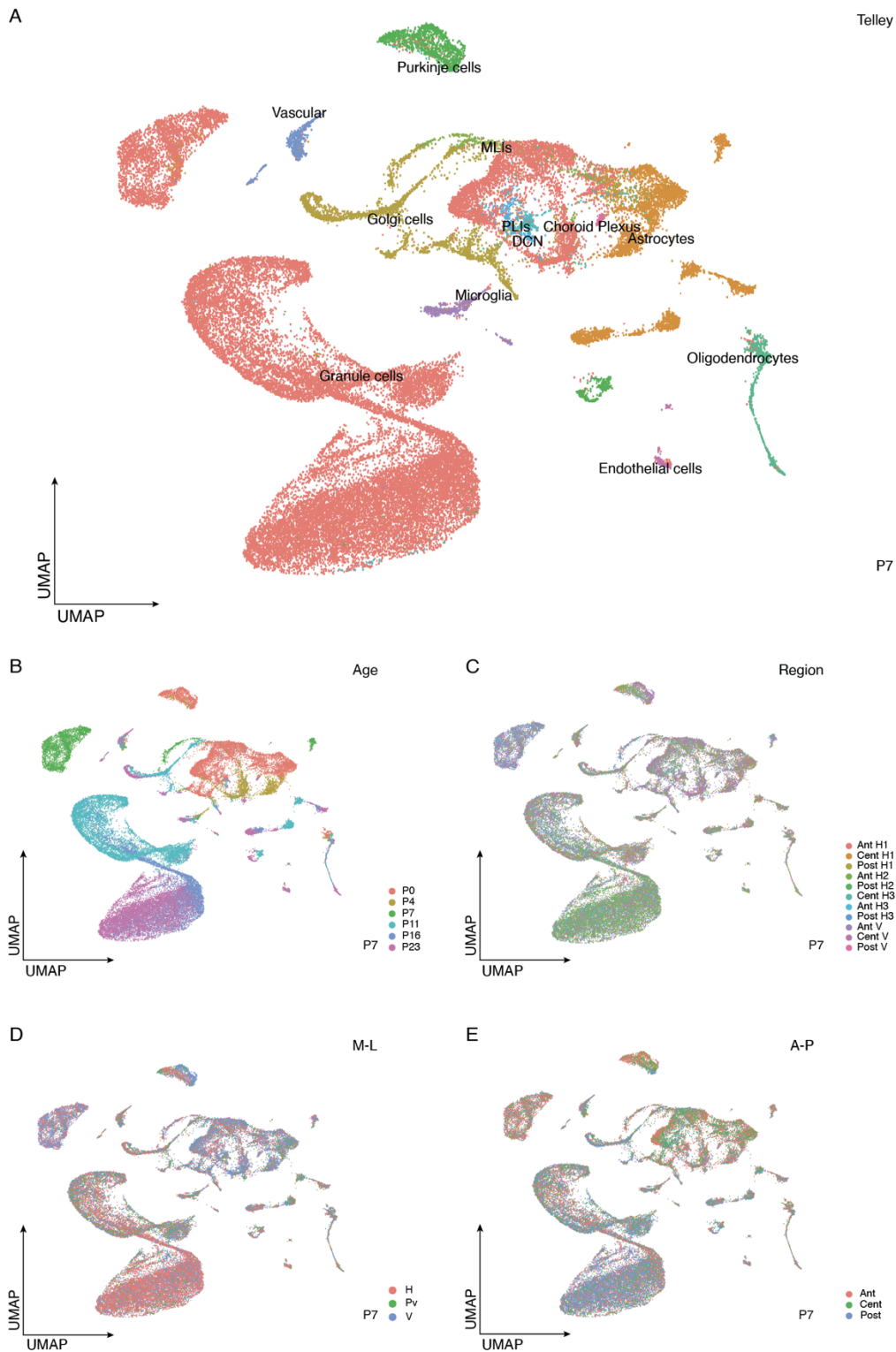


Figure 11. Transcriptomic profiling of the perinatal cerebellum linked to spatial information. **A)** Integrated cell clustering at P7 cerebellum for spatial multiplexing over postnatal developmental stages (P0, P4, P7, P11, P23). **B)** Age-coloured clustering **C)** Region-coloured clustering. Anterior hemisphere 1 (Ant H1), posterior hemisphere 1 (Post H1), Central hemisphere 2 (Central H1), Anterior hemisphere 2 (Ant H2), Posterior hemisphere 2 (Post H2), Central hemisphere 3 (Cent H1), Anterior hemisphere 3 (Ant H3), Posterior hemisphere 3 (Post H3), Anterior vermis (Ant V), Central vermis (Cent V), Posterior vermis (Post V) **D)** Medio-Lateral progression-coloured clustering. Hemisphere (H), Paravermis (Pv), Vermis (V) **E)** Antero-Posterior progression-coloured clustering. Anterior (Ant), Central (Cent), Posterior (Post).

The main achievements of this work can be listed as follows: (1) Generation of 4D-CbF, (2) CP proliferative progenitors spatio-temporal characterization, (3) Spatio-temporal analysis of cell cycle dynamics of proliferative cerebellar progenitors, (4) Time-dependent cell generation investigation in the CP using FT, (5) Postnatal tracking of cerebellar cells and its spatio-temporal characterization in the P7 cerebellum. Overall, suggesting a key role of time and space during cerebellar cells generation and differentiation. Thoroughly, these results contribute to the generation and description of an extensive dataset in the perspective of generating a 4D atlas of the developing CB.

4D-CbF generation

A dynamic cerebellar framework over time is required for sophisticated spatio-temporal multimodal data integration to ultimately model the cerebellar development. Although scientists have focused their attention into the understanding of cerebellar structure and its developmental process, there are still significant gaps, in part due to the lack of integrative approaches. Atlases generation has been perpetrated for years in the history of neurosciences. The method of use has adapted to technological advances, from the meticulous drawings of Ramón y Cajal to the 3D resources generated by the Allen Brain Institute. Last technology-based atlases generally are characterized by high anatomical resolution. This can be appreciated with the Allen Brain and its groundbreaking work on the comprehensive understanding of brain structure and circuitry. However, similar approaches were lacking for the CB up to now. Available resources limitations refer mostly to low spatial and temporal power. The 3D Allen Brain CCF, though remarkably extensive, presents a lack of substructure-specific resolution, especially for the CB. That is, incomplete or very broad spatial compartmentation. On the other hand, some of the available 2D atlases, despite being of low resolution, are available at different time points of embryonic and postnatal development. Yet, 3D available atlases are mainly single time point-based, as we can see with the Allen CCF, focused on the adult mouse brain. Therefore, 3D atlases through the developmental time-course are currently missing. My thesis represents a pioneering work on developing such an approach. The 4D-CbF is composed of annotated age-specific 3D references (3D-CbF) spanning from embryonic to adult stages. These include E11, E12, E13, E14, E15, E16, E17 and E18 for embryonic development, and P0, P7, P12, P21 and P56 for postnatal development. Thus far, we were able to complete the generation of 3D-CbF for E11, E12, E13 EDv stages and P7 PDv stage. For every developmental stage, we first reviewed relevant data from multiple sources, including available publications and atlases to define the appropriate reference compartmentalization. However,

the anatomical annotation was done without molecular guidance. To improve that on a second stage, molecular information could be gathered from immunofluorescence-based data, available and/or generated in the lab. Now that we have the possibility to register such information to the corresponding 3D-Ref, this would help to delimitate the molecular boundaries, especially within the CP, and therefore fine-tune its compartmentation.

The registration pipeline developed during the work of this thesis, has proved being effective and accurate for the different experimental conditions. However, this step has not been fully automatized yet. For a successful registration, first CP or CB in the experimental images need to be manually segmented from the rest and mapped to the corresponding level (section) of the 3D-Ref. Remarkably, registration accuracy is fairly high thanks to landmark guided optimization. Yet, manual landmark drawing is required per each single image. Optimization steps to increase the automatic flow of this step are still required.

Cell segmentation accuracy of our pipeline is also significantly high. Cell segmentation models were developed using Stardist-based method with training data obtained from manual delineation of FITC⁺ cells for postnatal ages and Hoechst⁺ cells for embryonic. However, there is still no model powerful enough to work on any images. Indeed, images acquired using different systems and/or resolution require a new training to ensure a high accuracy. Better algorithms need to be developed to solve this issue. In addition, a better combination of parameters in the Stardist Unet could help in that direction. Thus far, we were able to complete the generation of 3D-CbF for E11, E12, E13 EDv stages and P7 PDv stage. 3D-Ref for all remaining ages have been already generated as well as the corresponding anatomical compartmentation. Anatomical delineation of remaining atlases is ongoing. Altogether, the completion of the 4D-CbF generation will provide the possibility to extent our analysis to these complementary ages and provide an available tool for usage as well as inspiration for others in the field or beyond.

4D-CbF and its contribution to cerebellar development description and analysis has been proved in this work. Automatic cell detection analysis and spatial identity assignment for higher spatial resolution allowed us to greatly improve the output and interpretation of our data during embryonic and postnatal cerebellar development.

Proliferation patterns in the CP

Using Ki67 to identify proliferative cells in the developing CP, we observed a decrease of proliferative cells proportion over time. Two factors might contribute to that: first, a higher number of proliferative/progenitor cells at early stages of the development; and second, the development of a mantle zone/prospective white matter as the development advances, hosting post-mitotic and quiescent cells. Therefore, the CP balance between proliferative vs differentiated progenitors/precursors shifts during development, with a general decrease of the proliferative population. Interestingly, our results shed light into a switch on progenitors decreasing proportion at E15. This event suggests that a second wave of proliferation is detected at that time, which could be related to the developing MLIs. Located within the mantle zone of the CP, cell cycle locked MLIs precursors would reactivate in response to stage-specific external factors, most likely coming from the differentiation process of other cerebellar cell types.

A deeper spatial resolution analysis to further investigate this was not possible at that age up to now. Yet, with the progressing work on the remaining 3D-CbF frameworks we hope to provide an answer soon. Though high-resolution spatial analysis was not yet carried out on these remaining ages, our preliminary image observations support this hypothesis. Spatial resolution was possible from E11 to E13. We've detected significant differences in between the two main proliferative areas of the CP, the VZ and the RL. Differences in time-space proliferative activity could relate to the generation of different cell-lineage from each proliferative niche. It is however necessary to mention a potential registration limitation at embryonic stages, mainly in the RL. The small size of this area and its restricted location in the most posterior end of the CP, are reasons to consider a decrease in the registration performance to the reference.

Cell cycle dynamics of cerebellar precursors

Previous studies suggest a major role of cell cycle in nervous system development (Hindley and Philpott, 2012) (Donocan and Dyer, 2005) (Dally-Cuif and Hammerschidt, 2003) (Creimsi et al., 2003) (Cheffer et al., 2013) (Ohuma et al., 2003). Induction and patterning of neuronal development, regulation of proliferation, differentiation and fate determination, appear to be highly coordinated with cell cycle machinery and dynamics. The cell cycle influence during development relies on cell cycle length manipulation. Over time, neuronal progenitors pass through defined competence states, which

correspond to their ability to generate only a defined subset of cell types. Thus, the fine tuning of cell cycle exit timing, will directly influence cell fate determination and diversity generation. In the neocortex cortex, for example, a tendency for increased Tc has been detected which might link to heterogeneity generation. Several methods exist to study cell cycle dynamics (Continuous BrdU-based, FUCCI plasmid-based, etc.). Here we use an adapted protocol for dual labeling using BrdU and EdU. Our results support a temporal variability of cell cycle during cerebellar development. Spatio-specific dynamics between VZ and RL were as well observed when registration was possible (E11-E13). Consistent with our CP description, progenitors in these two areas have different behaviors. The variability observed in RL dynamics might be related to registration limitation mentioned previously for this specific area, although we cannot rule out a specific biological reason for this specific variability. Altogether, temporal and spatial components of Tc variability contribute to cell heterogeneity generation during cerebellar development. The spatio-temporal resolution of our analysis here is also possible thanks to the 3D-CbF and the registration pipeline. Yet, our results lack spatial information for latter EDv stages, which might be essential to elucidate the mechanisms underlying the potential second wave of proliferation that takes place at that moment.

Some limitations of this specific experiment are related to the detection methods which are quite tricky for thymidine analogues. While EdU can easily be revealed thanks to an immunofluorescence free Click-it reaction, BrdU requires harsh tissue treatment for DNA opening with HCl. In addition, most available BrdU antibodies cross react with other thymidine analogs, such as EdU. Here we used the DHSB mouse anti-BrdU antibody, whose recognition has been proved to be exclusive for BrdU and not others. However, mouse to mouse detection issues become evident from EDv E13, especially in the CB.

Ki67, used to delimitate the population of interest, is crucial in this analysis. Most CC dynamic analysis has been developed in “stable” populations, where the number of cells entering and leaving the cycle is supposed to be constant. Therefore, we might want to consider whether we are targeting the right population for assessing the accuracy of our study. Ki67 has been widely used as a proliferation marker. Interestingly, it’s cellular distribution dramatically changes during cell cycle progression, which is related to the multiple molecular functions that have recently been attributed to this protein. In mitotic cells, Ki67 coats the condensed chromosomes as the foundation of the perichromosomal layer, thus providing with a strong, about homogeneous signal. As cells exit mitosis and enter early G1 phase, small puncta of Ki67 leave the decondensing chromosomes. These then coalesce at the periphery of the reformed nucleoli as G1 phase progresses. (Matheson and Kaufman, 2017) (Sun and

Kaufman, 2018) Although Ki67 is a good biomarker for all stages in the cell cycle, it is absent in G0 quiescent cells. Hence, it has been suggested that Ki67 does not precisely reflect the whole of proliferating cells (Elmaci et al., 2018).

FT-based labeling and tracking of cerebellar progenitors

To better characterize the role of time in cerebellar mechanisms development we thought to track specifically time-locked cohorts of cells using FT. FT allows to specifically label spatially defined isochronic cohorts of cell cycle phase-locked (M-phase) progenitors, by the *in-utero* injection of the short-life fluorescent dye carboxyfluorescein ester (CFSE) into the ventricular system. Intracellularly, FT is linearly diluted at each mitosis, such that fluorescence intensity can be used as a proxy for cell division number since the time of injection. Noteworthy, only directly born cells will be tracked up to latter time points. That's the case for some MLIs, and mainly, for GCs. GCs, born from the RL, are known to reside in a transient state within the SS and later, within the EGL. It will be during postnatal stages, and thanks to molecular cues secreted by PCs among others, that they will reactivate their cell cycle and start a clonal expansion. Thereafter, the massive number of GCs will be generated from this small pool of intermediate progenitors. The mitosis-dependent FT dilution factor becomes therefore infinite in that case, which makes the detection of FT⁺ GCs impossible. Moreover, the absence of FT⁺ cells within the SS in our embryonic preliminary results could suggest a VZ-derived progenitor FT-labeling, rather than RL-derived. However, FT⁺ TBR2⁺ UBCs are detected at P7, which indicates that RL-derivates are indeed tracked with FT. Although UBC and GCs originate from Atho1⁺ precursors situated in the RL, their differentiation pathways and lineages are distinct. For example, distinct molecular features (early UBCs, are faintly PaX6⁺ and clearly TBR2⁺, while cells in the EGL present the opposite pattern), distinct migration paths (UBCs linger in the RL for one or more days before migrating, experience a burst of migration at P0.5 and most of them reside in their final location (GCL) by P10, well ahead of the completion of GCs neurogenesis.) (Englund et al., 2006). It is still unclear how gene expression programs are controlled as RL progenitors differentiate into specific lineages and subtypes, as well as the mechanisms by which UBCs are guided to specific cerebellar lobules position. Overall, our observations support the ability of FT for tracking specific time-locked cohorts of cells within the CP along the cerebellar development. The total amount of cells generated at each time do not seem to differ over time. However, time-dependent variability is observed. Like in the other cases, there is the need to complete the 4D-CbF, so it can be analyzed in higher resolution (space and

replicates). An additional approach to achieve a similar result could be whole brain FT tracking, using a combination of whole brain IF with 3D LSM imaging of FT in the whole CP. During my PhD I have generated this data for experimental samples injected at E11, E12, E13, E14, E15, E16 and collected at +1h, +6h, +12h, +24h and +96h. 3 replicates are available per condition. A next step will focus on the analysis of this dataset and its integration to the 4D-CbF. First, registration of LSM images to the 3D-CbF needs to be done so we can add anatomical information, followed by cell segmentation in 3D. This step requires the training of a new Stardist-based model. Stardist is indeed suited for this application since it was first developed specifically for 3D cell segmentation.

Altogether, our findings support a spatio-temporal dependent cell generation in the CP. Cells born at different EDv stages would display distinct migration behaviors, correlating with our finding in cell cycle variability (shorter at early ages, when migration is faster; longer at latter ages, when migration is slower). Ultimately this could be linked to fate determination variability. Cells migrate when they stop cycling, therefore we can imagine that migration rates are reduced as Tc increases. As previously discussed, cell cycle variation and cell heterogeneity might be closely related. Additionally, combining FT and molecular characterization-based analysis of early progenitors would help to better understand their heterogeneity and its origin.

Time-locked cell cohort classification in the P7 CB

How spatio-temporal variability is projected at later stages of the development, knowing that FT can track up to P7? In combination with registration pipeline and the accurate generation of the P7 3D-CbF we have analyzed FT spatio-temporal distribution in three main resolution levels: (1) Level I: CC and *vs* DCN, (2) Level II: Neu and non-Neu populations in both CC and DCN, (3) Level II: neuronal populations within the CC.

(1) Level I

FT cells production appeared to be more or less constant over time. Interestingly, interaction between time of generation and space seem to be key for spatial heterogeneity between and within both, CC and DCN. Constant tendency of CC and DCN generation has been observed, although an increase in DCN cells generation proportion is noticed in later ages, which might correspond to inhibitory projection neurons. Indeed, prior studies indicate that DCN cells generation would mainly occur in a short time window between E13-E15 for i-174-inhibitory, and from E9-10 for excitatory interneurons, which production might be extended up to latter stages but with small proportion (Fink

et al., 2006)[301] (Leto et al., 2006)[247]. Therefore, we hypothesized that FT injection earlier in development (E9-E10) could serve to elucidate this first wave of glutamatergic DCN cells generation and would clarify whether the balance of DCN generation is inclined towards early stages or in contrast revealing to be two waves of generation, first at E10-11 and second from E13-E15.

In this level we also assessed the M-L progression of cell generation in the CC (H, Pv, V) and DCN (Dent, Int, Fast). In our analysis, latero-medial generation of the distinct structures over time becomes especially clear for the DCN. For CC, there are clear differences in levels distribution in all EDv stages, which are not constant over time. However, we could think about homogeneous distribution if we consider the potential technical issue of sample level representation at each age. One potential solution would be to increase the number of levels contained in each serial set of images or increase the number of replicates that are included in the analysis, so we increase the chance that all levels are equally represented in the dataset. In addition, as proposed for embryonic FT tracking, 3D studies of FT distribution on cleared CBs would help to increase spatial resolution.

(2) Level II

Our results indicate that in both CC and DCN, although the generation of non-neuronal cells is lower than that of neuronal cells during development, a time-dependent increase for non-neuronal development does occur, especially marked at the DCN. This matches with the prevalent view of a neuro- to glio-genic behavior of the cerebellar neuroepithelium at later ages. Here we used BLBP, a marker for astrocytes, as a proxy for the non-neuronal population of the cerebellum. However, as already mentioned, the non-neuronal population of the CB contains a variety of cell types including microglia, oligodendrocytes, and epidermal cells. Markers for other non-neuronal populations could be added to increase accuracy of our calculations. However, we would have to demonstrate the possibility of tracking them with FT.

(3) Level III

Birth date of cerebellar cells seems to carry an important predictive power for their final identity. The *population marker* battery we use in this level is representative of some of the main cell populations of the CC, but presents some drawbacks that need to be mentioned before discussing the results: a) missing information on some cell types because of limited available markers (some cell types do not have identified markers, such as candelabrum cells), b) exclusivity (CALRET and NRG are not population-exclusive), c) combinations limitations related to the number of markers that can be simultaneously used (2-3 additionally to FT and Hoechst) and the host species in which were

generated. Another limitation, already discussed above, relates to the GCs which are not detected with the FT approach. Alternative methods for tracking this population would include specific transgenic reporter lines for *Atho1*⁺.

Thanks to 3D-CbF spatial resolution, it was possible to elucidate birth date-dependent spatial variability in cell populations generation dynamics. PCA analyses reveal M-L level-specific dynamics of cell type generation. However, the different levels of the A-P axis components seem to display very different dynamics. Interestingly, posterior levels have most different dynamics, especially in H and V. Posterior H and V compose part of the vestibulo-cerebellar circuit, which is the phylogenetically most ancient portion of the CB. It is therefore possible to imagine that mechanisms (spatio-temporal) of neuronal populations differ from the rest. On the same note, it is worth mentioning the pivotal role of UBCs, which are highly enriched in these areas. They participate in the modulation of signals in between MFs and Granule cells. Different types of UBCs are known to participate differently in the circuit (modulation, amplification, dampening). Are these different subtypes differently generated over time?

PC-type as cerebellar development conductor

Interestingly, a generation in canon for PCs and GIs has been revealed. PCs (*CALB*⁺) generation, most represented at early stages whereas it decreases as development advances. In contrast, immature GIs (*PAX2*⁺) generation is barely represented at E11 and E12 but increases from E13. A neurogenic change in VZ at that stage has been proposed, where PCPs shift to interneuron precursors.

These results support the potential role of PCs in GIs generation. Migration and differentiation cues from PCs would drive GIs towards their final destination in the circuit. Our analysis in the P7 transcriptomics data, showing just space-dependent molecular variability for PCs, suggests that it might be defined genetically early in the developmental course. Hence, (1) GIs differences would be then driven by external cues coming from PCs. Molecular differences might be detectable later in development, also driven by activity. Another possibility (2) would be that there would be a molecular diversity present early in development, which disappears as cells get differentiated and converge in their final phenotype. Transcriptomics analysis at later time-points of the development would help to clarify that. However, *Pax2* is a marker for immature interneurons, rather supporting the first scenario. In addition, functional differences in the distinct cerebellar areas might be due not only to cell type identity variability, but as well, in cell type ratio (different areas would share the same cell types, but

they would be different in the ratios of each of these cell types, ultimately generating functional diversity (ex; excitatory vs inhibitory balance).

Intriguingly, Pax2 appears as a common marker between GIs and astrocytes, indicating that they might share close lineage relations. Indeed, the metamorphic VZ developmental model suggests that astrocytes would arise from the same areas where MLIs and PCS are sequentially generated. The mechanisms responsible for the control of this regulation process are not completely understood. Transcriptomic analysis together with lineage tracing approaches would help to answer this question.

We also analyzed TBR2⁺ (UBCs), CALRET⁺ (LCs, UBCs, GoCs) and NRG⁺ (GoCs, PCs) cells generation. Interestingly, CALRET is shared between LCs and subset UBCs, which are GABAergic and Glutamatergic respectively. Is there a functional link between these two populations?

Generation occurs unceasing along the development in a lateral to medial fashion for all these populations, (less clear for NRG). Although generation is unceasing from E11 to E16, it increases at later stages. Noticeably, UBCs generated at E14, mainly localized in the posterior vermis indicating that the “classic” UBCs population would not be completely restricted but still dependent on that stage of cell generation. Together, this result hints towards a time-dependent mechanism for spatial restriction of this population.

Altogether, it is only for the PCs population that differential spatial distribution of cells generated at different time-points seems to correlate with the molecular variability detected in our perinatal transcriptomics analysis. Our data set with microdissection prior cell capture, adds spatial component into the available datasets for the perinatal cerebellum transcriptomic profiling. PCs cluster in a spatio-temporal fashion, therefore linking the variability observed in our imaged-based analysis with the molecular variability

Postnatal transcriptomic profiling reveals unique molecularly-defined PCs development

Here we presented a high throughput transcriptomics dataset of the developing CB with an unprecedented spatial resolution achieved by micro dissection. In combination with available perinatal cerebellum scRNAseq datasets, our analysis shed light into which could be one of the key molecular features for cerebellar cell generation and circuitry integration. While spatio-temporal analysis reveals a uniform distribution for most of the identified cell population in the integrated dataset, PCs clearly cluster according to M-L distribution and, remarkably, they also cluster in an A-P -zone dependent

manner. Therefore, our observations support a genetic origin of PCs spatial variability which would be exclusive for this cell population. This results again point towards the uniqueness of the PCs population. Together with our previous results on spatio-temporal cell generation distribution, this transcriptomic profiling confirms the idea that the PC are one of the main orchestrators of cerebellar development.

A mixed model for cerebellar development

The generation of the CB and its functional circuit could be explained by two different models: (1) genetically encoded, in which ultimate cell identity and destination would be already assigned at birth, or (2) later specification, with no final destination of the cells designated at birth. In that case, cells would be shaped depending on the environment (molecular cues and activity-driven changes). By this means, any cell from any specific cell type born at any given time would have the potential to occupy any of the possible positions in the circuit.

Here we suggest a mixt model for cerebellar development, combining both mechanisms mentioned above. The strong patterning and time-space correlation for the generation of PCs suggests that this cell type development would follow a generation model (1), and in turn act as an orchestrator of the final cerebellar circuitry formation. This would match observations in the neocortex where interneurons and astrocytes have been suggested to be “generic”, while projection neurons, here PCs, are specialized from the beginning.

PCs are located all along the CC, which make them also ideal for such conductor role. In contrast, other cell types, such as UBCs have a strong spatial restriction (lobule IX-X), which could be driven by external factors. In that case, cells ultimately residing in that specific zone would be generated at a specific time point. In that case, the spatial restriction could be driven by external factors. Therefore, cells finally located in that lobule would be generated all along the development and external factors would drive their migration specifically to that lobule. Our results indicated a possible correlation between the generation time and this final location. However, the constant generation of UBCs from E11 to E16, and their presence in other cerebellar zones, although in lower proportions, suggest that external factors acting in a time (and most likely spatial), dependent manner might be responsible for such spatial restriction. Moreover, previous studies (Chung et al., 2009) have demonstrated that PCs phenotype restricts distribution of UBCs, indicating the existence of non-cell autonomous mechanisms for UBCs spatial restriction/distribution. Their study supports the potential driver role of PCs, which

interestingly does not only participate in GABAergic cells development (as suggested for GIs), but also Glutamatergic.

Whether PCs conductor role expands beyond the CC remains to be elucidated. Given the tight interaction between PCs and DCN, correlative generation dynamics between these two structures could be imagined. However, Previous studies (Chung et al., 2007) report normal anatomy of DCN in the *scrambler* mouse, where PCs phenotypic alterations do not lead to DCB abnormalities. Overall, suggesting that DCN topography is independent of PCs positioning or of *Reelin* pathway. Moreover, our transcriptomic data reveals clear molecular distinction between the two main components of the CB, reinforcing the idea that these areas are independent.

Spatial transcriptomics: the bridge

A much needed integration of generation-time with molecular profiling is still missing to uncover the molecular mechanisms driving cell type generation spatio-temporal dynamics and correlations. Aiming to do that, during my thesis I generated a HiPlex-based spatial transcriptomics dataset. 12 probes representative of heterogeneity at P7 were defined, from which we can retrieve transcriptomic analysis-based cell clusters and therefore their high-resolution molecular information. The experiment was on sections from P7 CB injected from E11 to E16. Co-localization analysis for specific-probe expression together with FITC⁺ will serve as a bridge to link generation time point and molecular identity. Analysis of this dataset is currently ongoing. However, we anticipate that 12 probes might not be enough for targeting the whole cell variability. High-throughput techniques like HybISS would help to overcome this limitation. Collaborations on going in mouse and human. Furthermore, spatial transcriptomics does not only open the door for time-high-throughput profiling link, but also to 3D resolution integration. HiPlex or other Spatial transcriptomic approaches are image-based, therefore suited for registration into our 4D-CbF

Multimodal profiling of the developing CB

Overall, this works provides strong evidence of spatio-temporal developmental variability during embryonic and postnatal development of the CB. The next question is to understand how the variabilities observed at these different stages of the development, embryonic and postnatal, related to each other. Hence, we require high resolution molecular profiling during development. As previously discussed, during the last years scientists have provided the community with a myriad of available data

sets. However, they miss cell generation-time resolution. Thereby, during my thesis I have partly filled this gap by participating to the generation of a multimodal FT-enriched snRNAseq/snATACseq dataset for the embryonic cerebellar development, from E11 to E16 (**Figure 1**). FT was injected at E11, E12, E13, E14, E15, E16 and collections +1h, +6h, +12h and +24h after the injection. Primordium dissection and FACS sorting for FT⁺ cells detection was done, thus enriching for time-locked generated cells for a higher and unprecedented time resolution profiling during cerebellar development. Our preliminary results demonstrate the ability for capturing specifically FT⁺ cells at different point of cerebellar cell tracking and suggest dynamic molecular changes of cerebellar progenitors at that stage. However, further analyses are required to decipher cell-type specific underlying developmental programs.

Comprehensively, the work of this thesis provides the first steps towards a novel integrative view of cerebellar structure and development: the 4D-CbF. It also increases and improves the available datasets for the developing CB, providing detailed information about cerebellar progenitors behavioral, cellular, and cell birth dynamics during embryonic and perinatal development, as well as a high throughput transcriptomics analysis of the developing CB. Utterly, our results shed light into the time and space – dependent drive during the development of cerebellar structure and its cellular heterogeneity.

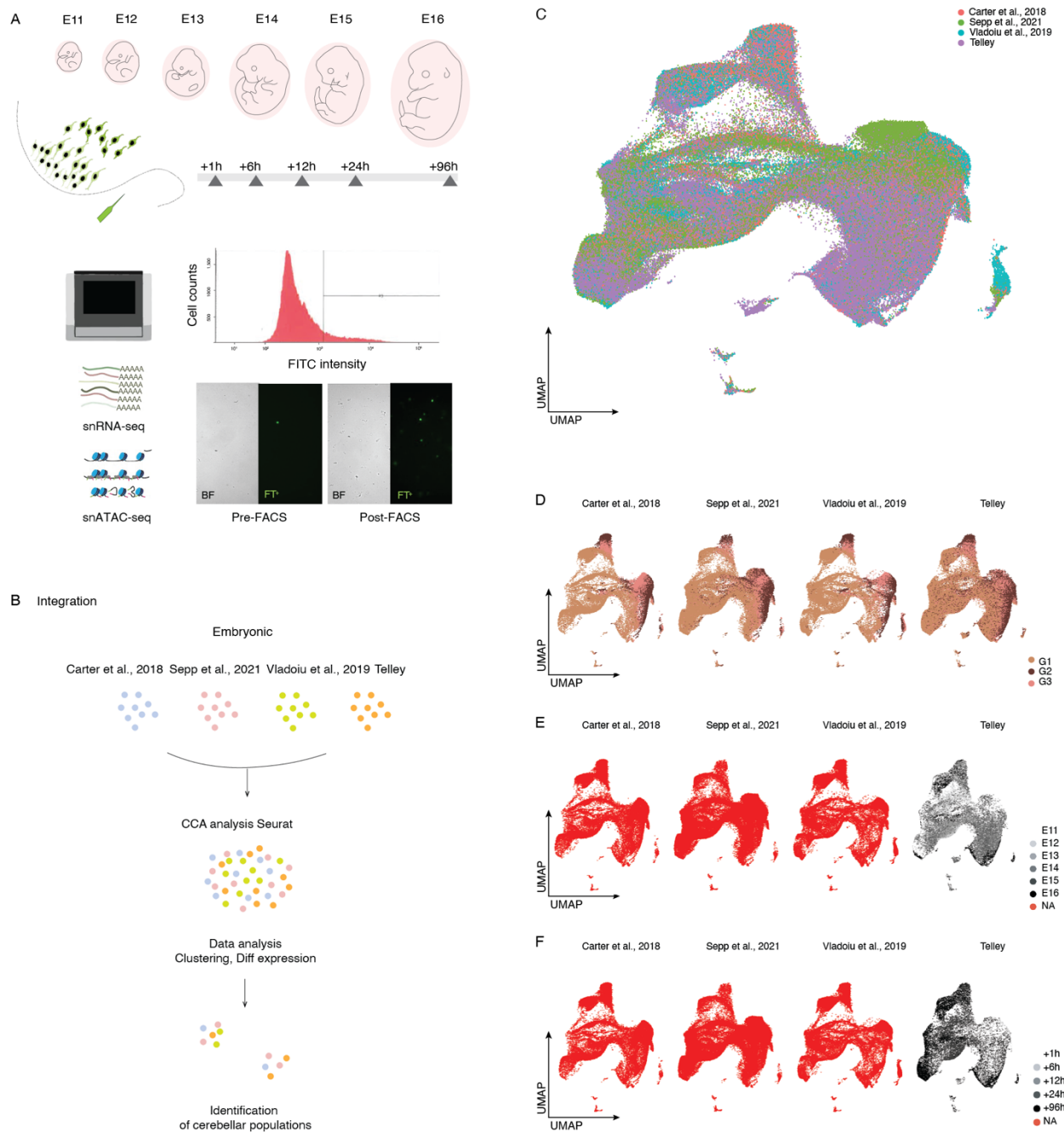


Figure 1. Perspectives: Embryonic cerebellar development profiling. **A)** Schematic representation of experimental approach. Embryos are injected with FT at E11, E12, E13, E14, E15, E16, and collected at +1h, +6h, +24h and +96h after injection. FT⁺ cerebellar primordiums are isolated prior nuclear extraction. FACS purification of FT⁺ cells allows enrichment of time-locked generated cells. snRNAseq and snATACseq. **B)** Schematic representation of embryonic cerebellar datasets integration and analysis. **C)** Integrated cells clustering for cerebellar cells during development. **D)** Individual data set cell clustering. Cell cycle-coloured. **E)** Injection time-coloured. **F)** Collection time-coloured.

TABLE M1 E11-E14 CP compartmentation

CT1						
Level1	Level2	Level3	Level 4	Level 5	Unique_ID	
Cerebellar primordium (CP)	Lateral (Lat)	Ventricular Zone (VZ)	C1	Precursor domain (PrC1)	CP_Lat_VZ_C1_PrC1	
				Post-mitotic domain (PmC1)	CP_Lat_VZ_C1_PmC1	
				Mantle zone (MC1)	CP_Lat_VZ_C1_MC1	
			C2	Precursor domain (PrC2)	CP_Lat_VZ_C2_PrC2	
				Post-mitotic domain (PmC2)	CP_Lat_VZ_C2_PmC2	
				Mantle zone (MC2)	CP_Lat_VZ_C2_MC2	
			Upper Rhombic Lip (URL) Subpial stream (SS) Nuclear Transitory zone (NTZ) Ventricular Zone (VZ)	C3	Precursor domain (PrC3)	CP_Lat_VZ_C3_PrC3
				Post-mitotic domain (PmC3)	CP_Lat_VZ_C3_PmC3	
				Mantle zone (MC3)	CP_Lat_VZ_C3_MC3	
				CP_Lat_URL		
				CP_Lat_EGL		
				CP_Lat_NTZ		
		Intermediate (Int)	Upper Rhombic Lip (URL) Subpial stream (SS) Nuclear Transitory zone (NTZ) Ventricular Zone (VZ)	C1	Precursor domain (PrC1)	CP_Int_VZ_C1_PrC1
				Post-mitotic domain (PmC1)	CP_Int_VZ_C1_PmC1	
				Mantle zone (MC1)	CP_Int_VZ_C1_MC1	
	C2			Precursor domain (PrC2)	CP_Int_VZ_C2_PrC2	
				Post-mitotic domain (PmC2)	CP_Int_VZ_C2_PmC2	
				Mantle zone (MC2)	CP_Int_VZ_C2_MC2	
			Upper Rhombic Lip (URL) Subpial stream (SS) Nuclear Transitory zone (NTZ) Ventricular Zone (VZ)	C3	Precursor domain (PrC3)	CP_Int_VZ_C3_PrC3
				Post-mitotic domain (PmC3)	CP_Int_VZ_C3_PmC3	
				Mantle zone (MC3)	CP_Int_VZ_C3_MC3	
				CP_Int_URL		
				CP_Int_EGL		
				CP_Int_NTZ		
	Medial (Med)	Upper Rhombic Lip (URL) Subpial stream (SS) Nuclear Transitory zone (NTZ) Ventricular Zone (VZ)	C1	Precursor domain (PrC1)	CP_Med_VZ_C1_PrC1	
			Post-mitotic domain (PmC1)	CP_Med_VZ_C1_PmC1		
			Mantle zone (MC1)	CP_Med_VZ_C1_MC1		
C2			Precursor domain (PrC2)	CP_Med_VZ_C2_PrC2		
			Post-mitotic domain (PmC2)	CP_Med_VZ_C2_PmC2		
			Mantle zone (MC2)	CP_Med_VZ_C2_MC2		
		Upper Rhombic Lip (URL) Subpial stream (SS) Nuclear Transitory zone (NTZ)	C3	Precursor domain (PrC3)	CP_Med_VZ_C3_PrC3	
			Post-mitotic domain (PmC3)	CP_Med_VZ_C3_PmC3		
			Mantle zone (MC3)	CP_Med_VZ_C3_MC3		
			CP_Med_URL			
			CP_Med_EGL			
			CP_Med_NTZ			

TABLE M2 P7 CB compartmentation

CT4									
Level1	Level2	Level3	Level5	Level4	Level6	Unique_ID			
Cerebellum (CB)	Cerebellar cortex (CBX)	Vermal regions (VERM)		Lingula I (LING)	PurkinjeMolecularLayer ExternalGranularLayer GranularLayer WhiteMatter	Lingula PurkinjeMolecularLayer (LINGpumol) Lingula ExternalGranularLayer (LINGextgr) Lingula GranularLayer (LINGgr) Lingula WhiteMatter (LINGwm)			
				Lobule II (CENT2)	PurkinjeMolecularLayer ExternalGranularLayer GranularLayer WhiteMatter	Lobule II PurkinjeMolecularLayer (CENT2pumol) Lobule II ExternalGranularLayer (CENT2extgr) Lobule II GranularLayer (CENT2gr) Lobule II WhiteMatter (CENT2wm)			
				Lobule III (CENT3)	PurkinjeMolecularLayer ExternalGranularLayer GranularLayer WhiteMatter	Lobule III PurkinjeMolecularLayer (CENT3pumol) Lobule III ExternalGranularLayer (CENT3extgr) Lobule III GranularLayer (CENT3gr) Lobule III WhiteMatter (CENT3wm)			
				Lobules IV- V (CUL4-5)	PurkinjeMolecularLayer ExternalGranularLayer GranularLayer WhiteMatter	Lobule IV-V PurkinjeMolecularLayer (CUL4-5pumol) Lobule IV-V ExternalGranularLayer (CUL4-5extgr) Lobule IV-V GranularLayer (CUL4-5gr) Lobule IV-V WhiteMatter (CUL4-5wm)			
				Declive VI (DEC)	PurkinjeMolecularLayer ExternalGranularLayer GranularLayer WhiteMatter	Declive VI PurkinjeMolecularLayer (DECpumol) Declive VI ExternalGranularLayer (DECextgr) Declive VI GranularLayer (DECgr) Declive VI WhiteMatter (DECwm)			
				Central region vermis (CENverm)		Folium-tuber vermis VII (FOTU)	PurkinjeMolecularLayer ExternalGranularLayer GranularLayer WhiteMatter	Folium tuber vermis VII PurkinjeMolecularLayer (FOTUpumol) Folium tuber vermis VII ExternalGranularLayer (FOTUextgr) Folium tuber vermis VII GranularLayer (FOTUgr) Folium tuber vermis VII WhiteMatter (FOTUwm)	
							PurkinjeMolecularLayer ExternalGranularLayer GranularLayer WhiteMatter	Pyramus VIII PurkinjeMolecularLayer (PYRpumol) Pyramus VIII ExternalGranularLayer (PYRextgr) Pyramus VIII GranularLayer (PYRgr) Pyramus VIII WhiteMatter (PYRwm)	
							PurkinjeMolecularLayer ExternalGranularLayer GranularLayer WhiteMatter	Uvula IX PurkinjeMolecularLayer (UVUpumol) Uvula IX ExternalGranularLayer (UVUextgr) Uvula IX GranularLayer (UVUgr) Uvula IX WhiteMatter (UVUwm)	
				Posterior region vermis (POSTverm)		Nodulus X (NOD)	PurkinjeMolecularLayer ExternalGranularLayer GranularLayer WhiteMatter	Nodulus X PurkinjeMolecularLayer (NODpumol) Nodulus X ExternalGranularLayer (NODextgr) Nodulus X GranularLayer (NODgr) Nodulus X WhiteMatter (NODwm)	
							PurkinjeMolecularLayer ExternalGranularLayer GranularLayer WhiteMatter	Simple Lobule PurkinjeMolecularLayer (SIMpumol) Simple Lobule ExternalGranularLayer (SIMextgr) Simple Lobule GranularLayer (SIMgr) Simple Lobule WhiteMatter (SIMwm)	
							PurkinjeMolecularLayer ExternalGranularLayer GranularLayer WhiteMatter	Crus 1 PurkinjeMolecularLayer (ANcr1pumol) Crus 1 ExternalGranularLayer (ANcr1extgr) Crus 1 GranularLayer (ANcr1gr) Crus 1 WhiteMatter (ANcr1wm)	
				Anterior region paravermis (ANTpar)		Simple Lobule (SIM)	PurkinjeMolecularLayer ExternalGranularLayer GranularLayer WhiteMatter	Crus 2 PurkinjeMolecularLayer (ANcr2pumol) Crus 2 ExternalGranularLayer (ANcr2extgr) Crus 2 GranularLayer (ANcr2gr) Crus 2 WhiteMatter (ANcr2wm)	
							PurkinjeMolecularLayer ExternalGranularLayer GranularLayer WhiteMatter	Paramedian Lobule PurkinjeMolecularLayer (PRM_pumol) Paramedian Lobule ExternalGranularLayer (PRMextgr) Paramedian Lobule GranularLayer (PRMgr) Paramedian Lobule WhiteMatter (PRMwm)	
							PurkinjeMolecularLayer ExternalGranularLayer GranularLayer WhiteMatter	Copula Pyramidis PurkinjeMolecularLayer (COPYpumol) Copula Pyramidis ExternalGranularLayer (COPYextgr) Copula Pyramidis GranularLayer (COPYgr) Copula Pyramidis WhiteMatter (COPYwm)	
				Paravermal regions (PAR)		Crus 1 (ANcr1)	PurkinjeMolecularLayer ExternalGranularLayer GranularLayer WhiteMatter	Crus 1 PurkinjeMolecularLayer (ANcr1pumol) Crus 1 ExternalGranularLayer (ANcr1extgr) Crus 1 GranularLayer (ANcr1gr) Crus 1 WhiteMatter (ANcr1wm)	
		PurkinjeMolecularLayer ExternalGranularLayer GranularLayer WhiteMatter	Crus 2 PurkinjeMolecularLayer (ANcr2pumol) Crus 2 ExternalGranularLayer (ANcr2extgr) Crus 2 GranularLayer (ANcr2gr) Crus 2 WhiteMatter (ANcr2wm)						
		PurkinjeMolecularLayer ExternalGranularLayer GranularLayer WhiteMatter	Paramedian Lobule PurkinjeMolecularLayer (PRM_pumol) Paramedian Lobule ExternalGranularLayer (PRMextgr) Paramedian Lobule GranularLayer (PRMgr) Paramedian Lobule WhiteMatter (PRMwm)						
		Central region paravermis (CENpar)		Paramedian Lobule (PRM)	PurkinjeMolecularLayer ExternalGranularLayer GranularLayer WhiteMatter	Copula Pyramidis PurkinjeMolecularLayer (COPYpumol) Copula Pyramidis ExternalGranularLayer (COPYextgr) Copula Pyramidis GranularLayer (COPYgr) Copula Pyramidis WhiteMatter (COPYwm)			
					PurkinjeMolecularLayer ExternalGranularLayer GranularLayer WhiteMatter	Simple Lobule PurkinjeMolecularLayer (SIMpumol) Simple Lobule ExternalGranularLayer (SIMextgr) Simple Lobule GranularLayer (SIMgr) Simple Lobule WhiteMatter (SIMwm)			
					PurkinjeMolecularLayer ExternalGranularLayer GranularLayer WhiteMatter	Crus 1 PurkinjeMolecularLayer (ANcr1pumol) Crus 1 ExternalGranularLayer (ANcr1extgr) Crus 1 GranularLayer (ANcr1gr) Crus 1 WhiteMatter (ANcr1wm)			
		Anterior region hemisphere (ANThem)		Simple Lobule (SIM)	PurkinjeMolecularLayer ExternalGranularLayer GranularLayer WhiteMatter	Crus 2 PurkinjeMolecularLayer (ANcr2pumol) Crus 2 ExternalGranularLayer (ANcr2extgr) Crus 2 GranularLayer (ANcr2gr) Crus 2 WhiteMatter (ANcr2wm)			
					PurkinjeMolecularLayer ExternalGranularLayer GranularLayer WhiteMatter	Paramedian Lobule PurkinjeMolecularLayer (PRM_pumol) Paramedian Lobule ExternalGranularLayer (PRMextgr) Paramedian Lobule GranularLayer (PRMgr) Paramedian Lobule WhiteMatter (PRMwm)			
					PurkinjeMolecularLayer ExternalGranularLayer GranularLayer WhiteMatter	Copula Pyramidis PurkinjeMolecularLayer (COPYpumol) Copula Pyramidis ExternalGranularLayer (COPYextgr) Copula Pyramidis GranularLayer (COPYgr) Copula Pyramidis WhiteMatter (COPYwm)			
		Crus 1 (ANcr1)			PurkinjeMolecularLayer ExternalGranularLayer GranularLayer WhiteMatter	Crus 1 PurkinjeMolecularLayer (ANcr1pumol) Crus 1 ExternalGranularLayer (ANcr1extgr) Crus 1 GranularLayer (ANcr1gr) Crus 1 WhiteMatter (ANcr1wm)			
					PurkinjeMolecularLayer ExternalGranularLayer GranularLayer WhiteMatter	Crus 2 PurkinjeMolecularLayer (ANcr2pumol) Crus 2 ExternalGranularLayer (ANcr2extgr) Crus 2 GranularLayer (ANcr2gr) Crus 2 WhiteMatter (ANcr2wm)			
					PurkinjeMolecularLayer ExternalGranularLayer GranularLayer WhiteMatter	Paramedian Lobule PurkinjeMolecularLayer (PRM_pumol) Paramedian Lobule ExternalGranularLayer (PRMextgr) Paramedian Lobule GranularLayer (PRMgr) Paramedian Lobule WhiteMatter (PRMwm)			
		Crus 2 (ANcr2)			PurkinjeMolecularLayer ExternalGranularLayer GranularLayer WhiteMatter	Crus 2 PurkinjeMolecularLayer (ANcr2pumol) Crus 2 ExternalGranularLayer (ANcr2extgr) Crus 2 GranularLayer (ANcr2gr) Crus 2 WhiteMatter (ANcr2wm)			
					PurkinjeMolecularLayer ExternalGranularLayer GranularLayer WhiteMatter	Paramedian Lobule PurkinjeMolecularLayer (PRM_pumol) Paramedian Lobule ExternalGranularLayer (PRMextgr) Paramedian Lobule GranularLayer (PRMgr) Paramedian Lobule WhiteMatter (PRMwm)			
					PurkinjeMolecularLayer ExternalGranularLayer GranularLayer WhiteMatter	Copula Pyramidis PurkinjeMolecularLayer (COPYpumol) Copula Pyramidis ExternalGranularLayer (COPYextgr) Copula Pyramidis GranularLayer (COPYgr) Copula Pyramidis WhiteMatter (COPYwm)			
		Central region hemisphere (CENhem)		Paramedian Lobule (PRM)	PurkinjeMolecularLayer ExternalGranularLayer GranularLayer WhiteMatter	Paraflocculus PurkinjeMolecularLayer (PFLpumol) Paraflocculus ExternalGranularLayer (PFLextgr) Paraflocculus GranularLayer (PFLgr) Paraflocculus WhiteMatter (PFLwm)			
					PurkinjeMolecularLayer ExternalGranularLayer GranularLayer WhiteMatter	Flocculus PurkinjeMolecularLayer (FLpumol) Flocculus ExternalGranularLayer (FLextgr) Flocculus GranularLayer (FLgr) Flocculus WhiteMatter (FLwm)			
					PurkinjeMolecularLayer ExternalGranularLayer GranularLayer WhiteMatter	Cerebellar Nuclei Cerebellar Nuclei Cerebellar Nuclei			
		Posterior region hemisphere (POSThem)		Paraflocculus (PFL)	PurkinjeMolecularLayer ExternalGranularLayer GranularLayer WhiteMatter	Paraflocculus PurkinjeMolecularLayer (PFLpumol) Paraflocculus ExternalGranularLayer (PFLextgr) Paraflocculus GranularLayer (PFLgr) Paraflocculus WhiteMatter (PFLwm)			
					PurkinjeMolecularLayer ExternalGranularLayer GranularLayer WhiteMatter	Flocculus PurkinjeMolecularLayer (FLpumol) Flocculus ExternalGranularLayer (FLextgr) Flocculus GranularLayer (FLgr) Flocculus WhiteMatter (FLwm)			
					PurkinjeMolecularLayer ExternalGranularLayer GranularLayer WhiteMatter	Cerebellar Nuclei Cerebellar Nuclei Cerebellar Nuclei			
		Fastigial Nucleus (FN) Interposed Nucleus (IP) Dentate Nucleus (DN)			PurkinjeMolecularLayer ExternalGranularLayer GranularLayer WhiteMatter	Paraflocculus PurkinjeMolecularLayer (PFLpumol) Paraflocculus ExternalGranularLayer (PFLextgr) Paraflocculus GranularLayer (PFLgr) Paraflocculus WhiteMatter (PFLwm)			
					PurkinjeMolecularLayer ExternalGranularLayer GranularLayer WhiteMatter	Flocculus PurkinjeMolecularLayer (FLpumol) Flocculus ExternalGranularLayer (FLextgr) Flocculus GranularLayer (FLgr) Flocculus WhiteMatter (FLwm)			
					PurkinjeMolecularLayer ExternalGranularLayer GranularLayer WhiteMatter	Cerebellar Nuclei Cerebellar Nuclei Cerebellar Nuclei			

TABLE M3 ANOVA Post-hoc tests

Figure 3C

Within	Group 1	Group 2	t-value	Ddof	p-value (uncorrected)	p-value (corrected)
intermediate	E11	E12	5.11	4	0.0069	0.055
intermediate	E11	E13	9.50	4	0.0006	*0.048
intermediate	E11	E14	12.86	4	0.0002	*0.048
intermediate	E11	E15	11.62	4	0.0003	*0.048
intermediate	E12	E13	1.62	4	0.1813	0.229
intermediate	E12	E14	4.20	4	0.0137	0.061
intermediate	E12	E15	3.10	4	0.0361	0.084
intermediate	E13	E14	8.84	4	0.0009	*0.049
intermediate	E13	E15	5.29	4	0.0061	0.054
intermediate	E14	E15	-7.82	4	0.0014	*0.049
lateral	E11	E12	3.40	4	0.0272	0.075
lateral	E11	E13	3.24	4	0.0315	0.079
lateral	E11	E14	7.28	4	0.0018	0.050
lateral	E11	E15	6.67	4	0.0026	0.050
lateral	E12	E13	-0.82	4	0.4586	0.506
lateral	E12	E14	3.01	4	0.0394	0.087
lateral	E12	E15	2.34	4	0.0791	0.127
lateral	E13	E14	6.43	4	0.0030	0.051
lateral	E13	E15	5.32	4	0.0059	0.054
lateral	E14	E15	-6.30	4	0.0032	0.051
medial	E11	E12	3.90	4	0.0176	0.065
medial	E11	E13	20.20	4	0.00004	*0.048
medial	E11	E14	21.06	4	0.00003	*0.048
medial	E11	E15	19.06	4	0.00004	*0.048
medial	E12	E13	7.59	4	0.0016	*0.049
medial	E12	E14	8.18	4	0.0012	*0.049
medial	E12	E15	7.11	4	0.0020	0.050
medial	E13	E14	2.90	4	0.0441	0.092
medial	E13	E15	-1.79	4	0.1479	0.196
medial	E14	E15	-4.19	4	0.0137	0.062
E11	intermediate	lateral	0.12	2	0.913	0.961
E11	intermediate	medial	-1.75	2	0.222	0.269
E11	lateral	medial	-2.99	2	0.096	0.144
E12	intermediate	lateral	0.22	2	0.846	0.894
E12	intermediate	medial	-4.07	2	0.055	0.103
E12	lateral	medial	-2.24	2	0.155	0.203
E13	intermediate	lateral	-2.74	2	0.112	0.159
E13	intermediate	medial	4.71	2	0.042	0.090
E13	lateral	medial	6.17	2	0.025	0.073
E14	intermediate	lateral	0.19	2	0.868	0.915
E14	intermediate	medial	-10.68	2	0.009	0.056
E14	lateral	medial	-1.91	2	0.196	0.244
E15	intermediate	lateral	1.55	2	0.260	0.308
E15	intermediate	medial	-1.39	2	0.300	0.348
E15	lateral	medial	-7.79	2	0.016	0.064

TABLE M4 ANOVA Post-hoc tests

Figure 3D VZ (Pr)

Within	Group 1	Group 2	t-value	Ddof	p-value (uncorrected)	p-value (corrected)
age	E11	E12	5.19	4	0.0065	*0.040
age	E11	E13	14.70	4	0.0001	*0.033
age	E12	E13	7.83	4	0.0014	*0.034

TABLE M5 ANOVA Post-hoc tests

Figure 3D VZ (Pr) medio-lateral

Within	Group 1	Group 2	t-value	Ddof	p-value (uncorrected)	p-value (corrected)
intermediate	E11	E12	2.18	2.43	0.139	0.186
intermediate	E11	E13	13.30	1.88	0.007	0.054
intermediate	E12	E13	3.06	4	0.038	0.085
lateral	E11	E12	9.27	2.46	0.006	0.053
lateral	E11	E13	3.32	2.19	0.071	0.118
lateral	E12	E13	-2.30	4	0.083	0.130
medial	E11	E12	0.56	2.30	0.628	0.675
medial	E11	E13	12.08	2.87	0.001	*0.049
medial	E12	E13	5.77	4	0.004	0.052
E11	intermediate	lateral	-1.78	1	0.326	0.373
E11	intermediate	medial	-4.48	1	0.140	0.187
E11	lateral	medial	1.38	1	0.400	0.447
E12	intermediate	lateral	1.68	2	0.234	0.282
E12	intermediate	medial	-3.49	2	0.073	0.120
E12	lateral	medial	-3.64	2	0.068	0.115
E13	intermediate	lateral	-2.73	2	0.112	0.159
E13	intermediate	medial	1.35	2	0.310	0.357
E13	lateral	medial	7.48	2	0.017	0.065

TABLE M6 ANOVA Post-hoc tests

Figure 3D (RL)

Within	Group 1	Group 2	t-value	Ddof	p-value (uncorrected)	p-value (corrected)
age	E11	E12	7.04	4	0.002	*0.035
age	E11	E13	4.16	4	0.014	*0.047
age	E12	E13	-5.36	4	0.006	*0.038

TABLE M7 ANOVA Post-hoc tests

Figure 3D (RL) medio-lateral

Within	Group 1	Group 2	t-value	Ddof	p-value (uncorrected)	p-value (corrected)
intermediate	E11	E12	1.64	2.90	0.2024	0.250
intermediate	E11	E13	-0.06	2.67	0.9530	1.000
intermediate	E12	E13	-1.69	4	0.1671	0.214
lateral	E11	E12	15.78	2.13	0.0031	0.050
lateral	E11	E13	1.60	2.08	0.2462	0.293
lateral	E12	E13	-8.77	4	0.0009	*0.048

medial	E11	E12	8.56	2.21	0.0098	0.057
medial	E11	E13	4.94	2.07	0.0358	0.083
medial	E12	E13	-0.15	4	0.8917	0.939
E11	intermediate	lateral	-4.33	1	0.1444	0.192
E11	intermediate	medial	-3.31	1	0.1869	0.234
E11	lateral	medial	-0.32	1	0.8028	0.850
E12	intermediate	lateral	0.90	2	0.4613	0.508
E12	intermediate	medial	0.23	2	0.8419	0.889
E12	lateral	medial	-1.03	2	0.4108	0.458
E13	intermediate	lateral	-1.63	2	0.2446	0.292
E13	intermediate	medial	1.44	2	0.2876	0.335
E13	lateral	medial	5.93	2	0.0273	0.074

TABLE M8 ANOVA Post-hoc tests

Figure 5C VZ (Pr)

Within	Group 1	Group 2	t-value	Ddof	p-value (uncorrected)	p-value (corrected)
age	E11	E12	-5.28	4	0.006	*0.039
age	E11	E13	-3.36	4	0.028	0.061
age	E12	E13	-2.18	4	0.095	0.128

TABLE M9 ANOVA Post-hoc tests

Figure 9D medio-lateral

Within	Group 1	Group 2	t-value	Ddof	p-value (uncorrected)	p-value (corrected)
HEM	E11	E12	1.06	16.97	0.3046	0.3535
HEM	E11	E13	2.33	8.20	0.0471	0.0959
HEM	E11	E14	4.25	10.84	0.0014	0.0503
HEM	E11	E15	4.38	11.16	0.0011	*0.0499
HEM	E11	E16	4.54	10.62	0.0009	*0.0498
HEM	E12	E13	1.48	6.72	0.1846	0.2334
HEM	E12	E14	3.28	14	0.0055	0.0543
HEM	E12	E15	3.44	8.09	0.0087	0.0575
HEM	E12	E16	3.61	7.57	0.0075	0.0564
HEM	E13	E14	0.75	3.21	0.5048	0.5537
HEM	E13	E15	0.91	3.33	0.4241	0.4729
HEM	E13	E16	1.00	3.15	0.3890	0.4378
HEM	E14	E15	0.58	4.73	0.5911	0.6400
HEM	E14	E16	1.01	10.81	0.3335	0.3824
HEM	E15	E16	0.26	3.86	0.8048	0.8536
PAR	E11	E12	-3.40	7.37	0.0106	0.0595
PAR	E11	E13	-0.35	3.24	0.7450	0.7939
PAR	E11	E14	1.13	16.27	0.2747	0.3236
PAR	E11	E15	0.24	2.82	0.8247	0.8736
PAR	E11	E16	3.00	10.56	0.0126	0.0615
PAR	E12	E13	2.44	9.55	0.0360	0.0849
PAR	E12	E14	3.66	14	0.0026	0.0515
PAR	E12	E15	3.32	8.50	0.0097	0.0586
PAR	E12	E16	3.94	7.01	0.0056	0.0545
PAR	E13	E14	0.67	3.26	0.5471	0.5959
PAR	E13	E15	0.44	4.11	0.6831	0.7320
PAR	E13	E16	0.97	3.01	0.4053	0.4542
PAR	E14	E15	-0.41	2.86	0.7135	0.7624

PAR	E14	E16	1.35	7.37	0.2162	0.2650
PAR	E15	E16	1.06	2.02	0.3990	0.4479
VER	E11	E12	-2.15	8.75	0.0607	0.1096
VER	E11	E13	0.24	3.84	0.8201	0.8690
VER	E11	E14	4.22	14.84	0.0008	*0.0496
VER	E11	E15	5.38	10.16	0.0003	*0.0492
VER	E11	E16	5.61	10.28	0.0002	0.0491
VER	E12	E13	1.83	8.69	0.1022	0.1510
VER	E12	E14	3.90	14	0.0016	0.0505
VER	E12	E15	4.18	7.01	0.0041	0.0530
VER	E12	E16	4.26	7.02	0.0037	0.0526
VER	E13	E14	1.47	3.24	0.2315	0.2803
VER	E13	E15	1.72	3.01	0.1832	0.2320
VER	E13	E16	1.81	3.01	0.1671	0.2159
VER	E14	E15	1.13	7.38	0.2949	0.3438
VER	E14	E16	1.57	7.68	0.1573	0.2061
VER	E15	E16	1.66	5.97	0.1489	0.1978
E11	HEM	PAR	4.76	10	0.0008	*0.0496
E11	HEM	VER	2.49	10	0.0319	0.0807
E11	PAR	VER	-3.83	10	0.0033	0.0522
E12	HEM	PAR	-1.46	7	0.1869	0.2357
E12	HEM	VER	-1.18	7	0.2766	0.3255
E12	PAR	VER	-0.07	7	0.9447	0.9935
E13	HEM	PAR	2.37	3	0.0984	0.1473
E13	HEM	VER	-3.60	3	0.0368	0.0856
E13	PAR	VER	-3.32	3	0.0452	0.0940
E14	HEM	PAR	0.32	7	0.7612	0.8100
E14	HEM	VER	-0.16	7	0.8753	0.9241
E14	PAR	VER	-0.39	7	0.7095	0.7583
E15	HEM	PAR	-1.28	2	0.3295	0.3784
E15	HEM	VER	0.14	2	0.9037	0.9525
E15	PAR	VER	0.65	2	0.5816	0.6305
E16	HEM	PAR	0.74	4	0.5013	0.5502
E16	HEM	VER	0.35	4	0.7415	0.7904
E16	PAR	VER	-1.40	4	0.2343	0.2832

TABLE M10 ANOVA Post-hoc tests

Figure 9D (PCs) antero-posterior

Within	Group 1	Group 2	t-value	Ddof	p-value (uncorrected)	p-value (corrected)
Anterior	E11	E12	-2.32	12.87	0.0375	0.086
Anterior	E11	E13	0.47	4.00	0.6609	0.710
Anterior	E11	E14	3.54	14.21	0.0032	0.052
Anterior	E11	E15	3.17	12.99	0.0074	0.056
Anterior	E11	E16	4.04	11.55	0.0018	0.051
Anterior	E12	E13	1.87	5.23	0.1183	0.167
Anterior	E12	E14	5.16	8.45	0.0007	0.050
Anterior	E12	E15	4.89	8.72	0.0009	0.050
Anterior	E12	E16	5.51	7.52	0.0007	0.050
Anterior	E13	E14	1.04	3.22	0.3690	0.418
Anterior	E13	E15	0.92	6	0.3920	0.441
Anterior	E13	E16	1.16	3.08	0.3262	0.375
Anterior	E14	E15	-0.39	7.47	0.7058	0.755
Anterior	E14	E16	0.50	11.77	0.6286	0.677
Anterior	E15	E16	0.90	4.56	0.4140	0.463
Central	E11	E12	-2.26	12.20	0.0428	0.092
Central	E11	E13	1.86	5.58	0.1167	0.166

Central	E11	E14	4.74	11.21	0.0006	*0.049
Central	E11	E15	4.85	11.14	0.0005	*0.049
Central	E11	E16	5.26	10.25	0.0003	*0.049
Central	E12	E13	3.43	8.46	0.0082	0.057
Central	E12	E14	5.64	7.33	0.0007	0.050
Central	E12	E15	5.71	7.33	0.0006	*0.049
Central	E12	E16	5.95	7.07	0.0006	*0.049
Central	E13	E14	0.87	3.15	0.4463	0.495
Central	E13	E15	0.94	6	0.3835	0.432
Central	E13	E16	1.13	3.03	0.3388	0.388
Central	E14	E15	0.33	8.67	0.7501	0.799
Central	E14	E16	1.50	10.75	0.1622	0.211
Central	E15	E16	1.07	4.22	0.3421	0.391
Posterior	E11	E12	-0.67	16.86	0.5103	0.559
Posterior	E11	E13	0.20	5.27	0.8506	0.899
Posterior	E11	E14	2.11	14.69	0.0527	0.102
Posterior	E11	E15	2.53	12.71	0.0255	0.074
Posterior	E11	E16	3.45	10.13	0.0061	0.055
Posterior	E12	E13	0.67	4.27	0.5399	0.589
Posterior	E12	E14	3.50	12.53	0.0041	0.053
Posterior	E12	E15	4.09	9.91	0.0022	0.051
Posterior	E12	E16	5.62	7.15	0.0007	0.050
Posterior	E13	E14	1.12	3.57	0.3320	0.381
Posterior	E13	E15	1.36	6	0.2218	0.271
Posterior	E13	E16	1.81	3.01	0.1669	0.216
Posterior	E14	E15	0.59	9.75	0.5674	0.616
Posterior	E14	E16	2.10	8.38	0.0676	0.116
Posterior	E15	E16	1.51	3.19	0.2228	0.272
E11	Anterior	Central	-0.90	10	0.3874	0.436
E11	Anterior	Posterior	2.42	10	0.0364	0.085
E11	Central	Posterior	4.81	10	0.0007	0.050
E12	Anterior	Central	-0.46	7	0.6562	0.705
E12	Anterior	Posterior	4.74	7	0.0021	0.051
E12	Central	Posterior	5.01	7	0.0016	0.050
E13	Anterior	Central	1.48	3	0.2363	0.285
E13	Anterior	Posterior	0.96	3	0.4079	0.457
E13	Central	Posterior	0.34	3	0.7572	0.806
E14	Anterior	Central	0.18	8	0.8605	0.909
E14	Anterior	Posterior	0.02	8	0.9814	1.030
E14	Central	Posterior	-0.22	8	0.8328	0.882
E15	Anterior	Central	1.56	3	0.2175	0.266
E15	Anterior	Posterior	0.78	3	0.4943	0.543
E15	Central	Posterior	0.02	3	0.9868	1.036
E16	Anterior	Central	0.67	4	0.5417	0.591
E16	Anterior	Posterior	1.00	4	0.3739	0.423
E16	Central	Posterior	0.55	4	0.6094	0.658

TABLE M11 ANOVA Post-hoc tests

Figure 9F (UBCs) medio-lateral

Within	Group 1	Group 2	t-value	Ddof	p-value (uncorrected)	p-value (corrected)
HEM	E11	E12	-0.90	3.15	0.432	0.480
HEM	E11	E13	-1.27	2.15	0.323	0.372
HEM	E11	E14	-1.31	3.30	0.272	0.321
HEM	E11	E15	-0.73	2.26	0.533	0.581

HEM	E11	E16	1.66	1.80	0.251	0.300
HEM	E12	E13	-0.12	5.00	0.909	0.958
HEM	E12	E14	-0.02	6	0.985	1.034
HEM	E12	E15	0.38	4.71	0.723	0.772
HEM	E12	E16	1.22	3.06	0.308	0.357
HEM	E13	E14	0.12	4.38	0.908	0.957
HEM	E13	E15	0.58	4	0.593	0.642
HEM	E13	E16	1.67	4	0.170	0.219
HEM	E14	E15	0.50	4.96	0.638	0.687
HEM	E14	E16	1.79	3.13	0.168	0.217
HEM	E15	E16	1.25	4	0.280	0.329
PAR	E11	E12	-0.85	3.24	0.453	0.502
PAR	E11	E13	-1.11	2.32	0.367	0.416
PAR	E11	E14	-2.94	3.87	0.044	0.093
PAR	E11	E15	-2.20	2.64	0.127	0.176
PAR	E11	E16	-1.95	2.89	0.150	0.198
PAR	E12	E13	0.04	4.90	0.967	1.015
PAR	E12	E14	-0.17	6	0.867	0.916
PAR	E12	E15	-0.23	4.16	0.829	0.878
PAR	E12	E16	0.06	3.74	0.957	1.006
PAR	E13	E14	-0.31	2.70	0.779	0.828
PAR	E13	E15	-0.37	4	0.733	0.782
PAR	E13	E16	0.01	4	0.994	1.043
PAR	E14	E15	-0.13	3.52	0.903	0.952
PAR	E14	E16	0.52	4.27	0.627	0.676
PAR	E15	E16	0.53	4	0.622	0.671
VER	E11	E12	-0.67	3.43	0.547	0.596
VER	E11	E13	-2.56	2.22	0.113	0.162
VER	E11	E14	-6.09	3.22	0.007	0.056
VER	E11	E15	-3.00	2.05	0.092	0.141
VER	E11	E16	-3.26	2.10	0.077	0.126
VER	E12	E13	-1.56	4.38	0.187	0.236
VER	E12	E14	-4.70	6	0.003	0.052
VER	E12	E15	-2.54	2.67	0.095	0.144
VER	E12	E16	-2.52	3.29	0.078	0.127
VER	E13	E14	-3.13	5.00	0.026	0.075
VER	E13	E15	-1.58	4	0.190	0.239
VER	E13	E16	-1.26	4	0.277	0.325
VER	E14	E15	0.55	3.36	0.619	0.668
VER	E14	E16	1.41	4.33	0.227	0.276
VER	E15	E16	0.54	4	0.616	0.665
E11	HEM	PAR	2.29	1	0.262	0.311
E11	HEM	VER	0.73	1	0.601	0.649
E11	PAR	VER	-49.90	1	0.013	0.062
E12	HEM	PAR	1.89	3	0.155	0.204
E12	HEM	VER	1.13	3	0.339	0.388
E12	PAR	VER	-1.06	3	0.368	0.417
E13	HEM	PAR	2.57	2	0.124	0.172
E13	HEM	VER	0.02	2	0.983	1.032
E13	PAR	VER	-1.53	2	0.266	0.315
E14	HEM	PAR	1.20	3	0.315	0.364
E14	HEM	VER	-3.20	3	0.049	0.098
E14	PAR	VER	-5.63	3	0.011	0.060
E15	HEM	PAR	0.68	2	0.565	0.614
E15	HEM	VER	-1.43	2	0.289	0.338
E15	PAR	VER	-3.19	2	0.086	0.135
E16	HEM	PAR	-1.47	2	0.280	0.329
E16	HEM	VER	-3.92	2	0.059	0.108
E16	PAR	VER	-4.14	2	0.054	0.103

- [1] T. C. Lacalli, "Apical organs, epithelial domains, and the origin of the chordate central nervous system," *Integrative and Comparative Biology*, vol. 34, no. 4, pp. 533–541, 1994, doi: 10.1093/icb/34.4.533.
- [2] C. Hudson, "The central nervous system of ascidian larvae," *Wiley Interdisciplinary Reviews: Developmental Biology*, vol. 5, no. 5, pp. 538–561, 2016, doi: 10.1002/wdev.239.
- [3] N. L. Cerminara, E. J. Lang, R. v Sillitoe, and R. Apps, "Redefining the cerebellar cortex," *Nature Publishing Group*, vol. 16, no. 2, pp. 79–93, 2015, doi: 10.1038/nrn3886.
- [4] K. Leto *et al.*, "Consensus Paper: Cerebellar Development," *The Cerebellum*, vol. 15, no. 6, pp. 789–828, 2016, doi: 10.1007/s12311-015-0724-2.
- [5] P. L. Strick, R. P. Dum, and J. A. Fiez, "Cerebellum and Nonmotor Function," *Annual Review of Neuroscience*, vol. 32, no. 1, pp. 413–434, 2009, doi: 10.1146/annurev.neuro.31.060407.125606.
- [6] I. Carta, C. H. Chen, A. L. Schott, S. Dorizan, and K. Khodakhah, "Cerebellar modulation of the reward circuitry and social behavior," *Science (1979)*, vol. 363, no. 6424, 2019, doi: 10.1126/science.aav0581.
- [7] E. D'Angelo and S. Casali, "Seeking a unified framework for cerebellar function and dysfunction: From circuit operations to cognition," *Frontiers in Neural Circuits*, vol. 6, no. DEC, pp. 1–23, 2012, doi: 10.3389/fncir.2012.00116.
- [8] M. Watabe-Uchida, L. Zhu, S. K. Ogawa, A. Vamanrao, and N. Uchida, "Whole-Brain Mapping of Direct Inputs to Midbrain Dopamine Neurons," *Neuron*, vol. 74, no. 5, pp. 858–873, 2012, doi: 10.1016/j.neuron.2012.03.017.
- [9] and L. L. Kevin T. Beier^{1, 2}, Elizabeth E. Steinberg², Katherine E. DeLoach¹, Stanley Xie¹, Kazunari Miyamichi^{1, 5}, Lindsay Schwarz¹, Xiaojing J. Gao^{1, 6}, Eric J. Kremer^{3, 4}, Robert C. Malenka^{2,*}, "Circuit Architecture of VTA Dopamine Neurons Revealed by Systematic Input–Output Mapping," *Cell*, vol. 162, no. 3, pp. 622–623, 2015, doi: 10.1016/j.cell.2015.07.015.
- [10] S. S.-H. Wang, A. D. Kloth, and A. Badura, "The Cerebellum, Sensitive Periods, and Autism," *Neuron*, vol. 83, no. 3, pp. 518–532, 2014, doi: 10.1016/j.neuron.2014.07.016.
- [11] P. Haldipur *et al.*, "Spatiotemporal expansion of primary progenitor zones in the developing human cerebellum," *Science (1979)*, vol. 366, no. 6464, pp. 454–460, 2019, doi: 10.1126/science.aax7526.
- [12] S. Ramon y Cajal, "Sobre las fibras nerviosas de la capa molecular del cerebelo," *Revista trimestral de Histología Normal y Patológica*, vol. 2, pp. 33–49, 1888, doi: 10.1016/b978-84-458-1764-3.50004-4.
- [13] C. Sotelo, "Viewing the Cerebellum through the Eyes of Ramón Y Cajal," no. October, pp. 517–522, 2008, doi: 10.1007/s12311-008-0078-0.
- [14] Q. Wang *et al.*, "The Allen Mouse Brain Common Coordinate Framework: A 3D Reference Atlas," *Cell*, vol. 181, no. 4, pp. 936–953.e20, 2020, doi: 10.1016/j.cell.2020.04.007.
- [15] N. A. Bermingham *et al.*, "Proprioceptor pathway development is dependent on MATH1," *Neuron*, vol. 30, no. 2, pp. 411–422, 2001, doi: 10.1016/S0896-6273(01)00305-1.
- [16] H. Neuroscience, S. Herculano-houzel, and R. Barton, "The human brain in numbers : a linearly scaled-up primate brain," vol. 3, no. November, pp. 1–11, 2009, doi: 10.3389/neuro.09.031.2009.
- [17] K. Leto *et al.*, "Consensus Paper: Cerebellar Development," *Cerebellum*, vol. 15, no. 6, pp. 789–828, 2016, doi: 10.1007/s12311-015-0724-2.
- [18] K. Schilling, J. Oberdick, F. Rossi, and S. L. Baader, "Besides Purkinje cells and granule neurons : an appraisal of the cell biology of the interneurons of the cerebellar cortex," *Histochemistry and Cell Biology*, vol. 130, pp. 601–615, 2008, doi: 10.1007/s00418-008-0483-y.
- [19] R. v. Sillitoe, Y. H. Fu, and C. Watson, *Cerebellum*. Elsevier Inc., 2012. Doi: 10.1016/B978-0-12-369497-3.10011-1.
- [20] A. Sudarov, R. K. Turnbull, E. J. Kim, M. Lebel-Potter, F. Guillemot, and A. L. Joyner, "Ascl1 Genetics Reveals Insights into Cerebellum Local Circuit Assembly," *Journal of Neuroscience*, vol. 31, no. 30, pp. 11055–11069, 2011, doi: 10.1523/JNEUROSCI.0479-11.2011.
- [21] O. Larsell, "The morphogenesis and adult pattern of the lobules and fissures of the cerebellum of the white rat," *Journal of Comparative Neurology*, vol. 97, no. 2, pp. 281–356, 1952, doi: 10.1002/cne.900970204.
- [22] A. Sudarov and A. L. Joyner, "Cerebellum morphogenesis: The foliation pattern is orchestrated by multi-cellular anchoring centers," *Neural Development*, vol. 2, no. 1, 2007, doi: 10.1186/1749-8104-2-26.

- [23] R. v. Sillitoe and A. L. Joyner, "Morphology, Molecular Codes, and Circuitry Produce the Three-Dimensional Complexity of the Cerebellum," *Annual Review of Cell and Developmental Biology*, vol. 23, no. 1, pp. 549–577, 2007, doi: 10.1146/annurev.cellbio.23.090506.123237.
- [24] M. Rahimi-Balaei, P. Afsharinezhad, K. Bailey, M. Buchok, B. Yeganeh, and H. Marzban, "Embryonic stages in cerebellar afferent development," *Cerebellum & Ataxias*, vol. 2, no. 1, p. 7, 2015, doi: 10.1186/s40673-015-0026-y.
- [25] S. C. Carleton and M. B. Carpenter, "Afferent and Efferent Connections of the Medial, Inferior and Lateral Vestibular Nuclei in the Cat and Monkey," vol. 278, pp. 29–51, 1983.
- [26] E. Mugnaini, M. R. Dino, and D. Jaarsma, "The unipolar brush cells of the mammalian cerebellum and cochlear nucleus: Cytology and microcircuitry," *Progress in Brain Research*, vol. 114, no. 1, pp. 131–150, 1997, doi: 10.1016/s0079-6123(08)63362-2.
- [27] M. J. Wagner, T. H. Kim, J. Savall, M. J. Schnitzer, and L. Luo, "Cerebellar granule cells encode the expectation of reward," *Nature*, vol. 544, no. 7648, pp. 96–100, 2017, doi: 10.1038/nature21726.
- [28] J. Voogd and M. Glickstein, "The anatomy of the cerebellum," vol. 2, no. 9, pp. 307–313, 1998.
- [29] J. Lainé and H. Axelrad, "The candelabrum cell: A new interneuron in the cerebellar cortex," *Journal of Comparative Neurology*, vol. 339, no. 2, pp. 159–173, 1994, doi: 10.1002/cne.903390202.
- [30] M. A. Schilling *et al.*, "Transcriptional innate immune response of the developing chicken embryo to Newcastle disease virus infection," *Frontiers in Genetics*, vol. 9, no. FEB, pp. 1–9, 2018, doi: 10.3389/fgene.2018.00061.
- [31] A. Buffo and F. Rossi, "Origin, lineage and function of cerebellar glia," *Progress in Neurobiology*, vol. 109, pp. 42–63, 2013, doi: 10.1016/j.pneurobio.2013.08.001.
- [32] S. Tellmann, S. Bludau, S. Eickhoff, H. Mohlberg, M. Minnerop, and K. Amunts, "Cytoarchitectonic mapping of the human brain cerebellar nuclei in stereotaxic space and delineation of their co-activation patterns," *Frontiers in Neuroanatomy*, vol. 9, no. MAY, pp. 1–14, 2015, doi: 10.3389/fnana.2015.00054.
- [33] H. S. Haroun, "Cerebellar Nuclei and Connections in Man," *Anatomy Physiology & Biochemistry International Journal*, vol. 1, no. 1, 2016, doi: 10.19080/apbij.2016.01.555552.
- [34] I. Sugihara, "Compartmentalization of the deep cerebellar nuclei based on afferent projections and aldolase C expression," *Cerebellum*, vol. 10, no. 3, pp. 449–463, 2011, doi: 10.1007/s12311-010-0226-1.
- [35] S. H. Chung, H. Marzban, and R. Hawkes, "Compartmentation of the cerebellar nuclei of the mouse," *Neuroscience*, vol. 161, no. 1, pp. 123–138, 2009, doi: 10.1016/j.neuroscience.2009.03.037.
- [36] P. A. L. and R. I. M., "Purkinje neuron synchrony elicits time-locked spiking in the cerebellar nuclei," *Nature*, vol. 481, no. 7382, pp. 502–505, 2012, doi: 10.1038/nature10732.Purkinje.
- [37] M. W. Bagnall, B. Zingg, A. Sakatos, S. H. Moghadam, H. U. Zeilhofer, and S. Du Lac, "Glycinergic projection neurons of the cerebellum," *Journal of Neuroscience*, vol. 29, no. 32, pp. 10104–10110, 2009, doi: 10.1523/JNEUROSCI.2087-09.2009.
- [38] T. J. H. Ruigrok, R. v. Sillitoe, and J. Voogd, *Cerebellum and Cerebellar Connections*, Fourth Edi. Elsevier Inc., 2015. Doi: 10.1016/B978-0-12-374245-2.00009-7.
- [39] S. Hamodeh, J. Baizer, I. Sugihara, and F. Sultan, "Systematic analysis of neuronal wiring of the rodent deep cerebellar nuclei reveals differences reflecting adaptations at the neuronal circuit and internuclear levels," *Journal of Comparative Neurology*, vol. 522, no. 11, pp. 2481–2497, 2014, doi: 10.1002/cne.23545.
- [40] S. L. Reeber, T. S. Otis, and R. v. Sillitoe, "New roles for the cerebellum in health and disease," *Frontiers in Systems Neuroscience*, vol. 7, no. NOV, pp. 1–11, 2013, doi: 10.3389/fnsys.2013.00083.
- [41] J. J. White and R. v. Sillitoe, "Postnatal development of cerebellar zones revealed by neurofilament heavy chain protein expression," *Frontiers in Neuroanatomy*, vol. 7, no. APR, pp. 1–10, 2013, doi: 10.3389/fnana.2013.00009.
- [42] R. Hawkes and N. Leclerc, "Immunocytochemical demonstration of topographic ordering of purkinje cell axon terminals in the fastigial nuclei of the rat," *Journal of Comparative Neurology*, vol. 244, no. 4, pp. 481–491, 1986, doi: 10.1002/cne.902440406.
- [43] T. Tabuchi, T. Umetani, and T. Yamadori, "Corticonuclear and corticovestibular projections from the uvula in the albino rat: differential projections from sublobuli of the uvula," *Brain Research*, vol. 492, no. 1–2, pp. 176–186, 1989, doi: 10.1016/0006-8993(89)90900-1.
- [44] Z. Gao *et al.*, "Excitatory Cerebellar Nucleocortical Circuit Provides Internal Amplification during Associative Conditioning," *Neuron*, vol. 89, no. 3, pp. 645–657, 2016, doi: 10.1016/j.neuron.2016.01.008.

- [45] M. E. Fox and M. K. Lobo, “The molecular and cellular mechanisms of depression: a focus on reward circuitry,” *Mol Psychiatry*, vol. 24, no. 12, pp. 1798–1815, 2019, doi: 10.1038/s41380-019-0415-3.
- [46] S. J. Baek, J. S. Park, J. Kim, and Y. Yamamoto, “projecting cerebellar neurons mediate stress- dependent depression- like behaviors,” pp. 1–38, 2022.
- [47] A. Y. T. Low *et al.*, “Reverse-translational identification of a cerebellar satiation network,” *Nature*, vol. 600, no. 7888, pp. 269–273, 2021, doi: 10.1038/s41586-021-04143-5.
- [48] R. L. Jakab and J. Hámori, “Quantitative morphology and synaptology of cerebellar glomeruli in the rat,” *Anatomy and Embryology*, vol. 179, no. 1, pp. 81–88, 1988, doi: 10.1007/BF00305102.
- [49] M. Ito, “Cerebellar circuitry as a neuronal machine,” *Progress in Neurobiology*, vol. 78, no. 3–5, pp. 272–303, 2006, doi: 10.1016/j.pneurobio.2006.02.006.
- [50] R. M. A. Napper and R. J. Harvey, “Number of parallel fiber synapses on an individual Purkinje cell in the cerebellum of the rat,” *Journal of Comparative Neurology*, vol. 274, no. 2, pp. 168–177, 1988, doi: 10.1002/cne.902740204.
- [51] Y. Zang and E. de Schutter, “Climbing Fibers Provide Graded Error Signals in Cerebellar Learning,” *Frontiers in Systems Neuroscience*, vol. 13, no. September, pp. 1–11, 2019, doi: 10.3389/fnsys.2019.00046.
- [52] F. Ango, G. di Cristo, H. Higashiyama, V. Bennett, P. Wu, and Z. J. Huang, “Ankyrin-based subcellular gradient of neurofascin, an immunoglobulin family protein, directs GABAergic innervation at Purkinje axon initial segment,” *Cell*, vol. 119, no. 2, pp. 257–272, 2004, doi: 10.1016/j.cell.2004.10.004.
- [53] C. I. de Zeeuw *et al.*, “Expression of a protein kinase C inhibitor in purkinje cells blocks cerebellar LTD and adaptation of the vestibulo-ocular reflex,” *Neuron*, vol. 20, no. 3, pp. 495–508, 1998, doi: 10.1016/S0896-6273(00)80990-3.
- [54] R. R. Llinas, “Cerebellar motor learning versus cerebellar motor timing: The climbing fibre story,” *Journal of Physiology*, vol. 589, no. 14, pp. 3423–3432, 2011, doi: 10.1113/jphysiol.2011.207464.
- [55] A. Mathy, B. A. Clark, and M. Häusser, “Synaptically induced long-term modulation of electrical coupling in the inferior olive,” *Neuron*, vol. 81, no. 6, pp. 1290–1296, 2014, doi: 10.1016/j.neuron.2014.01.005.
- [56] B. Y. J. C. Eccles, R. Llinas, and K. Sasaki, “The excitatory synaptic action of climbing fibres on the purkinje cells of the cerebellum,” pp. 268–296, 1966.
- [57] B. Y. D. Marr, “A theory of cerebellar cortex,” pp. 437–470, 1969.
- [58] J. S. Albus, “A theory of cerebellar function,” *Mathematical Biosciences*, vol. 10, no. 1–2, pp. 25–61, 1971, doi: 10.1016/0025-5564(71)90051-4.
- [59] M. Ito and M. Kano, “Long-lasting depression of parallel fiber-Purkinje cell transmission induced by conjunctive stimulation of parallel fibers and climbing fibers in the cerebellar cortex,” *Neuroscience Letters*, vol. 33, no. 3, pp. 253–258, 1982, doi: 10.1016/0304-3940(82)90380-9.
- [60] Z. Gao, B. J. van Beugen, and C. I. de Zeeuw, “Distributed synergistic plasticity and cerebellar learning,” *Nature Reviews Neuroscience*, vol. 13, no. 9, pp. 619–635, 2012, doi: 10.1038/nrn3312.
- [61] G. Szapiro and B. Barbour, “Multiple climbing fibers signal to molecular layer interneurons exclusively via glutamate spillover,” *Nature Neuroscience*, vol. 10, no. 6, pp. 735–742, 2007, doi: 10.1038/nn1907.
- [62] V. Lev-Ram, S. T. Wong, D. R. Storm, and R. Y. Tsien, “A new form of cerebellar long-term potentiation is postsynaptic and depends on nitric oxide but not cAMP,” *Proc Natl Acad Sci U S A*, vol. 99, no. 12, pp. 8389–8393, 2002, doi: 10.1073/pnas.122206399.
- [63] M. Coesmans, J. T. Weber, C. I. de Zeeuw, and C. Hansel, “Bidirectional parallel fiber plasticity in the cerebellum under climbing fiber control,” *Neuron*, vol. 44, no. 4, pp. 691–700, 2004, doi: 10.1016/j.neuron.2004.10.031.
- [64] M. Palkovits, É. Mezey, J. Hámori, and J. Szentágothai, “Quantitative histological analysis of the cerebellar nuclei in the cat. I. Numerical data on cells and on synapses,” *Experimental Brain Research*, vol. 28, no. 1–2, pp. 189–209, 1977, doi: 10.1007/BF00237096.
- [65] C. I. de Zeeuw and A. S. Berrebi, “Postsynaptic Targets of Purkinje Cell Terminals in the Cerebellar and Vestibular Nuclei of the Rat,” *European Journal of Neuroscience*, vol. 7, no. 11, pp. 2322–2333, 1995, doi: 10.1111/j.1460-9568.1995.tb00653.x.
- [66] M. Uusisaari and T. Knöpfel, “GABAergic synaptic communication in the GABAergic and non-GABAergic cells in the deep cerebellar nuclei,” *Neuroscience*, vol. 156, no. 3, pp. 537–549, 2008, doi: 10.1016/j.neuroscience.2008.07.060.

- [67] E. J. Lang and T. A. Blenkinsop, “Control of cerebellar nuclear cells: A direct role for complex spikes?,” *Cerebellum*, vol. 10, no. 4, pp. 694–701, 2011, doi: 10.1007/s12311-011-0261-6.
- [68] I. M. Raman, A. E. Gustafson, and D. Padgett, “Ionic currents and spontaneous firing in neurons isolated from the cerebellar nuclei,” *Journal of Neuroscience*, vol. 20, no. 24, pp. 9004–9016, 2000, doi: 10.1523/jneurosci.20-24-09004.2000.
- [69] N. Schweighofer, K. Doya, and S. Kuroda, “Cerebellar aminergic neuromodulation: Towards a functional understanding,” *Brain Research Reviews*, vol. 44, no. 2–3, pp. 103–116, 2004, doi: 10.1016/j.brainresrev.2003.10.004.
- [70] M. Longley, J. Ballard, M. Andres-Alonso, R. C. Varatharajah, H. Cuthbert, and C. H. Yeo, “A Patterned Architecture of Monoaminergic Afferents in the Cerebellar Cortex: Noradrenergic and Serotonergic Fibre Distributions within Lobules and Parasagittal Zones,” *Neuroscience*, vol. 462, pp. 106–121, 2021, doi: 10.1016/j.neuroscience.2020.09.001.
- [71] P. Place *et al.*, “The Cerebellar Dopaminergic System,” *Frontiers in Systems Neuroscience*, vol. 15, no. August, pp. 1–19, 2021, doi: 10.3389/fnsys.2021.650614.
- [72] R. Papay *et al.*, “Mouse α 1B-adrenergic receptor is expressed in neurons and NG2 oligodendrocytes,” *Journal of Comparative Neurology*, vol. 478, no. 1, pp. 1–10, 2004, doi: 10.1002/cne.20215.
- [73] P. Robert *et al.*, “Localization of the Mouse α 1A- Adrenergic Receptor (AR) in the Brain: α 1AAR Is Expressed in Neurons, GABAergic Interneurons, and NG2 Oligodendrocyte Progenitor,” *The journal of comparative neurology*, vol. 497, pp. 209–222, 2006, doi: 10.1002/cne.
- [74] M. Hirono, W. Matsunaga, T. Chimura, and K. Obata, “Developmental enhancement of α 2-adrenoceptor-mediated suppression of inhibitory synaptic transmission onto mouse cerebellar Purkinje cells,” *Neuroscience*, vol. 156, no. 1, pp. 143–154, 2008, doi: 10.1016/j.neuroscience.2008.07.018.
- [75] E. Fleming and C. Hull, “Serotonin regulates dynamics of cerebellar granule cell activity by modulating tonic inhibition,” *Journal of Neurophysiology*, vol. 121, no. 1, pp. 105–114, 2019, doi: 10.1152/jn.00492.2018.
- [76] T. E. Nelson, J. S. King, and G. A. Bishop, “Distribution of tyrosine hydroxylase-immunoreactive afferents to the cerebellum differs between species,” *Journal of Comparative Neurology*, vol. 379, no. 3, pp. 443–454, 1997, doi: 10.1002/(SICI)1096-9861(19970317)379:3<443::AID-CNE9>3.0.CO;2-3.
- [77] T. Fujii, M. Sakai, and I. Nagatsu, “Immunohistochemical demonstration of expression of tyrosine hydroxylase in cerebellar Purkinje cells of the human and mouse,” *Neuroscience Letters*, vol. 165, no. 1–2, pp. 161–163, 1994, doi: 10.1016/0304-3940(94)90734-X.
- [78] E. de Schutter, “Cerebellar long term depression may normalize excitation of purkinje cells: a hypothesis,” *Trends in Neurosciences*, vol. 18, pp. 291–295, 1995.
- [79] T. M. Nguyen *et al.*, “Structured connectivity in the cerebellum enables noise-resilient pattern separation,” *bioRxiv*, pp. 1–36, 2021.
- [80] K. Doya, “Complementary roles of basal ganglia and cerebellum in learning and motor control,” *Current Opinion in Neurobiology*, vol. 10, no. 6, pp. 732–739, 2000, doi: 10.1016/S0959-4388(00)00153-7.
- [81] C. Habas *et al.*, “Distinct cerebellar contributions to intrinsic connectivity networks,” *Journal of Neuroscience*, vol. 29, no. 26, pp. 8586–8594, 2009, doi: 10.1523/JNEUROSCI.1868-09.2009.
- [82] M. Molinari, “Cerebellum,” *Encyclopedia of the human Brain*, vol. 1, pp. 611–627, 2002.
- [83] A. R. Luft, M. U. Manto, and N. O. ben Taib, “Modulation of motor cortex excitability by sustained peripheral stimulation: The interaction between the motor cortex and the cerebellum,” *Cerebellum*, vol. 4, no. 2, pp. 90–96, 2005, doi: 10.1080/14734220410019084.
- [84] R. P. Dum and P. L. Strick, “An unfolded map of the cerebellar dentate nucleus and its projections to the cerebral cortex,” *Journal of Neurophysiology*, vol. 89, no. 1, pp. 634–639, 2003, doi: 10.1152/jn.00626.2002.
- [85] E. M. Rouiller, F. Liang, A. Babalian, V. Moret, and M. Wiesendanger, “Cerebellothalamocortical and pallidothalamocortical projections to the primary and supplementary motor cortical areas: A multiple tracing study in macaque monkeys,” *Journal of Comparative Neurology*, vol. 345, no. 2, pp. 185–213, 1994, doi: 10.1002/cne.903450204.
- [86] M. Panouillères *et al.*, “A role for the parietal cortex in sensorimotor adaptation of saccades,” *Cerebral Cortex*, vol. 24, no. 2, pp. 304–314, 2014, doi: 10.1093/cercor/bhs312.
- [87] P. Lefèvre, C. Quaia, and L. M. Optican, “Distributed model of control of saccades by superior colliculus and cerebellum,” *Neural Networks*, vol. 11, no. 7–8, pp. 1175–1190, 1998, doi: 10.1016/S0893-6080(98)00071-9.

- [88] A. Fabrice and D. R. Raphaël, “Sensing how to balance: How does the inner ear communicate with the cerebellar cortex to maintain balance and posture?,” *Elife*, vol. 8, pp. 8–10, 2019, doi: 10.7554/eLife.44964.
- [89] C. Fernandez, R. A. Baird, and J. M. Goldberg, “The vestibular nerve of the chinchilla. I. Peripheral innervation patterns in the horizontal and superior semicircular canals,” *Journal of Neurophysiology*, vol. 60, no. 1, pp. 167–181, 1988, doi: 10.1152/jn.1988.60.1.167.
- [90] T. S. Balmer and L. O. Trussell, “Selective targeting of unipolar brush cell subtypes by cerebellar mossy fibers,” *Elife*, vol. 8, pp. 1–28, 2019, doi: 10.7554/eLife.44964.
- [91] C. Borges-Merjane and L. O. Trussell, “ON and OFF unipolar brush cells transform multisensory inputs to the auditory system,” *Neuron*, vol. 85, no. 5, pp. 1029–1042, 2015, doi: 10.1016/j.neuron.2015.02.009.ON.
- [92] K. Stecina, B. Fedirchuk, and H. Hultborn, “Information to cerebellum on spinal motor networks mediated by the dorsal spinocerebellar tract,” *Journal of Physiology*, vol. 591, no. 22, pp. 5433–5443, 2013, doi: 10.1113/jphysiol.2012.249110.
- [93] M. Steinlin and K. Wingeier, “Cerebellum and Cognition,” *Handbook of the Cerebellum and Cerebellar Disorders*, pp. 1–2424, 2013, doi: 10.1007/978-94-007-1333-8_75.
- [94] P. L. Strick, R. P. Dum, and J. A. Fiez, “Cerebellum and Nonmotor Function,” *Annual Review of Neuroscience*, vol. 32, no. 1, pp. 413–434, 2009, doi: 10.1146/annurev.neuro.31.060407.125606.
- [95] L. Koziol, “Consensus Paper: The Cerebellum’s role in movement and cognition,” *Cerebellum*, vol. 13, no. 1, pp. 155–177, 2014, doi: 10.3109/01913128509055487.
- [96] P. Mariën *et al.*, “Consensus paper: Language and the cerebellum: An ongoing enigma,” *Cerebellum*, vol. 13, no. 3, pp. 386–410, 2014, doi: 10.1007/s12311-013-0540-5.
- [97] J. F. Medina, “Teaching the cerebellum about reward,” *Nature Neuroscience*, vol. 22, no. 6, pp. 846–848, 2019, doi: 10.1038/s41593-019-0409-0.
- [98] N. Sendhilnathan, A. E. Ipata, and M. E. Goldberg, “Neural Correlates of Reinforcement Learning in Mid-lateral Cerebellum,” *Neuron*, vol. 106, no. 1, pp. 188–198.e5, 2020, doi: 10.1016/j.neuron.2019.12.032.
- [99] W. Heffley *et al.*, “Coordinated cerebellar climbing fiber activity signals learned sensorimotor predictions,” *Nature Neuroscience*, vol. 21, no. 10, pp. 1431–1441, 2018, doi: 10.1038/s41593-018-0228-8.Coordinated.
- [100] D. Kostadinov, M. Beau, M. B. Pozo, and M. Häusser, “Predictive and reactive reward signals conveyed by climbing fiber inputs to cerebellar Purkinje cells,” *Nature Neuroscience*, vol. 22, no. 6, pp. 950–962, 2019, doi: 10.1038/s41593-019-0381-8.
- [101] C. M. Vacher *et al.*, “Placental endocrine function shapes cerebellar development and social behavior,” *Nature Neuroscience*, 2021, doi: 10.1038/s41593-021-00896-4.
- [102] H. G. Serra *et al.*, “ROR α -Mediated Purkinje Cell Development Determines Disease Severity in Adult SCA1 Mice,” *Cell*, vol. 127, no. 4, pp. 697–708, 2006, doi: 10.1016/j.cell.2006.09.036.
- [103] M. Tada, M. Nishizawa, and O. Onodera, “Redefining cerebellar ataxia in degenerative ataxias: Lessons from recent research on cerebellar systems,” *Journal of Neurology, Neurosurgery and Psychiatry*, vol. 86, no. 8, pp. 922–928, 2015, doi: 10.1136/jnnp-2013-307225.
- [104] M. S. Keiser, J. H. Kordower, P. Gonzalez-Alegre, and B. L. Davidson, “Broad distribution of ataxin 1 silencing in rhesus cerebella for spinocerebellar ataxia type 1 therapy,” *Brain*, vol. 138, no. 12, pp. 3555–3566, 2015, doi: 10.1093/brain/awv292.
- [105] M. R. Stefanescu *et al.*, “Structural and functional MRI abnormalities of cerebellar cortex and nuclei in SCA3, SCA6 and Friedreich’s ataxia,” *Brain*, vol. 138, no. 5, pp. 1182–1197, 2015, doi: 10.1093/brain/awv064.
- [106] M. Saeed Dar, “Ethanol-induced cerebellar ataxia: Cellular and molecular mechanisms,” *Cerebellum*, vol. 14, no. 4, pp. 447–465, 2015, doi: 10.1007/s12311-014-0638-4.
- [107] M. M. Lewis, S. Galley, S. Johnson, J. Stevenson, X. Huang, and M. J. McKeown, “The role of the cerebellum in the pathophysiology of Parkinson’s disease,” *Can J Neurol Sci*, vol. 40, no. 3, pp. 299–306, 2013, doi: 10.1017/S0317167100014232.
- [108] J. L. Mirdamadi, “Cerebellar role in Parkinson’s disease,” *Journal of Neurophysiology*, vol. 116, no. 3, pp. 917–919, 2016, doi: 10.1152/jn.01132.2015.
- [109] S. C. Lefaiivre, M. J. N. Brown, and Q. J. Almeida, “Cerebellar involvement in Parkinson’s disease resting tremor,” *Cerebellum & Ataxias*, vol. 3, no. 1, pp. 1–7, 2016, doi: 10.1186/s40673-016-0051-5.
- [110] T. Wu and M. Hallett, “The cerebellum in Parkinson’s disease,” *Brain*, vol. 136, no. 3, pp. 696–709, 2013, doi: 10.1093/brain/aws360.

- [111] T. B. Room, F. Lauderdale, and I. J. Goldberg, “The cerebellum and neurodevelopmental disorders,” *HHS Public Access*, vol. 12, no. 2, pp. 130–140, 2015, doi: 10.1007/s11897-014-0247-z.Pathophysiology.
- [112] E. B. E. Becker and C. J. Stoodley, *Autism spectrum disorder and the cerebellum*, 1st ed., vol. 113. Elsevier Inc., 2013. Doi: 10.1016/B978-0-12-418700-9.00001-0.
- [113] S. H. Fatemi, “Cerebellar pathology in autism,” *Essentials of Cerebellum and Cerebellar Disorders: A Primer for Graduate Students*, vol. 11, no. 3, pp. 539–543, 2016, doi: 10.1007/978-3-319-24551-5_72.
- [114] T. D. Rogers, E. Mckimm, P. E. Dickson, D. Goldowitz, C. D. Blaha, and G. Mittleman, “Is autism a disease of the cerebellum?: An integration of clinical and pre-clinical research,” *Frontiers in Systems Neuroscience*, vol. 7, no. APR 2013, pp. 1–16, 2013, doi: 10.3389/fnsys.2013.00015.
- [115] J. Wegiel *et al.*, “Stereological study of the neuronal number and volume of 38 brain subdivisions of subjects diagnosed with autism reveals significant alterations restricted to the striatum, amygdala and cerebellum,” *Acta Neuropathologica Communications*, vol. 2, no. 1, pp. 1–18, 2014, doi: 10.1186/s40478-014-0141-7.
- [116] S. J. Webb *et al.*, “Cerebellar vermal volumes and behavioral correlates in children with autism spectrum disorder,” *Psychiatry Research – Neuroimaging*, vol. 172, no. 1, pp. 61–67, 2009, doi: 10.1016/j.psychres.2008.06.001.
- [117] P. Strømme *et al.*, “X-linked Angelman-like syndrome caused by Slc9a6 knockout in mice exhibits evidence of endosomal-lysosomal dysfunction,” *Brain*, vol. 134, no. 11, pp. 3369–3383, 2011, doi: 10.1093/brain/awr250.
- [118] H. Marzban, M. R. del Bigio, J. Alizadeh, S. Ghavami, R. M. Zachariah, and M. Rastegar, “Cellular commitment in the developing cerebellum,” *Frontiers in Cellular Neuroscience*, vol. 8, no. January, pp. 1–26, 2015, doi: 10.3389/fncel.2014.00450.
- [119] Y. Fukutani, N. J. Cairns, M. N. Rossor, and P. L. Lantos, “Cerebellar pathology in sporadic and familial Alzheimer’s disease including APP 717 (Val→Ile) mutation cases: A morphometric investigation,” *Journal of the Neurological Sciences*, vol. 149, no. 2, pp. 177–184, 1997, doi: 10.1016/S0022-510X(97)05399-9.
- [120] J. R. Sarna and R. Hawkes, *Patterned Purkinje cell death in the cerebellum*, vol. 70, no. 6. 2003. Doi: 10.1016/S0301-0082(03)00114-X.
- [121] M. Sjöbeck and E. Englund, “Alzheimer’s disease and the cerebellum: A morphologic study on neuronal and glial changes,” *Dementia and Geriatric Cognitive Disorders*, vol. 12, no. 3, pp. 211–218, 2001, doi: 10.1159/000051260.
- [122] J. Wegiel *et al.*, “Cerebellar atrophy in Alzheimer’s disease – Clinicopathological correlations,” *Brain Research*, vol. 818, no. 1, pp. 41–50, 1999, doi: 10.1016/S0006-8993(98)01279-7.
- [123] A. S. Guerreiro Stucklin and M. A. Grotzer, *Cerebellar tumors*, 1st ed., vol. 155. Elsevier B.V., 2018. Doi: 10.1016/B978-0-444-64189-2.00019-6.
- [124] S. Khatua, A. Song, D. C. Sridhar, and S. C. Mack, “Childhood Medulloblastoma: Current Therapies, Emerging Molecular Landscape and Newer Therapeutic Insights,” *Current Neuropharmacology*, vol. 16, no. 7, pp. 1045–1058, 2018, doi: 10.2174/1570159x15666171129111324.
- [125] S. L. Pomeroy *et al.*, “Prediction of central nervous system embryonal tumour outcome based on gene expression,” *Nature*, vol. 415, no. January, pp. 436–442, 2002.
- [126] H. J. Cho *et al.*, “Distinct genomic profile and specific targeted drug responses in adult cerebellar glioblastoma,” *Neuro-Oncology*, vol. 21, no. 1, pp. 47–58, 2019, doi: 10.1093/neuonc/noy123.
- [127] S. Fattet *et al.*, “Beta-catenin status in paediatric medulloblastomas: correlation of immunohistochemical expression with mutational status, genetic profiles, and clinical characteristics,” *Journal of Pathology*, vol. 218, no. January, pp. 86–94, 2009, doi: 10.1002/path.
- [128] M. Kool *et al.*, “Integrated genomics identifies five medulloblastoma subtypes with distinct genetic profiles, pathway signatures and clinicopathological features,” *PloS ONE*, vol. 3, no. 8, 2008, doi: 10.1371/journal.pone.0003088.
- [129] P. A. Northcott *et al.*, “Medulloblastoma comprises four distinct molecular variants,” *Journal of Clinical Oncology*, vol. 29, no. 11, pp. 1408–1414, 2011, doi: 10.1200/JCO.2009.27.4324.
- [130] M. C. Thompson *et al.*, “Genomics identifies medulloblastoma subgroups that are enriched for specific genetic alterations,” *Journal of Clinical Oncology*, vol. 24, no. 12, pp. 1924–1931, 2006, doi: 10.1200/JCO.2005.04.4974.
- [131] P. Taylor *et al.*, “REST is a Novel Prognostic Factor and Therapeutic Target for Medulloblastoma Pete,” *Molecular cancer therapy*, vol. 11, no. 8, pp. 1713–1723, 2012, doi: 10.1158/1535-7163.MCT-11-0990.REST.
- [132] M. C. Vladoiu *et al.*, “Childhood cerebellar tumours mirror conserved fetal transcriptional programs,” *Nature*, vol. 572, no. 7767, pp. 67–73, 2019, doi: 10.1038/s41586-019-1158-7.

- [133] R. J. Vanner *et al.*, “Quiescent Sox2+ Cells Drive Hierarchical Growth and Relapse in Sonic Hedgehog Subgroup Medulloblastoma,” *Cancer Cell*, vol. 26, no. 1, pp. 33–47, 2014, doi: 10.1016/j.ccr.2014.05.005.Quiescent.
- [134] O. Larsell, “The development of the cerebellum in man in relation to its comparative anatomy,” *Journal of Comparative Neurology*, vol. 87, no. 2, pp. 85–129, 1947, doi: 10.1002/cne.900870203.
- [135] R. Nieuwenhuys, “Cerebellum of Mormyrids,” *Nature*, vol. 215, pp. 754–765, 1967.
- [136] H. L. Grishkat and L. M. Eisenman, “Development of the spinocerebellar projection in the prenatal mouse,” *Journal of Comparative Neurology*, vol. 363, no. 1, pp. 93–108, 1995, doi: 10.1002/cne.903630109.
- [137] Y. K. Bae *et al.*, “Anatomy of zebrafish cerebellum and screen for mutations affecting its development,” *Developmental Biology*, vol. 330, no. 2, pp. 406–426, 2009, doi: 10.1016/j.ydbio.2009.04.013.
- [138] L. Heap, C. C. Goh, K. S. Kassahn, and E. K. Scott, “Cerebellar output in zebrafish: An analysis of spatial patterns and topography in eurydendroid cell projections,” *Frontiers in Neural Circuits*, vol. 7, no. MAR, pp. 1–14, 2013, doi: 10.3389/fncir.2013.00053.
- [139] R. Llinas, J. R. Bloedel, and D. E. Hillman, “Functional characterization of neuronal circuitry of frog cerebellar cortex,” *J Neurophysiol*, vol. 32, no. 6, pp. 847–870, 1969, doi: 10.1152/jn.1969.32.6.847.
- [140] P. Sepp, Mari Leiss, Kevin Sarropoulos, Ioannis Murat, Florent Okonechnikov, Konstantin Joshi, Piyush Leushkin, Evgeny Mbengue, Noe Schneider, Céline Schmidt, Julia Trost, Nils Spänig, Lisa Giere, “Cellular development and evolution of the mammalian cerebellum,” *bioRxiv*, 2021, doi: <https://doi.org/10.1101/2021.12.20.473443>.
- [141] J. M. D. Corrales, G. L. Rocco, S. Blaess, Q. Guo, and A. L. Joyner, “Spatial pattern of sonic hedgehog signaling through Gli genes during cerebellum development,” *Development*, vol. 131, no. 22, pp. 5581–5590, 2004, doi: 10.1242/dev.01438.
- [142] J. M. D. Corrales, S. Blaess, E. M. Mahoney, and A. L. Joyner, “The level of sonic hedgehog signaling regulates the complexity of cerebellar foliation,” *Development*, vol. 133, no. 9, pp. 1811–1821, 2006, doi: 10.1242/dev.02351.
- [143] J. Fleming *et al.*, “The Purkinje neuron acts as a central regulator of spatially and functionally distinct cerebellar precursors,” *Developmental Cell*, vol. 27, no. 3, 2013, doi: 10.1016/j.devcel.2013.10.008.The.
- [144] S. Herculano-Houzel, P. R. Manger, and J. H. Kaas, “Brain scaling in mammalian evolution as a consequence of concerted and mosaic changes in numbers of neurons and average neuronal cell size,” *Frontiers in Neuroanatomy*, vol. 8, no. AUG, pp. 1–28, 2014, doi: 10.3389/fnana.2014.00077.
- [145] M. Hibi, K. Matsuda, M. Takeuchi, T. Shimizu, and Y. Murakami, “Evolutionary mechanisms that generate morphology and neural-circuit diversity of the cerebellum,” *Development Growth and Differentiation*, vol. 59, no. 4, pp. 228–243, 2017, doi: 10.1111/dgd.12349.
- [146] E. D’Angelo, S. Solinas, J. Mapelli, D. Gandolfi, L. Mapelli, and F. Prestori, “The cerebellar Golgi cell and spatiotemporal organization of granular layer activity,” *Frontiers in Neural Circuits*, vol. 7, no. APR 2013, pp. 1–21, 2013, doi: 10.3389/fncir.2013.00093.
- [147] R. v. Sillitoe and A. L. Joyner, “Morphology, Molecular Codes, and Circuitry Produce the Three-Dimensional Complexity of the Cerebellum,” *Annual Review of Cell and Developmental Biology*, vol. 23, no. 1, pp. 549–577, 2007, doi: 10.1146/annurev.cellbio.23.090506.123237.
- [148] N. Ben-arie, H. J. Bellen, and D. L. Armstrong, “Math1 is essential for genesis of cerebellar granule neurons,” vol. 95, no. August, pp. 169–172, 1997.
- [149] P. S. Knoepfler, P. F. Cheng, and R. N. Eisenman, “N-myc is essential during neurogenesis for the rapid expansion of progenitor cell populations and the inhibition of neuronal differentiation,” *Genes and Development*, vol. 16, no. 20, pp. 2699–2712, 2002, doi: 10.1101/gad.1021202.
- [150] C. Sotelo, “Cellular and genetic regulation of the development of the cerebellar system,” *Progress in Neurobiology*, vol. 72, no. 5, pp. 295–339, 2004, doi: 10.1016/j.pneurobio.2004.03.004.
- [151] N. Dahmane and A. Ruiz I Altaba, “Sonic hedgehog regulates the growth and patterning of the cerebellum,” *Development*, vol. 126, no. 14, pp. 3089–3100, 1999, doi: 10.1242/dev.126.14.3089.
- [152] V. A. Wallace, “Purkinje-cell-derived Sonic hedgehog regulates granule neuron precursor cell proliferation in the developing mouse cerebellum,” *Current Biology*, vol. 9, no. 8, pp. 445–448, 1999, doi: 10.1016/S0960-9822(99)80195-X.
- [153] R. J. Wechsler-Reya and M. P. Scott, “Control of neuronal precursor proliferation in the cerebellum by sonic hedgehog,” *Neuron*, vol. 22, no. 1, pp. 103–114, 1999, doi: 10.1016/S0896-6273(00)80682-0.

- [154] M. E. Hatten, D. J. Solecki, X. Liu, T. Tomoda, Y. Fang, and M. E. Hatten, “Solecki DJ , Liu XL , Tomoda T , Fang Y , Hatten ME Activated Notch2 signaling inhibits differentiation of ... Activated Notch2 Signaling Inhibits Differentiation of Cerebellar Granule Neuron Precursors by Maintaining Proliferation,” vol. 31, no. January 2015, pp. 557–568, 2001.
- [155] M. Hoser, S. L. Baader, M. R. Bösl, A. Ihmer, M. Wegner, and E. Sock, “Prolonged glial expression of Sox4 in the CNS leads to architectural cerebellar defects and ataxia,” *Journal of Neuroscience*, vol. 27, no. 20, pp. 5495–5505, 2007, doi: 10.1523/JNEUROSCI.1384-07.2007.
- [156] S. Ma, H. J. Kwon, and Z. Huang, “Ric-8a, a guanine nucleotide exchange factor for heterotrimeric g proteins, regulates bergmann glia-basement membrane adhesion during cerebellar foliation,” *Journal of Neuroscience*, vol. 32, no. 43, pp. 14979–14993, 2012, doi: 10.1523/JNEUROSCI.1282-12.2012.
- [157] K. Li, A. W. Leung, Q. Guo, W. Yang, and J. Y. H. Li, “Shp2-dependent ERK signaling is essential for induction of bergmann glia and foliation of the cerebellum,” *Journal of Neuroscience*, vol. 34, no. 3, pp. 922–931, 2014, doi: 10.1523/JNEUROSCI.3476-13.2014.
- [158] G. G. Consalez, D. Goldowitz, F. Casoni, and R. Hawkes, “Origins, Development, and Compartmentation of the Granule Cells of the Cerebellum,” *Frontiers in Neural Circuits*, vol. 14, no. January, pp. 1–23, 2021, doi: 10.3389/fncir.2020.611841.
- [159] V. Chockkan and R. Hawkes, “Functional and antigenic maps in the rat cerebellum: Zebrin compartmentation and vibrissal receptive fields in lobule Ixa,” *Journal of Comparative Neurology*, vol. 345, no. 1, pp. 33–45, 1994, doi: 10.1002/cne.903450103.
- [160] L. Chen, S. Bao, J. M. Lockard, J. J. Kim, and R. F. Thompson, “Impaired classical eyeblink conditioning in cerebellar-lesioned and Purkinje cell degeneration (pcd) mutant mice,” *Journal of Neuroscience*, vol. 16, no. 8, pp. 2829–2838, 1996, doi: 10.1523/jneurosci.16-08-02829.1996.
- [161] J. S. Hallem, J. H. Thompson, G. Gundappa-Sulur, R. Hawkes, J. G. Bjaalie, and J. M. Bower, “Spatial correspondence between tactile projection patterns and the distribution of the antigenic Purkinje cell markers anti-zebrin I and anti-zebrin II in the cerebellar folium crus Iia of the rat,” *Neuroscience*, vol. 93, no. 3, pp. 1083–1094, 1999, doi: 10.1016/S0306-4522(99)00144-X.
- [162] R. Apps and M. Garwicz, “Anatomical and physiological foundations of cerebellar information processing,” *Nature Reviews Neuroscience*, vol. 6, no. 4, pp. 297–311, 2005, doi: 10.1038/nrn1646.
- [163] J. I. Wadiche and C. E. Jahr, “Patterned expression of Purkinje cell glutamate transporters controls synaptic plasticity,” *Nature Neuroscience*, vol. 8, no. 10, pp. 1329–1334, 2005, doi: 10.1038/nn1539.
- [164] I. Sugihara, “Crus I in the Rodent Cerebellum: Its Homology to Crus I and II in the Primate Cerebellum and Its Anatomical Uniqueness Among Neighboring Lobules,” *Cerebellum*, vol. 17, no. 1, pp. 49–55, 2018, doi: 10.1007/s12311-017-0911-4.
- [165] D. van Essen, “Surface-Based Atlases of Cerebellar Cortex in Human, Macaque, and Mouse,” *Annals New York Academy of Scienc*, vol. 978, pp. 468–479, 2002, [Online]. Available: <http://dx.doi.org/10.1016/j.meatsci.2017.01.005%0Ahttps://linkinghub.elsevier.com/retrieve/pii/S0309174016301395>
- [166] S. Martinez, A. Andreu, N. Mecklenburg, and D. Echevarria, “Cellular and molecular basis of cerebellar development,” *Frontiers in Neuroanatomy*, vol. 7, no. June, pp. 1–12, 2013, doi: 10.3389/fnana.2013.00018.
- [167] T. Butts, M. J. Green, and R. J. T. Wingate, “Development of the cerebellum: Simple steps to make a ‘little brain,’” *Development (Cambridge)*, vol. 141, no. 21, pp. 4031–4041, 2014, doi: 10.1242/dev.106559.
- [168] E. D. Lowenstein, K. Cui, and L. R. Hernandez-Miranda, “Regulation of early cerebellar development,” *The FEBS Journal*, pp. 1–19, 2022, doi: 10.1111/febs.16426.
- [169] A. J. Barkovich, K. J. Millen, and W. B. Dobyns, “A developmental and genetic classification for midbrain-hindbrain malformations,” *Brain*, vol. 132, no. 12, pp. 3199–3230, 2009, doi: 10.1093/brain/awp247.
- [170] W. Wurst and L. Bally-cuif, “Neural plate patterning: Upstream and downstream of the isthmic organizer,” vol. 2, no. February, 2001.
- [171] A. Lumsden and R. Krumlauf, “Patterning the vertebrate neuraxis,” *Science (1979)*, vol. 274, no. 5290, pp. 1109–1115, 1996, doi: 10.1126/science.274.5290.1109.
- [172] L. Solanelles-Farré and L. Telley, “New insights into CNS development from multiomics approaches,” *Current Opinion in Neurobiology*, vol. 66, pp. 116–124, 2021, doi: 10.1016/j.conb.2020.09.010.

- [173] J. A. Moreno-Bravo *et al.*, “Role of Shh in the development of molecularly characterized tegmental nuclei in mouse rhombomere 1,” *Brain Structure and Function*, vol. 219, no. 3, pp. 777–792, 2014, doi: 10.1007/s00429-013-0534-6.
- [174] G. Lupo, M. Bertacchi, N. Carucci, G. Augusti-Tocco, S. Biagioni, and F. Cremisi, “From pluripotency to forebrain patterning: An in vitro journey astride embryonic stem cells,” *Cellular and Molecular Life Sciences*, vol. 71, no. 15, pp. 2917–2930, 2014, doi: 10.1007/s00018-014-1596-1.
- [175] H. Nakamura, T. Katahira, E. Matsunaga, and T. Sato, “Isthmus organizer for midbrain and hindbrain development,” *Brain Research Reviews*, vol. 49, no. 2, pp. 120–126, 2005, doi: 10.1016/j.brainresrev.2004.10.005.
- [176] D. Acampora, V. Avantaggiato, F. Tuorto, and A. Simeone, “Brain morphogenesis controlled by Otx.pdf,” vol. 3650, pp. 3639–3650, 1997.
- [177] Y. Suda, I. Matsuo, and S. Aizawa, “Cooperation between Otx1 and Otx2 genes in developmental patterning of rostral brain,” *Mechanisms of Development*, vol. 69, no. 1–2, pp. 125–141, 1997, doi: 10.1016/S0925-4773(97)00161-5.
- [178] T. de Haas *et al.*, “OTX1 and OTX2 expression correlates with the clinicopathologic classification of medulloblastomas,” *Journal of Neuropathology and Experimental Neurology*, vol. 65, no. 2, pp. 176–186, 2006, doi: 10.1097/01.jnen.0000199576.70923.8a.
- [179] K. B. Larsen, M. C. Lutterodt, K. Møllgård, and M. Møller, “Expression of the homeobox genes OTX2 and OTX1 in the early developing human brain,” *Journal of Histochemistry and Cytochemistry*, vol. 58, no. 7, pp. 669–678, 2010, doi: 10.1369/jhc.2010.955757.
- [180] S. Millet, K. Campbell, D. Epstein, K. Losis, E. Harris, and A. Joyner, “A role for Gbx2 in repression of Otx2 and positioning the mid/hindbrain organizer,” *Nature*, pp. 161–164, 1999.
- [181] S. Martínez, F. Marín, M. A. Nieto, and L. Puellas, “Induction of ectopic engrailed expression and fate change in avian rhombomeres: intersegmental boundaries as barriers,” *Mechanisms of Development*, vol. 51, no. 2–3, pp. 289–303, 1995, doi: 10.1016/0925-4773(95)00376-2.
- [182] J. M. Dias, Z. Alekseenko, J. M. Applequist, and J. Ericson, “Tgf β signaling regulates temporal neurogenesis and potency of neural stem cells in the CNS,” *Neuron*, vol. 84, no. 5, pp. 927–939, 2014, doi: 10.1016/j.neuron.2014.10.033.
- [183] E. Meyers and J. Kessler, “TFG β Family Signaling in Neural and Neuronal differentiation, Development, and function,” vol. 9, 2017, doi: 10.1097/CCM.0b013e3181b6e760.
- [184] A. M. Rossi and C. Desplan, “Extrinsic activin signaling cooperates with an intrinsic temporal program to increase mushroom body neuronal diversity,” *Elife*, vol. 9, pp. 1–23, 2020, doi: 10.7554/eLife.58880.
- [185] S. Martinez and R. -M Alvarado-Mallart, “Rostral Cerebellum Originates from the Caudal Portion of the So-Called ‘Mesencephalic’ Vesicle: A Study Using Chick/Quail Chimeras,” *European Journal of Neuroscience*, vol. 1, no. 6, pp. 549–560, 1989, doi: 10.1111/j.1460-9568.1989.tb00362.x.
- [186] M. E. R. Hallonet, M. A. Teillet, and N. M. le Douarin, “A new approach to the development of the cerebellum provided by the quail-chick marker system,” *Development*, vol. 108, no. 1, pp. 19–31, 1990, doi: 10.1242/dev.108.1.19.
- [187] R. M. Alvarado-Mallart, “The chick/quail transplantation model: Discovery of the isthmus organizer center,” *Brain Research Reviews*, vol. 49, no. 2, pp. 109–113, 2005, doi: 10.1016/j.brainresrev.2005.03.001.
- [188] K. R. Thomas and M. R. Capecchi, “Targeted disruption of the murine int-1 proto-oncogene resulting in severe abnormalities in midbrain and cerebellar development,” *Nature*, vol. 346, no. 6287, pp. 847–850, 1990, doi: 10.1038/346847a0.
- [189] A. P. McMahon and A. Bradley, “The Wnt-1 (int-1) proto-oncogene is required for development of a large region of the mouse brain,” *Cell*, vol. 62, no. 6, pp. 1073–1085, 1990, doi: 10.1016/0092-8674(90)90385-R.
- [190] W. Wurst, A. B. Auerbach, and A. L. Joyner, “Multiple developmental defects in Engrailed-1 mutant mice: An early mid-hindbrain deletion and patterning defects in forelimbs and sternum,” *Development*, vol. 120, no. 7, pp. 2065–2075, 1994, doi: 10.1242/dev.120.7.2065.
- [191] J. Favor *et al.*, “The mouse Pax21Neu mutation is identical to a human PAX2 mutation in a family with renal-coloboma syndrome and results in developmental defects of the brain, ear, eye, and kidney,” *Proc Natl Acad Sci U S A*, vol. 93, no. 24, pp. 13870–13875, 1996, doi: 10.1073/pnas.93.24.13870.
- [192] E. N. Meyers, M. Lewandoski, and G. R. Martin, “Cre- and Flp-mediated recombination,” vol. 18, no. february, pp. 1–6, 1998.

- [193] V. Broccoli, E. Boncinelli, and W. Wurst, “The caudal limit of Otx2 expression positions the isthmus organizer,” *Nature*, vol. 401, no. 6749, pp. 164–168, 1999, doi: 10.1038/43670.
- [194] P. H. Crossley, G. Minowada, C. A. MacArthur, and G. R. Martin, “Roles for FGF8 in the induction, initiation, and maintenance of chick limb development,” *Cell*, vol. 84, no. 1, pp. 127–136, 1996, doi: 10.1016/S0092-8674(00)80999-X.
- [195] T. Sato, I. Araki, and H. Nakamura, “Inductive signal and tissue responsiveness defining the tectum and the cerebellum,” *Development*, vol. 128, no. 13, pp. 2461–2469, 2001, doi: 10.1242/dev.128.13.2461.
- [196] Q. Guo and J. Y. H. Li, “Distinct functions of the major Fgf8 spliceform, before and during mouse gastrulation,” *Development*, vol. 134, no. 12, pp. 2251–2260, 2007, doi: 10.1242/dev.004929.
- [197] F. Marín and L. Puelles, “Morphological Fate of Rhombomeres in Quail/Chick Chimeras: A Segmental Analysis of Hindbrain Nuclei,” *European Journal of Neuroscience*, vol. 7, no. 8, pp. 1714–1738, 1995, doi: 10.1111/j.1460-9568.1995.tb00693.x.
- [198] M. Hidalgo-Sánchez, A. Simeone, and R. M. Alvarado-Mallart, “Fgf8 and Gbx2 induction concomitant with Otx2 regression is correlated with midbrain-hindbrain fate of caudal prosencephalon,” *Development*, vol. 126, no. 14, pp. 3191–3203, 1999, doi: 10.1242/dev.126.14.3191.
- [199] S. Martinez, P. H. Crossley, I. Cobos, J. L. R. Rubenstein, and G. R. Martin, “FGF8 induces ectopic isthmus organizer.pdf,” *Development*, vol. 1200, pp. 1189–1200, 1999.
- [200] C. L. Chi, S. Martinez, W. Wurst, and G. R. Martin, “The isthmus organizer signal FGF8 is required for cell survival in the prospective midbrain and cerebellum,” *Development*, vol. 130, no. 12, pp. 2633–2644, 2003, doi: 10.1242/dev.00487.
- [201] H. Shamim, R. Mahmood, C. Logan, P. Doherty, A. Lumsden, and I. Mason, “Sequential roles for Fgf4, En1 and Fgf8 in specification and regionalisation of the midbrain,” *Development*, vol. 126, no. 5, pp. 945–959, 1999, doi: 10.1242/dev.126.5.945.
- [202] J. Xu, Z. Liu, and D. M. Ornitz, “Temporal and spatial gradients of Fgf8 and Fgf17 regulate proliferation and differentiation of midline cerebellar structures,” *Development*, vol. 127, no. 9, pp. 1833–1843, 2000, doi: 10.1242/dev.127.9.1833.
- [203] A. Suzuki-Hirano, H. Harada, T. Sato, and H. Nakamura, “Activation of Ras-ERK pathway by Fgf8 and its downregulation by Sprouty2 for the isthmus organizing activity,” *Developmental Biology*, vol. 337, no. 2, pp. 284–293, 2010, doi: 10.1016/j.ydbio.2009.10.044.
- [204] M. Eddison, L. Toole, E. Bell, and R. J. T. Wingate, “Segmental identity and cerebellar granule cell induction in rhombomere 1,” *BMC Biology*, vol. 2, pp. 1–13, 2004, doi: 10.1186/1741-7007-2-14.
- [205] A. de Luca, V. Cerrato, E. Fucà, E. Parmigiani, A. Buffo, and K. Leto, “Sonic hedgehog patterning during cerebellar development,” *Cellular and Molecular Life Sciences*, vol. 73, no. 2, pp. 291–303, 2016, doi: 10.1007/s00018-015-2065-1.
- [206] V. Y. Wang, M. F. Rose, and H. Y. Zoghbi, “Math1 expression redefines the rhombic lip derivatives and reveals novel lineages within the brainstem and cerebellum,” *Neuron*, vol. 48, no. 1, pp. 31–43, 2005, doi: 10.1016/j.neuron.2005.08.024.
- [207] M. Hoshino *et al.*, “Ptf1a, a bHLH transcriptional gene, defines GABAergic neuronal fates in cerebellum,” *Neuron*, vol. 47, no. 2, pp. 201–213, 2005, doi: 10.1016/j.neuron.2005.06.007.
- [208] M. Pascual *et al.*, “Cerebellar GABAergic progenitors adopt an external granule cell-like phenotype in the absence of Ptf1a transcription factor expression,” *Proc Natl Acad Sci U S A*, vol. 104, no. 12, pp. 5193–5198, 2007, doi: 10.1073/pnas.0605699104.
- [209] M. Yamada *et al.*, “Specification of Spatial Identities of Cerebellar Neuron Progenitors by Ptf1a and Atoh1 for Proper Production of GABAergic and Glutamatergic Neurons,” *Journal of Neuroscience*, vol. 34, no. 14, 2014, doi: 10.1523/JNEUROSCI.2722-13.2014.
- [210] S. W. Wilson and J. L. R. Rubenstein, “Induction and dorsoventral patterning of the telencephalon,” *Neuron*, vol. 28, no. 3, pp. 641–651, 2000, doi: 10.1016/S0896-6273(00)00171-9.
- [211] K. J. Millen, E. Y. Steshina, I. Y. Iskusnykh, and V. v. Chizhikov, “Transformation of the cerebellum into more ventral brainstem fates causes cerebellar agenesis in the absence of Ptf1a function,” *Proc Natl Acad Sci U S A*, vol. 111, no. 17, 2014, doi: 10.1073/pnas.1315024111.

- [212] K. K. Tong, T. C. Ma, and K. M. Kwan, "BMP/Smad signaling and embryonic cerebellum development: Stem cell specification and heterogeneity of anterior rhombic lip," *Development Growth and Differentiation*, vol. 57, no. 2, pp. 121–134, 2015, doi: 10.1111/dgd.12198.
- [213] V. Pibiri, A. Ravarino, C. Gerosa, M. C. Pintus, V. Fanos, and G. Faa, "Stem/progenitor cells in the developing human cerebellum: An immunohistochemical study," *European Journal of Histochemistry*, vol. 60, no. 3, pp. 204–208, 2016, doi: 10.4081/ejh.2016.2686.
- [214] K. Muguruma, A. Nishiyama, H. Kawakami, K. Hashimoto, and Y. Sasai, "Self-organization of polarized cerebellar tissue in 3D culture of human pluripotent stem cells," *Cell Reports*, vol. 10, no. 4, pp. 537–550, 2015, doi: 10.1016/j.celrep.2014.12.051.
- [215] H. J. Selvadurai *et al.*, "Medulloblastoma Arises from the Persistence of a Rare and Transient Sox2+ Granule Neuron Precursor," *Cell Reports*, vol. 31, no. 2, p. 107511, 2020, doi: 10.1016/j.celrep.2020.03.075.
- [216] T. Zhang *et al.*, "Generation of excitatory and inhibitory neurons from common progenitors via Notch signaling in the cerebellum," *Cell Reports*, vol. 35, no. 10, p. 109208, 2021, doi: 10.1016/j.celrep.2021.109208.
- [217] D. Hirsch, A. Kohl, Y. Wang, and D. Sela-Donenfeld, "Axonal Projection Patterns of the Dorsal Interneuron Populations in the Embryonic Hindbrain," *Frontiers in Neuroanatomy*, vol. 15, no. December, pp. 1–23, 2021, doi: 10.3389/fnana.2021.793161.
- [218] R. J. T. Wingate, "The rhombic lip and early cerebellar development," *Current Opinion in Neurobiology*, vol. 11, no. 1, pp. 82–88, 2001, doi: 10.1016/S0959-4388(00)00177-X.
- [219] V. v. Chizhikov and K. J. Millen, "Mechanisms of roof plate formation in the vertebrate CNS," *Nature Reviews Neuroscience*, vol. 5, no. 10, pp. 808–812, 2004, doi: 10.1038/nrn1520.
- [220] Y. Mishima, A. G. Lindgren, V. v. Chizhikov, R. L. Johnson, and K. J. Millen, "Overlapping function of Lmx1a and Lmx1b in anterior hindbrain roof plate formation and cerebellar growth," *Journal of Neuroscience*, vol. 29, no. 36, pp. 11377–11384, 2009, doi: 10.1523/JNEUROSCI.0969-09.2009.
- [221] Y. Kita, K. Kawakami, Y. Takahashi, and F. Murakami, "Development of Cerebellar Neurons and Glia Revealed by in Utero Electroporation: Golgi-Like Labeling of Cerebellar Neurons and Glia," *PloS ONE*, vol. 8, no. 7, 2013, doi: 10.1371/journal.pone.0070091.
- [222] M. J. Green and R. J. T. Wingate, "Developmental origins of diversity in cerebellar output nuclei," *Neural Development*, vol. 9, no. 1, pp. 2–9, 2014, doi: 10.1186/1749-8104-9-1.
- [223] N. Hagan and M. Zervas, "Wnt1 expression temporally allocates upper rhombic lip progenitors and defines their terminal cell fate in the cerebellum," *Molecular and Cellular Neuroscience*, vol. 49, no. 2, pp. 217–229, 2012, doi: 10.1016/j.mcn.2011.11.008.
- [224] E. D. Lowenstein *et al.*, "Olig3 regulates early cerebellar development," *Elife*, vol. 10, pp. 1–25, 2021, doi: 10.7554/eLife.64684.
- [225] M. E. Hatten and N. Heintz, "Mechanisms of neural patterning and specification in the developing cerebellum," *Annual Review of Neuroscience*, vol. 18, pp. 385–408, 1995, doi: 10.1146/annurev.ne.18.030195.002125.
- [226] L. Mathis, C. Bonnerot, L. Ruelles, and J. F. Nicolas, "Retrospective clonal analysis of the cerebellum using genetic lacZ/lacZ mouse mosaics," *Development*, vol. 124, no. 20, pp. 4089–4104, 1997, doi: 10.1242/dev.124.20.4089.
- [227] F. v. Dastjerdi, G. G. Consalez, and R. Hawkes, "Pattern formation during development of the embryonic cerebellum," *Frontiers in Neuroanatomy*, vol. 6, no. MARCH, pp. 1–53, 2012, doi: 10.3389/fnana.2012.00010.
- [228] K. Hori and M. Hoshino, "GABAergic neuron specification in the spinal cord, the cerebellum, and the cochlear nucleus," *Neural Plasticity*, vol. 2012, 2012, doi: 10.1155/2012/921732.
- [229] Y. Minaki, T. Nakatani, E. Mizuhara, T. Inoue, and Y. Ono, "Identification of a novel transcriptional corepressor, Corl2, as a cerebellar Purkinje cell-selective marker," *Gene Expression Patterns*, vol. 8, no. 6, pp. 418–423, 2008, doi: 10.1016/j.gep.2008.04.004.
- [230] E. Mizuhara *et al.*, "Purkinje cells originate from cerebellar ventricular zone progenitors positive for Neph3 and E-cadherin," *Developmental Biology*, vol. 338, no. 2, pp. 202–214, 2010, doi: 10.1016/j.ydbio.2009.11.032.
- [231] Y. Seto, S. Ishiwata, and M. Hoshino, "Characterization of Olig2 expression during cerebellar development," *Gene Expression Patterns*, vol. 15, no. 1, pp. 1–7, 2014, doi: 10.1016/j.gep.2014.02.001.
- [232] P. Zordan, L. Croci, R. Hawkes, and G. G. Consalez, "Comparative analysis of proneural gene expression in the embryonic cerebellum," *Developmental Dynamics*, vol. 237, no. 6, pp. 1726–1735, 2008, doi: 10.1002/dvdy.21571.

- [233] T. yia Vue *et al.*, “Age-Dependent Effect of Nitric Oxide on Subventricular Zone and Olfactory Bulb,” *Journal of Comparative Neurology*, vol. 505, no. October 2007, pp. 73–91, 2007, doi: 10.1002/cne.
- [234] T. G. Lundell, Q. Zhou, and M. L. Doughty, “Neurogenin1 expression in cell lineages of the cerebellar cortex in embryonic and postnatal mice,” *Developmental Dynamics*, vol. 238, no. 12, pp. 3310–3325, 2009, doi: 10.1002/dvdy.22165.
- [235] E. J. Kim *et al.*, “the Mouse Central Nervous System,” vol. 519, no. 7, pp. 1355–1370, 2014, doi: 10.1002/cne.22574.Spatiotemporal.
- [236] M. Florio *et al.*, “Neurogenin 2 regulates progenitor cell-cycle progression and Purkinje cell dendritogenesis in cerebellar development,” *Development (Cambridge)*, vol. 139, no. 13, pp. 2308–2320, 2012, doi: 10.1242/dev.075861.
- [237] P. Grimaldi, C. Parras, F. Guillemot, F. Rossi, and M. Wassef, “Origins and control of the differentiation of inhibitory interneurons and glia in the cerebellum,” *Developmental Biology*, vol. 328, no. 2, pp. 422–433, 2009, doi: 10.1016/j.ydbio.2009.02.008.
- [238] L. Telley *et al.*, “Sequential transcriptional waves direct the differentiation of newborn neurons in the mouse neocortex,” *Science (1979)*, vol. 351, no. 6280, pp. 1443–1446, 2016, doi: 10.1126/science.aad8361.
- [239] D. A. Galloway, L. A. Laimins, B. Division, and F. Hutchinson, “Generating neuronal diversity in the mammalian cerebral cortex,” pp. 87–92, 2016, doi: 10.1016/j.coviro.2015.09.001.Human.
- [240] M. Wilsch-Briegleb, M. Florio, and W. B. Huttner, “Neocortex expansion in development and evolution – from cell biology to single genes,” *Current Opinion in Neurobiology*, vol. 39, pp. 122–132, 2016, doi: 10.1016/j.conb.2016.05.004.
- [241] I. L. Miale and R. L. Sidman, “An autoradiographic analysis of histogenesis in the mouse cerebellum,” *Experimental Neurology*, vol. 4, no. 4, pp. 277–296, 1961, doi: 10.1016/0014-4886(61)90055-3.
- [242] E. T. Pierce, “Histogenesis of the deep cerebellar nuclei in the mouse: an autoradiographic study,” *Brain Research*, vol. 95, no. 2–3, pp. 503–518, 1975, doi: 10.1016/0006-8993(75)90124-9.
- [243] D. Morales and M. E. Hatten, “Molecular Markers of Neuronal Progenitors in the Embryonic Cerebellar Anlage,” *Journal of Neuroscience*, vol. 26, no. 47, pp. 12226–12236, 2006, doi: 10.1523/JNEUROSCI.3493-06.2006.
- [244] L. Zhang and J. E. Goldman, “Generation of cerebellar interneurons from dividing progenitors in white matter,” *Neuron*, vol. 16, no. 1, pp. 47–54, 1996, doi: 10.1016/S0896-6273(00)80022-7.
- [245] K. Schilling, “Lineage, development and morphogenesis of cerebellar interneurons,” *Progress in Brain Research*, vol. 124, pp. 51–68, 2000, doi: 10.1016/s0079-6123(00)24007-7.
- [246] K. Leto, B. Carletti, I. M. Williams, L. Magrassi, and F. Rossi, “Different Types of Cerebellar GABAergic Interneurons Originate from a Common Pool of Multipotent Progenitor Cells,” *Journal of Neuroscience*, vol. 26, no. 45, pp. 11682–11694, 2006, doi: 10.1523/JNEUROSCI.3656-06.2006.
- [247] K. Leto, A. Bartolini, and F. Rossi, “Development of cerebellar GABAergic interneurons: Origin and shaping of the ‘minibrain’ local connections,” *Cerebellum*, vol. 7, no. 4, pp. 523–529, 2008, doi: 10.1007/s12311-008-0079-z.
- [248] V. Kozareva *et al.*, “A transcriptomic atlas of mouse cerebellar cortex comprehensively defines cell types,” *Nature*, vol. 598, no. March 2020, pp. 214–219, 2021, doi: 10.1038/s41586-021-03220-z.
- [249] R. J. Harvey and R. M. A. Napper, “Quantitative study of granule and Purkinje cells in the cerebellar cortex of the rat,” *Journal of Comparative Neurology*, vol. 274, no. 2, pp. 151–157, 1988, doi: 10.1002/cne.902740202.
- [250] J. O’Brien and N. Unwin, “Organization of spines on the dendrites of Purkinje cells,” *Proc Natl Acad Sci U S A*, vol. 103, no. 5, pp. 1575–1580, 2006, doi: 10.1073/pnas.0507884103.
- [251] M. R. Pantò, A. Zappalà, R. Parenti, M. F. Serapide, and F. Cicirata, “Corticonuclear projections of the cerebellum preserve both anteroposterior and mediolateral pairing patterns,” *European Journal of Neuroscience*, vol. 13, no. 4, pp. 694–708, 2001, doi: 10.1046/j.0953-816X.2000.01442.x.
- [252] G. Giacomo Consalez and R. Hawkes, “The compartmental restriction of cerebellar interneurons,” *Frontiers in Neural Circuits*, vol. 6, no. DEC, pp. 1–14, 2012, doi: 10.3389/fncir.2012.00123.
- [253] R. Hawkes, “The Ferdinando Rossi Memorial Lecture: Zones and Stripes – Pattern Formation in the Cerebellum,” *Cerebellum*, vol. 17, no. 1, pp. 12–16, 2018, doi: 10.1007/s12311-017-0887-0.
- [254] C. Redies, F. Neudert, and J. Lin, “Cadherins in cerebellar development: Translation of embryonic patterning into mature functional compartmentalization,” *Cerebellum*, vol. 10, no. 3, pp. 393–408, 2011, doi: 10.1007/s12311-010-0207-4.

- [255] G. Brochu, L. Maler, and R. Hawkes, “Zebrin II: A polypeptide antigen expressed selectively by purkinje cells reveals compartments in rat and fish cerebellum,” *Journal of Comparative Neurology*, vol. 291, no. 4, pp. 538–552, 1990, doi: 10.1002/cne.902910405.
- [256] A. H. Ahn, S. Dziennis, R. Hawkes, and K. Herrup, “The cloning of zebrin II reveals its identity with aldolase C,” *Development*, vol. 120, no. 8, pp. 2081–2090, 1994, doi: 10.1242/dev.120.8.2081.
- [257] L. M. Eisenman and R. Hawkes, “Antigenic compartmentation in the mouse cerebellar cortex: Zebrin and HNK-1 reveal a complex, overlapping molecular topography,” *Journal of Comparative Neurology*, vol. 335, no. 4, pp. 586–605, 1993, doi: 10.1002/cne.903350410.
- [258] S. I. Murase and Y. Hayashi, “Expression pattern of integrin β 1 subunit in Purkinje cells of rat and cerebellar mutant mice,” *Journal of Comparative Neurology*, vol. 375, no. 2, pp. 225–237, 1996, doi: 10.1002/(SICI)1096-9861(19961111)375:2<225::AID-CNE4>3.0.CO;2-4.
- [259] J. M. Mateos *et al.*, “Parasagittal compartmentalization of the metabotropic glutamate receptor mGluR1b in the cerebellar cortex,” *European Journal of Anatomy*, vol. 5, no. 1, pp. 15–21, 2001.
- [260] C. L. Armstrong, A. M. R. Krueger-Naug, R. W. Currie, and R. Hawkes, “Expression of heat-shock protein Hsp25 in mouse purkinje cells during development reveals novel features of cerebellar compartmentation,” *Journal of Comparative Neurology*, vol. 429, no. 1, pp. 7–21, 2001, doi: 10.1002/1096-9861(2000101)429:1<7::AID-CNE2>3.0.CO;2-Q.
- [261] Y. G. Jeong *et al.*, “The cyclin-dependent kinase 5 activator, p39, is expressed in stripes in the mouse cerebellum,” *Neuroscience*, vol. 118, no. 2, pp. 323–334, 2003, doi: 10.1016/S0306-4522(03)00002-2.
- [262] H. Marzban, C. T. Kim, D. Doorn, S. H. Chung, and R. Hawkes, “A novel transverse expression domain in the mouse cerebellum revealed by a neurofilament-associated antigen,” *Neuroscience*, vol. 153, no. 4, pp. 1190–1201, 2008, doi: 10.1016/j.neuroscience.2008.02.036.
- [263] J. R. Sarna, H. Marzban, M. Watanabe, and R. Hawkes, “Complementary stripes of phospholipase C β 3 and C β 4 expression by Purkinje cell subsets in the mouse cerebellum,” *Journal of Comparative Neurology*, vol. 496, no. 3, pp. 303–313, 2006, doi: 10.1002/cne.20912.
- [264] L. Croci *et al.*, “A key role for the HLH transcription factor EBF2/COE2, O/E-3 in Purkinje neuron migration and cerebellar cortical topography,” *Development*, vol. 133, no. 14, pp. 2719–2729, 2006, doi: 10.1242/dev.02437.
- [265] S. Chung, Y. Zhang, F. van der Hoorn, and R. Hawkes, “The anatomy of the cerebellar nuclei in the normal and scrambler mouse as revealed by the expression of the microtubule-associated protein kinesin light chain 3,” *Brain Research*, vol. 1140, no. 1, pp. 120–131, 2007, doi: 10.1016/j.brainres.2006.01.100.
- [266] J. W. Wizeman, Q. Guo, E. M. Wilion, and J. Y. H. Li, “Specification of diverse cell types during early neurogenesis of the mouse cerebellum,” *Elife*, vol. 8, pp. 1–24, 2019, doi: 10.7554/eLife.42388.
- [267] V. Kozareva *et al.*, “A transcriptomic atlas of the mouse cerebellum reveals regional specializations and novel cell types Correspondence: emacosko@broadinstitute.org Transcriptional definition of cerebellar cell types Characterization of spatial variation and patterning in n,” 2020.
- [268] K. Tran-Anh, J. Zhang, V. T. Nguyen-Minh, H. Fujita, T. Hirata, and I. Sugihara, “Common origin of the cerebellar dual somatotopic areas revealed by tracking embryonic purkinje cell clusters with birthdate tagging,” *eNeuro*, vol. 7, no. 6, pp. 1–23, 2020, doi: 10.1523/ENEURO.0251-20.2020.
- [269] G. D’Arcangelo, G. G. Miao, S. C. Chen, H. D. Scars, J. I. Morgan, and T. Curran, “A protein related to extracellular matrix proteins deleted in the mouse mutant reeler,” *Nature*, vol. 374, no. 6524, pp. 719–723, 1995. Doi: 10.1038/374719a0.
- [270] J. Ju *et al.*, “Olig2 regulates Purkinje cell generation in the early developing mouse cerebellum,” *Scientific Reports*, vol. 6, no. March, pp. 1–11, 2016, doi: 10.1038/srep30711.
- [271] J. C. Eccles, “Circuits in the cerebellar control of movement.,” *Proc Natl Acad Sci U S A*, vol. 58, no. 1, pp. 336–343, 1967, doi: 10.1073/pnas.58.1.336.
- [272] R. Llinás and M. Sugimori, “Electrophysiological properties of in vitro Purkinje cell dendrites in mammalian cerebellar slices.,” *The Journal of Physiology*, vol. 305, no. 1, pp. 197–213, 1980, doi: 10.1113/jphysiol.1980.sp013358.
- [273] D. Cohen and Y. Yarom, “Unravelling cerebellar circuitry: An optical imaging study,” *Progress in Brain Research*, vol. 124, pp. 107–114, 2000, doi: 10.1016/s0079-6123(00)24011-9.

- [274] F. Sultan and J. M. Bower, “Quantitative golgi study of the rat cerebellar molecular layer interneurons using principal component analysis,” *Journal of Comparative Neurology*, vol. 393, no. 3, pp. 353–373, 1998, doi: 10.1002/(SICI)1096-9861(19980413)393:3<353::AID-CNE7>3.0.CO;2-0.
- [275] W. Mittmann and M. Häusser, “Linking synaptic plasticity and spike output at excitatory and inhibitory synapses onto cerebellar Purkinje cells,” *Journal of Neuroscience*, vol. 27, no. 21, pp. 5559–5570, 2007, doi: 10.1523/JNEUROSCI.5117-06.2007.
- [276] J. Bao, K. Reim, and T. Sakaba, “Target-dependent feedforward inhibition mediated by short-term synaptic plasticity in the cerebellum,” *Journal of Neuroscience*, vol. 30, no. 24, pp. 8171–8179, 2010, doi: 10.1523/JNEUROSCI.0276-10.2010.
- [277] L. Telley *et al.*, “Dual Function of NR1 in Axon Guidance and Subcellular Target Recognition in Cerebellum,” *Neuron*, vol. 91, no. 6, pp. 1276–1291, 2016, doi: 10.1016/j.neuron.2016.08.015.
- [278] S. Chen and D. E. Hillman, “Colocalization of neurotransmitters in the deep cerebellar nuclei,” *Journal of Neurocytology*, vol. 22, no. 2, pp. 81–91, 1993, doi: 10.1007/BF01181572.
- [279] R. A. Carter *et al.*, “A Single-Cell Transcriptional Atlas of the Developing Murine Cerebellum,” *Current Biology*, vol. 28, no. 18, pp. 2910–2920.e2, 2018, doi: 10.1016/j.cub.2018.07.062.
- [280] B. Carletti and F. Rossi, “Neurogenesis in the cerebellum,” *Neuroscientist*, vol. 14, no. 1, pp. 91–100, 2008, doi: 10.1177/1073858407304629.
- [281] J. Altman and W. J. Anderson, “Experimental reorganization of the cerebellar cortex. I. Morphological effects of elimination of all microneurons with prolonged x-irradiation started at birth,” *Journal of Comparative Neurology*, vol. 146, no. 3, pp. 355–405, 1972, doi: 10.1002/cne.901460305.
- [282] C. Cadilhac *et al.*, “Excitatory granule neuron precursors orchestrate laminar localization and differentiation of cerebellar inhibitory interneuron subtypes,” *Cell Reports*, vol. 34, no. 13, 2021, doi: 10.1016/j.celrep.2021.108904.
- [283] A. Pieper *et al.*, “NeuroD2 controls inhibitory circuit formation in the molecular layer of the cerebellum,” *Scientific Reports*, vol. 9, no. 1, pp. 1–17, 2019, doi: 10.1038/s41598-018-37850-7.
- [284] E. D. Buttermore, C. Piochon, M. L. Wallace, B. D. Philpot, C. Hansel, and M. A. Bhat, “Pinceau organization in the cerebellum requires distinct functions of neurofascin in purkinje and basket neurons during postnatal development,” *Journal of Neuroscience*, vol. 32, no. 14, pp. 4724–4742, 2012, doi: 10.1523/JNEUROSCI.5602-11.2012.
- [285] J. M. Cioni *et al.*, “SEMA3A signaling controls layer-specific interneuron branching in the cerebellum,” *Current Biology*, vol. 23, no. 10, pp. 850–861, 2013, doi: 10.1016/j.cub.2013.04.007.
- [286] H. Mertz *et al.*, “Regional cerebral activation in irritable bowel syndrome and control subjects with painful and nonpainful rectal distention,” *Gastroenterology*, vol. 118, no. 5, pp. 842–848, 2000, doi: 10.1016/S0016-5085(00)70170-3.
- [287] K. Konno *et al.*, “Enriched expression of GluD1 in higher brain regions and its involvement in parallel fiber-interneuron synapse formation in the cerebellum,” *Journal of Neuroscience*, vol. 34, no. 22, pp. 7412–7424, 2014, doi: 10.1523/JNEUROSCI.0628-14.2014.
- [288] E. Galliano, P. Mazzarello, and E. D’Angelo, “Discovery and rediscoveries of Golgi cells,” *Journal of Physiology*, vol. 588, no. 19, pp. 3639–3655, 2010, doi: 10.1113/jphysiol.2010.189605.
- [289] N. H. Barmack and V. Yakhnitsa, “Distribution of granule cells projecting to focal Purkinje cells in mouse uvula-nodulus,” *Neuroscience*, vol. 156, no. 1, pp. 216–221, 2008, doi: 10.1016/j.neuroscience.2008.07.030.
- [290] E. D’Angelo and C. I. de Zeeuw, “Timing and plasticity in the cerebellum: focus on the granular layer,” *Trends in Neurosciences*, vol. 32, no. 1, pp. 30–40, 2009, doi: 10.1016/j.tins.2008.09.007.
- [291] K. Vervaeke, A. Lorincz, Z. Nusser, and R. A. Silver, “Gap junctions compensate for sublinear dendritic integration in an inhibitory network,” *Science (1979)*, vol. 335, no. 6076, pp. 1624–1628, 2012, doi: 10.1126/science.1215101.
- [292] M. Szoboszlai, A. Lőrincz, F. Lanore, K. Vervaeke, R. A. Silver, and Z. Nusser, “Functional Properties of Dendritic Gap Junctions in Cerebellar Golgi Cells,” *Neuron*, vol. 90, no. 5, pp. 1043–1056, 2016, doi: 10.1016/j.neuron.2016.03.029.
- [293] D. Watanabe *et al.*, “Ablation of cerebellar Golgi cells disrupts synaptic integration involving GABA inhibition and NMDA receptor activation in motor coordination,” *Cell*, vol. 95, no. 1, pp. 17–27, 1998, doi: 10.1016/S0092-8674(00)81779-1.

- [294] F. J. Geurts, E. de Schutter, and S. Dieudonné, “Unraveling the cerebellar cortex: Cytology and cellular physiology of large-sized interneurons in the granular layer,” *Cerebellum*, vol. 2, no. 4, pp. 290–299, 2003, doi: 10.1080/14734220310011948.
- [295] M. Simat, F. Parpan, and J.-M. Fritschy, “Heterogeneity of Glycinergic and Gabaergic Interneurons in the Granule Cell Layer of Mouse Cerebellum,” *Journal of Comparative Neurology*, vol. 500, no. October 2007, pp. 71–83, 2007.
- [296] B. Hausmann and J. Sievers, “Cerebellar external granule cells are attached to the basal lamina from the onset of migration up to the end of their proliferative activity,” *Journal of Comparative Neurology*, vol. 241, no. 1, pp. 50–62, 1985, doi: 10.1002/cne.902410105.
- [297] S.-H. Chung *et al.*, “Zac1 plays a key role in the development of specific neuronal subsets in the mouse cerebellum,” pp. 1–15, 2011, doi: 10.1186/1749-8104-6-25.
- [298] A. B. Melik-Musyan and V. v. Fanardzhyan, “Morphological characteristics of Lugaro cells in the cerebellar cortex,” *Neuroscience and Behavioral Physiology*, vol. 34, no. 6, pp. 633–638, 2004, doi: 10.1023/B:NEAB.0000028297.30474.f9.
- [299] T. Miyazaki, M. Yamasaki, K. F. Tanaka, and M. Watanabe, “Compartmentalized Input–Output Organization of Lugaro Cells in the Cerebellar Cortex,” *Neuroscience*, vol. 462, pp. 89–105, 2021, doi: 10.1016/j.neuroscience.2020.05.026.
- [300] J. Lainé and H. Axelrad, “Extending the cerebellar Lugaro cell class,” *Neuroscience*, vol. 115, no. 2, pp. 363–374, 2002, doi: 10.1016/S0306-4522(02)00421-9.
- [301] A. J. Fink, “Development of the Deep Cerebellar Nuclei: Transcription Factors and Cell Migration from the Rhombic Lip,” *Journal of Neuroscience*, vol. 26, no. 11, pp. 3066–3076, 2006, doi: 10.1523/JNEUROSCI.5203-05.2006.
- [302] C. Englund, “Unipolar Brush Cells of the Cerebellum Are Produced in the Rhombic Lip and Migrate through Developing White Matter,” *Journal of Neuroscience*, vol. 26, no. 36, pp. 9184–9195, 2006, doi: 10.1523/JNEUROSCI.1610-06.2006.
- [303] B. B. Andersen, L. Korbo, and B. Pakkenberg, “A quantitative study of the human cerebellum with unbiased stereological techniques,” *Journal of Comparative Neurology*, vol. 326, no. 4, pp. 549–560, 1992, doi: 10.1002/cne.903260405.
- [304] F. A. C. Azevedo *et al.*, “Equal numbers of neuronal and nonneuronal cells make the human brain an isometrically scaled-up primate brain,” *Journal of Comparative Neurology*, vol. 513, no. 5, pp. 532–541, 2009, doi: 10.1002/cne.21974.
- [305] R. Machold, C. Klein, and G. Fishell, “Genes expressed in Atoh1 neuronal lineages arising from the r1/isthmus rhombic lip,” *Gene Expression Patterns*, vol. 11, no. 5–6, pp. 349–359, 2011, doi: 10.1016/j.gep.2011.03.007.
- [306] J. S. Espinosa and L. Luo, “Timing neurogenesis and differentiation: Insights from quantitative clonal analyses of cerebellar granule cells,” *Journal of Neuroscience*, vol. 28, no. 10, pp. 2301–2312, 2008, doi: 10.1523/JNEUROSCI.5157-07.2008.
- [307] T. Miyata, T. Maeda, and J. E. Lee, “NeuroD is required for differentiation of the granule cells in the cerebellum and hippocampus,” *Genes and Development*, vol. 13, no. 13, pp. 1647–1652, 1999, doi: 10.1101/gad.13.13.1647.
- [308] A. Chédotal and L. J. Richards, “Wiring the brain: The biology of neuronal guidance,” *Cold Spring Harbor Perspectives in Biology*, vol. 2, no. 6, pp. 1–17, 2010, doi: 10.1101/cshperspect.a001917.
- [309] J. C. Edmondson, R. K. H. Liem, J. E. Kuster, and M. E. Hatten, “Astrotactin: A novel neuronal cell surface antigen that mediates neuron-astroglial interactions in cerebellar microcultures,” *Journal of Cell Biology*, vol. 106, no. 2, pp. 505–517, 1988, doi: 10.1083/jcb.106.2.505.
- [310] G. Kerjan *et al.*, “The transmembrane semaphorin Sema6A controls cerebellar granule cell migration,” *Nature Neuroscience*, vol. 8, no. 11, pp. 1516–1524, 2005, doi: 10.1038/nn1555.
- [311] H. Zong, J. S. Espinosa, H. H. Su, M. D. Muzumdar, and L. Luo, “Mosaic analysis with double markers in mice,” *Cell*, vol. 121, no. 3, pp. 479–492, 2005, doi: 10.1016/j.cell.2005.02.012.
- [312] A. C. Hall, F. R. Lucas, and P. C. Salinas, “Axonal Remodeling and Synaptic Differentiation in the Cerebellum Is Regulated by WNT-7a Signaling becomes multilobulated as it interdigitates with GC den- drites (Hamori and Somogyi, 1983). The increase in mossy fiber surface area permits the formation of,” *Cell*, vol. 100, pp. 525–535, 2000, [Online]. Available: <http://ac.els-cdn.com/S0092867400806893/1-s2.0-S0092867400806893->

[main.pdf? tid=4d2ea9fa-5092-11e7-814d-00000aab0f6b&acdnat=1497397675_39fe16129d5ff7a323afb29f8e695a0e](#)

- [313] S. G. Kalinichenko and V. E. Okhotin, “Unipolar brush cells – A new type of excitatory interneuron in the cerebellar cortex and cochlear nuclei of the brainstem,” *Neuroscience and Behavioral Physiology*, vol. 35, no. 1, pp. 21–36, 2005, doi: 10.1023/B:NEAB.0000049648.20702.ad.
- [314] J. Harris, S. Moreno, G. Shaw, and E. Mugnaini, “Unusual neurofilament composition in cerebellar unipolar brush neurons,” *Journal of Neurocytology*, vol. 22, no. 12, pp. 1039–1059, 1993, doi: 10.1007/BF01235748.
- [315] E. Mugnaini and A. Floris, “The unipolar brush cell: A neglected neuron of the mammalian cerebellar cortex,” *Journal of Comparative Neurology*, vol. 339, no. 2, pp. 174–180, 1994, doi: 10.1002/cne.903390203.
- [316] M. G. Nunzi, S. Birnstiel, B. J. Bhattacharyya, N. T. Slater, and E. Mugnaini, “Unipolar brush cells form a glutamatergic projection system within the mouse cerebellar cortex,” *Journal of Comparative Neurology*, vol. 434, no. 3, pp. 329–341, 2001, doi: 10.1002/cne.1180.
- [317] M. R. Diño, F. H. Willard, and E. Mugnaini, “Distribution of unipolar brush cells and other calretinin immunoreactive components in the mammalian cerebellar cortex,” *Journal of Neurocytology*, vol. 28, no. 2, pp. 99–123, 1999, doi: 10.1023/A:1007072105919.
- [318] J. E. Canton-Josh, J. Qin, and Y. Kozorovitskiy, “Dopaminergic regulation of vestibulo-cerebellar circuits through unipolar brush cells,” *bioRxiv*, vol. 4, no. 1, p. 6, 2021.
- [319] Y. Arai *et al.*, “Evolutionary Gain of Dbx1 Expression Drives Subplate Identity in the Cerebral Cortex,” *Cell Reports*, vol. 29, no. 3, pp. 645–658.e5, 2019, doi: 10.1016/j.celrep.2019.09.007.
- [320] A. Floris, M. Diño, D. M. Jacobowitz, and E. Mugnaini, “The unipolar brush cells of the rat cerebellar cortex and cochlear nucleus are calretinin-positive: a study by light and electron microscopic immunocytochemistry,” *Anatomy and Embryology*, vol. 189, no. 6, pp. 495–520, 1994, doi: 10.1007/BF00186824.
- [321] F. Morin, M. R. Dio, and E. Mugnaini, “Postnatal differentiation of unipolar brush cells and mossy fiber-unipolar brush cell synapses in rat cerebellum,” *Neuroscience*, vol. 104, no. 4, pp. 1127–1139, 2001, doi: 10.1016/S0306-4522(01)00144-0.
- [322] J. Takács, L. Markova, Z. Borostyánkői, T. J. Görös, and J. Hámori, “Metabotropic glutamate receptor type 1a expressing unipolar brush cells in the cerebellar cortex of different species: A comparative quantitative study,” *Journal of Neuroscience Research*, vol. 55, no. 6, pp. 733–748, 1999, doi: 10.1002/(SICI)1097-4547(19990315)55:6<733::AID-JNR8>3.0.CO;2-8.
- [323] W. B. Spatz, “Unipolar brush cells in the human cochlear nuclei identified by their expression of a metabotropic glutamate receptor (mGluR2/3),” *Neuroscience Letters*, vol. 316, no. 3, pp. 161–164, 2001, doi: 10.1016/S0304-3940(01)02392-8.
- [324] I.-M. Pimeisl *et al.*, “Generation and Characterization of a Tamoxifen-Inducible eomes CreER mouse line,” *Genesis*, vol. 51, no. 10, pp. 725–733, 2013, doi: 10.1002/dvg.22417.Generation.
- [325] A. McDonough *et al.*, “Unipolar (Dendritic) Brush Cells Are Morphologically Complex and Require Tbr2 for Differentiation and Migration,” *Frontiers in Neuroscience*, vol. 14, no. January, pp. 1–13, 2021, doi: 10.3389/fnins.2020.598548.
- [326] L. C. Abbott and D. M. Jacobowitz, “Development of calretinin-immunoreactive unipolar brush-like cells and an afferent pathway to the embryonic and early postnatal mouse cerebellum,” *Anatomy and Embryology*, vol. 191, no. 6, pp. 541–559, 1995, doi: 10.1007/BF00186743.
- [327] G. Sekerková, E. Ilijic, and E. Mugnaini, “Time of origin of unipolar brush cells in the rat cerebellum as observed by prenatal bromodeoxyuridine labeling,” *Neuroscience*, vol. 127, no. 4, pp. 845–858, 2004, doi: 10.1016/j.neuroscience.2004.05.050.
- [328] E. Ilijic, A. Guidotti, and E. Mugnaini, “Moving up or moving down? Malpositioned cerebellar unipolar brush cells in reeler mouse,” *Neuroscience*, vol. 136, no. 3, pp. 633–647, 2005, doi: 10.1016/j.neuroscience.2005.01.030.
- [329] R. MacHold and G. Fishell, “Math1 is expressed in temporally discrete pools of cerebellar rhombic-lip neural progenitors,” *Neuron*, vol. 48, no. 1, pp. 17–24, 2005, doi: 10.1016/j.neuron.2005.08.028.
- [330] T. Osorno *et al.*, “Candelabrum cells are molecularly distinct, ubiquitous interneurons of the cerebellar cortex with specialized circuit properties,” *bioRxiv*, pp. 1–37, 2021, doi: <https://doi.org/10.1101/2021.04.09.439172>.
- [331] J. Altman and S. A. Bayer, “Embryonic development of the rat cerebellum. II. Translocation and regional distribution of the deep neurons,” *Journal of Comparative Neurology*, vol. 231, no. 1, pp. 27–41, 1985, doi: 10.1002/cne.902310104.

- [332] C. Englund *et al.*, “Pax6, Tbr2, and Tbr1 are expressed sequentially by radial glia, intermediate progenitor cells, and postmitotic neurons in developing neocortex,” *Journal of Neuroscience*, vol. 25, no. 1, pp. 247–251, 2005, doi: 10.1523/JNEUROSCI.2899-04.2005.
- [333] S. Yuasa, K. Kawamura, R. Kuwano, and O. Katsuhiko, “Neuron-glia interrelations during migration of Purkinje cells in the mouse embryonic cerebellum,” *International Journal of Developmental Neuroscience*, vol. 14, no. 4, pp. 429–438, 1996, doi: 10.1016/0736-5748(96)00021-4.
- [334] T. E. Anthony and N. Heintz, “Genetic lineage tracing defines distinct neurogenic and gliogenic stages of ventral telencephalic radial glial development,” *Neural Development*, vol. 3, no. 1, 2008, doi: 10.1186/1749-8104-3-30.
- [335] T. Mori, K. Tanaka, A. Buffo, W. Wurst, R. Kuhn, and M. Gotz, “Inducible Gene Deletion in Astroglia and Radial Glia—A Valuable Tool for Functional and Lineage Analysis,” *Glia*, vol. 54, pp. 21–34, 2006, doi: 10.1002/glia.
- [336] P. Jensen, R. Smeyne, and D. Goldowitz, “Analysis of Cerebellar Development in math1 Null Embryos and Chimeras,” *Journal of Neuroscience*, vol. 24, no. 9, pp. 2202–2211, 2004, doi: 10.1523/JNEUROSCI.3427-03.2004.
- [337] O. A. Bayraktar, L. C. Fuentealba, A. Alvarez-Buylla, and D. H. Rowitch, “Astrocyte development and heterogeneity,” *Cold Spring Harbor Perspectives in Biology*, vol. 7, no. 1, pp. 1–16, 2015, doi: 10.1101/cshperspect.a020362.
- [338] L. ben Haim and D. H. Rowitch, “Functional diversity of astrocytes in neural circuit regulation,” *Nature Reviews Neuroscience*, vol. 18, no. 1, pp. 31–41, 2016, doi: 10.1038/nrn.2016.159.
- [339] W. T. Farmer *et al.*, “Neurons diversify astrocytes in the adult brain through sonic hedgehog signaling,” *Science (1979)*, vol. 351, no. 6275, pp. 849–854, 2016, doi: 10.1126/science.aab3103.
- [340] K. Yamada *et al.*, “Dynamic transformation of Bergmann glial fibers proceeds in correlation with dendritic outgrowth and synapse formation of cerebellar Purkinje cells,” *Journal of Comparative Neurology*, vol. 418, no. 1, pp. 106–120, 2000, doi: 10.1002/(SICI)1096-9861(20000228)418:1<106::AID-CNE8>3.0.CO;2-N.
- [341] F. Ango, C. Wu, J. J. van der Want, P. Wu, M. Schachner, and Z. J. Huang, “Bergmann glia and the recognition molecule CHL1 organize GABAergic axons and direct innervation of Purkinje cell dendrites,” *PLoS Biology*, vol. 6, no. 4, pp. 739–756, 2008, doi: 10.1371/journal.pbio.0060103.
- [342] T. M. Hoogland and B. Kuhn, “Recent developments in the understanding of astrocyte function in the Cerebellum in vivo,” *Cerebellum*, vol. 9, no. 3, pp. 264–271, 2010, doi: 10.1007/s12311-009-0139-z.
- [343] H. K. Kimelberg, “Functions of mature mammalian astrocytes: A current view,” *Neuroscientist*, vol. 16, no. 1, pp. 79–106, 2010, doi: 10.1177/1073858409342593.
- [344] A. Mallamaci, “Developmental control of cortico-cerebral astrogenesis,” *International Journal of Developmental Biology*, vol. 57, no. 9–10, pp. 689–706, 2013, doi: 10.1387/ijdb.130148am.
- [345] S. C. Noctor, V. Martínez-Cerdeño, L. Ivic, and A. R. Kriegstein, “Cortical neurons arise in symmetric and asymmetric division zones and migrate through specific phases,” *Nature Neuroscience*, vol. 7, no. 2, pp. 136–144, 2004, doi: 10.1038/nn1172.
- [346] S. C. Noctor, V. Martínez-Cerdeño, and A. R. Kriegstein, “Distinct behaviors of neural stem and progenitor cells underlie cortical neurogenesis,” *Journal of Comparative Neurology*, vol. 508, no. 1, pp. 28–44, 2008, doi: 10.1002/cne.21669.
- [347] W.-P. Ge, A. Miyawaki, F. Gage, Y.-N. Jan, and L. Y. Jan, “Local generation of glia is a major astrocyte source in postnatal cortex,” *Nature*, vol. 484, no. 7394, pp. 376–380, 2012, doi: 10.1038/nature10959.Local.
- [348] J. Sievers, R. Parwaresch, and H. -U Wottge, “Blood monocytes and spleen macrophages differentiate into microglia-like cells on monolayers of astrocytes: Morphology,” *Glia*, vol. 12, no. 4, pp. 245–258, 1994, doi: 10.1002/glia.440120402.
- [349] M. Hoshino, “Neuronal subtype specification in the cerebellum and dorsal hindbrain,” *Development Growth and Differentiation*, vol. 54, no. 3, pp. 317–326, 2012, doi: 10.1111/j.1440-169X.2012.01330.x.
- [350] V. Cerrato *et al.*, *Multiple origins and modularity in the spatiotemporal emergence of cerebellar astrocyte heterogeneity*, vol. 16, no. 9. 2018. Doi: 10.1371/journal.pbio.2005513.
- [351] N. Mecklenburg, J. E. Martínez-Lopez, J. A. Moreno-Bravo, A. Perez-Balaguer, E. Puelles, and S. Martínez, “Growth and differentiation factor 10 (Gdf10) is involved in bergmann glial cell development under Shh regulation,” *Glia*, vol. 62, no. 10, pp. 1713–1723, 2014, doi: 10.1002/glia.22710.

- [352] E. Parmigiani *et al.*, “Heterogeneity and bipotency of astroglial-like cerebellar progenitors along the interneuron and glial lineages,” *Journal of Neuroscience*, vol. 35, no. 19, pp. 7388–7402, 2015, doi: 10.1523/JNEUROSCI.5255-14.2015.
- [353] L. Grandbarbe, J. Bouissac, M. Rand, M. Hrabé de Angelis, S. Artavanis-Tsakonas, and E. Mohier, “Delta-Notch signaling controls the generation of neurons/glia from neural stem cells in a stepwise process,” *Development*, vol. 130, no. 7, pp. 1391–1402, 2003, doi: 10.1242/dev.00374.
- [354] H. Zhang *et al.*, “Several rAAV vectors efficiently cross the blood-brain barrier and transduce neurons and astrocytes in the neonatal mouse central nervous system,” *Molecular Therapy*, vol. 19, no. 8, pp. 1440–1448, 2011, doi: 10.1038/mt.2011.98.
- [355] J. Silbereis, E. Cheng, Y. M. Ganat, L. R. Ment, and F. M. Vaccarino, “Precursors with glial fibrillary acidic protein promoter activity transiently generate GABA interneurons in the postnatal cerebellum,” *Stem Cells*, vol. 27, no. 5, pp. 1152–1163, 2009, doi: 10.1002/stem.18.
- [356] C. Klein, S. J. B. Butt, R. P. Machold, J. E. Johnson, and G. Fishell, “Cerebellum- and forebrain-derived stem cells possess intrinsic regional character,” *Development*, vol. 132, no. 20, pp. 4497–4508, 2005, doi: 10.1242/dev.02037.
- [357] K. I. Vong, C. K. Y. Leung, R. R. Behringer, and K. M. Kwan, “Sox9 is critical for suppression of neurogenesis but not initiation of gliogenesis in the cerebellum,” *Molecular Brain*, vol. 8, no. 1, pp. 0–17, 2015, doi: 10.1186/s13041-015-0115-0.
- [358] L. Bouslama-Oueghlani *et al.*, “Purkinje Cell Maturation Participates in the Control of Oligodendrocyte Differentiation: Role of Sonic Hedgehog and Vitronectin,” *PLoS ONE*, vol. 7, no. 11, 2012, doi: 10.1371/journal.pone.0049015.
- [359] R. Hashimoto *et al.*, “Origins of oligodendrocytes in the cerebellum, whose development is controlled by the transcription factor, Sox9,” *Mechanisms of Development*, vol. 140, pp. 25–40, 2016, doi: 10.1016/j.mod.2016.02.004.
- [360] K. Ashwell, “Microglia and cell death in the developing mouse cerebellum,” *Developmental Brain Research*, vol. 55, no. 2, pp. 219–230, 1990, doi: 10.1016/0165-3806(90)90203-B.
- [361] F. L. Cardoso *et al.*, “Systemic inflammation in early neonatal mice induces transient and lasting neurodegenerative effects,” *Journal of Neuroinflammation*, vol. 12, no. 1, pp. 1–18, 2015, doi: 10.1186/s12974-015-0299-3.
- [362] R. D. Stowell *et al.*, “Cerebellar microglia are dynamically unique and survey Purkinje neurons in vivo,” *Developmental Neurobiology*, vol. 78, no. 6, pp. 627–644, 2018, doi: 10.1002/dneu.22572.
- [363] K. Grabert *et al.*, “Microglial brain regionâ ’dependent diversity and selective regional sensitivities to aging,” *Nature Neuroscience*, vol. 19, no. 3, pp. 504–516, 2016, doi: 10.1038/nn.4222.
- [364] T. L. Tay *et al.*, “A new fate mapping system reveals context-dependent random or clonal expansion of microglia,” *Nature Neuroscience*, vol. 20, no. 6, pp. 793–803, 2017, doi: 10.1038/nn.4547.
- [365] A. MacDonald *et al.*, “Single Cell Transcriptomics of Ependymal Cells Across Age, Region and Species Reveals Cilia-Related and Metal Ion Regulatory Roles as Major Conserved Ependymal Cell Functions,” *Frontiers in Cellular Neuroscience*, vol. 15, no. July, pp. 1–12, 2021, doi: 10.3389/fncel.2021.703951.
- [366] F. Ginhoux, A. Yalin, C. A. Dutertre, and I. Amit, “Perspective Single-cell immunology : Past , present , and future,” *Immunity*, vol. 55, no. 3, pp. 393–404, 2022, doi: 10.1016/j.immuni.2022.02.006.
- [367] A. Lopes, E. Magrinelli, and L. Telley, “Emerging roles of single-cell multi-omics in studying developmental temporal patterning,” *International Journal of Molecular Sciences*, vol. 21, no. 20, pp. 1–18, 2020, doi: 10.3390/ijms21207491.
- [368] H. Zeng, “Mesoscale Connectomics,” *Current Opinion in Neurobiology*, vol. 50, pp. 154–162, 2018, doi: 10.1016/j.conb.2018.03.003.Mesoscale.
- [369] M. Sahores and P. C. Salinas, *Activity-Mediated Synapse Formation. A Role for Wnt-Fz Signaling*, 1st ed., vol. 97. Elsevier Inc., 2011. Doi: 10.1016/B978-0-12-385975-4.00011-5.
- [370] S. D. Glasgow, R. McPhedrain, J. F. Madranges, T. E. Kennedy, and E. S. Ruthazer, “Approaches and limitations in the investigation of synaptic transmission and plasticity,” *Frontiers in Synaptic Neuroscience*, vol. 11, no. JUL, pp. 1–16, 2019, doi: 10.3389/fnsyn.2019.00020.
- [371] R. H. Roth and J. B. Ding, “From Neurons to Cognition: Technologies for Precise Recording of Neural Activity Underlying Behavior,” *BME Frontiers*, vol. 2020, pp. 1–20, 2020, doi: 10.34133/2020/7190517.

- [372] S. E. Jones, B. R. Buchbinder, and I. Aharon, “Three-dimensional mapping of cortical thickness using Laplace’s equation,” *Human Brain Mapping*, vol. 11, no. 1, pp. 12–32, 2000, doi: 10.1002/1097-0193(200009)11:1<12::AID-HBM20>3.0.CO;2-K.
- [373] P. A. Yushkevich *et al.*, “User-guided 3D active contour segmentation of anatomical structures: Significantly improved efficiency and reliability,” *Neuroimage*, vol. 31, no. 3, pp. 1116–1128, 2006, doi: 10.1016/j.neuroimage.2006.01.015.
- [374] P. Garcia-Lopez, V. Garcia-Marin, and M. Freire, “The histological slides and drawings of Cajal,” *Frontiers in Neuroanatomy*, vol. 4, no. MARCH, pp. 1–16, 2010, doi: 10.3389/neuro.05.009.2010.
- [375] R. J. Morris, J. N. Beech, P. C. Barber, and G. Raisman, “Early stages of Purkinje cell maturation demonstrated by Thy-1 immunohistochemistry on postnatal rat cerebellum,” *Journal of Neurocytology*, vol. 14, no. 3, pp. 427–452, 1985, doi: 10.1007/BF01217754.
- [376] L. M. Bolin and R. v. Rouse, “Localization of Thy-1 expression during postnatal development of the mouse cerebellar cortex,” *Journal of Neurocytology*, vol. 15, no. 1, pp. 29–36, 1986, doi: 10.1007/BF02057902.
- [377] V. Knoll and E. Ruska, “Das Elektronenmikroskop,” *Ann d Phys*, vol. 69, 1932, doi: 10.1055/s-0028-1122268.
- [378] Y. Kubota, J. Sohn, and Y. Kawaguchi, “Large volume electron microscopy and neural microcircuit analysis,” *Frontiers in Neural Circuits*, vol. 12, no. November, pp. 1–12, 2018, doi: 10.3389/fncir.2018.00098.
- [379] A. B. Scheibel, L. Paul, and I. Fried, “Scannin electron microscopy of the central nervous system. I. The cerebellum,” *Brain Research Reviews*, vol. 3, pp. 207–228, 1981.
- [380] M. Igarashi *et al.*, “New observations in neuroscience using superresolution microscopy,” *Journal of Neuroscience*, vol. 38, no. 44, pp. 9459–9467, 2018, doi: 10.1523/JNEUROSCI.1678-18.2018.
- [381] M. Dyba, S. Jakobs, and S. W. Hell, “Immunofluorescence stimulated emission depletion microscopy,” *Nature Biotechnology*, vol. 21, no. 11, pp. 1303–1304, 2003, doi: 10.1038/nbt897.
- [382] M. G. L. Gustafsson, “Nonlinear structured-illumination microscopy: Wide-field fluorescence imaging with theoretically unlimited resolution,” *Proc Natl Acad Sci U S A*, vol. 102, no. 37, pp. 13081–13086, 2005, doi: 10.1073/pnas.0406877102.
- [383] M. J. Rust, M. Bates, and X. Zhuang, “Sub-diffraction-limit imaging by stochastic optical reconstruction microscopy (STORM),” *Nature Methods*, vol. 3, no. 10, pp. 793–795, 2006, doi: 10.1038/nmeth929.
- [384] S. Manley *et al.*, “High-density mapping of single-molecule trajectories with photoactivated localization microscopy,” *Nature Methods*, vol. 5, no. 2, pp. 155–157, 2008, doi: 10.1038/nmeth.1176.
- [385] S. Reinhard, S. Aufmkolk, M. Sauer, and S. Doose, “Registration and Visualization of Correlative Super-Resolution Microscopy Data,” *Biophysical Journal*, vol. 116, no. 11, pp. 2073–2078, 2019, doi: 10.1016/j.bpj.2019.04.029.
- [386] F. Chen, P. W. Tillberg, and E. S. Boyden, “Expansion microscopy,” *Science (1979)*, vol. 347, no. 6221, pp. 543–548, 2015.
- [387] H. Siedentopf and R. Zsigmondy, “Über Sichtbarmachung und Grössenbestimmung ultramikroskopischer Teilchen,” *Ann Phys*, vol. 4, no. 1, pp. 1–39, 1903.
- [388] E. M. C. Hillman, V. Voleti, W. Li, and H. Yu, “Light-Sheet Microscopy in Neuroscience,” *Annual Review of Neuroscience*, vol. 42, pp. 295–313, 2019, doi: 10.1146/annurev-neuro-070918-050357.
- [389] H. U. Dodt *et al.*, “Ultramicroscopy: Three-dimensional visualization of neuronal networks in the whole mouse brain,” *Nature Methods*, vol. 4, no. 4, pp. 331–336, 2007, doi: 10.1038/nmeth1036.
- [390] A. Ertürk *et al.*, “Three-dimensional imaging of solvent-cleared organs using 3DISCO,” *Nature Protocols*, vol. 7, no. 11, pp. 1983–1995, 2012, doi: 10.1038/nprot.2012.119.
- [391] K. Chung and K. Deisseroth, “CLARITY for mapping the nervous system,” *Nature Methods*, vol. 10, no. 6, pp. 508–513, 2013, doi: 10.1038/nmeth.2481.
- [392] N. Renier, Z. Wu, D. J. Simon, J. Yang, P. Ariel, and M. Tessier-Lavigne, “IDISCO: A simple, rapid method to immunolabel large tissue samples for volume imaging,” *Cell*, vol. 159, no. 4, pp. 896–910, 2014, doi: 10.1016/j.cell.2014.10.010.
- [393] T. C. Murakami *et al.*, “A three-dimensional single-cell-resolution whole-brain atlas using CUBIC-X expansion microscopy and tissue clearing,” *Nature Neuroscience*, vol. 21, no. 4, pp. 625–637, 2018, doi: 10.1038/s41593-018-0109-1.
- [394] B. P. Bean, “The action potential in mammalian central neurons,” *Nature Reviews Neuroscience*, vol. 8, no. 6, pp. 451–465, 2007, doi: 10.1038/nrn2148.

- [395] Rubaiy H.N., “A short guide to electrophysiology and ion channels,” *Journal of Pharmacy and Pharmaceutical Sciences*, vol. 20, no. 1, pp. 48–67, 2017.
- [396] E. Neher, B. Sakmann, and J. H. Steinbach, “The extracellular patch clamp: A method for resolving currents through individual open channels in biological membranes,” *Pflügers Archiv European Journal of Physiology*, vol. 375, no. 2, pp. 219–228, 1978, doi: 10.1007/BF00584247.
- [397] A. L. Hodgkin and A. F. Huxley, “Resting and action potentials in single nerve fibres,” *The Journal of Physiology*, vol. 104, no. 2, pp. 176–195, 1945, doi: 10.1113/jphysiol.1945.sp004114.
- [398] M. E. Spira, N. Shmoel, S. H. M. Huang, and H. Erez, “Multisite attenuated intracellular recordings by extracellular multielectrode arrays, a perspective,” *Frontiers in Neuroscience*, vol. 12, no. APR, pp. 1–8, 2018, doi: 10.3389/fnins.2018.00212.
- [399] J. J. Jun *et al.*, “Fully integrated silicon probes for high-density recording of neural activity,” *Nature*, vol. 551, no. 7679, pp. 232–236, 2017, doi: 10.1038/nature24636.
- [400] M. Z. Lin and M. J. Schnitzer, “Genetically encoded indicators of neuronal activity,” *Nature Neuroscience*, vol. 19, no. 9, pp. 1142–1153, 2016, doi: 10.1038/nn.4359.
- [401] S. N. Cohen, A. C. Y. Chang, H. W. Boyer, and R. B. Helling, “Construction of biologically functional bacterial plasmids in vitro,” *Proc Natl Acad Sci U S A*, vol. 70, no. 11, pp. 3240–3244, 1973, doi: 10.1073/pnas.70.11.3240.
- [402] J. F. Morrow, S. N. Cohen, A. C. Y. Chang, H. W. Boyer, H. M. Goodman, and R. B. Helling, “Replication and transcription of eukaryotic DNA in *Escherichia coli*,” *Proc Natl Acad Sci U S A*, vol. 71, no. 5, pp. 1743–1747, 1974, doi: 10.1073/pnas.71.5.1743.
- [403] S. N. Cohen, “DNA cloning: A personal view after 40 years,” *Proc Natl Acad Sci U S A*, vol. 110, no. 39, pp. 15521–15529, 2013, doi: 10.1073/pnas.1313397110.
- [404] E. S. Lein, E. M. Callaway, T. D. Albright, and F. H. Gage, “Redefining the boundaries of the hippocampal CA2 subfield in the mouse using gene expression and 3-dimensional reconstruction,” *Journal of Comparative Neurology*, vol. 485, no. 1, pp. 1–10, 2005, doi: 10.1002/cne.20426.
- [405] E. S. Lein *et al.*, “Genome-wide atlas of gene expression in the adult mouse brain,” *Nature*, vol. 445, no. 7124, pp. 168–176, 2007, doi: 10.1038/nature05453.
- [406] A. R. Jones, C. C. Overly, and S. M. Sunkin, “The allen brain atlas: 5 years and beyond,” *Nature Reviews Neuroscience*, vol. 10, no. 11, pp. 821–828, 2009, doi: 10.1038/nrn2722.
- [407] Z. Zeng, N. Miao, and T. Sun, “Revealing cellular and molecular complexity of the central nervous system using single cell sequencing,” *Stem Cell Research and Therapy*, vol. 9, no. 1, pp. 1–11, 2018, doi: 10.1186/s13287-018-0985-z.
- [408] F. Tang *et al.*, “mRNA-Seq whole-transcriptome analysis of a single cell,” *Nature Methods*, vol. 6, no. 5, pp. 377–382, 2009, doi: 10.1038/nmeth.1315.
- [409] J. D. Buenrostro *et al.*, “Single-cell chromatin accessibility reveals principles of regulatory variation,” *Nature*, vol. 523, no. 7561, pp. 486–490, 2015, doi: 10.1038/nature14590.
- [410] D. A. Cusanovich *et al.*, “The cis-regulatory dynamics of embryonic development at single-cell resolution,” *Nature*, vol. 555, no. 7697, pp. 538–542, 2018, doi: 10.1038/nature25981.
- [411] R. Stark, M. Grzelak, and J. Hadfield, “RNA sequencing: the teenage years,” *Nature Reviews Genetics*, vol. 20, no. 11, pp. 631–656, 2019, doi: 10.1038/s41576-019-0150-2.
- [412] D. Ramsköld *et al.*, “Full-Length mRNA-Seq from single cell levels of RNA and individual circulating tumor cells,” vol. 30, no. 8, pp. 777–782, 2012, doi: 10.1038/nbt.2282.Full-Length.
- [413] T. Hashimshony, F. Wagner, N. Sher, and I. Yanai, “CEL-Seq: Single-Cell RNA-Seq by Multiplexed Linear Amplification,” *Cell Reports*, vol. 2, no. 3, pp. 666–673, 2012, doi: 10.1016/j.celrep.2012.08.003.
- [414] E. Z. Macosko *et al.*, “Highly parallel genome-wide expression profiling of individual cells using nanoliter droplets,” *Cell*, vol. 161, no. 4, pp. 1202–1214, 2015, doi: 10.1016/j.cell.2015.05.002.Highly.
- [415] Y. Sasagawa *et al.*, “Quartz-Seq: A highly reproducible and sensitive single-cell RNA sequencing method, reveals nongenetic gene-expression heterogeneity,” *Genome Biology*, vol. 14, no. 4, p. R31, 2013, doi: 10.1186/gb-2013-14-4-r31.
- [416] X. Han *et al.*, “Mapping the Mouse Cell Atlas by Microwell-Seq,” *Cell*, vol. 172, no. 5, pp. 1091–1107.e17, 2018, doi: 10.1016/j.cell.2018.02.001.

- [417] T. Hayashi, H. Ozaki, Y. Sasagawa, M. Umeda, H. Danno, and I. Nikaido, “Single-cell full-length total RNA sequencing uncovers dynamics of recursive splicing and enhancer RNAs,” *Nature Communications*, vol. 9, no. 1, 2018, doi: 10.1038/s41467-018-02866-0.
- [418] T. Kouno *et al.*, “C1 CAGE detects transcription start sites and enhancer activity at single-cell resolution,” *Nature Communications*, vol. 10, no. 1, 2019, doi: 10.1038/s41467-018-08126-5.
- [419] Y. Kashima, Y. Sakamoto, K. Kaneko, M. Seki, Y. Suzuki, and A. Suzuki, “Single-cell sequencing techniques from individual to multiomics analyses,” *Experimental and Molecular Medicine*, vol. 52, no. 9, pp. 1419–1427, 2020, doi: 10.1038/s12276-020-00499-2.
- [420] S. Baek and I. Lee, “Single-cell ATAC sequencing analysis: From data preprocessing to hypothesis generation,” *Computational and Structural Biotechnology Journal*, vol. 18, pp. 1429–1439, 2020, doi: 10.1016/j.csbj.2020.06.012.
- [421] N. Khouri-Farah, Q. Guo, K. Morgan, J. Shin, and J. Y. H. Li, “Integrated single-cell transcriptomic and epigenetic analyses of cell-state transition and lineage commitment in the embryonic mouse cerebellum,” *bioRxiv*, vol. 9156, no. April, p. 2021.08.08.455565, 2021, [Online]. Available: <https://www.biorxiv.org/content/10.1101/2021.08.08.455565v1%0Ahttps://www.biorxiv.org/content/10.1101/2021.08.08.455565v1.abstract>
- [422] B. Tasic *et al.*, “Shared and distinct transcriptomic cell types across neocortical areas,” *Nature*, vol. 563, no. 7729, pp. 72–78, 2018, doi: 10.1038/s41586-018-0654-5.
- [423] A. B. Muñoz-Manchado *et al.*, “Diversity of Interneurons in the Dorsal Striatum Revealed by Single-Cell RNA Sequencing and PatchSeq,” *Cell Reports*, vol. 24, no. 8, pp. 2179–2190.e7, 2018, doi: 10.1016/j.celrep.2018.07.053.
- [424] J. Cao *et al.*, “The single cell transcriptional landscape of mammalian organogenesis,” vol. 566, no. 7745, pp. 496–502, 2019, doi: 10.1038/s41586-019-0969-x.The.
- [425] B. Pijuan-Sala *et al.*, “A single-cell molecular map of mouse gastrulation and early organogenesis,” *Nature*, vol. 566, no. 7745, pp. 490–495, 2019, doi: 10.1038/s41586-019-0933-9.
- [426] C. Mayer *et al.*, “Developmental diversification of cortical inhibitory interneurons,” *Nature*, vol. 555, no. 7697, pp. 457–462, 2018, doi: 10.1038/nature25999.
- [427] K. Leto *et al.*, “Laminar fate and phenotype specification of cerebellar GABAergic interneurons,” *Journal of Neuroscience*, vol. 29, no. 21, pp. 7079–7091, 2009, doi: 10.1523/JNEUROSCI.0957-09.2009.
- [428] C. Sotelo, “Molecular Layer Interneurons of the Cerebellum: Developmental and Morphological Aspects,” *Cerebellum*, vol. 14, no. 5, pp. 534–556, 2015, doi: 10.1007/s12311-015-0648-x.
- [429] I. Gupta *et al.*, “Single-cell isoform RNA sequencing characterizes isoforms in thousands of cerebellar cells,” *Nature Biotechnology*, vol. 36, no. 12, pp. 1197–1202, 2018, doi: 10.1038/nbt.4259.
- [430] J. Peng *et al.*, “Single-cell transcriptomes reveal molecular specializations of neuronal cell types in the developing cerebellum,” *Journal of Molecular Cell Biology*, vol. 11, no. 8, pp. 636–648, 2019, doi: 10.1093/jmcb/mjy089.
- [431] D. E. Buchholz *et al.*, “Novel genetic features of human and mouse Purkinje cell differentiation defined by comparative transcriptomics,” *Proc Natl Acad Sci U S A*, vol. 117, no. 26, pp. 15085–15095, 2020, doi: 10.1073/pnas.2000102117.
- [432] A. Sagner, I. Zhang, T. Watson, J. Lazaro, M. Melchionda, and J. Briscoe, *A shared transcriptional code orchestrates temporal patterning of the central nervous system*, vol. 19, no. 11. 2021. Doi: 10.1371/journal.pbio.3001450.
- [433] C. Trapnell *et al.*, “Pseudo-temporal ordering of individual cells reveals dynamics and regulators of cell fate decisions,” *Nat Biotechnol*, vol. 32, no. 4, pp. 381–386, 2014, doi: 10.1038/nbt.2859.Pseudo-temporal.
- [434] X. Qiu *et al.*, “Reversed graph embedding resolves complex single-cell trajectories,” *Nature Methods*, vol. 14, no. 10, pp. 979–982, 2017, doi: 10.1038/nmeth.4402.
- [435] M. Guo, E. L. Bao, M. Wagner, J. A. Whitsett, and Y. Xu, “SLICE: Determining cell differentiation and lineage based on single cell entropy,” *Nucleic Acids Research*, vol. 45, no. 7, pp. 1–14, 2017, doi: 10.1093/nar/gkw1278.
- [436] Z. Ji and H. Ji, “TSCAN: Pseudo-time reconstruction and evaluation in single-cell RNA-seq analysis,” *Nucleic Acids Research*, vol. 44, no. 13, p. e117, 2016, doi: 10.1093/nar/gkw430.
- [437] J. Shin *et al.*, “Single-Cell RNA-Seq with Waterfall Reveals Molecular Cascades underlying Adult Neurogenesis,” *Cell Stem Cell*, vol. 17, no. 3, pp. 360–372, 2015, doi: 10.1016/j.stem.2015.07.013.

- [438] M. Eugenio *et al.*, “Bifurcation analysis of single-cell gene expression data reveals epigenetic landscape,” *Proc Natl Acad Sci U S A*, vol. 111, no. 52, pp. E5643–E5650, 2014, doi: 10.1073/pnas.1408993111.
- [439] 9 Kelly Street^{1,8}, Davide Risso², Russell B. Fletcher³, Diya Das^{3,9}, John Ngai^{3,6,7}, Nir Yosef^{4,8}, Elizabeth Purdom^{5,8} and Sandrine Dudoit^{1,5,8}, “Slingshot: cell lineage and pseudotime inference for single-cell transcriptomics,” pp. 1–16, 2010.
- [440] S. C. Bendall *et al.*, “Single-cell trajectory detection uncovers progression and regulatory coordination in human B cell development,” *Cell*, vol. 157, no. 3, pp. 714–725, 2014, doi: 10.1016/j.cell.2014.04.005.
- [441] M. Setty *et al.*, “Wishbone identifies bifurcating developmental trajectories from single-cell data,” *Nature Biotechnology*, vol. 34, no. 6, pp. 637–645, 2016, doi: 10.1038/nbt.3569.
- [442] D. van Dijk *et al.*, “Recovering Gene Interactions from Single-Cell Data Using Data Diffusion,” *Cell*, vol. 174, no. 3, pp. 716–729.e27, 2018, doi: 10.1016/j.cell.2018.05.061.
- [443] F. A. Wolf *et al.*, “PAGA: graph abstraction reconciles clustering with trajectory inference through a topology preserving map of single cells,” *Genome Biology*, vol. 20, no. 1, pp. 1–9, 2019, doi: 10.1186/s13059-019-1663-x.
- [444] C. Weinreb, S. Wolock, B. K. Tusi, M. Socolovsky, and A. M. Klein, “Fundamental limits on dynamic inference from single-cell snapshots,” *Proc Natl Acad Sci U S A*, vol. 115, no. 10, pp. E2467–E2476, 2018, doi: 10.1073/pnas.1714723115.
- [445] G. la Manno *et al.*, “RNA velocity of single cells,” *Nature*, vol. 560, no. 7719, pp. 494–498, 2018, doi: 10.1038/s41586-018-0414-6.
- [446] L. Kester and A. van Oudenaarden, “Single-Cell Transcriptomics Meets Lineage Tracing,” *Cell Stem Cell*, vol. 23, no. 2, pp. 166–179, 2018, doi: 10.1016/j.stem.2018.04.014.
- [447] A. McKenna and J. A. Gagnon, “Recording development with single cell dynamic lineage tracing,” *Development (Cambridge)*, vol. 146, no. 12, pp. 1–10, 2019, doi: 10.1242/dev.169730.
- [448] D. E. Wagner and A. M. Klein, “Lineage tracing meets single-cell omics: opportunities and challenges,” *Nat Rev Genet*, 2020, doi: 10.1038/s41576-020-0223-2.
- [449] R. C. Bandler *et al.*, “Single-cell delineation of lineage and genetic identity in the mouse brain,” *Nature*, vol. 601, no. 7893, pp. 404–409, 2022, doi: 10.1038/s41586-021-04237-0.
- [450] R. Kalhor *et al.*, “Developmental barcoding of whole mouse via homing CRISPR,” *Science (1979)*, vol. 361, no. 6405, 2018, doi: 10.1126/science.aat9804.
- [451] R. J. Ihry *et al.*, “P53 inhibits CRISPR-Cas9 engineering in human pluripotent stem cells,” *Nature Medicine*, vol. 24, no. 7, pp. 939–946, 2018, doi: 10.1038/s41591-018-0050-6.
- [452] E. Haapaniemi, S. Botla, J. Persson, B. Schmierer, and J. Taipale, “CRISPR-Cas9 genome editing induces a p53-mediated DNA damage response,” *Nature Medicine*, vol. 24, no. 7, pp. 927–930, 2018, doi: 10.1038/s41591-018-0049-z.
- [453] M. M. Chan *et al.*, “Molecular recording of mammalian embryogenesis,” *Nature*, vol. 570, no. 7759, pp. 77–82, 2019, doi: 10.1038/s41586-019-1184-5.
- [454] S. Bowling *et al.*, “Erratum: An Engineered CRISPR-Cas9 Mouse Line for Simultaneous Readout of Lineage Histories and Gene Expression Profiles in Single Cells (*Cell* (2020) 181(6) (1410–1422.e27), (S0092867420305547), (10.1016/j.cell.2020.04.048)),” *Cell*, vol. 181, no. 7, pp. 1693–1694, 2020, doi: 10.1016/j.cell.2020.06.018.
- [455] B. Spanjaard *et al.*, “Simultaneous lineage tracing and cell-type identification using CrIsPr-Cas9-induced genetic scars,” *Nature Biotechnology*, vol. 36, no. 5, pp. 469–473, 2018, doi: 10.1038/nbt.4124.
- [456] S. Hormoz, Z. S. Singer, J. M. Linton, Y. E. Antebi, B. I. Shraiman, and M. B. Elowitz, “Inferring Cell-State Transition Dynamics from Lineage Trees and Endpoint Single-Cell Measurements,” *Cell Systems*, vol. 3, no. 5, pp. 419–433.e8, 2016, doi: 10.1016/j.cels.2016.10.015.
- [457] R. J. Kimmerling *et al.*, “A microfluidic platform enabling single-cell RNA-seq of multigenerational lineages,” *Nature Communications*, vol. 7, 2016, doi: 10.1038/ncomms10220.
- [458] T. Noel, Q. S. Wang, A. Greka, and J. L. Marshall, “Principles of Spatial Transcriptomics Analysis: A Practical Walk-Through in Kidney Tissue,” *Frontiers in Physiology*, vol. 12, no. January, pp. 1–7, 2022, doi: 10.3389/fphys.2021.809346.
- [459] A. Rao, D. Barkley, G. S. França, and I. Yanai, “Exploring tissue architecture using spatial transcriptomics,” *Nature*, vol. 596, no. 7871, pp. 211–220, 2021, doi: 10.1038/s41586-021-03634-9.

- [460] A. Zeisel *et al.*, “Molecular Architecture of the Mouse Nervous System,” *Cell*, vol. 174, no. 4, pp. 999-1014.e22, 2018, doi: 10.1016/j.cell.2018.06.021.
- [461] A. Chen *et al.*, “Spatiotemporal transcriptomic atlas of mouse organogenesis using DNA nanoball patterned arrays,” *bioRxiv*, p. 2021.01.17.427004, 2021, [Online]. Available: <https://www.biorxiv.org/content/10.1101/2021.01.17.427004v3%0Ahttps://www.biorxiv.org/content/10.1101/2021.01.17.427004v3.abstract>
- [462] D. Gyllborg *et al.*, “Hybridization-based in situ sequencing (HyBISS) for spatially resolved transcriptomics in human and mouse brain tissue,” *Nucleic Acids Research*, vol. 48, no. 19, p. E112, 2020, doi: 10.1093/nar/gkaa792.
- [463] S. G. Rodriques *et al.*, “Slide-seq: A Scalable Technology for Measuring Genome-Wide Expression at High Spatial Resolution,” *Science (1979)*, vol. 363, no. 6434, pp. 1463–1467, 2019, doi: 10.5281/zenodo.2571615.
- [464] E. Lubeck, A. F. Coskun, T. Zhiyentayev, M. Ahmad, and L. Cai, “Single-cell in situ RNA profiling by sequential hybridization,” *Nature Methods*, vol. 11, no. 4, pp. 360–361, 2014, doi: 10.1038/nmeth.2892.
- [465] C.-H. L. Eng *et al.*, “Transcriptome-scale super-resolved imaging in tissues by RNA seqFISH+,” *Nature*, vol. 568, no. 7751, pp. 235–239, 2019, doi: 10.1038/s41586-019-1049-y.Transcriptome-scale.
- [466] C. Xia, J. Fan, G. Emanuel, J. Hao, and X. Zhuang, “Spatial transcriptome profiling by MERFISH reveals subcellular RNA compartmentalization and cell cycle-dependent gene expression,” *Proc Natl Acad Sci U S A*, vol. 116, no. 39, pp. 19490–19499, 2019, doi: 10.1073/pnas.1912459116.
- [467] S. K. Longo, M. G. Guo, A. L. Ji, and P. A. Khavari, “Integrating single-cell and spatial transcriptomics to elucidate intercellular tissue dynamics,” *Nature Reviews Genetics*, vol. 22, no. 10, pp. 627–644, 2021, doi: 10.1038/s41576-021-00370-8.
- [468] D. Lähnemann *et al.*, *Eleven grand challenges in single-cell data science*, vol. 21, no. 1. *Genome Biology*, 2020. Doi: 10.1186/s13059-020-1926-6.
- [469] L. Ng *et al.*, “An anatomic gene expression atlas of the adult mouse brain,” *Nature Neuroscience*, vol. 12, no. 3, pp. 356–362, 2009, doi: 10.1038/nm.2281.
- [470] C. Lau *et al.*, “Exploration and visualization of gene expression with neuroanatomy in the adult mouse brain,” *BMC Bioinformatics*, vol. 9, pp. 1–11, 2008, doi: 10.1186/1471-2105-9-153.
- [471] L. Ng *et al.*, “NeuroBlast: a 3D spatial homology search tool for gene expression,” *BMC Neuroscience*, vol. 8, no. S2, pp. 2–3, 2007, doi: 10.1186/1471-2202-8-s2-p11.
- [472] S. F. Altschul, W. Gish, W. Miller, E. W. Myers, and D. J. Lipman, “Basic local alignment search tool,” *Journal of Molecular Biology*, vol. 215, no. 3, pp. 403–410, 1990, doi: 10.1016/S0022-2836(05)80360-2.
- [473] G. la Manno *et al.*, “Molecular architecture of the developing mouse brain,” *Nature*, vol. 596, no. 7870, pp. 92–96, 2021, doi: 10.1038/s41586-021-03775-x.
- [474] A. B. Rosenberg *et al.*, “Single-cell profiling of the developing mouse brain and spinal cord with split-pool barcoding,” *Science (1979)*, vol. 360, no. 6385, pp. 176–182, 2018, doi: 10.1126/science.aam8999.
- [475] T. Biancalini *et al.*, “Deep learning and alignment of spatially-resolved whole transcriptomes of single cells in the mouse brain with Tangram,” *bioRxiv*, 2020.
- [476] A. Saunders *et al.*, “Molecular Diversity and Specializations among the Cells of the Adult Mouse Brain,” *Cell*, vol. 174, no. 4, pp. 1015-1030.e16, 2018, doi: 10.1016/j.cell.2018.07.028.
- [477] M. Heiman, R. Kulicke, R. J. Fenster, P. Greengard, and N. Heintz, “Cell-Type-Specific mRNA Purification by Translating Ribosome Affinity Purification (TRAP),” *Nat Protoc*, vol. 9, no. 6, pp. 1-1282–1291, 2014, doi: 10.1038/nprot.2014.085.Cell-Type-Specific.
- [478] T. Hirata *et al.*, “NeuroGT: A brain atlas of neurogenic tagging CreER drivers for birthdate-based classification and manipulation of mouse neurons,” *Cell Reports Methods*, vol. 1, no. 3, p. 100012, 2021, doi: 10.1016/j.crmeth.2021.100012.
- [479] J. D. Welch, V. Kozareva, A. Ferreira, C. Vanderburg, C. Martin, and E. Z. Macosko, “Single-Cell Multi-omic Integration Compares and Contrasts Features of Brain Cell Identity,” *Cell*, vol. 177, no. 7, pp. 1873-1887.e17, 2019, doi: 10.1016/j.cell.2019.05.006.
- [480] V. Kleshchevnikov *et al.*, “Cell2location maps fine-grained cell types in spatial transcriptomics,” *Nature Biotechnology*, 2022, doi: 10.1038/s41587-021-01139-4.
- [481] N. Moriel, E. Senel, N. Friedman, N. Rajewsky, N. Karaiskos, and M. Nitzan, “NovoSpaRc: flexible spatial reconstruction of single-cell gene expression with optimal transport,” *Nature Protocols*, vol. 16, no. 9, pp. 4177–4200, 2021, doi: 10.1038/s41596-021-00573-7.

- [482] B. J. C. Quah and C. R. Parish, "The Use of Carboxyfluorescein Diacetate Succinimidyl Ester (CFSE) to Monitor Lymphocyte Proliferation 3) Representative Results," no. October, pp. 4–7, 2010, doi: 10.3791/2259.
- [483] B. Martynoga, H. Morrison, D. J. Price, and J. O. Mason, "Foxg1 is required for specification of ventral telencephalon and region-specific regulation of dorsal telencephalic precursor proliferation and apoptosis," *Developmental Biology*, vol. 283, no. 1, pp. 113–127, 2005, doi: 10.1016/j.ydbio.2005.04.005.
- [484] L. Harris, O. Zalucki, and M. Piper, "BrdU/EdU dual labeling to determine the cell-cycle dynamics of defined cellular subpopulations," *Journal of Molecular Histology*, vol. 49, no. 3, pp. 229–234, 2018, doi: 10.1007/s10735-018-9761-8.
- [485] R. S. Nowakowski, S. B. Lewin, and M. W. Miller, "Bromodeoxyuridine immunohistochemical determination of the lengths of the cell cycle and the DNA-synthetic phase for an anatomically defined population," *Journal of Neurocytology*, vol. 18, no. 3, pp. 311–318, 1989, doi: 10.1007/BF01190834.
- [486] F. Wang *et al.*, "RNAscope: A novel in situ RNA analysis platform for formalin-fixed, paraffin-embedded tissues," *Journal of Molecular Diagnostics*, vol. 14, no. 1, pp. 22–29, 2012, doi: 10.1016/j.jmoldx.2011.08.002.
- [487] F. V. Dastjerdi, G. G. Consalez, and R. Hawkes, "Pattern formation during development of the embryonic cerebellum," *Frontiers in Neuroanatomy*, vol. 6, no. April, pp. 1–11, 2012, doi: 10.3389/fnana.2012.00010.
- [488] M. Rahimi-Balaei, H. Bergen, J. Kong, and H. Marzban, "Neuronal migration during development of the cerebellum," *Frontiers in Cellular Neuroscience*, vol. 12, no. December, pp. 1–16, 2018, doi: 10.3389/fncel.2018.00484.
- [489] L. R. Martinez *et al.*, *Components of endocannabinoid signaling system are expressed in the perinatal mouse cerebellum and required for its normal development*, vol. 7, no. 2. 2020. Doi: 10.1523/ENEURO.0471-19.2020.
- [490] A. K. Lawton *et al.*, "Cerebellar folding is initiated by mechanical constraints on a fluid-like layer without a cellular pre-pattern," *Elife*, vol. 8, pp. 1–22, 2019, doi: 10.7554/eLife.45019.
- [491] E. M. McNeill, M. Klöckner-Bormann, E. C. Roesler, L. E. Talton, D. Moechars, and M. Clagett-Dame, "Nav2 hypomorphic mutant mice are ataxic and exhibit abnormalities in cerebellar development," *Developmental Biology*, vol. 353, no. 2, pp. 331–343, 2011, doi: 10.1016/j.ydbio.2011.03.008.
- [492] U. Schmidt, M. Weigert, C. Broaddus, and G. Myers, "Cell detection with star-convex polygons," *Lecture Notes in Computer Science (including subseries Lecture Notes in Artificial Intelligence and Lecture Notes in Bioinformatics)*, vol. 11071 LNCS, pp. 265–273, 2018, doi: 10.1007/978-3-030-00934-2_30.
- [493] F. Cremisi, A. Philpott, and S. I. Ohnuma, "Cell cycle and cell fate interactions in neural development," *Current Opinion in Neurobiology*, vol. 13, no. 1, pp. 26–33, 2003, doi: 10.1016/S0959-4388(03)00005-9.
- [494] M. Hashimoto and K. Mikoshiba, "Mediolateral Compartmentalization of the Cerebellum Is Determined on the 'Birth Date' of Purkinje Cells," *Journal of Neuroscience*, vol. 23, no. 36, pp. 11342–11351, 2003, doi: 10.1523/jneurosci.23-36-11342.2003.

~ ~ ~ ~ ~ AAAA
~ ~ ~ ~ ~
~ ~ ~ ~ ~
~ ~ ~ ~ ~
~ ~ ~ ~ ~
~ ~ ~ ~ ~

